University of Tasmania

Doctoral Thesis

Diagnosing the relation between ocean circulation, mixing and water-mass transformation from an ocean hydrography and air-sea fluxes.

Sjoerd Groeskamp

MSc. in Meteorology, Physical Oceanography and Climate

Supervisors:
Trevor J. McDougall
Bernadette M. Sloyan
Jan D. Zika
Nathan L. Bindoff

A thesis submitted in complete fulfilment of the requirements of the Doctor of Philosophy in the CSIRO-UTAS PhD Program in Quantitative Marine Science.

Institute for Marine and Antarctic Studies
(IMAS)

April 2015

Declaration of Authorship

This thesis contains no material which has been accepted for a degree or a diploma by the University or any other institution, except by way of background information and duly acknowledged in the thesis, and to the best of my knowledge and belief, no material previously published or written by another person except where due acknowledgment is made in the text of the thesis, nor does the thesis contain any material that infringes copyright.

This thesis may be made available for loan and limited copying and communication in accordance with the Copyright Act 1968.

Sjoerd Groeskamp

Signed: _____

Date: _____

Statement of Co-Authorship

The following people and institutions contributed to the publication of work undertaken as part of this thesis:

Sjoerd Groeskamp[1,2,3]
Trevor J. McDougall[4]
Bernadette M. Sloyan[1]
Jan D. Zika[6]
Frédéric Laliberté[7]
Peter C. McIntosh[5]
Stephen M. Griffies[8]

The related institutions:

[1] *CSIRO Ocean and Atmosphere Flagship, Hobart, Australia*

[2] *Institute for Marine and Antarctic Studies, University of Tasmania, Hobart, Australia*

[3] *Centre of Excellence for Climate System Science, Hobart, Tasmania, Australia*

[4] *School of Mathematics and Statistics, University of New South Wales, Sydney, Australia*

[6] *University of Southampton, National Oceanography Centre, Southampton, United Kingdom*

[7] *Department of Physics, University of Toronto, Toronto, Ontario, Canada*

[8] *NOAA/Geophysical Fluid Dynamics Laboratory, Princeton, New Jersey, USA*

The authors details and their roles:

Paper 1, Chapter 2, On geometrical aspects of interior ocean mixing

Trevor J. McDougall[4], Sjoerd Groeskamp[1,2,3] and Stephen M. Griffies[8].

This paper is chapter 2 of this PhD thesis and is published in the Journal of Physical Oceanography as McDougall et al. (2014).

The candidate pointed out the incorrect representation of epineutral tracer gradients in ocean models, as used in the past 2 decades. The lead author picked up these mistakes and understood and quantified the implications. During many discussions and correspondence the lead author and the candidate wrote a draft of this chapter. The draft was sent to the third author who then made a significant contribution to the refinement and presentation of the work.

Paper 2, Chapter 3, The representation of ocean circulation and variability in thermodynamic coordinates

Sjoerd Groeskamp[1,2,3], Jan D. Zika[6], Trevor J. McDougall[4], Bernadette M. Sloyan[1,5] and Frédéric Laliberté[7].

This paper is chapter 3 of this PhD thesis and is published in the Journal of Physical Oceanography as Groeskamp et al. (2014a).

The candidate was the primary author and developer of this theory and formalism. Authors 2 and 5 mainly contributed to the ideas. Authors 2 and 3 contributed to the development of the theory and formalism and authors 4 and 5 contributed to the interpretation, refinement and presentation.

Paper 3, Chapter 4, A Thermohaline Inverse Method For Estimating Diathermohaline Circulation and Mixing

Sjoerd Groeskamp[1,2,3], Jan D. Zika[6], Bernadette M. Sloyan[1,5], Trevor J. McDougall[4] and Peter C. McIntosh[5].

This paper is chapter 4 of this PhD thesis and is published in the Journal of Physical Oceanography as Groeskamp et al. (2014b).

The candidate was the primary author and developer of this theory and formalism. Author 2 contributed to the ideas and theory. Authors 3 and 4 contributed to the development of the theory, refinement and presentation. Author 5 contributed to the development and correct implementation of the inverse technique.

Chapter 5, Diathermohaline Circulation and Mixing; An Inverse Estimate From Observations

Sjoerd Groeskamp[1,2,3], Bernadette M. Sloyan[1,5], Trevor J. McDougall[4] and Jan D. Zika[6].

A concise version of Chapter 5 of this thesis chapter will be submitted to Nature Geosciences.

The candidate was the primary author and developer of this theory and formalism and did the majority of the work that applied the tools of Chapter 4 to observations. Authors 2 and 3 have had a significant contribution to details associated with the application and with the discussion of the results, while author 4 was involved in the interpretation, refinement and presentation of the results.

Abstract

The aim of this thesis is to understand the relationship between surface freshwater and heat fluxes, (interior) ocean mixing and the resulting changes in the ocean circulation and distribution of water-masses.

The ocean circulation is analysed in Absolute Salinity (S_A) and Conservative Temperature (Θ) coordinates. It is separated into 1) an advective component related to geographical displacements in the direction normal to S_A and Θ iso-surfaces, and quantified by the advective thermohaline streamfunction $\Psi^{\mathrm{adv}}_{S_\mathrm{A}\Theta}$, and 2) into a local component, related to local changes in S_A and Θ-values, without a geographical displacement, and quantified by the local (temporal) thermohaline streamfunction $\Psi^{\mathrm{loc}}_{S_\mathrm{A}\Theta}$. In this decomposition, the sum of the advective and local components of the circulation is given by the diathermohaline streamfunction $\Psi^{\mathrm{dia}}_{S_\mathrm{A}\Theta}$ and is directly related to the salt and heat fluxes of the surface forcing and ocean mixing. Interpretations of the streamfunctions is given and it is argued that the diathermohaline streamfunction provides a powerful tool for the analysis of and comparison amongst numerical ocean models and observational-based gridded climatologies.

The relation between $\Psi^{\mathrm{dia}}_{S_\mathrm{A}\Theta}$ and fluxes of salt and heat is expressed as the Thermohaline Inverse Method (THIM). The THIM uses conservation statements for volume, salt and heat in (S_A, Θ) coordinates to express the unknown $\Psi^{\mathrm{dia}}_{S_\mathrm{A}\Theta}$ as surface freshwater and heat fluxes, and mixing parameterised by a down-gradient epineutral diffusion coefficient, and an isotropic down-gradient turbulent diffusion coefficient of small scale mixing processes. The resulting system of equations that is solved in the THIM is tested against a numerical model and shown to provide accurate estimates of the unknowns ($\Psi^{\mathrm{dia}}_{S_\mathrm{A}\Theta}$, and the epineutral and small-scale diffusion coefficients).

The THIM has been applied to observations to obtain constrained estimates of the epineutral and small-scale diffusion coefficients and $\Psi^{\mathrm{dia}}_{S_\mathrm{A}\Theta}$. New insights in $\Psi^{\mathrm{dia}}_{S_\mathrm{A}\Theta}$ are revealed and the estimate of small-scale diffusion coefficient compares well with previous estimates. The estimates of the epineutral diffusion coefficient is about 50 times smaller than those typically used in coarse resolution climate models, suggesting that either the surfaces fluxes that are used under-estimate the production of epineutral anomalies of S_A and Θ or the epineutral diffusion coefficients commonly used in climate models are too large.

The geometry of interior ocean mixing is analysed and it is found that under the small-slope approximation there is a small gradient of tracer in a direction in which there is no actual epineutral gradient of tracer. The difference between the correct epineutral

tracer gradient and the small-slope approximation to it, is quantified and it is shown that it points in the direction of the thermal wind. The fraction of the epineutral flux in this direction is very small and is negligible for all foreseeable applications. Small-scale mixing processes act to diffuse tracers isotropically (i.e. directionally uniformly in space), hence it is a misnomer to call this process 'dianeutral diffusion'. Both realisations affect the diffusion tensor, and a more concise diffusion tensor is derived for use in ocean models.

The techniques, diagnostics and insights presented in this thesis lead to increased understanding of the relationship between ocean circulation and water-mass transformation due to ocean mixing and surface fluxes, and result in enhanced ability to model the ocean and its role in the climate system.

Contents

List of Figures

List of Tables

Dedicated to

My parents, Joop and Ria Groeskamp, and my wife, Malou Zuidema.

Chapter 1

Introduction

The work in this thesis is physical oceanography and is focused on understanding the ocean circulation and its relation with mixing and air-sea fluxes of salt and heat. This study provides new understanding of this relationship that can lead to a more accurate representation of the ocean in global scale ocean-atmosphere coupled climate models. This allows for a better understanding of the ocean and improved prediction of future climate.

1.1 Ocean circulation

One of the first applications of knowledge of the ocean circulation was the mapping of surface currents for shipping routes. The resulting maps, mainly for the Atlantic Ocean, showed the first evidence of large scale ocean circulation patterns including the ocean gyres and western boundary currents (Rennel, 1832). Rumford (1798) and Lenz (1845) combined these observations with that of deep temperature measurements by Ellis (1751), and presented the first conceptual model of a 3-dimensional (overturning) circulation by suggesting that cold water is subducted at the poles and returns to the surface near the equator.

By combining observations of ocean currents and tracers with newly developed theories, many scientists further developed our understanding of the ocean circulation towards the idea of a global 3-dimensional ocean circulation (Schott (1902), Brennecke (1921), Merz (1925), Spiess (1928), Wust (1935), Defant (1941) and Stommel (1957, 1958), amongst others). A detailed review of these advances is provided by Richardson (2008). Using this understanding it was Broecker (1982) who pieced all the evidence together to first raise the concept of a 'global conveyor belt', or in other words a globally interconnected

ocean circulation. This was then further developed by Gordon (1986), leading up to the now famous illustration of the 'Great Ocean Conveyor Belt' by Broecker (1987) (Fig. 1.1).

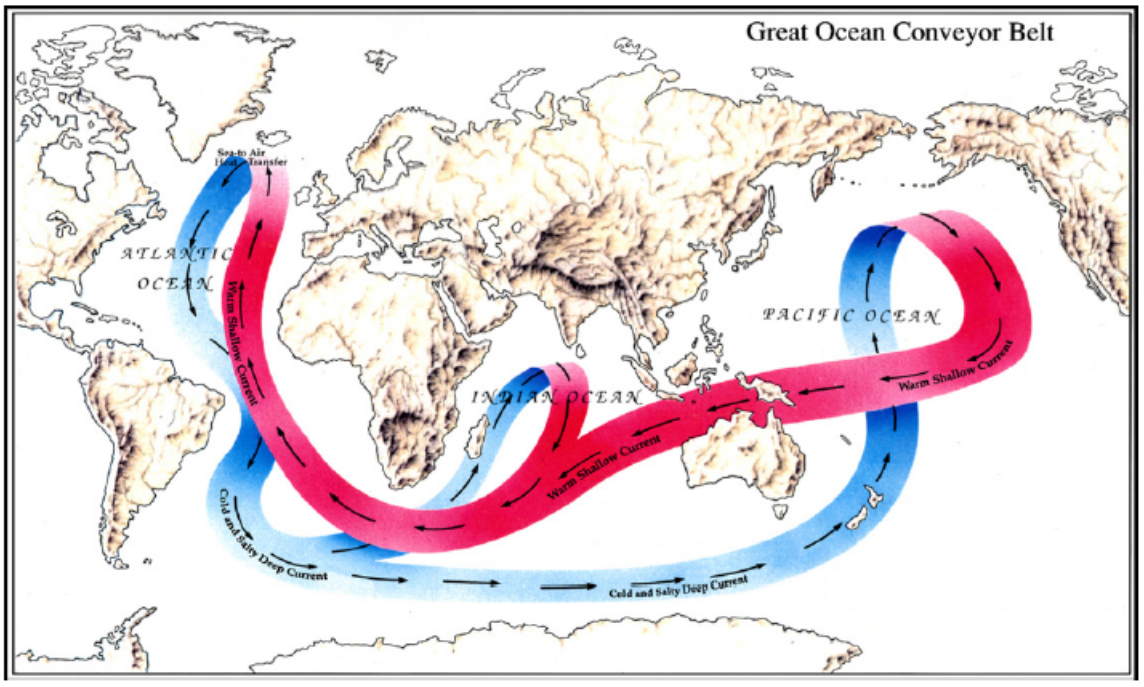

FIGURE 1.1: A colored version of the 'Great Global Conveyor' by Broecker (1987). The simplicity of this diagram is both its strength and weakness.

The simplicity of this diagram is both its strength and weakness. The diagram shows a schematic of a long term averaged globally interconnected ocean circulation with subduction in the North Atlantic due to deepwater formation. This subduction is a result of strong cooling at the surface leading to densification of surface seawater. The dense water then subduct and at great depths, flows towards the Indian Ocean and Pacific Ocean basins where this cold and dense water is warmed due to downward diffusion of heat by small-scale mixing processes. This warming makes the water in the ocean interior lighter, leading this water to rise to the surface. Once at the surface, winds lead to a net flow back to the North Atlantic, closing the great ocean conveyor.

Because of the simplicity of Broecker's diagram, it does not provide many details on flow fields (no ocean gyres, western boundary currents, eddies, etc) and does not show any variability of the flow strengths and direction. Also it does not include deep water formation in Antarctica and therefore does not include Antarctic Bottom Water formation. The diagram also ignores the effect of the circumpolar eastward winds around Antarctica that lead to a northward surface transport of water due to the Coriolis effect. This transport leads to wind driven Ekman transport, returning abyssal water to the surface along outcropping isopycnals. It is now thought that water below 2000m depth

is brought up to 2000m by small-scale turbulent mixing as suggested by Munk (1966). The water then moves at constant density towards the Southern Ocean, where it is then 'pulled' to the surface along isopycnals, by the wind-driven Ekman pumping as shown in a model by Toggweiler and Samuels (1998) and from observations by Sloyan and Rintoul (2001).

Most of the diagrams representing the global ocean circulation, since the publication of the 'Great Ocean Conveyor Belt' by Broecker (1987) (Fig. 1.1), do include these advances in our understanding (Gordon, 1991, Schmitz, 1995, Rahmstorf, 2002). A recent illustration of the global ocean circulation includes these new insights showing both diapycnal and isopycnal upwelling occurring for different water-masses, in different basins at different depths (Fig. 1.2).

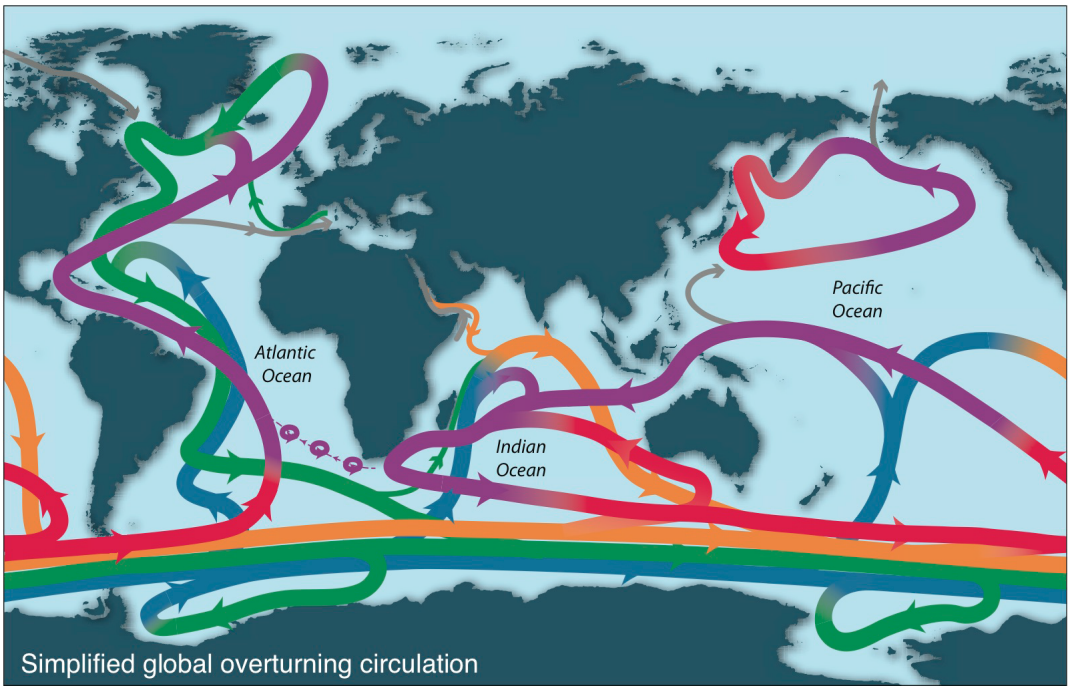

FIGURE 1.2: This schematic of the global overturning circulation is taken from Talley (2013). Purple (upper ocean and thermocline), red (denser thermocline and intermediate water), orange (Indian Deep Water and Pacific Deep Water), green (North Atlantic Deep Water), blue (Antarctic Bottom Water), grey (Bering Strait components; Mediterranean and Red Sea inflows).

1.2 Ocean Mixing

The global ocean circulation is of great importance for the earth's climate system through its ability to cycle and store freshwater, heat and biochemical tracers such as oxygen and carbon. Because mixing influences the (closure) of the ocean circulation, mixing also influences the earth's climate system. An improved understanding and quantification of

both the ocean circulation and its complex relation with mixing is therefore essential for our ability to understand and model the earths climate system.

To understand ocean mixing, neutral surfaces are used. A neutral surface is a surface along which a fluid parcel can move, without there being any restoring buoyancy forces acting upon it. Moving along this surface (the epineutral or isoneutral direction) is therefore easier than moving through this surface (the dianeutral direction). As a result of this directional preference of fluid parcel motion, the interior ocean mixing is parameterised as, 1) epineutral down-gradient tracer diffusion due to mesoscale eddies by means of an eddy diffusion coefficient K and, 2) small-scale isotropic down-gradient turbulent diffusion by means of a turbulent diffusion coefficient D. The ratio of the diffusivities in these different directions are typically in the order $K/D = 10^7$, meaning that the mixing processes in the epineutral direction are much more efficient than small-scale isotropic turbulent mixing (hereafter referred to as small-scale mixing). In Chapter 2 of this thesis, we will discuss new insights into the representation of interior mixing processes in ocean models. Here we also discuss the isotropic nature of D that has previously been regarded to be dianeutral (Redi, 1982, Griffies, 2004), or vertical in the small slope approximation (an approximation first used by Gent and McWilliams (1990) in which the angle of an isoneutral surface with the horizontal is assumed to be small enough to be neglected).

1.2.1 Small-Scale Mixing

Despite the relative smallness of small-scale mixing processes, they are critical in the simulation of present day ocean and climate and are a key element in closing the ocean's global overturning circulation, in particular for the deepest half of the ocean (Munk, 1966, Munk and Wunsch, 1998, Wunsch and Ferrari, 2004), and the transports involved are significant (Munk, 1966, Munk and Wunsch, 1998, Ganachaud and Wunsch, 2000, Sloyan and Rintoul, 2001, Wunsch and Ferrari, 2004, Nikurashin and Ferrari, 2013).

One of the first estimate of D was obtained by Munk (1966), by deriving a balance between (vertical) ocean advection and mixing to obtain global, steady state, estimates of $D = 1.3 \text{ x } 10^{-4} \text{ m}^2 \text{ s}^{-1}$, using estimates of ocean circulation from observations. Sources of this small-scale mixing are wind generated mixing by breaking of near-inertial waves at the surface and in the ocean interior (D'Asaro, 1985, Alford, 2001, Alford et al., 2011), dissipation of the internal tides (Nycander, 2005) and generation and dissipation of lee waves (Nikurashin and Ferrari, 2011). The combination of these mechanism does not result in a global spatially similar amount of small-scale mixing (Fig. 1.3). Observations have shown that D increases toward the ocean floor with maximum values exceeding

$D = 1$ x 10^{-3} m^2 s^{-1} in regions of rough topography due to dissipation of the internal tides near the ocean floor (within 500m), and generation and dissipation of lee waves (Polzin et al., 1997, Garabato et al., 2004, Ledwell et al., 2010, St. Laurent et al., 2012, Waterhouse et al., 2014).

Different parameterisations have been developed to represent the small-scale interior ocean mixing. Some represent the general tendency of increased mixing near topography (Bryan and Lewis, 1979, St. Laurent et al., 2002), while others focus on the mixing due to breaking internal waves initiated from the internal tide (Polzin, 2009, Melet et al., 2012, Nikurashin and Ferrari, 2013). The sensitivity of ocean and climate models to the explicit values of vertical mixing argues that much more research in this area of physical oceanography is needed (Simmons, 2004, Melet et al., 2012, Garabato, 2012). Obtaining observational based estimates of D will help to constrain the variability in the existing parameterisations used to represent the effect of small-scale mixing.

1.2.2 Mesoscale Mixing

The mesoscale eddy diffusion coefficient K parameterises tracer diffusion due to eddies that are not resolved by the (numerical) model. The capability to resolve these eddy-based tracer fluxes depends on the resolution of the model. Therefore as a rule of thumb the higher (lower) the resolution of a model, the better (worse) the eddy transports are resolved and therefore the lower (larger) the diffusion coefficients (K) needs to be to parameterise the unresolved eddy component. As eddy transports dominate dispersion of particles and mixing of tracers on large spatial and temporal time scales, a correct parameterisation of the spatial and temporal varying effect of eddies in coarse-resolution climate models is essential.

Historically a typical constant value of $K \approx 1000$ m^2 s^{-1} has been used in (numerical) models. However observations have showed highly spatial varying eddy mixing fields, emphasising the need for a parameterisation (K) that takes into account spatial and temporal variability (Holloway (1986), Zhurbas and Oh (2004), Abernathey and Marshall (2013), Klocker and Abernathey (2013) amongst others, Fig. 1.4). Allowing for spatial variation of eddies in climate models can reduce systematic drift (Ferreira et al., 2005, Danabasoglu and Marshall, 2007). Changing K in numerical models can lead to a different prediction of the global temperature of 1^oC for climate simulation runs (Pradal and Gnanadesikan, 2014) and influence the stability of the overturning circulation (Sijp et al., 2006). A correct parameterisation of the spatial and temporal varying effect of eddies in coarse-resolution climate models is therefore essential. In spite of the recent progress made, lack of knowledge of global eddy tracer transports in the real ocean at

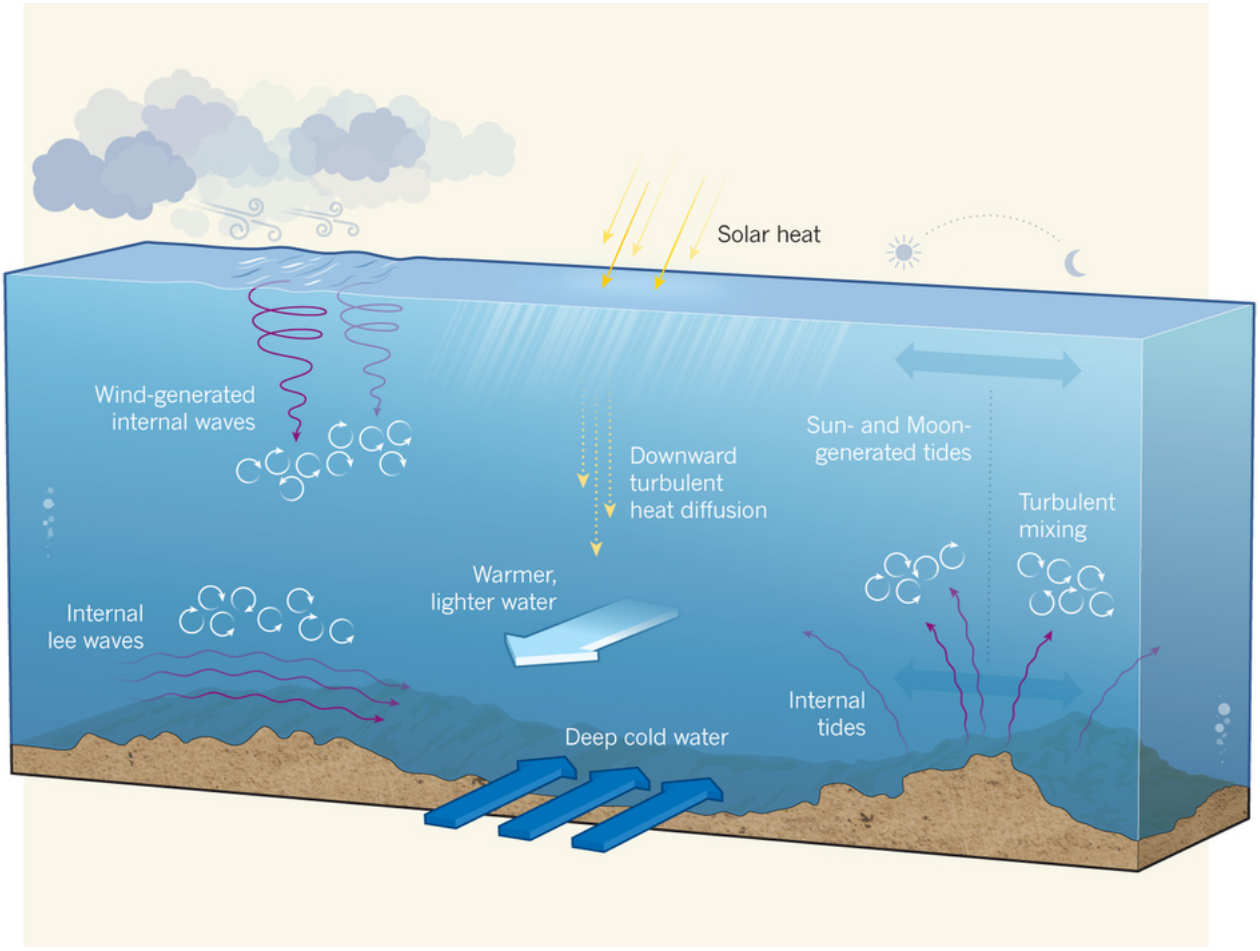

FIGURE 1.3: This schematic of the Small-scale mixing Processes is taken from MacKinnon (2013). Turbulent mixing (curly arrows) is driven by breaking internal waves in the ocean interior. It transports solar heat downwards from the surface to the abyss and transforms the deepest, coldest waters into warmer, less-dense waters. Internal waves are generated by three main mechanisms: Moon- and Sun-generated tidal flow over steep or rough topography (lower right); fluctuating wind stress on the ocean surface (upper left); and quasi-steady flow over rough topography (lower left). This last mechanism, which produces the internal lee waves investigated by Nikurashin and Ferrari (2013), is analogous to mountain waves in the atmosphere.

for example the equator or its variation with depth is limited, reducing the ability to improve eddy transports in (numerical) models.

In this thesis we will develop a method that will allow us to estimate both epineutral and small-scale diffusion coefficients. This will provide better constraints on their values and improve the implementation of mixing into (numerical) models.

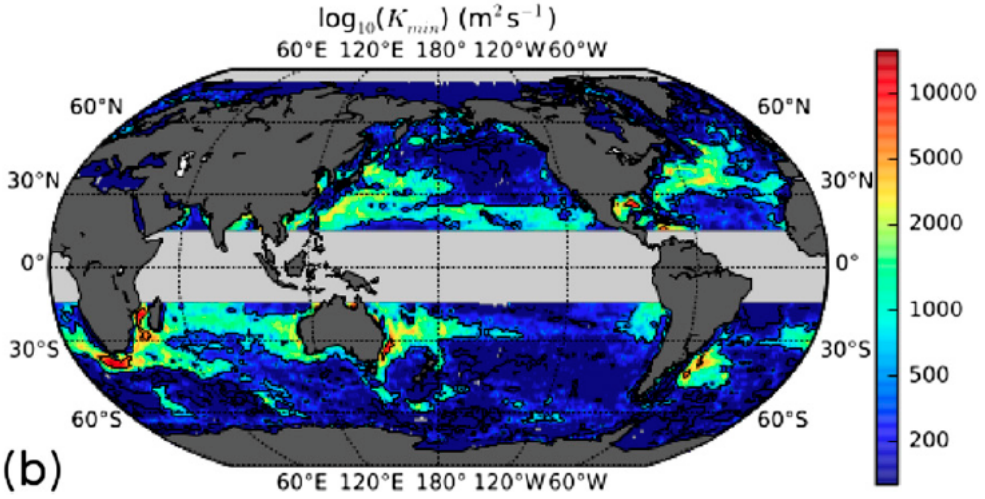

FIGURE 1.4: Observation of variability of the magnitude of K at the ocean's surface taken from Klocker and Abernathey (2013). The diffusivities are shown on a $\log_{10}$ scale.

1.3 Quantification of ocean circulation using streamfunctions

The ocean circulation can be studied through the use of streamfunctions (often represented by Ψ). A streamfunction is a mathematical tool that is capable of reducing the three-dimensional time varying ocean circulation into a more comprehendible two-dimensional time-averaged circulation. The only requirement to be able to construct a streamfunction is a two-dimensional non-divergent flow field. Streamfunctions have been widely used as a model diagnostic to study ocean circulation.

The most classic example of the streamfunction applied to oceanography is perhaps the barotropic streamfunction (Stommel, 1948). The barotropic streamfunction is basically a vertical integration of the ocean circulation, with boundary condition such that volume is exactly conserved. This leads to a two dimensional (in this case exactly horizontal in x and y direction, thus Ψ_{xy}) representation of the depth-integrated ocean circulation (Fig. 1.5).

The Meridional overturning streamfunction, Ψ_{yz}, represents the zonally averaged ocean circulation in (y, z) coordinates. Because ocean currents tend to follow isopycnal surfaces rather then surfaces of constant depth, Döös and Webb (1994) calculated a streamfunction in potential density and latitude $(\sigma\&\lambda)$-coordinates, i.e. $\Psi_{\sigma\lambda}$. Not only did they find circulation cells related to the Atlantic overturning, the subtropical gyres and the Antarctic bottom water circulation, they mainly showed that the Deacon cell, which is a strong circulation cell visible in Ψ_{yz}, almost entirely disappeared. This clearly illustrated that interpretation of the results shown by streamfunctions is not straightforward as the

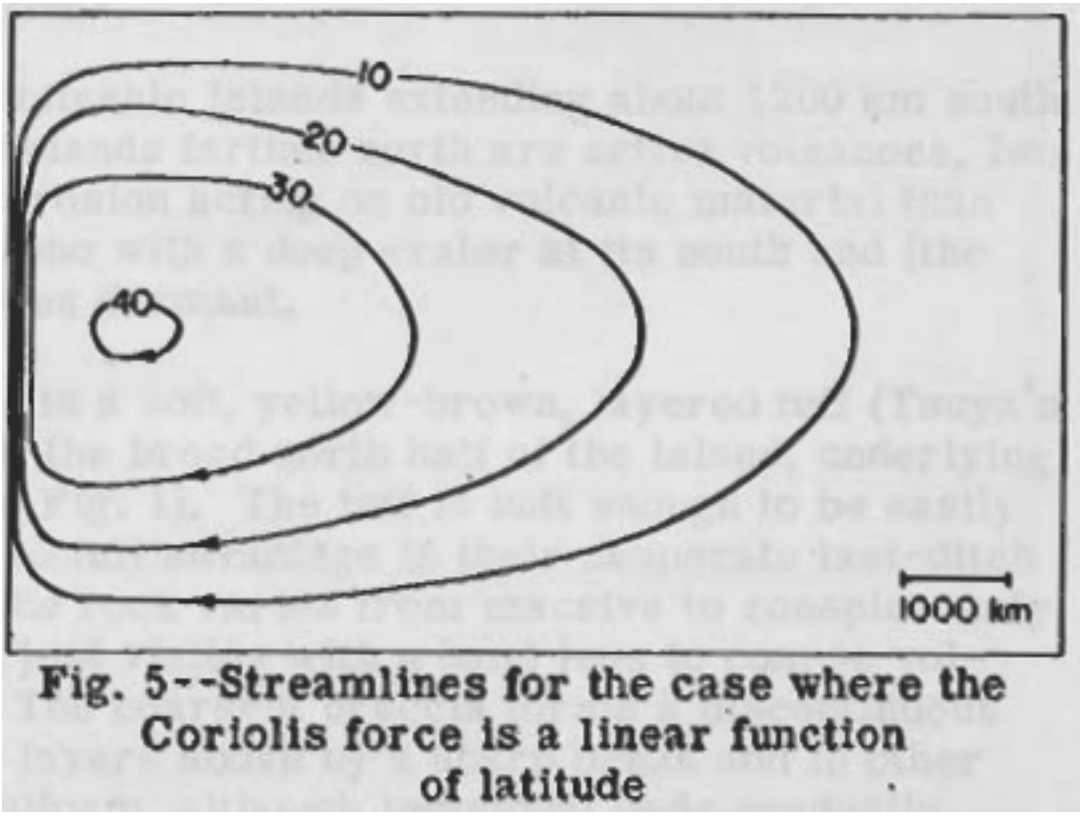

FIGURE 1.5: Figure taken from Stommel (1948), showing streamlines for an idealised horizontal ocean basin with constant depth as calculated by Stommel (1948). Streamlines represent the direction of the ocean circulation in this basin. The units are in Sv and there is an equal amount of water flowing between two streamlines. As a result, there is a faster flow when streamlines are close together (larger spatial gradients), showing intensification of the western boundary currents, compared to the rest of the ocean basin.

resolved circulations patterns are dependent on the choice of coordinates in which the stream-function is evaluated.

Streamfunctions are now a widely used model diagnostic to understand circulation pathways and to quantify the associated transports. This has lead to the development of streamfunctions in many different coordinates. However, all the streamfunctions that have previously been constructed (Marotzke et al. (1988), Hirst et al. (1996), Hirst and McDougall (1998), Nurser and Lee (2004), Boccaletti et al. (2005), amongst others), have always used at least one fixed x, y or z coordinate. That also applies to the more thermodynamic streamfunction such as $\Psi_{z\sigma}$ calculated by Nycander et al. (2007), or that by Ferrari and Ferreira (2011) who quantified heat transports using a streamfunction in latitude and potential temperature coordinates ($\Psi_{\lambda\theta}$). However, it was Zika et al. (2012) and Döös et al. (2012) who for the first time, simultaneously and independently of each other, calculated a streamfunction in two tracer coordinates that are not fixed in space and time.

Zika et al. (2012) and Döös et al. (2012) calculated the thermohaline streamfunction Ψ_{ST}, a streamfunction in Salinity (S) and Temperature (T) coordinates (Fig. 1.6). The thermohaline streamfunction allowed for the analyses of the ocean circulation in (S,T) coordinates, thereby isolating the component of the global ocean circulation that is related to salt and heat fluxes. As different ocean basins at different depths have clearly distinguished S and T properties, different ocean basins are clearly distinguished in (S,T) coordinates. As a result Ψ_{ST}, in contrast to previously defined streamfunctions, for the first time showed a circulation that could be interpret as an interconnected global ocean circulation as that proposed by Broecker (1982) (the global cell in Fig. 1.6).

The thermohaline streamfunction as calculated by Zika et al. (2012) and Döös et al. (2012) made use of model output of the velocity $\mathbf{u} = (u, v, w)$, where u, v and w are the velocities in the x, y and z direction, respectively. They calculated the component of the circulation in the direction normal to the surfaces of constant S and T, providing the advective component of the circulation in (S,T). They did not calculate the component of the circulation in (S,T) coordinates due to the movement of surfaces of constant S and T in space and time. The latter component is a result of using a combination of two tracers coordinates that are not fixed in space and time. In Chapter 3 of this thesis (published as Groeskamp et al. (2014a)), we will calculate the diathermohaline streamfunction $\Psi^{\mathrm{dia}}_{\mathrm{ST}}$, which is a streamfunction in (S,T) coordinates that takes into account both the advective component and the component due to the movement of the tracers surfaces themselves.

1.4 Quantification of ocean circulation using Inverse Methods

The ocean's hydrography changes in time and space due to the combination of processes acting upon it. Such processes are for example tides, winds, surface freshwater and heat fluxes and mixing. As a result the ocean's hydrography contains information about the forcing acting upon it, including the circulation. That is why we are able to obtain estimates of the circulation from the ocean's hydrography, through the use of inverse methods. An inverse method is a mathematical technique that can be used to estimate a solution to an under- or over-determined set of equations. Inverse techniques are used in oceanography to quantify mass and tracer transports and mixing from an ocean hydrography.

$\Psi^{\mathrm{dia}}_{\mathrm{ST}}$ as defined by Groeskamp et al. (2014a) can only be calculated from numerical ocean models as it requires knowledge of $\mathbf{u}$ that is not available from measurements. To be able

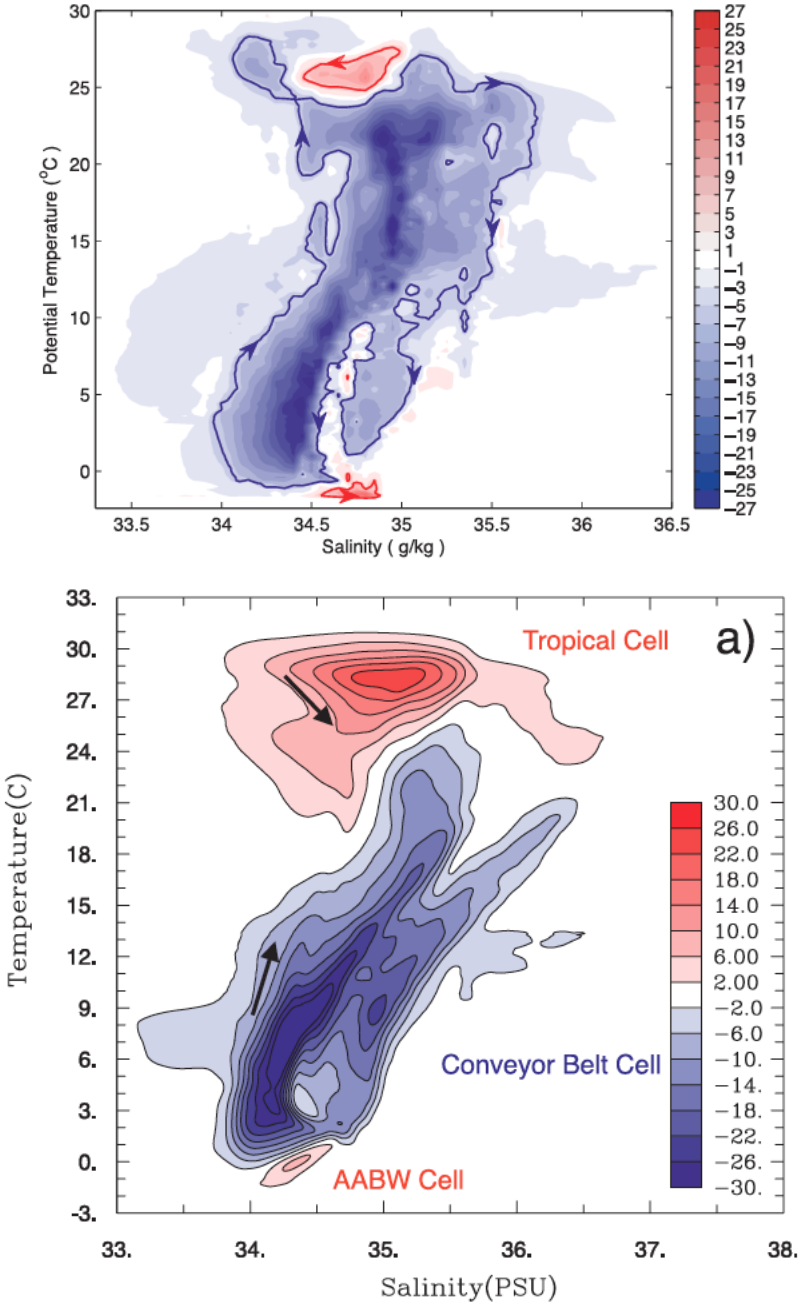

FIGURE 1.6: The thermohaline streamfunction Ψ_{ST} , as calculated by Zika et al. (2012)(top) and Döös et al. (2012) (bottom). They both identified their major cells, a clockwise rotating Global Cell (the large blue cell), an anticlockwise rotating Tropical Cell (red, high temperatures) and an Antarctic Bottom Water Cell (red cell, at low temperatures). The differences occur because they have used different models.

to calculate $\Psi_{\mathrm{ST}}^{\mathrm{dia}}$ without the use of $\mathbf{u}$ an inverse method can be used, which extracts $\Psi_{\mathrm{ST}}^{\mathrm{dia}}$ from the information embedded in ocean's S and T distribution (hydrography), in combination with surface freshwater and heat fluxes.

1.4.1 The Box Inverse Method

Wunsch (1977, 1978) was the first to apply an inverse method to an oceanographic problem. He applied the 'box inverse method' to estimate the absolute velocity vector $\mathbf{v_{abs}}$. The box inverse method uses conservation of mass (or volume) and tracers such as heat and salt, to constrain an under-determined set of equations in which the unknowns are $\mathbf{v_{abs}}$. To construct the box-inverse model, $\mathbf{v_{abs}}$ is expressed as the vertically integrated thermal wind balance,

$$\tilde{v}(x,y) = \frac{g}{\rho_0 f}\int_{z_0}^{z}\frac{\partial \rho}{\partial x}dz + \tilde{v}_0 = v_r(\rho) + \tilde{v}_0. \tag{1.1}$$

Here $\tilde{v}$ is the component of v_{abs} normal to the line connecting a station pair, g is the gravitational acceleration, f is the Coriolis frequency, $\rho = \rho(S,T,p)$ is the density of seawater and p is pressure. In Eq. (1.1) $\tilde{v}_r(\rho)$ is often referred to as the baroclinic velocity. As ρ depends on S, T and p, $\tilde{v}_r(\rho) = \tilde{v}_r(S,T,p)$ and can subsequently be calculated from an ocean hydrography. The integration is performed from z_0 to z, such that $\tilde{v}_0$ is the velocity at z_0, often referred to as the reference velocity or barotropic velocity and is the unknown that needs to be solved for to be able to calculate $v_{\mathbf{abs}}$.

The box inverse model uses a box in the ocean, defined by for example geographical sections at which measurement of S, T, and p were provided at different locations (stations). This lead to a certain number of stations (M) and station-pairs ($M-1$) enclosing the box. At each station Eq. (1.1) was evaluated, leaving M unknowns (one $\tilde{v}_0$ at each station). Using the velocity from Eq. (1.1), conservation of mass within this box that is given as the sum of the total flow through each station pair would have to sum to zero. This leads to the following equation

$$\sum_{m=1}^{M}\left(\tilde{v}_{r_m}(\rho) + \tilde{v}_{0_m}\right) dp_m dx_m = 0. \tag{1.2}$$

Here $m = 1 : M-1$ is the number of station pairs, such that dx_m and dp_m are the distance and pressure difference between two station pairs. Conservation of mass, thus leads to one equation and M unknowns. By adding conservation of for example heat, salt and other tracers, one can increase the number of equations (N), while the number

of unknowns remain similar. This set of equation can be written in the form

$$\mathbf{Ax} = \mathbf{b}. \tag{1.3}$$

Here each row of $\mathbf{A}$ is an equation based on all the coefficients with which $\tilde{v}_{0_m}$ is multiplied (these are $dp_m dx_m$). Then $\mathbf{x}$ are the unknown $\tilde{v}_0$ values, while $\mathbf{b}$ contain all the known values (these are $\sum_{j=1}^{M} \tilde{v}_{r_m}(\rho) dp_m dx_m$). Box inverse methods are generally heavily under-determined as the number of unknowns outweigh the number of equations ($M > N$), leading to an infinite number of possible solutions.

The advantage of a box inverse method now comes into play. To obtain the optimal solution, physical knowledge of the system can be included. This generally involves down weighting equations that are expected to have large errors (due to for example inaccuracies of data) and adding constraints, e.g. using prior estimates of the (volume, heat, etc.) transports. A least squares minimisation will then provide the best fit solution, taking into account the prior added weights and constraints. The accuracy and sensitivity of the solution depends heavily on the modeler's choice of the weighting and constraints applied.

Since Wunsch (1978), further development of the box inverse method have attempted to estimate the (global) ocean circulation and sometimes also included diapycnal fluxes and diffusivities (Wunsch et al. (1983), Hogg (1987), Rintoul and Wunsch (1991), Zhang and Hogg (1992), Ganachaud and Wunsch (2000), Sloyan and Rintoul (2000, 2001), Lumpkin and Speer (2007) and Macdonald et al. (2009), amongst many others). The use of box-inverse models has allowed for significant progress in the understanding and quantification of the global ocean circulation. Nonetheless data sparseness and inaccuracies lead to remaining uncertainties in the obtained transport rates and especially small-scale turbulent diffusivities (Zika et al., 2010a).

1.4.2 β-Spiral Inverse Method

A different type of inverse-model is the β-Spiral Inverse Method introduced by Stommel and Schott (1977) and Schott and Stommel (1978), also introduced to estimate $\mathbf{v_{abs}}$. The β-Spiral Inverse method vertically integrating the thermal wind balance in both x and y direction and then using the linear vorticity equation and a steady state density conservation equation with no diapycnal flux to obtain

$$u_0 \frac{\partial^2 h}{\partial x \partial z} + v_0 \left(\frac{\partial^2 h}{\partial y \partial z} - \frac{\beta}{f} \right) + u_r \frac{\partial^2 h}{\partial x \partial z} + v_r(\rho) \left(\frac{\partial^2 h}{\partial y \partial z} - \frac{\beta}{f} \right) = 0. \tag{1.4}$$

Here h is the height of a given density surface and u_0 and v_0 (u_r and v_r) are the reference level velocities (baroclinic velocities) direct to the north and west respectively. This equation can be determined for multiple densities per geographical location, such that one may obtain a set of equations (rewritten in the form of 1.3) that is overdetermined ($M < N$). Unfortunately this method requires the evaluation of the double derivative of the height of a density surface in space, which is sensitive to noise. As a result the β-spiral method has not gained the popularity of the box-inverse model.

1.4.3 The Bernoulli Inverse Method

Another inverse method aimed to estimate $\mathbf{v_{abs}}$, is the Bernoulli inverse method by (Killworth, 1986). When one starts with the Navier-Stokes equations and assumes a non-turbulent, incompressible, and barotropic fluid undergoing steady motion, then motion of a fluid is described by the so called Bernoulli function

$$B = \frac{p}{\rho} + gz. \tag{1.5}$$

Cunningham (2000) showed that Eq. (1.5) can be rewritten such that it depends on T and S. It assumes that a contour of constant S and T on an isopycnal is also a contour of constant geostrophic flow. However, the contour may start and end at different depths. Using conservation of Eq. (1.5) along this contour to obtain $B(z_1) = B(z_2)$ resulting in

$$p_1 - p_2 = \rho g(z_1 - z_2). \tag{1.6}$$

Here $p_1 - p_2$ is obtained for every density surface, providing an overdetermined set of equations to determine the surface pressure fields. From the surface pressure fields $\mathbf{v_{abs}}$ can be determined.

1.4.4 The Tracer-Contour Inverse Method

The inverse methods above are aimed to estimate $\mathbf{v_{abs}}$. However, with increasing spatial and temporal observations of the ocean's hydrography, it may now be possible to obtain estimates of more complicated (higher order) processes such as ocean mixing. The first such inverse method specifically designed to estimate mixing is the Tracer-Contour Inverse Method (TCIM) developed by Zika et al. (2010a). The TCIM includes aspects of the box-inverse model (Wunsch, 1978), β-spiral method (Stommel and Schott, 1977) and the Bernoulli inverse method (Killworth, 1986). The TCIM is capable to solve for both circulation in geographical space and diffusion coefficients.

The TCIM combines 3 equations, 1) an adapted from of box-model equations that includes small-scale and mesoscale mixing terms, 2) an expression for the geostrophic streamfunction on a neutral surface and, 3) an expression that relates mixing processes with cross S and T contour transports on a neutral surface.

To conceptually explain the TCIM we consider a neutral density surface γ on which a contour of constant S is also a contour of constant T. Between the start and the end of this contour there may be a pressure difference. This pressure difference represents a cross-contour velocity that can be expressed as a streamfunction difference ($\Delta\Psi^{\gamma}$). To calculate the streamfunction (Ψ^{γ}) at each end of the contour, we consider a reference neutral density surface γ^0. The streamfunction can then be expressed as a reference streamfunction on the reference neutral density surface, plus a vertical integration over steric height. The latter can be obtained from an ocean hydrography. We can then express the streamfunction difference at both ends of the contour as a difference in reference streamfunction ($\Delta\Psi^{\gamma^0}$) and steric height integration ($f(S,T,p)$),

$$\Delta\Psi^{\gamma^0} = \Delta\Psi^{\gamma} - f(S,T,p). \tag{1.7}$$

Here $f(S,T,p)$ is determined from an ocean hydrography leaving the streamfunctions (Ψ^{γ} and Ψ^{γ^0}) as unknowns.

Zika et al. (2010a) then used an adapted form of the water mass transformation equation derived by McDougall (1984) to express the cross-contour velocity (the component of the geostrophic velocity along a neutral density surface directed in the direction normal to the S and T contour) with the related mesoscale and small-scale mixing processes. In simplified form this leaves

$$\Delta\Psi^{\gamma} = Kc_1^{\mathrm{st}}(S,T,p) + Dc_2^{\mathrm{st}}(S,T,p) \tag{1.8}$$

Here $c_1^{\mathrm{st}}(S,T,p)$ and $c_2^{\mathrm{st}}(S,T,p)$ is a complicated term made up of constants and tracer gradients integrated along the tracer-contour. However, these terms can be evaluated from an ocean hydrography only, such that combining Eqs (1.7) and (1.8) leaves

$$\Delta\Psi^{\gamma^0} = Kc_1^{\mathrm{st}}(S,T,p) + Dc_2^{\mathrm{st}}(S,T,p) + f(S,T,p), \tag{1.9}$$

and results in an equation in which unknown reference level streamfunction differences are related to unknown diffusion coefficients. An equation can be obtained for each contour on each density layers. Using multiple density layers and contours, an overdetermined set of equations is obtained that can be solved for using an inversion (Eq. 1.3). Note that the Bernoulli method is similar to Eq. (1.9) when assuming $K = D = 0$, and thus no cross-contour transports.

The extent to which the tracer contour method will provide reliable estimates of the unknowns, depends on the information content in $c_1^{\mathrm{st}}(S,T,p)$ and $c_2^{\mathrm{st}}(S,T,p)$ on the right hand side of Eq. (1.9). This depends on both the resolution of the hydrography and the S and T distribution of the ocean. To allow for estimates of the unknowns in area's where such information content is reduced, Eq. (1.9) is solved simultaneously with an adapted form of box-conservation equation. These box-conservation equations are derived by combining the tracer conservation equation with tracer continuity equation and an expression for the diapycnal velocity from Zika et al. (2009). This enabled the re-writing of the traditional box-inverse model using the unknowns K, D and $\Delta\Psi^{\gamma^0}$ and thereby allowing them to be combined with the contour equations.

Using a model, Zika et al. (2010a) showed that the TCIM provides improved estimates of both the diffusion coefficient and the absolute velocity vector compared to other inverse methods. Zika et al. (2010b) applied the TCIM to observations and showed that this method is also capable of obtaining (local) estimates of velocities and diffusion coefficients in the ocean interior. The TCIM is specifically aimed to provide estimate of K and D, but is also capable of estimating $\mathbf{v_{abs}}$. Currently the TCIM has not been applied globally and is not connected to the surface, such that the results are local interior estimates of K, D and $\mathbf{v_{abs}}$. In this thesis an inverse method is developed that provides global estimates of K and D and includes effects near the surface.

1.4.5 The Thermohaline Inverse Method

In Chapter 4 of this thesis (published as Groeskamp et al. (2014b)) we will develop the Thermohaline Inverse Method (THIM), which is specifically designed to obtained global estimates of mixing, taking into account the effect of air-sea fluxes. The THIM estimates the small-scale turbulent diffusion coefficient D, the mesoscale eddy diffusion coefficient K, and the diathermohaline streamfunction $\Psi_{\mathrm{ST}}^{\mathrm{dia}}$. This method is different from other methods, because it uses conservation statements in (S,T) coordinates rather than in Cartesian coordinates. This isolates the component that influence ocean mixing, making it the ideal framework to obtain global estimates of mixing.

In Chapter 5 of this thesis, we will apply the THIM method to observations to obtain the first global estimate of K and D and $\Psi_{\mathrm{ST}}^{\mathrm{dia}}$. This allows us to gain insight in the global spatial distribution of the magnitude of different mixing processes and simultaneously understand its influence on the global ocean circulation provided by $\Psi_{\mathrm{ST}}^{\mathrm{dia}}$. The latter allows us to capture a globally interconnected ocean circulation in one diagram, based on observations.

1.5 The content of this Thesis

1.5.1 Chapter 2

For the development of the Thermohaline Inverse Method (THIM, Chapter 4), we required to accurately calculate isotropic and epineutral tracer gradients (epineutral being along a neutral surface). When re-deriving some of the rotation tensors that are related to calculate the epineutral tracer gradient, the author of this thesis in correspondence with Prof. Trevor McDougall, found two surprising inaccuracies in present ocean modelling practice. The first was that under the small-slope approximation there is a small gradient of tracer in a direction in which there is no actual epineutral gradient of tracer. This is an undesirable property of the projected non-orthogonal coordinate system that is used in layered ocean models and in theoretical oceanographic studies. The second was that small-scale mixing processes act to diffuse tracers isotropically (i.e. directionally uniformly in space), and not vertically or diapycnal as used in many models. These discoveries lead to Chapter 2 of this thesis and is published as McDougall et al. (2014).

1.5.2 Chapter 3

During a meeting on the Walin (1982) framework, at the Department of Meteorology of the University of Stockholm, hosted by Jonas Nycander, Johan Nillson and Kristoffer Döös, the idea of developing the THIM was presented by the author of this thesis. In a forthcoming discussion with Frédéric Laliberté, we concluded that the only way we can directly relate water-mass transformation in (S, T) coordinates with fluxes of salt and heat, is by taking into account the effect that S and T are not fixed coordinates in time and space. Hence this lead to the calculation and formulation of the local thermohaline streamfunction $\Psi^{\mathrm{loc}}_{\mathrm{ST}}$. The diathermohaline streamfunction $\Psi^{\mathrm{dia}}_{\mathrm{ST}}$ is the sum of the $\Psi^{\mathrm{loc}}_{\mathrm{ST}}$ and the advective thermohaline streamfunction $\Psi^{\mathrm{adv}}_{\mathrm{ST}}$, the latter being equivalent to the thermohaline streamfunction as calculated by Zika et al. (2012) and Döös et al. (2012). Only the diathermohaline streamfunction can be directly related to salt and heat fluxes. The method presented in Chapter 3 and published as Groeskamp et al. (2014a), is the correct diagnostic to calculate circulation in tracer-tracer coordinates.

1.5.3 Chapter 4

In Chapter 4 we develop the Thermohaline Inverse Method (THIM). This method uses a balance between surface forcing, mixing and circulation to estimate the small-scale turbulent diffusion coefficient D, the mesoscale eddy diffusion coefficient K and the

diathermohaline streamfunction $\Psi^{\mathrm{dia}}_{\mathrm{ST}}$. The surface forcing can be obtained from a surface flux product and the tracer gradients upon which the diffusion coefficients operate can be obtained from an ocean hydrography. As a result, there is enough information to estimate the unknowns (D, K and $\Psi^{\mathrm{dia}}_{\mathrm{ST}}$). We test the THIM by calculating Ψ^{dia}_{ST} directly using a model's hydrographic and velocity output as described in Chapter 2 (Groeskamp et al., 2014a) and compare this with the THIM inverse estimate of Ψ^{dia}_{ST} based on the model's boundary fluxes of salt and heat in combination with its hydrography. It turns out that the THIM is able to accurately estimate the unknowns, encouraging an application to observations.

1.5.4 Chapter 5

In Chapter 5 we apply the THIM developed in Chapter 4 to observations. This results in observationally based estimates of the diathermohaline streamfunction $\Psi^{\mathrm{dia}}_{\mathrm{ST}}$, (mesoscale) eddy diffusion coefficients operating on either horizontal gradients in the mixed layer (K_{H}) or epineutral gradients below the mixed layer (K_{I}) and the small-scale turbulent diffusion coefficient D. The results provide a general insight into the relation between water-mass transformation induced by the surface freshwater and heat fluxes and the effects on ocean mixing processes. Estimates of the diffusion coefficients and $\Psi^{\mathrm{dia}}_{\mathrm{ST}}$ can be compared with models and they provide insights into how well models do or do not resolve the water-mass transformation induced component of ocean circulation. For example, we find that the eddy diffusion coefficients we estimate are much smaller those that used in models. This may suggest that models should lower their tracer diffusion coefficient. More results and details are provided in Chapter 5.

1.5.5 Chapter 6

The work presented in this thesis has lead to 1) new insights on the geometry of interior ocean mixing processes, 2) a new model diagnostic to analyse ocean circulation in tracer-tracer coordinates, 3) a new inverse method to estimate diffusion coefficients and water-mass transformation in (S, T) coordinates and 4) the first observationally based estimates of $\Psi^{\mathrm{dia}}_{\mathrm{ST}}$ and globally balanced diffusion coefficients. In Chapter 6 we will provide a detailed summary of the results presented in this thesis and future applications and improvements.

Chapter 2

On geometrical aspects of interior ocean mixing

2.1 Introduction

The idea that ocean properties are advected and mixed predominantly along 'isopycnal' surfaces dates back at least to Iselin (1939) who noted the similarity between the salinity temperature diagram of vertical casts in the centre of a subtropical gyre and that plotted from data in the winter surface mixed layer in the whole hemisphere. This concept of 'isopycnal mixing' has become part of the underpinning assumptions of physical oceanography. Papers by Veronis (1975), Solomon (1971), Redi (1982) and McDougall and Church (1986) pointed out that ocean models needed to rotate their diffusion tensor to be aligned with the locally-referenced potential density surface in order to avoid the ill effects of having density mixed horizontally at fixed depth.

2.1.1 A physical argument for orienting lateral mixing along neutral tangent planes

While the strong lateral mixing achieved by the energetic mesoscale eddies is widely believed to be oriented along 'isopycnals', we are aware of only one convincing argument that supports this assumption; the argument has been made in section 7.2 of Griffies (2004) and in section 2 of McDougall and Jackett (2005), and is explained here with the aid of Fig. 2.1. The argument involves the rather small amount of dissipation of turbulent kinetic energy that is measured in the ocean interior.

We begin by initially adopting the counter-argument, so that we take the lateral mesoscale dispersion to occur along a surface that differs in slope from the neutral tangent plane.

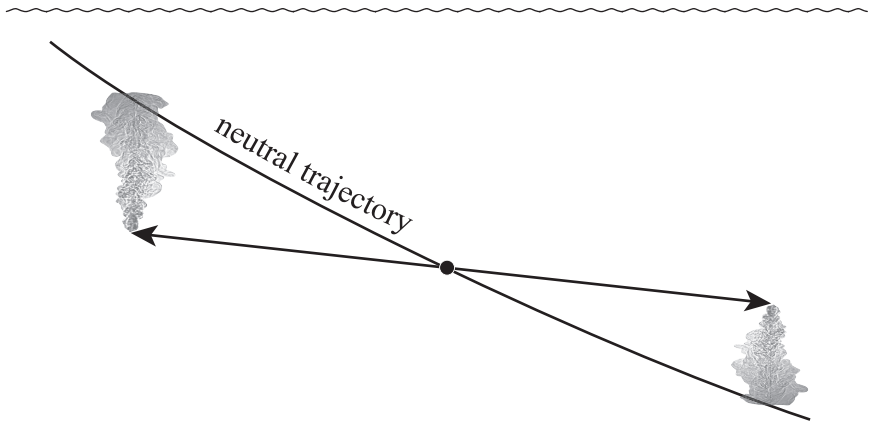

FIGURE 2.1: Sketch of a central seawater parcel being moved adiabatically and without change in its salinity to either the right or the left of its original position in a direction which is not neutral. When the parcel is then released it feels a vertical buoyant force and begins to move vertically (upwards on the left and downwards on the right) towards its original 'isopycnal'.

Individual fluid parcels are then transported above and below the neutral tangent plane and would need to subsequently rise or sink in order to regain a vertical position of neutral buoyancy. This situation is illustrated in Fig. 2.1 where a central seawater parcel is moved adiabatically and without exchange of salinity in a non-neutral direction to either the left or right and then released. The fluid parcel then feels a vertical buoyant force (upwards if displaced to the left and downwards if displaced to the right) and it begins to move back to its original 'density' surface. This vertical motion would either

1. involve no small-scale turbulent mixing, in which case the combined process is adiabatic and isohaline, and so is equivalent to epineutral dispersion, or

2. the sinking and rising parcels would mix and entrain in a plume-like fashion with the ocean environment, so experiencing irreversible mixing.

If the second case were to happen, the dissipation of mechanical energy associated with the dianeutral mixing would be observed. But in fact mechanical energy dissipation in the main thermocline is consistent with a dianeutral diffusivity of only 10^{-5} m^2 s^{-1} (MacKinnon et al., 2013). This relatively small value of the dianeutral (vertical) diffusivity has been confirmed by purposely released tracer experiments (e. g. Ledwell et al. (2010)).

McDougall and Jackett (2005) showed that even if all the observed dissipation of turbulent kinetic energy were due to the second case above of non-neutral lateral mixing, (implying no contribution from breaking internal waves to ϵ) the maximum tangent of the angle between the mixing plane and the neutral tangent plane is of order 10^{-4}. Since the dominant cause of the observed dissipation of turbulent kinetic energy in the

ocean interior is likely the breaking of internal gravity waves (MacKinnon et al., 2013), no matter whether they are forced by winds, by internal tides, or by lee waves above bottom topography, the allowable angle between the plane of mesoscale mixing and the neutral tangent plane is much less than 10^{-4}.

Nycander (2010) has examined mixing in the ocean along inclined planes and has concluded that an exchange between potential and kinetic energies is required to move seawater parcels along a neutral tangent plane. He also concluded that such energetic arguments do not shed light on the question of which mixing direction is preferred by the energetic ocean mesoscale eddies. Nycander's results confirm the long-standing practice (since the 1980s) of defining the neutral direction using parcel movement arguments in terms of the lack of vertical buoyant restoring forces, rather than in terms of the changes in gravitational potential energy.

We conclude that the only evidence to support the notion that strong lateral mixing is directed along neutral tangent planes is the measured smallness of the dissipation of turbulent kinetic energy in the ocean interior, coupled with the arguments of McDougall and Jackett (2005) and Griffies (2004). Furthermore, this evidence from measured dissipation rates accords with the interpretation of tracer distributions as per isopycnal water-mass analysis, with this framework originating from Iselin (1939). The relatively small dissipation of mechanical energy in the ocean interior represents a key distinction from the troposphere, where radiative damping leads to relatively large levels of dissipation and associated diabatic mixing. Consequently, oceanographers have a fundamental reason to be concerned about details of how mixing is oriented. This concern motivates our examination of the geometry of ocean interior mixing.

2.1.2 Specification of the neutral tangent plane

To provide a mathematical foundation for later discussions, we present a physical and mathematical review of a neutral tangent plane. Physically, the neutral tangent plane is that plane in space in which a seawater parcel can be moved an infinitesimal distance without being subject to a vertical buoyant restoring force. That is, the neutral tangent plane is the plane of neutral- or zero- buoyancy.

As a thought experiment, consider the seawater parcel at a point in the ocean, and enclose it in an insulating plastic bag. Upon moving to a new location a small distance away, the parcel will experience an increment in pressure δP. Its *in situ* density will thus change by $\rho\kappa\delta P$ where κ is the adiabatic and isohaline compressibility. At the same new location the seawater environment surrounding the enclosed parcel has an Absolute

Salinity that is different to that at the original location by δS_A, a Conservative Temperature difference of $\delta\Theta$, and a density difference of $\rho\,(\kappa\delta P + \beta\delta S_A - \alpha\delta\Theta)$, where β and α are the appropriate saline contraction and thermal expansion coefficients, defined with respect to Absolute Salinity S_A and Conservative Temperature Θ (IOC et al. (2010)). If at the new location the displaced parcel does not feel a buoyant (Archimedean) force, its density must be equal to that of the environment at its new location, $\delta\rho = \rho\kappa\delta P$. That is,

$$\rho\kappa\delta P = \rho\,(\kappa\delta P + \beta\delta S_A - \alpha\delta\Theta) \tag{2.1}$$

Hence, along an infinitesimal neutral trajectory in the neutral tangent plane the variations of S_A and Θ of the ocean must obey

$$\beta\delta S_A = \alpha\delta\Theta \tag{2.2}$$

This thought experiment is typical of our thinking about turbulent fluxes. We imagine the adiabatic and isohaline movement of fluid parcels, and then let these parcels mix molecularly with their surroundings. Central to this way of thinking about turbulent fluxes are the following two properties of the tracer that is being mixed, (1) It must be a 'potential' fluid property, for otherwise its value will change during the displacement even though the displacement is done without exchange of heat or mass, and (2) it should be close to being a 'conservative' fluid property so that when it does mix intimately (that is, molecularly) with its surroundings, we can be sure that there is negligible production or destruction of the property.

The present chapter is concerned with the mixing of tracers by both epineutral mixing and by small-scale mixing processes. The processes we examine are different to the separation of diffusion from advection (or the separation between symmetric and anti-symmetric diffusion) that are crucial in the Temporal Residual Mean theory and its parameterisation (McDougall and McIntosh, 2001, Gent et al., 1995, Griffies, 1998). Rather, our focus concerns two basic geometric aspects of ocean interior mixing.

In sections 2.2 and 2.3 we show that the use of the projected non-orthogonal coordinate system gives the same diffusive tracer fluxes as the small-slope approximation to the Redi (1982) diffusion tensor. Thereafter, we show that this tracer flux has a component that is nonzero in a direction in which there is no tracer gradient. We show that for temperature and salinity, this unphysical aspect of the small-slope diffusive flux is proportional to neutral helicity. In Section 2.4 we turn from epineutral diffusion to consider the mixing achieved by small-scale mixing processes such as breaking internal gravity waves. As a three-dimensional isotropic diffusion process, small-scale mixing should not be included in ocean mixing parameterisations as a one-dimensional 'dianeutral' or vertical diffusion. This realisation leads to a simplification of the Redi (1982) diffusion tensor.

2.2 The small-slope approximation to epineutral diffusion

2.2.1 The exact epineutral gradient

Using standard three-dimensional geometry (rather than the projected non-orthogonal approach considered in Section 2.2.2) we know that the gradient of a scalar C in a surface, which in our case is the neutral tangent plane, is

$$\begin{aligned} \nabla_N C &= \nabla C - \mathbf{n}\,(\nabla C \cdot \mathbf{n}) \\ &= -\mathbf{n} \times (\mathbf{n} \times \nabla C)\,. \end{aligned} \tag{2.3}$$

In these expressions, $\mathbf{n}$ is the unit normal to the neutral tangent plane,

$$\begin{aligned} \mathbf{n} &= \frac{\mathbf{m}}{|\mathbf{m}|} \\ &= \frac{-\nabla_n z + \mathbf{k}}{\sqrt{1 + \nabla_n z \cdot \nabla_n z}} \\ &= \frac{\alpha \nabla\Theta - \beta \nabla S_{\rm A}}{|\alpha \nabla\Theta - \beta \nabla S_{\rm A}|} \\ &= -\frac{\nabla \rho^l_\Theta}{|\nabla \rho^l_\Theta|} \\ &= -\frac{\nabla \gamma}{|\nabla \gamma|}. \end{aligned} \tag{2.4}$$

The vector $\mathbf{m}$ is parallel to the unit normal vector $\mathbf{n}$, but has unit length in the vertical direction (parallel to gravity), that is,

$$\mathbf{m} = -\nabla_n z + \mathbf{k}. \tag{2.5}$$

We define the projected horizontal gradient operator ∇_n in 2.2.2 which summarises the projected non-orthogonal approach. The slope of the neutral tangent plane $\nabla_n z$ is discussed in Appendix A, where we find the following expression in terms of the horizontal (∇_z) and vertical gradients of Absolute Salinity and Conservative Temperature,

$$\nabla_n z = (s_x, s_y) = -\frac{(\alpha \nabla_z \Theta - \beta \nabla_z S_{\rm A})}{(\alpha \Theta_z - \beta S_{{\rm A}_z})}. \tag{2.6}$$

The last parts of Eq. (2.4) expresses $\mathbf{n}$ in terms of the spatial gradient of locally-referenced potential density, ρ^l_Θ, and of Neutral Density, γ (Jackett and McDougall, 1997). Both $\mathbf{n}$ and $\mathbf{m}$ have a positive (i.e. upwards) vertical component. Eq. (2.6) has introduced the x and y components s_x and s_y of the vector slope $\nabla_n z$, and we will also use the shorthand notation s^2 for the inner product $\nabla_n z \cdot \nabla_n z$.

The epineutral gradient $\nabla_N C$, (Eq. (2.3)) can be written in tensor form in terms of the Cartesian gradient components $\nabla C = (C_x, C_y, C_z)$ as

$$\nabla_N C = \frac{1}{1+s^2} \begin{pmatrix} 1+s_y^2 & -s_x s_y & s_x \\ -s_x s_y & 1+s_x^2 & s_y \\ s_x & s_y & s^2 \end{pmatrix} \begin{pmatrix} C_x \\ C_y \\ C_z \end{pmatrix}, \tag{2.7}$$

which introduces the Redi (1982) tensor for epineutral diffusion; the full Redi diffusion tensor also includes small-scale turbulent mixing which we deliberately exclude from discussion until Section 2.4.

The parcel-based definition of the neutral tangent plane, $\beta \delta S_{\rm A} = \alpha \delta \Theta$, of Eq. (2.2), can now be expressed in terms of the (exact) epineutral gradients of $S_{\rm A}$ and Θ as

$$\beta \nabla_N S_{\rm A} = \alpha \nabla_N \Theta \quad \text{or} \quad \rho^{-1} \nabla_N \rho = \kappa \nabla_N P. \tag{2.8}$$

2.2.2 The projected non-orthogonal version of the epineutral gradient

The epineutral gradient that is used in many theoretical oceanographic studies (e.g. McDougall and Jackett (1988), McDougall (1995)) and in layered ocean models (Bleck, 1978a,b) is based on the projected non-orthogonal coordinate system first introduced by Starr (1945), which is widely used in geophysical fluid theory and modelling. In this coordinate system the vertical coordinate is strictly vertical (parallel to the effective gravitational force); planes of constant latitude and longitude are strictly vertical cones and planes respectively; and tracer gradients are calculated with respect to an undulating coordinate surface defined by the layer coordinate. This procedure for computing a tracer gradient is illustrated in Fig. 2.2. Note particularly that the lateral gradient of a tracer C in the undulating isopycnal or neutral density surface is calculated using the difference in tracer values between points b and a on this surface (see Fig. 2.2b), but the distance increment in the denominator of the projected non-orthogonal gradient is given by δx, that is, the distance is measured at constant height. Hence, the projected non-orthogonal gradient in a general undulating r surface is given by

$$\nabla_r C = \frac{\partial C}{\partial x}|_r \mathbf{i} + \frac{\partial C}{\partial y}|_r \mathbf{j} + 0\mathbf{k} \tag{2.9}$$

Importantly, horizontal distances are measured between vertical surfaces of constant latitude x and longitude y while values of the scalar property C are evaluated on the r surface (e. g. an isopycnal surface, or in the case of ∇_n, a neutral tangent plane). Note that $\nabla_r C$ has no vertical component; it is not directed along the r surface, but rather it points in the horizontal direction and thus is perpendicular to gravity.

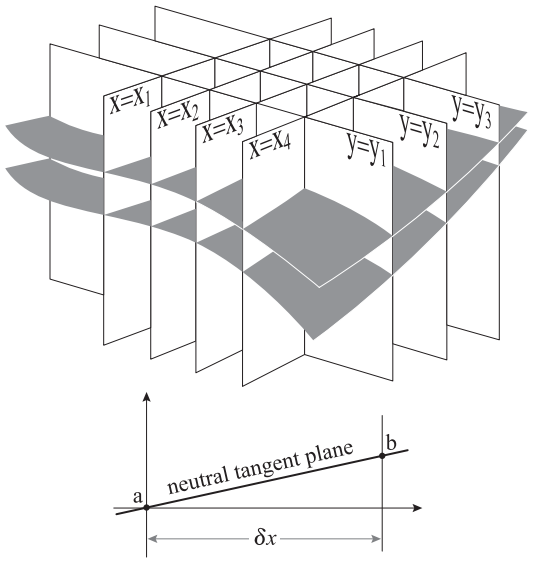

FIGURE 2.2: (a/top) A three-dimensional perspective of the projected non-orthogonal coordinate system that is commonly used in layered ocean models. (b/bottom) The projected non-orthogonal gradient of a property in the neutral tangent plane, in the limit as the distances tend to zero, is equal to the tracer difference between points a and b in the above figure, divided by the exactly horizontal distance δx or δy.

The projected non-orthogonal epineutral tracer gradient $\nabla_n C$ can be written in terms of the regular Cartesian gradients (e. g. $\nabla_z C$ is the exactly horizontal gradient of C) as (from McDougall and Jackett (1988), McDougall (1995) and Griffies (2004))

$$\begin{aligned} \nabla_n C &= \nabla_z C + C_z \nabla_n z \\ &= \nabla C - C_z \mathbf{m}, \end{aligned} \tag{2.10}$$

using $\mathbf{m} = -\nabla_n z + \mathbf{k}$ as defined in Eq. (2.5). Note that $\nabla_n C$, $\nabla_z C$ and $\nabla_n z = (s_x, s_y)$ are each horizontal two-dimensional vectors. In Appendix A we prove that the neutral tangent definition of Eq. (2.8) can be expressed in terms of the corresponding projected non-orthogonal gradients as

$$\beta \nabla_n S_\mathrm{A} = \alpha \nabla_n \Theta, \quad \text{or} \quad \rho^{-1} \nabla_n \rho = \kappa \nabla_n P. \tag{2.11}$$

2.2.3 Equivalence of the small-slope approximation and the projected coordinate approach

The three-dimensional tracer gradient based on the projected non-orthogonal approach is

$$\nabla_n C + \mathbf{k} \left(\nabla_n C \cdot \nabla_n z \right) = \nabla_z C + C_z \nabla_n z + \mathbf{k} \left(\nabla_z C \cdot \nabla_n z + s^2 C_z \right), \tag{2.12}$$

which is the flux in the neutral tangent plane (this property can be checked by showing that the scalar product of Eq. (2.12) with $\mathbf{n}$ is zero) whose horizontal component is $\nabla_n C$. The use of the projected non-orthogonal gradient $\nabla_n C$ in an ocean model or in a theoretical study is equivalent to using the three-dimensional flux (Eq. 2.12) in Cartesian coordinates.

This three-dimensional flux, Eq. (2.12), can be expressed in tensor form in Eq. (2.13) below, which we note is the same as the commonly-used small-slope approximation, $\nabla_N^{\text{small}} C$ (first introduced by Gent and McWilliams (1990)) to the exact epineutral gradient $\nabla_N C$. That is, we have found that the use of the projected non-orthogonal coordinate framework gives the same three-dimensional tracer gradient as the small-slope approximation to the exact epineutral gradient $\nabla_N C$, since

$$\nabla_n C + \mathbf{k}\,(\nabla_n C \cdot \nabla_n z) = \nabla_N^{\text{small}} C = \begin{pmatrix} 1 & 0 & s_x \\ 0 & 1 & s_y \\ s_x & s_y & s^2 \end{pmatrix} \begin{pmatrix} C_x \\ C_y \\ C_z \end{pmatrix}. \tag{2.13}$$

This equivalence between the projected non-orthogonal coordinate version of an epineutral gradient, $\nabla_n C + \mathbf{k}\,(\nabla_n C \cdot \nabla_n z)$, and the small-slope approximation of epineutral diffusion, $\nabla_N^{\text{small}} C$, was built into the small-slope approximation of Gent and McWilliams (1990), as pointed out in section 6.3 of Griffies and Greatbatch (2012). In Section 2.3 we compare the exact epineutral tracer gradient, $\nabla_N C$, of Eqs. (2.3) and (2.7) with the approximate small-slope form, $\nabla_N^{\text{small}} C$, of Eqs. (2.12) and (2.13). We emphasize (from Eq. 2.13) that this comparison is equivalent to comparing the projected non-orthogonal version of the epineutral gradient, $\nabla_n C + \mathbf{k}\,(\nabla_n C \cdot \nabla_n z)$, with its exact version $\nabla_N C$.

2.2.4 The two versions of the epineutral gradient are not parallel

One might have hoped that the two forms of the epineutral gradient $\nabla_N C$ and $\nabla_N^{\text{small}} C$ would be parallel and differ by the factor $\left(1 + s^2\right)$, which is the ratio of the lateral distances measured in the neutral tangent plane to those measured exactly horizontally, in the $\nabla_n z$ direction. However, this is not the case. We expose the issues by asking whether the direction of the isoline of constant tracer within the neutral tangent plane as determined by using the projected non-orthogonal coordinate system, namely $\mathbf{m} \times \nabla_N^{\text{small}} C$, is in fact an isoline of C. That is, we ask whether $\left(\mathbf{m} \times \nabla_N^{\text{small}} C\right) \cdot \nabla C$ is zero.

Using Eqs. (2.10) and (2.13) we find that,

$$\begin{aligned}\left(\mathbf{m}\times\nabla_N^{\text{small}}C\right)\cdot\nabla C &= \mathbf{m}\times\left(\nabla_n C+\mathbf{k}\left(\nabla_n C\cdot\nabla_n z\right)\right)\cdot\left(\nabla_n C+C_z\mathbf{m}\right) \\ &= \left(\mathbf{m}\times\mathbf{k}\cdot\nabla_n C\right)\left(\nabla_n C\cdot\nabla_n z\right) \\ &= \left(\mathbf{k}\cdot\nabla_n z\times\nabla_n C\right)\left(\nabla_n C\cdot\nabla_n z\right).\end{aligned} \tag{2.14}$$

This result shows that unless either $\mathbf{k}\cdot\nabla_n z\times\nabla_n C$ or $\nabla_n C\cdot\nabla_n z$ are zero, the direction of constant tracer calculated using the projected coordinate approach, or equivalently by using the small-angle approximation, is incorrect. In other words, in order for $\nabla_N^{\text{small}}C$ and $\nabla_N C$ to be parallel, either $\mathbf{k}\cdot\nabla_n z\times\nabla_n C$ or $\nabla_n C\cdot\nabla_n z$ must be zero, that is, the two-dimensional gradients $\nabla_n C$ and $\nabla_n z$ must either be parallel or perpendicular. In the general situation when $\nabla_n C$ and $\nabla_n z$ are neither parallel nor perpendicular, we note that while the two gradients $\nabla_N^{\text{small}}C$ and $\nabla_N C$ are both directed in the neutral tangent plane, they are not parallel. This mis-alignment means that when using $\nabla_N^{\text{small}}C$ to parameterise eddy fluxes, there will be a component of the tracer flux in a direction in which there is in fact no tracer gradient. In addition, even when $\nabla_N^{\text{small}}C$ and $\nabla_N C$ are parallel (say because $\mathbf{k}\cdot\nabla_n z\times\nabla_n C=0$) these gradients differ in magnitude, but this difference is of little concern.

2.3 Comparing the two versions of the epineutral gradient

2.3.1 Deriving equations relating the two epineutral gradients

To help understand the relationships between the two gradients $\nabla_N C$ and $\nabla_n C$, we begin by finding an expression for the exact epineutral gradient $\nabla_N C$ in terms of the projected non-orthogonal gradients $\nabla_n C$ and $\nabla_n z$. Using Eqs. (2.3) and (2.10) we find

$$\begin{aligned}\nabla_N C &= \nabla_n C+C_z\mathbf{m}-\frac{\mathbf{m}}{(1+s^2)}\left[\left(\nabla_n C+C_z\mathbf{m}\right)\cdot\mathbf{m}\right] \\ &= \nabla_n C+\frac{\left(\nabla_n C\cdot\nabla_n z\right)}{(1+s^2)}\mathbf{m} \\ &= \nabla_n C-\frac{\left(\nabla_n C\cdot\nabla_n z\right)}{(1+s^2)}\nabla_n z+\frac{\left(\nabla_n C\cdot\nabla_n z\right)}{(1+s^2)}\mathbf{k}.\end{aligned} \tag{2.15}$$

Using Eqs. (2.13) and (2.15) we can relate the following components of $\nabla_N C$ to those of $\nabla_N^{\text{small}}C$. The magnitude of the vertical component of $\nabla_N C$ is

$$\mathbf{k}\cdot\nabla_N C=\frac{\left(\nabla_n C\cdot\nabla_n z\right)}{(1+s^2)}=\frac{\mathbf{k}\cdot\nabla_N^{\text{small}}C}{(1+s^2)}, \tag{2.16}$$

the horizontal component of $\nabla_N C$ is

$$\begin{aligned} -\,\mathbf{k}\times(\mathbf{k}\times\nabla_N C) &= \nabla_n C - \frac{(\nabla_n C\cdot\nabla_n z)}{(1+s^2)}\nabla_n z \\ &= -\mathbf{k}\times\left(\mathbf{k}\times\nabla_N^{\text{small}} C\right) - \frac{(\nabla_n C\cdot\nabla_n z)}{(1+s^2)}\nabla_n z, \end{aligned} \tag{2.17}$$

the magnitude of $\nabla_N C$ in the $s^{-1}\nabla_n z$ direction (where $s=|\nabla_n z|$) is

$$s^{-1}\nabla_n z\cdot\nabla_N C = \frac{(\nabla_n C\cdot\nabla_n z)}{S\,(1+s^2)} = \frac{\left(\nabla_n z\cdot\nabla_N^{\text{small}} C\right)}{S\,(1+s^2)}, \tag{2.18}$$

while the magnitude of $\nabla_N C$ in the $s^{-1}\mathbf{k}\times\nabla_n z$ direction is

$$\begin{aligned} s^{-1}\mathbf{k}\times\nabla_n z\cdot\nabla_N C &= s^{-1}\mathbf{k}\times\nabla_n z\cdot\nabla_n C \\ &= s^{-1}\mathbf{k}\times\nabla_n z\cdot\nabla_N^{\text{small}} C \\ &= s^{-1}\left(\mathbf{k}\cdot\nabla_n z\times\nabla_n C\right). \end{aligned} \tag{2.19}$$

Another very useful combination that we can derive from Eqs. (2.13) and (2.15) is the difference between $\left(1+s^2\right)\nabla_N C$ and $\nabla_N^{\text{small}} C$ (recall that the factor $\left(1+s^2\right)$ is the ratio of the lateral distances measured along the neutral tangent plane versus horizontally, for displacements in the horizontal direction $\nabla_n z$)

$$\begin{aligned} \left(1+s^2\right)\nabla_N C - \nabla_N^{\text{small}} C &= s^2\nabla_n C - (\nabla_n C\cdot\nabla_n z)\,\nabla_n z \\ &= (\mathbf{k}\cdot\nabla_n z\times\nabla_n C)\,\mathbf{k}\times\nabla_n z. \end{aligned} \tag{2.20}$$

The last part of this equation is obtained by first noticing that $s^2\nabla_n C-(\nabla_n C\cdot\nabla_n z)\,\nabla_n z$ is (i) perpendicular to $s^{-1}\nabla_n z$ and (ii) is a horizontal vector, so it must be in the $s^{-1}\mathbf{k}\times\nabla_n z$ direction.

Eq. (2.20) is a convenient starting point to derive an expression for the cross product of $\nabla_N C$ and $\nabla_N^{\text{small}} C$ (which would be zero if these three-dimensional gradients were parallel),

$$\begin{aligned} \left(1+s^2\right)\nabla_N^{\text{small}} C\times\nabla_N C &= (\mathbf{k}\cdot\nabla_n z\times\nabla_n C)\,[(\nabla_n C+\mathbf{k}\nabla_n C\cdot\nabla_n z)\times(\mathbf{k}\times\nabla_n z)] \\ &= (\mathbf{k}\cdot\nabla_n z\times\nabla_n C)\,[\nabla_n C\times(\mathbf{k}\times\nabla_n z)-(\nabla_n C\cdot\nabla_n z)\,\nabla_n z] \\ &= (\mathbf{k}\cdot\nabla_n z\times\nabla_n C)\,(\nabla_n C\cdot\nabla_n z)\,\mathbf{m}. \end{aligned} \tag{2.21}$$

This result confirms that found in Eq. (2.14). Namely, in order for the exact and the approximate versions of the two epineutral tracer gradients, $\nabla_N C$ and $\nabla_N^{\text{small}} C$, to be parallel, either $\mathbf{k}\cdot\nabla_n z\times\nabla_n C$ or $\nabla_n C\cdot\nabla_n z$ must be zero. That is, the two-dimensional gradients $\nabla_n C$ and $\nabla_n z$ must either be parallel or perpendicular.

2.3.2 Visualising the difference between the two epineutral gradients

The geometry of the horizontal components of the projected and exact forms of the epineutral gradients, $\nabla_N^{\text{small}} C$ and $\nabla_N C$, is sketched in Fig. 2.3, using what we have learnt from the above Eqs. (2.18-2.20). The slope of the neutral tangent plane $\nabla_n z$ is taken to be directed due south (having the Southern Ocean in mind). Because both $\nabla_N^{\text{small}} C$ and $\nabla_N C$ lie in the neutral tangent plane (that is, both $\mathbf{n} \cdot \nabla_N^{\text{small}} C$ and $\mathbf{n} \cdot \nabla_N C$ are zero), it is sufficient to examine the horizontal components of $\nabla_N^{\text{small}} C$ and $\nabla_N C$ in order to understand their differences.

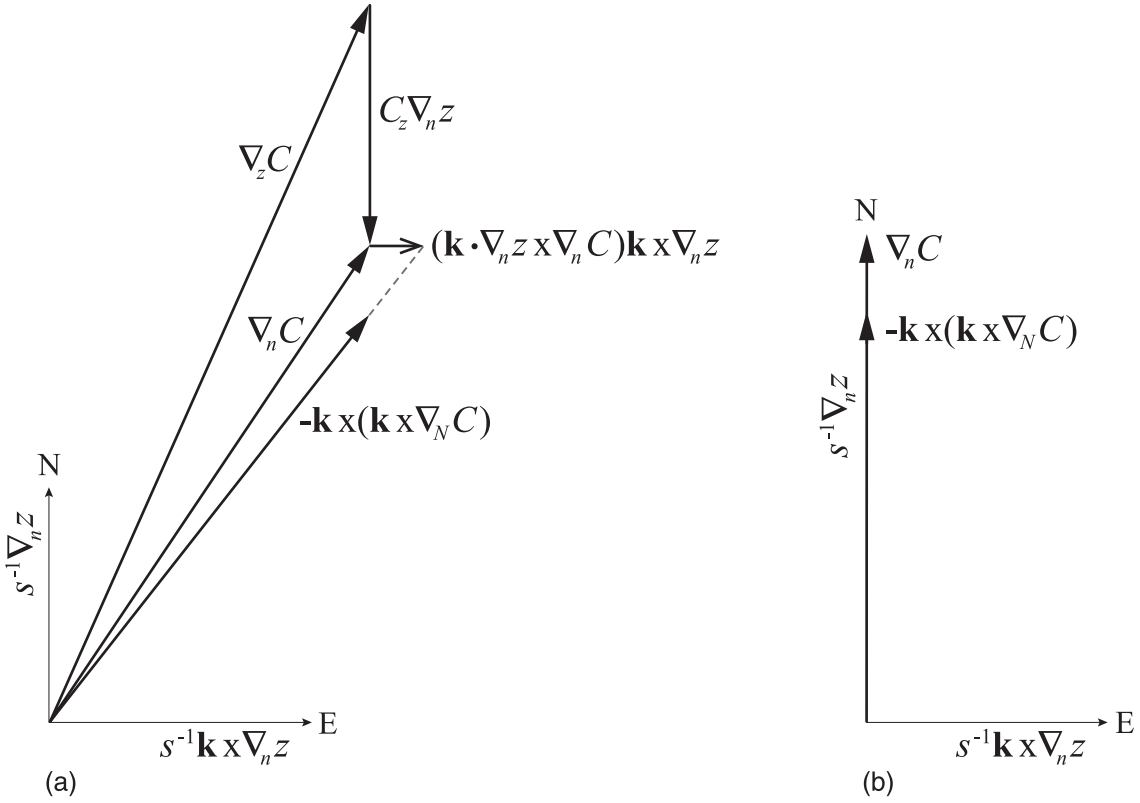

FIGURE 2.3: (a) Sketch of the horizontal components of the projected non-orthogonal epineutral tracer gradient, $\nabla_N^{\text{small}} C$, and the exact epineutral tracer gradient, $\nabla_N C$. The horizontal components of these gradients are $\nabla_n C = \nabla_z C + C_z \nabla_n z$ and $-\mathbf{k} \times (\mathbf{k} \times \nabla_N C)$, respectively. The components of these horizontal fluxes in the $s^{-1}\mathbf{k} \times \nabla_n z$ direction are equal (see Eq. (2.19)), while the components in the $s^{-1} \nabla_n z$ direction are in the ratio $\left(1 + s^2\right)$ (see Eqn. (2.18)). The vector $(\mathbf{k} \cdot \nabla_n z \times \nabla_n C)\, \mathbf{k} \times \nabla_n z$ points in the $s^{-1}\mathbf{k} \times \nabla_n z$ direction and is equal to $\left(1 + s^2\right) \nabla_N C - \nabla_N^{\text{small}} C$ (see Eq. (2.20)). Panel (a) has been drawn with $(\mathbf{k} \cdot \nabla_n z \times \nabla_n C) > 0$. (b) This panel illustrates the special case $(\mathbf{k} \cdot \nabla_n z \times \nabla_n C) = 0$ when both $\nabla_n C$ and $-\mathbf{k} \times (\mathbf{k} \times \nabla_N C)$ point due 'north' (or due 'south') and these gradients are in the ratio $\left(1 + s^2\right)$.

From Eq. (2.19) we see that the components of $\nabla_N^{\text{small}} C$ and $\nabla_N C$ in the $s^{-1}\mathbf{k} \times \nabla_n z$ direction are equal, while from Eq. (2.18) the components of $\nabla_N^{\text{small}} C$ and $\nabla_N C$ in the $s^{-1} \nabla_n z$ direction are in the ratio $\left(1 + s^2\right)$, that is, $s^{-1} \nabla_n z \cdot \nabla_N^{\text{small}} C = \left(1 + s^2\right) s^{-1} \nabla_n z \cdot \nabla_N C$. From Eq. (2.20), the difference between the three-dimensional gradients $\left(1 + s^2\right) \nabla_N C$

and $\nabla_N^{\text{small}} C$ is the exactly horizontal vector $(\mathbf{k} \cdot \nabla_n z \times \nabla_n C)\, \mathbf{k} \times \nabla_n z$, and this vector is shown in Fig. 2.3a. This vector points in the direction $s^{-1} \mathbf{k} \times \nabla_n z$ and its magnitude is $(\mathbf{k} \cdot \nabla_n z \times \nabla_n C)$. In the special case where $(\mathbf{k} \cdot \nabla_n z \times \nabla_n C) = 0$ (illustrated in Fig. 2.3b), $\nabla_n C$ points due 'north' and $\nabla_N^{\text{small}} C = \left(1 + s^2\right) \nabla_N C$, showing that the projected non-orthogonal version of the epineutral tracer gradient $\nabla_N^{\text{small}} C$ is now parallel to the exact epineutral gradient $\nabla_N C$, but that these gradients differ in magnitude by the expected factor $\left(1 + s^2\right)$. This special case of $(\mathbf{k} \cdot \nabla_n z \times \nabla_n C)$ being zero provides excellent motivation for emphasizing the comparison between $\left(1 + s^2\right) \nabla_N C$ and $\nabla_N^{\text{small}} C$ in Eq. (2.20) and Fig. 2.3a in the general case when $(\mathbf{k} \cdot \nabla_n z \times \nabla_n C)$ is not zero.

This geometric discussion serves to illustrate that the relevant comparison between the exact and the small-slope approximated versions of the epineutral tracer gradient is between $\left(1 + s^2\right) \nabla_N C$ and $\nabla_N^{\text{small}} C$ (or equivalently between $\nabla_N C$ and $\left(1 + s^2\right) \nabla_N^{\text{small}} C$). In the diffusion tensor form, the relevant difference between these fluxes is

$$\nabla_N C - \frac{1}{(1+s^2)} \nabla_N^{\text{small}} C = \frac{1}{(1+s^2)} \begin{pmatrix} s_y^2 & -s_x s_y & 0 \\ -s_x s_y & s_x^2 & 0 \\ 0 & 0 & 0 \end{pmatrix} \begin{pmatrix} C_x \\ C_y \\ C_z \end{pmatrix}. \tag{2.22}$$

The fact that the use of the small-slope approximation leads to gradients in the $s^{-1} \nabla_n z$ and $s^{-1} \mathbf{k} \times \nabla_n z$ directions that differ in relative magnitude (compared to the corresponding components of $\nabla_N C$) by the factor $\left(1 + s^2\right)$ has been pointed out in section 14.1.4.3 of Griffies (2004) (see his equation (14.26) in which this result is couched in terms of an amplified isopycnal diffusivity by the factor $\left(1 + s^2\right)$ in the $s^{-1} \nabla_n z$ direction). However, the fact that the small-slope approximation involves the flux of tracer in a direction in which there is no actual tracer gradient has, to our knowledge, not been noticed heretofore.

2.3.3 How different are the two epineutral gradients?

Since the horizontal component of $\nabla_N^{\text{small}} C$ is $\nabla_n C$ it would seem that the relative error in neglecting the difference between $|\left(1 + s^2\right) \nabla_N C$ and $\nabla_N^{\text{small}} C$ would scale as (using Eq. (2.20))

$$\frac{|\nabla_N^{\text{small}} C - \left(1 + s^2\right) \nabla_N C|}{|\nabla_n C|} = \frac{|\left(\mathbf{k} \cdot \nabla_n z \times \nabla_n C\right) \mathbf{k} \times \nabla_n z|}{|\nabla_n C|} \sim s^2. \tag{2.23}$$

However, the relative error is actually significantly less than this scaling suggests because the magnitude of $(\mathbf{k} \cdot \nabla_n z \times \nabla_n C)$ in the ocean is usually much less than $s|\nabla_n C|$. Here we develop expressions for $(\mathbf{k} \cdot \nabla_n z \times \nabla_n C)$ and make the connection to neutral helicity.

Since $\nabla_n C + \nabla_z C + C_z \nabla_n z$, $(\mathbf{k} \cdot \nabla_z C \times \nabla_n C)$ is also equal to $(\mathbf{k} \cdot \nabla_z C \times \nabla_n C)$. Using the expression (Eq. A.5) for the neutral tangent plane slope, we find

$$(\mathbf{k} \cdot \nabla_z \times \nabla_n C) = -\frac{g}{N^2} \mathbf{k} \cdot (\alpha \nabla_z \Theta - \beta \nabla_z S_\mathrm{A}) \times \nabla_z C. \tag{2.24}$$

Consider now the case where the tracer C is Conservative Temperature Θ (we could equally well have chosen Absolute Salinity S_A for this purpose since their epineutral gradients are parallel), so that Eq. (2.24) becomes

$$(\mathbf{k} \cdot \nabla_z \times \nabla_n \Theta) = \frac{g\beta}{N^2} (\nabla_z S_\mathrm{A} \times \nabla_z \Theta) \cdot \mathbf{k}. \tag{2.25}$$

To within the Boussinesq approximation we may take $\nabla_z \Theta$ and $\nabla_z S_\mathrm{A}$ to be equal to the corresponding gradients in an isobaric surface, $\nabla_p \Theta$ and $\nabla_p S_\mathrm{A}$, so that

$$\begin{aligned}
(\mathbf{k} \cdot \nabla_z \times \nabla_n \Theta) &= \frac{g\beta}{N^2} (\nabla_z S_\mathrm{A} \times \nabla_z \Theta) \cdot \mathbf{k} \\
&\approx \frac{g\beta}{N^2} (\nabla_p S_\mathrm{A} \times \nabla_p \Theta) \cdot \mathbf{k} \\
&= -\frac{1}{g\rho} (\nabla_n P \times \nabla_n \Theta) \cdot \mathbf{k} \\
&= -\frac{\beta}{\rho N^2} \nabla P \cdot \nabla S_\mathrm{A} \times \nabla \Theta \\
&= -\frac{H^n}{\rho T_b N^2},
\end{aligned} \tag{2.26}$$

where the last three parts of this equation have used the results of McDougall and Jackett (1988, 2007) and section 3.13 of IOC et al. (2010) that relate these various triple scalar products to neutral helicity, H^n, defined as $H^n = \beta T_b \nabla P \cdot \nabla S_\mathrm{A} \times \nabla \Theta$ where T_b is the thermobaric parameter (McDougall, 1987b) that expresses the non-linear dependence of specific volume on both Conservative Temperature and pressure; a non-linear property that does not concern us in this section of the chapter.

The triple scalar product $\nabla P \cdot \nabla S_\mathrm{A} \times \nabla \Theta$ of neutral helicity has arisen in the context of

1. The ill-defined nature of neutral surfaces and the empty nature of ocean hydrographic data in $S_\mathrm{A} - \Theta - P$ space (McDougall and Jackett, 1988, 2007),

2. The mean vertical downwelling advection achieved by the helical nature of neutral trajectories (Klocker and McDougall, 2010),

3. The close connection between $\nabla P \cdot \nabla S_\mathrm{A} \times \nabla \Theta$ and the spiraling of epineutral Θ contours when the ocean is not motionless Zika et al. (2010a), and now,

4. The difference between the projected non-orthogonal epineutral gradient of Θ, $\nabla_N^{\mathrm{small}} \Theta$, and its exact epineutral gradient counterpart $\nabla_N \Theta$.

The quantification of the magnitude of neutral helicity in the ocean is far from complete, yet the above studies have shown that the angle between $\nabla_n P$ and $\nabla_n \Theta$ is quite small in most of the ocean, even in the Southern Ocean where the influence of processes related to neutral helicity seem to be the largest (Klocker and McDougall, 2010). These results for neutral helicity were obtained in both a smooth ocean atlas and in an eddy-less ocean model, but neutral helicity has not yet been examined in the context of a high-resolution eddy-permitting ocean model. Nevertheless, if we take these results of McDougall and Jackett (2007) and Klocker and McDougall (2010) at face value then we would conclude that the relative magnitude of the error in the tracer flux due to using the small-slope approximation may be no more than a few percent of the magnitude estimated by the scale analysis of Eq. (2.23), that is, no more than a few percent of $s^2 = |\nabla_n z|^2$. It must be said that the reason why neutral helicity is as small as it is in the ocean is far from clear; see McDougall and Jackett (2007) and Klocker and McDougall (2010) regarding neutral helicity and the consequent requirement that the ocean is 'thin' in $S_A - \Theta - P$ space.

Specifically, if we let ϕ be the (small) angle between the two-dimensional gradients $\nabla_n C$ and $\nabla_n z$, then from Eq. (2.23) we see that the relative error in neglecting the difference between $\left(1 + s^2\right) \nabla_N C$ and $\nabla_N^{\text{small}} C$ is actually

$$\frac{|\nabla_N^{\text{small}} C - \left(1 + s^2\right) \nabla_N C|}{|\nabla_n C|} = s^2 \sin\phi. \tag{2.27}$$

The error made by neglecting this fraction of the epineutral tracer gradient can be compared with the very small errors that are made by taking Conservative Temperature Θ to be 100% conservative. From McDougall (2003) and Graham and McDougall (2013) we know that Conservative Temperature is approximately two orders of magnitude more conservative than is potential temperature (see Figures 2(a) and 4 of McDougall (2003) and Figure 8 of Graham and McDougall (2013)), while from Figure 11(a) of Graham and McDougall (2013) and Appendix A.14 of IOC et al. (2010) we see that the epineutral gradient of potential temperature, $\nabla_n \theta$, is often about 1% different to that of Conservative Temperature, $\nabla_n \Theta$. This 1% difference is due to the non-conservative nature of potential temperature. We conclude that the relative error in using the epineutral gradient of Conservative Temperature is the product of these two factors of 10^{-2}, namely 10^{-4}. This can be compared with the relative error, Eq. (2.27), involved in fluxing a tracer in a direction in which there is no gradient. For an epineutral slope s of as large as 10^{-2} this relative error is $s^2 \sin\phi = 10^{-4} \sin\phi$ which is smaller that the relative error in using Conservative Temperature by the factor $\sin\phi$, this factor representing the influence of neutral helicity. Since we expect $\sin\phi$ to be no larger than 0.05 (McDougall and Jackett, 2007), we conclude that this effect is absolutely tiny, even when compared

with the use of Conservative Temperature, which itself is an improvement by two orders of magnitude on oceanographic practice under EOS-80.

2.3.4 The component of the small-slope gradient in a direction in which there is no actual gradient

The component of the small-slope approximated gradient $\nabla_N^{\text{small}} C$ in the direction in three-dimensional space in which there is no tracer gradient is $\nabla_N^{\text{small}} C \cdot (\nabla_N C \times \mathbf{n}) / |\nabla_N C|$. The magnitude of this component can be calculated with the use of Eq. (2.21) as follows,

$$\begin{aligned} \frac{|\nabla_N^{\text{small}} C \cdot (\nabla_N C \times \mathbf{n})|}{|\nabla_N C|} &= \frac{|\nabla_N^{\text{small}} C \times \nabla_N C \cdot \mathbf{n}|}{|\nabla_N C|} \\ &= \frac{|(\mathbf{k} \cdot \nabla_n z \times \nabla_n C)(\nabla_n C \cdot \nabla_n z)|}{|\nabla_N C| (1+s^2)^{0.5}} \\ &\approx |\nabla_n C| s^2 \sin\phi \cos\phi \end{aligned} \tag{2.28}$$

where the approximations are (i) $s^2 << 1$ so that $|\nabla_N^{\text{small}} C| \approx |\nabla_N C| \approx |\nabla_n C|$, and (ii) that $\nabla_n C$ is close to being parallel to $\nabla_n z$ so that the sine of the angle between these two-dimensional vectors, $\sin\phi$, is small.

We conclude that the relative magnitude of the component of $\nabla_N^{\text{small}} C$ in the direction in which there is no tracer gradient is the same as Eq. (2.27), namely $s^2 \sin\phi$. In other words, the salient approximation in using the projected non-orthogonal approach to calculating tracer gradients manifests itself in the direction in space in which there is no tracer gradient. This result can be understood from Eq. (2.20) and Fig. 2.3a; for the usual situation where $\nabla_n C$ is close to being parallel to $\nabla_n z$, the error vector of Eq. (2.20), $(\mathbf{k} \cdot \nabla_n z \times \nabla_n C)\, \mathbf{k} \times \nabla_n z$, is close to being aligned in the direction $\mathbf{n} \times \nabla_N C = \left(1+s^2\right)^{-0.5} (\mathbf{k} - \nabla_n z) \times \nabla_n C \approx \mathbf{k} \times \nabla_n C$ in which there is no epineutral tracer gradient.

2.3.5 Incorporating the full epineutral gradient into ocean models

It is possible for a layered ocean model to incorporate the full epineutral tracer flux while retaining the projected non-orthogonal nature of its coordinate system. This correction can be achieved by replacing the existing horizontal component of the projected epineutral flux, $\nabla_n C$, with the horizontal component of the full epineutral flux $\nabla_N C$ (from Eq. (2.15)),

$$\nabla_n C - \frac{(\nabla_n C \cdot \nabla_n z)}{(1+s^2)} \nabla_n z. \tag{2.29}$$

The projected non-orthogonal coordinate system of the layered model will treat this gradient as the horizontal component of its projected epineutral gradient whose three-dimensional expression has the additional exactly vertical component whose magnitude is the scalar product of $\nabla_n z$ with Eq. (2.29), namely $\mathbf{k}\,(\nabla_n C \cdot \nabla_n z)\,/\left(1+s^2\right)$, exactly as it should be, from Eq. (2.15). So this approach provides a straightforward fix for layered ocean models. For Cartesian coordinate models, the solution is to simply use the full diffusion tensor (Eq. (2.7)) rather than its small-slope approximation, Eq. (2.13).

This same suggestion of replacing the horizontal component of the projected epineutral gradient, $\nabla_n C$, with Eq. (2.29) applies to theoretical studies that use the projected non-orthogonal coordinate system, in order that they accurately represent epineutral diffusion.

2.4 The isotropic diffusivity of small-scale mixing processes

The so-called 'vertical diffusivity' or 'dianeutral diffusivity' used in physical oceanography is a diffusion coefficient that parameterises mixing from a variety of small-scale mixing processes, with the primary mixing associated with breaking internal gravity waves. The turbulent cascade in breaking internal waves begins at vertical scales of order 1m and proceeds downscale to the molecular dissipation scale of a few millimetres. The turbulent fluxes achieved by this turbulent cascade do not occur only in the vertical direction or the dianeutral direction, but rather the diffusion occurs almost isotropically (Osborn, 1980, Gargett et al., 1984). Hence the isotropic diffusivity D of small-scale turbulent mixing processes causes fluxes per unit area in (x, y, z) Cartesian coordinates at the rate

$$-D\nabla C = -D\nabla_z C - DC_z\mathbf{k}. \tag{2.30}$$

This small-scale isotropic turbulent diffusion can be added to the full diffusion tensor of epineutral mixing, Eq. (2.7), to obtain (with $\epsilon = D\left(1+s^2\right)/K$)

$$\text{accurate diffusive flux} = \frac{-K}{(1+s^2)} \begin{pmatrix} 1+\epsilon+s_y^2 & -s_x s_y & s_x \\ -s_x s_y & 1+\epsilon+s_x^2 & s_y \\ s_x & s_y & \epsilon+s^2 \end{pmatrix} \begin{pmatrix} C_x \\ C_y \\ C_z \end{pmatrix}, \tag{2.31}$$

where K is the epineutral diffusion coefficient. The small-slope approximation to Eq. (2.31) becomes (now with $\epsilon = D/K$)

$$\text{small} - \text{slope diffusive flux} = -K \begin{pmatrix} 1+\epsilon & 0 & s_x \\ 0 & 1+\epsilon & s_y \\ s_x & s_y & \epsilon + s^2 \end{pmatrix} \begin{pmatrix} C_x \\ C_y \\ C_z \end{pmatrix}. \tag{2.32}$$

The small-slope approximation by itself does not change the contribution of the 'dianeutral' diffusivity D in going from Eq. (2.31) to Eq. (2.32). An isolated blob of tracer will still diffuse spherically in a stationary ocean with no mesoscale diffusion. In practice one might drop the two occurrences of ϵ from the $1+\epsilon$ terms in the (1,1) and (2,2) positions in the tensor and then the small-scale turbulent diffusion would act one-dimensionally in the vertical direction, the same as in the usual small-slope approximation. But there is no need to get rid of these horizontal ϵ diffusion terms from Eqns. (2.31) or (2.32); these terms are not part of a small-slope approximation.

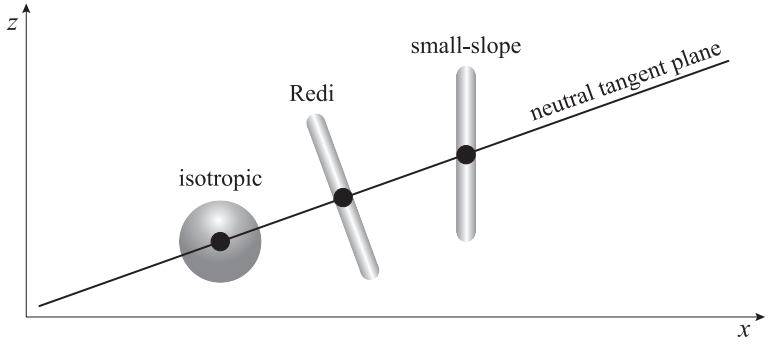

FIGURE 2.4: Sketch showing how, in the absence of epineutral diffusion, the so-called 'dianeutral diffusion' of the Redi (1982) diffusion tensor diffuses a small initial blob of tracer (the black dot) only in the dianeutral direction, leading to a line of tracer in the direction normal to a neutral tangent plane. In the small-slope approximation to the Redi diffusion tensor, the so-called 'dianeutral diffusion' diffuses tracer only in the vertical direction, leading to a vertical line of tracer. However, in reality, small-scale mixing processes actually diffuse properties isotropically so that a small initial blob of tracer will spread spherically in the absence of epineutral diffusion.

The above treatment of 'dianeutral diffusion' in Eqs. (2.30)-(2.32) is different to what has been done previously in ocean modelling (e.g. Redi (1982), Hirst et al. (1996), and Gent and McWilliams (1990)). In the traditional treatment of 'dianeutral diffusion', mixing is taken to occur exactly in the dianeutral direction with zero component along the neutral tangent plane. However, this orientation does not accord with how the ocean works. Instead, a blob of dye is diffused by small-scale turbulent mixing in a spherical manner. In contrast, as illustrated in Fig. 2.4, the dianeutral diffusion tensor of Redi (1982) diffuses this blob only in the dianeutral direction. Hence, if dianeutral diffusion is allowed to operate in the absence of epineutral diffusion, an initial blob of

tracer will be diffused dianeutrally into a thin line in space, as in Fig. 2.4. This one-dimensional dianeutral diffusion is not how small-scale turbulent mixing works; rather the diffusion should be in three dimensions. Likewise, in the now-common small-slope approximation of the full Redi diffusion tensor, the 'dianeutral' diffusion becomes purely vertical diffusion, which is again a purely one-dimensional diffusion. In this case a small spherical blob of dye, when acted upon by only this small-slope approximated 'dianeutral' diffusion will spread vertically in a thin vertical line and it will never be any wider in the x and y directions than its initial size in these directions.

We contend that an ocean model should be able to increase the dianeutral diffusivity and decrease the epineutral diffusivity (even to zero), and achieve three-dimensional spherical diffusion. For this purpose, Eqn. (2.31) is the proper form of the full diffusion tensor and Eqn. (2.32) its small-slope approximation. The existing Redi (1982) and Gent and McWilliams (1990) versions of these tensors are not appropriate for this purpose.

2.5 Conclusions

The points raised in this note are of a conceptual nature, and heretofore incompletely explored in the literature. We anticipate that their importance for ocean modelling practice, though yet to be tested, may in fact be negligible. That is, the niceties exposed in this chapter may have little impact on large-scale simulation integrity, particularly compared to uncertainties associated with other aspects of diffusive closures (e.g., values for the diffusivities). We are nonetheless compelled to raise the ideas here to clarify basic notions regarding geometric aspects of ocean interior mixing parameterised by diffusion. In this way this note complements the warnings of Young (2011) regarding the unconventional (but not incorrect) use of projected non-orthogonal coordinates in atmospheric and oceanic science. Specifically, the key points made in this note are the following:

- The epineutral diffusion achieved by the small-slope approximation is not down the correct epineutral tracer gradient $\nabla_N C$. That is, under the small-slope approximation there is a small gradient of tracer in a direction in which there is no actual epineutral gradient of tracer. This is also an undesirable property of the projected non-orthogonal coordinate system that is used in layered ocean models and in theoretical oceanographic studies.

- The difference between the correct epineutral tracer gradient, $\nabla_N C$, and the small-slope approximation to it, $\nabla_N^{\text{small}} C$, is explained geometrically; see Fig. 2.3. The relevant difference between the tracer gradients, $\left(1 + s^2\right) \nabla_N C - \nabla_N^{\text{small}} C$, is equal

to $(\mathbf{k} \cdot \nabla_n z \times \nabla_n C)\, \mathbf{k} \times \nabla_n z$ (from Eq. (2.20)), and points in the direction of the thermal wind (here s^2 is the square of the slope of the neutral tangent plane).

- For (the tracer) Conservative Temperature, the difference between the correct (Redi) epineutral gradient, $\nabla_N C$, and the small-slope approximation to it is proportional to neutral helicity and to the square of the slope of the neutral tangent plane.

- While it is uncomfortable to realize that the small-angle approximation to epineutral diffusion (and equivalently, the use of the projected non-orthogonal coordinate system) gives rise to an epineutral property flux in a direction in which there is actually no epineutral tracer gradient, it must be said that the fraction of the epineutral flux in this direction is very small and is negligible for all foreseeable applications. For example, we have shown that for an epineutral slope S as large as 10^{-2} the error in using Conservative Temperature (which is not in fact 100% conservative) is greater than the error discussed in this chapter of having a lateral tracer flux in a direction in which there is no gradient.

- Small-scale mixing processes act to diffuse tracers isotropically (i.e. directionally uniformly in space), hence it is a misnomer to call this process 'dianeutral diffusion'. This realization simplifies the diffusion tensor that is used in ocean models. This is illustrated by a thought experiment in which a tiny blob of tracer is diffused by small-scale mixing processes (see Fig. 2.4). The blob should diffuse spherically whereas the full Redi (1982) tensor has it diffusing as a line (a pencil) normal to the neutral tangent plane, and the small-slope approximation has this line being vertical.

Chapter 3

The representation of ocean circulation and variability in thermodynamic coordinates

3.1 Introduction

The global ocean circulation is of great importance for the earth's climate system through its heat transport and the cycling and storage of carbon. Understanding the underlying physical processes that drive the global ocean circulation is essential for our understanding of the earth's climate system and our ability to model it accurately. However, observing and modelling the global ocean circulation remains a challenge.

A component of the ocean circulation is buoyantly- or density-driven due to thermohaline forcing and is often referred to as thermohaline circulation. Here thermohaline forcing refers to boundary freshwater and heat fluxes, and salt and heat fluxes by diffusive mixing. In this chapter we develop a description of the thermohaline circulation using it's unambiguous relationship to the thermohaline forcing. The use of thermodynamic coordinates for understanding the relationship between the circulation and thermodynamic forcing was first made clear by Walin (1982). He showed that the area-integrated surface heat flux between two outcropping isotherms could be used to calculate the diathermal advection in a steady state ocean.

Speer and Tziperman (1992) applied Walin's framework to isopycnals instead of isotherms, which together with many subsequent studies (Marshall, 1997, Marshall et al., 1999, Nurser et al., 1999, Sloyan and Rintoul, 2000, 2001, Iudicone et al., 2008, Badin and

Williams, 2010, Nikurashin and Ferrari, 2013) allowed understanding of ocean circulation driven by thermohaline forcing. Using this framework Nurser and Marsh (1998) showed that the total diapycnal transport can be expressed as a sum of a streamfunction difference and non-steady component. The diapycnal transport can be fully expressed as a streamfunction only when the non-steady component is small.

Streamfunctions have been widely used as a diagnostic to the study ocean circulation. The advantage of scalar streamfunctions lies in their ability to represent the complex 3-dimensional and time varying ocean circulation in two dimensions, allowing new insight into the ocean circulation. A classic example is perhaps the meridional overturning streamfunction, $\Psi_{\lambda \mathrm{z}}$, representing the zonally averaged ocean circulation in latitude (λ) and depth (z) coordinates. Because ocean currents tend to follow isopycnal surfaces rather then surfaces of constant depth, Döös and Webb (1994) calculated a streamfunction in latitude and potential density (σ) coordinates, ($\Psi_{\lambda\sigma}$). They identified circulation cells related to the Atlantic overturning, the subtropical gyres and the Antarctic bottom water circulation, and showed that the Deacon cell, which is a strong circulation cell visible in $\Psi_{\lambda \mathrm{z}}$, almost entirely disappeared in (λ, σ) coordinates. From observations, Marsh (2000) used Walin's framework to derive a streamfunction in latitude and density (ρ) coordinates, $\Psi_{\lambda\rho}$. A more thermodynamic streamfunction was presented by Nycander et al. (2007), who constructed a streamfunction in density and depth coordinates ($\Psi_{\rho z}$). This study showed that certain ocean circulation cells are either mechanically forced, buoyantly forced or forced by a combination of both. The above clearly illustrates that streamfunctions provide a different representation of the ocean circulation for each choice of coordinates.

Simultaneously, Zika et al. (2012) and Döös et al. (2012) (hereafter referred to as ZD12) constructed the thermohaline streamfunction, a streamfunction in salinity (S) and temperature (T) coordinates (Ψ_{ST}). The Ψ_{ST} is essentially a 2-dimensional extension of Walin's framework, applied in (S, T) coordinates. However, ZD12 calculated Ψ_{ST}, using a model's 3-dimensional velocity field instead of using the thermohaline forcing. Therefore their Ψ_{ST} represented only advection normal to (S, T) iso-surfaces and not necessarily net water-mass transformation rates. ZD12 identified similar circulation cells and obtained estimates for circulation timescales and diapycnal freshwater and heat transports. A recent study by Zika et al. (2013) shows the influence of the magnitude of the Southern Ocean winds with circulation in different coordinates, including (S, T) coordinates.

Although ZD12 were the first to calculate Ψ_{ST}, Speer (1993) used salt and heat fluxes, in Walin's framework, and projected the water-mass transformation rates in (S, T) coordinates. This provided a distinction between transformation of different water masses and

their locations. They emphasised that they were unable to distinguish if this transformation was associated with either local changes in density without actual motion of water, or due to advective fluxes. Kjellsson et al. (2013) analysed the atmospheric circulation in dry and moist isentropic coordinates to construct the hydrothermal streamfunction. They considered both the effect of Eularian advection and local changes of properties and found that the latter was negligible for these coordinates.

Here we derive the complete ocean circulation in (S, T) coordinates (Section 3.2), namely the diathermohaline circulation. We show that the diathermohaline circulation is comprised of an advective component and a component due to local changes in (S, T) values, without fluid motion in geographical space. The advective component is due to ocean circulation normal to isohaline and isothermal surfaces, and can be expressed as an advective thermohaline streamfunction (Section 3.3). The local component is due to local changes of the S and T values, expressed as geographical displacements of isohalines and isotherms. This results in changes in the ocean volume distribution in (S, T) coordinates, and can be expressed as a local thermohaline streamfunction, after removing a trend (Section 3.4). The sum of the advective and local thermohaline streamfunctions is the diathermohaline streamfunction and represents the non-divergent diathermohaline circulation in (S, T) coordinates, and is the novel aspect of this chapter (Section 3.5). The analysis of a numerical model and observational climatology in (S, T) coordinates show that the local thermohaline streamfunction is a significant component of the ocean circulation in (S, T) coordinates and cannot be ignored (Section 3.6). We suggest that the diathermohaline streamfunction provides a tool for the analysis of, and comparison amongst, ocean models and observational-based gridded climatologies (Section 3.7 and 3.8).

3.2 Circulation in (S_A, Θ) coordinates

Here we construct a formalism to calculate circulation in Conservative Temperature (Θ) and Absolute Salinity (S_A) coordinates. Conservative Temperature is proportional to potential enthalpy (by the constant heat capacity factor c_p^0), which represents the 'heat content' per unit mass of seawater (McDougall, 2003, Graham and McDougall, 2013). Absolute Salinity is measured on the Reference Composition Salinity Scale (Millero et al., 2008) and represents the mass fraction of dissolved material in seawater (in g kg^{-1}), (IOC et al., 2010, McDougall et al., 2012). The framework presented here could in principle be applied to any two coordinates defined by two conservative tracers.

3.2.1 Thermohaline forcing

The (S_A, Θ) values of a fluid parcel defines its position in (S_A, Θ) coordinates. For the fluid parcel to change its position in (S_A, Θ) coordinates, it must change its S_A and/or Θ values. The Conservative Temperature, Θ, represents the ocean's heat content. Processes by which the heat content of a fluid parcel can be changed are, 1) heat fluxes at the oceans boundary and 2) diffusive mixing (Graham and McDougall, 2013). There are three processes by which one can change the S_A of a fluid parcel, 1) surface freshwater fluxes, 2) diffusive mixing, and 3) by biogeochemical processes. The latter is assumed to be negligible (IOC et al., 2010). Hence, all changes of a fluid parcel's S_A and Θ and it's motion in (S_A, Θ) coordinates, are driven by boundary freshwater and heat fluxes, and salt and heat fluxes by diffusive mixing, i.e., thermohaline forcing. Using continuity, it can be shown that for volume V, this results in the following conservation equation for S_A

$$\frac{DS_A}{Dt} = \frac{\partial S_A}{\partial t} + \mathbf{u} \cdot \nabla S_A = \frac{1}{\rho V} \left(f_{S_A} + d_{S_A} \right), \tag{3.1}$$

and Θ

$$\frac{D\Theta}{Dt} = \frac{\partial \Theta}{\partial t} + \mathbf{u} \cdot \nabla \Theta = \frac{1}{\rho V} \left(f_{\Theta} + d_{\Theta} \right). \tag{3.2}$$

Here the velocity $\mathbf{u} = (u, v, w)$, f_{S_A} and d_{S_A} (f_{Θ} and d_{Θ}) are the net convergence of salt (heat) due to boundary fluxes and diffusive mixing processes, respectively.

Surface radiative and sensible heat fluxes cause movement in the Θ-direction (Fig. 3.1). Precipitation results in movement in the negative S_A-direction and evaporation results in movement in the positive S_A-direction and simultaneously movement in the negative Θ-direction due to the related latent heat loss (Fig. 3.1). Mixing acts to reduce both the stratification and the (S_A, Θ) range of the fluid parcels. Hence the initial range enclosed by an isolated fluid parcel in (S_A, Θ) coordinates will never be increased by mixing processes. In the absence of external forcing, loss of salt, heat or mass, the initial range will eventually be reduced to a point in (S_A, Θ) coordinates. Mixing depends on the magnitude and orientation of geographical gradients of S_A and Θ (Fig. 3.1). In geographical coordinates mixing occurs as down-gradient tracer diffusion due to epineutral mesoscale eddies or as small-scale vertical turbulent diffusion (Gent et al., 1995, Griffies, 2004). However, the latter is in fact small-scale isotropic (rather then vertical) turbulent diffusion (Chapter 2, based on McDougall et al. (2014)).

3.2.2 The diathermohaline velocity

A fluid parcel that moves in (S_A, Θ) coordinates, must cross isohalines and/or isotherms, leading to a diahaline or diathermal velocity and related volume transport. For example,

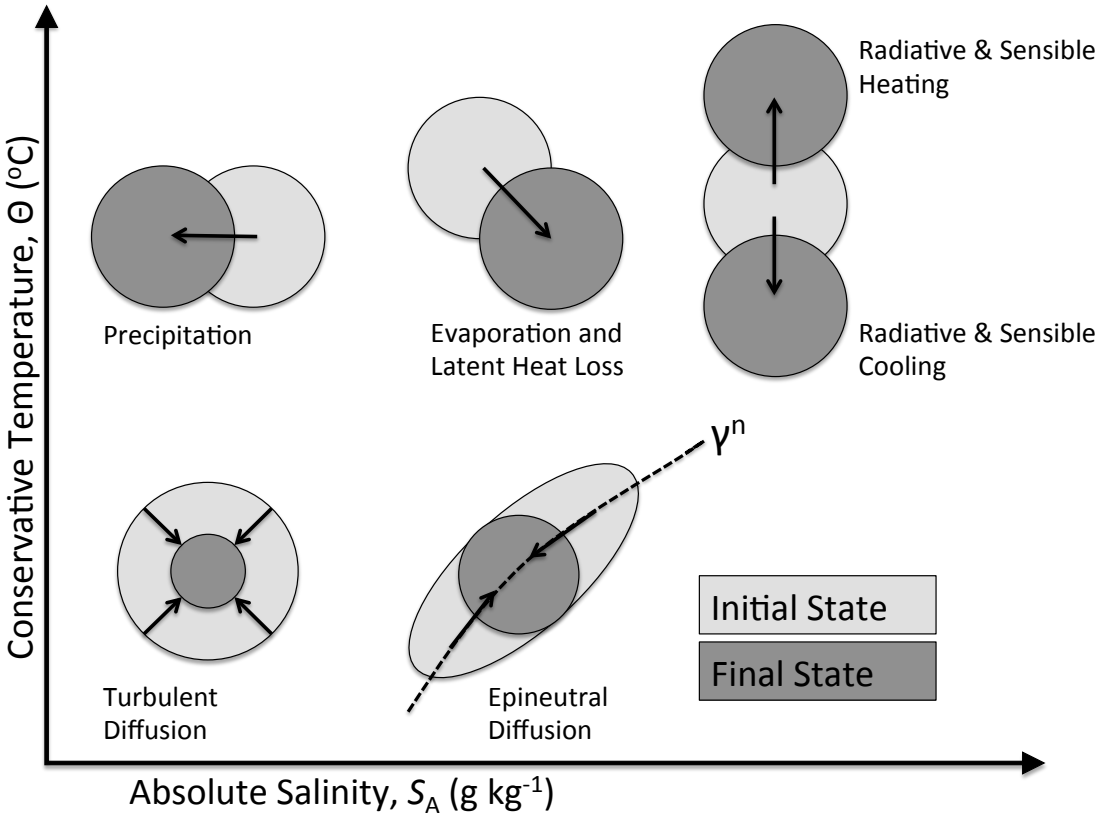

FIGURE 3.1: Schematic describing how fluid parcels are displaced in (S_A, Θ) coordinates by different thermohaline forcing, i.e., surface fluxes (top row) and diffusive mixing (bottom row), with γ^n referring to a neutral surface. The representation of mixing in this diagram is idealised, showing an isolated volume only influenced by isotropic turbulent diffusive mixing (left) or along isopycnal eddy diffusive mixing (right), reducing the volume's spread in S_A and Θ in an isotropic or isopycnal manner, respectively.

consider a volume V, with uniform Θ. If the Θ increases, this volume will be displaced, leading to a diathermal volume transport, in the positive Θ-direction in (S_A, Θ) coordinates. Equivalently, if the S_A of V increases, this volume will be displaced, leading to a diahaline volume transport in the positive S_A-direction in (S_A, Θ) coordinates. We reserve the use of the prefix 'dia' for the net displacement through a surface (for a discussion on a dia-surface velocity, refer to Griffies (2004), pp 138-141).

To calculate the diahaline or diathermal volume transport we first define $u^{\rm dia}_{S_A}$ as the diahaline velocity with which a fluid parcel moves through an isohaline in the positive S_A-direction (in geographical coordinates, in the ∇S_A-direction). Equivalently we define $u^{\rm dia}_{\Theta}$ as the diathermal velocity with which a fluid parcel moves through an isotherm in the positive Θ-direction (in geographical coordinates, in the $\nabla\Theta$-direction). With this definition we can construct the diathermohaline velocity vector,

$$\mathbf{u}^{\rm dia}_{S_A\Theta} = (u^{\rm dia}_{S_A}, u^{\rm dia}_{\Theta}), \tag{3.3}$$

where $u^{\rm dia}_{S_{\rm A}}$ and $u^{\rm dia}_{\Theta}$ are perpendicular in $(S_{\rm A},\Theta)$ coordinates, but may have any angle relative to each other in Cartesian-coordinates (Fig. 3.2). We define and relate the diathermohaline velocity with boundary fluxes and mixing by dividing (3.1) by $|\nabla S_{\rm A}|$ and (3.2) by $|\nabla\Theta|$ to obtain the diahaline velocity,

$$\begin{aligned} u^{\rm dia}_{S_{\rm A}} &= \frac{1}{|\nabla S_{\rm A}|}\frac{DS_{\rm A}}{Dt} = \frac{1}{\rho V|\nabla S_{\rm A}|}\left[f_\Theta + d_\Theta\right] \\ &= \frac{1}{|\nabla S_{\rm A}|}\frac{\partial S_{\rm A}}{\partial t} + \mathbf{u}\cdot\frac{\nabla S_{\rm A}}{|\nabla S_{\rm A}|} \\ &= -u^{\rm iso}_{S_{\rm A}} + u^{\rm adv}_{S_{\rm A}}, \end{aligned} \tag{3.4}$$

and the diathermal velocity

$$\begin{aligned} u^{\rm dia}_{\Theta} &= \frac{1}{|\nabla\Theta|}\frac{D\Theta}{Dt} = \frac{1}{\rho V|\nabla\Theta|}\left[f_\Theta + d_\Theta\right] \\ &= \frac{1}{|\nabla\Theta|}\frac{\partial\Theta}{\partial t} + \mathbf{u}\cdot\frac{\nabla\Theta}{|\nabla\Theta|} \\ &= -u^{\rm iso}_{\Theta} + u^{\rm adv}_{\Theta}. \end{aligned} \tag{3.5}$$

Here $u^{\rm adv}_{S_{\rm A}} = \mathbf{u}\cdot\nabla S_{\rm A}/|\nabla S_{\rm A}|$ is the component of the fluid's velocity with which a fluid parcel is geographically advected normal to the isohalines, and $u^{\rm adv}_{\Theta} = \mathbf{u}\cdot\nabla\Theta/|\nabla\Theta|$ is the the component of the fluid's velocity, with which a fluid parcel is geographically advected normal to the isotherms. We define $u^{\rm iso}_{S_{\rm A}} = -(\partial S_{\rm A}/\partial t)/|\nabla S_{\rm A}|$ as the velocity of the displacement of an isohaline in geographical coordinates, normal to the isohalines, due to local changes of $S_{\rm A}$. Finally, $u^{\rm iso}_{\Theta} = -(\partial\Theta/\partial t)/|\nabla\Theta|$ is the velocity of the displacement of an isotherm in geographical coordinates, normal to the isotherms, due to local changes of Θ. This derivation results in the diathermohaline velocity vector,

$$\mathbf{u}^{\rm dia}_{S_{\rm A}\Theta} = \mathbf{u}^{\rm adv}_{S_{\rm A}\Theta} - \mathbf{u}^{\rm iso}_{S_{\rm A}\Theta}, \tag{3.6}$$

where $\mathbf{u}^{\rm adv}_{S_{\rm A}\Theta} = (u^{\rm adv}_{S_{\rm A}}, u^{\rm adv}_{\Theta})$ and $\mathbf{u}^{\rm iso}_{S_{\rm A}\Theta} = (u^{\rm iso}_{S_{\rm A}}, u^{\rm iso}_{\Theta})$ (Fig. 3.3). To analyse the diathermohaline circulation (3.6), it is convenient to express $\mathbf{u}^{\rm dia}_{S_{\rm A}\Theta}$, using the diathermohaline streamfunction ($\Psi^{\rm dia}_{S_{\rm A}\Theta}$). However, only a velocity that is non-divergent in two coordinates, can be represented by a streamfunction. To obtain the diathermohaline streamfunction we will first represent $\mathbf{u}^{\rm adv}_{S_{\rm A}\Theta}$ by the advective thermohaline streamfunction ($\Psi^{\rm adv}_{S_{\rm A}\Theta}$) as previously obtained by ZD12. We will show that $\mathbf{u}^{\rm iso}_{S_{\rm A}\Theta}$, after subtracting a trend, can be represented with the local thermohaline streamfunction ($\Psi^{\rm loc}_{S_{\rm A}\Theta}$). The sum of both the advective and local thermohaline streamfunction is the diathermohaline streamfunction.

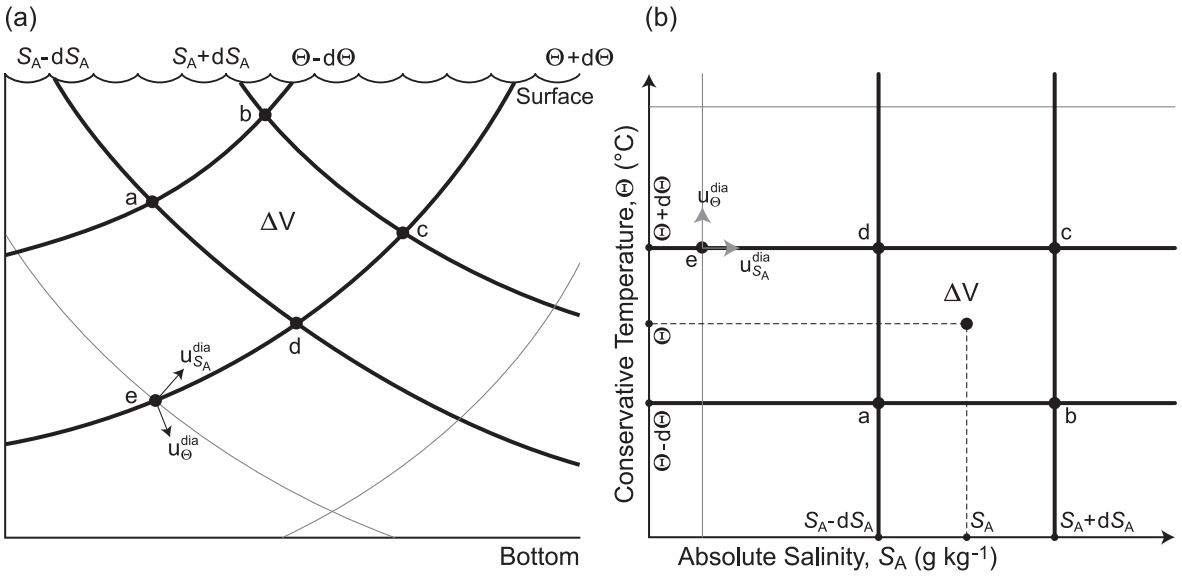

FIGURE 3.2: Schematic of the diathermohaline velocity $\mathbf{u}^{\mathrm{dia}}_{S_A\Theta}$ and a volume ΔV enclosed by the same isohalines and isotherms, in geographical coordinates (left) and (S_A, Θ) coordinates (right).

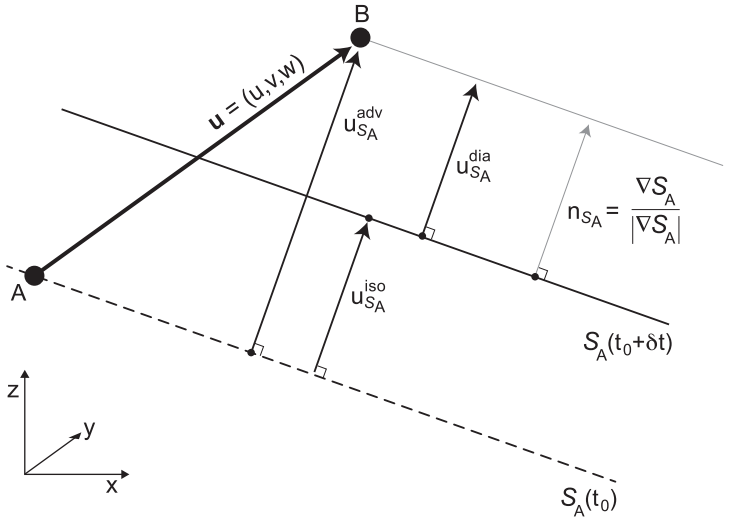

FIGURE 3.3: Construction of the diahaline velocity $u^{\mathrm{dia}}_{S_A}$, viewed with the isohaline directed into the page. Here $\mathbf{u}$ advects a fluid parcel from A to B, over time δt, and the isohaline moves from its initial position (dashed line) to its final position (black line). The diahaline velocity ($u^{\mathrm{dia}}_{S_A}$) is given by the difference between the component of geographical velocity normal to the isohaline ($u^{\mathrm{adv}}_{S_A}$) and the velocity of the isohaline itself ($u^{\mathrm{iso}}_{S_A}$).

3.3 The advective thermohaline streamfunction

Based on an averaging technique developed by Nurser and Lee (2004), Ferrari and Ferreira (2011) defined a meridional streamfunction, $\Psi_{C_1 y}$, for an arbitrary tracer C_1. Where $\Psi_{C_1 y}$ represents the advective meridional transport of C_1, for an instantaneous velocity field v. Zika et al. (2012) generalised this technique to compute a mean streamfunction ($\Psi_{C_1 C_2}$) for any two tracers, C_1 and C_2. This represents advection of fluid parcels in $C_1 - C_2$ coordinates. Applied to an instantaneous velocity field, for a boussinesq ocean such that $\nabla \cdot \mathbf{u} = 0$ and for tracers S_A and Θ, this results in,

$$\begin{aligned} \Psi^{\mathrm{adv}}_{S_\mathrm{A}\Theta}(S_\mathrm{A}, \Theta) &= \frac{1}{\Delta t} \int_t^{t+\Delta t} \int_{\Theta' \leq \Theta|_{S_\mathrm{A}}} u^{\mathrm{adv}}_{S_\mathrm{A}} dA dt \\ &= -\frac{1}{\Delta t} \int_t^{t+\Delta t} \int_{S'_\mathrm{A} \leq S_\mathrm{A}|_\Theta} u^{\mathrm{adv}}_{\Theta} dA dt, \end{aligned} \tag{3.7}$$

Here, $\int_{\Theta' \leq \Theta|_{S_\mathrm{A}}} dA$ is the area integral over all Θ', smaller than or equal to Θ on a surface of constant S_A. Equivalently, $\int_{S'_\mathrm{A} \leq S_\mathrm{A}|_\Theta} dA$ is the area integral over all S'_A, smaller than or equal to S_A on a surface of constant Θ and $\frac{1}{\Delta t} \int_t^{t+\Delta t}(...)dt$, is a time average. $\Psi^{\mathrm{adv}}_{S_\mathrm{A}\Theta}$ is the advective thermohaline streamfunction, and represents time-averaged thermohaline component of a non-divergent geographical ocean circulation, in (S_A, Θ) coordinates, as previously obtained by ZD12.

3.4 The local thermohaline streamfunction

We separate $\mathbf{u}^{\mathrm{iso}}_{S_\mathrm{A}\Theta}$ into a cycle and a trend term. We can then construct the local thermohaline streamfunction ($\Psi^{\mathrm{loc}}_{S_\mathrm{A}\Theta}$), using the de-trended component of $\mathbf{u}^{\mathrm{iso}}_{S_\mathrm{A}\Theta}$.

For a conceptual description, imagine a control volume containing a motionless fluid with fixed volume V_{control}, and uniform (S_A, Θ) values which (uniformly) change over time. Changing the (S_A, Θ) properties of the fluid in V_{control} over time, leads to a volume transport in (S_A, Θ) coordinates. We now consider different changes of the (S_A, Θ) values of V_{control}, to analyse and understand the resulting motion in (S_A, Θ) coordinates.

3.4.1 The diathermohaline trend

First, consider heating the control volume from time t_1 to t_2. When the fluid with volume V_{control} is heated, it may cross several isotherms and the related volume transport through these isotherms, in positive Θ-direction, will be $V_{\mathrm{control}}/\Delta t$, where Δt is a constant time step (Fig. 3.4a, cycle 1). Equivalently a change in S_A causes the properties

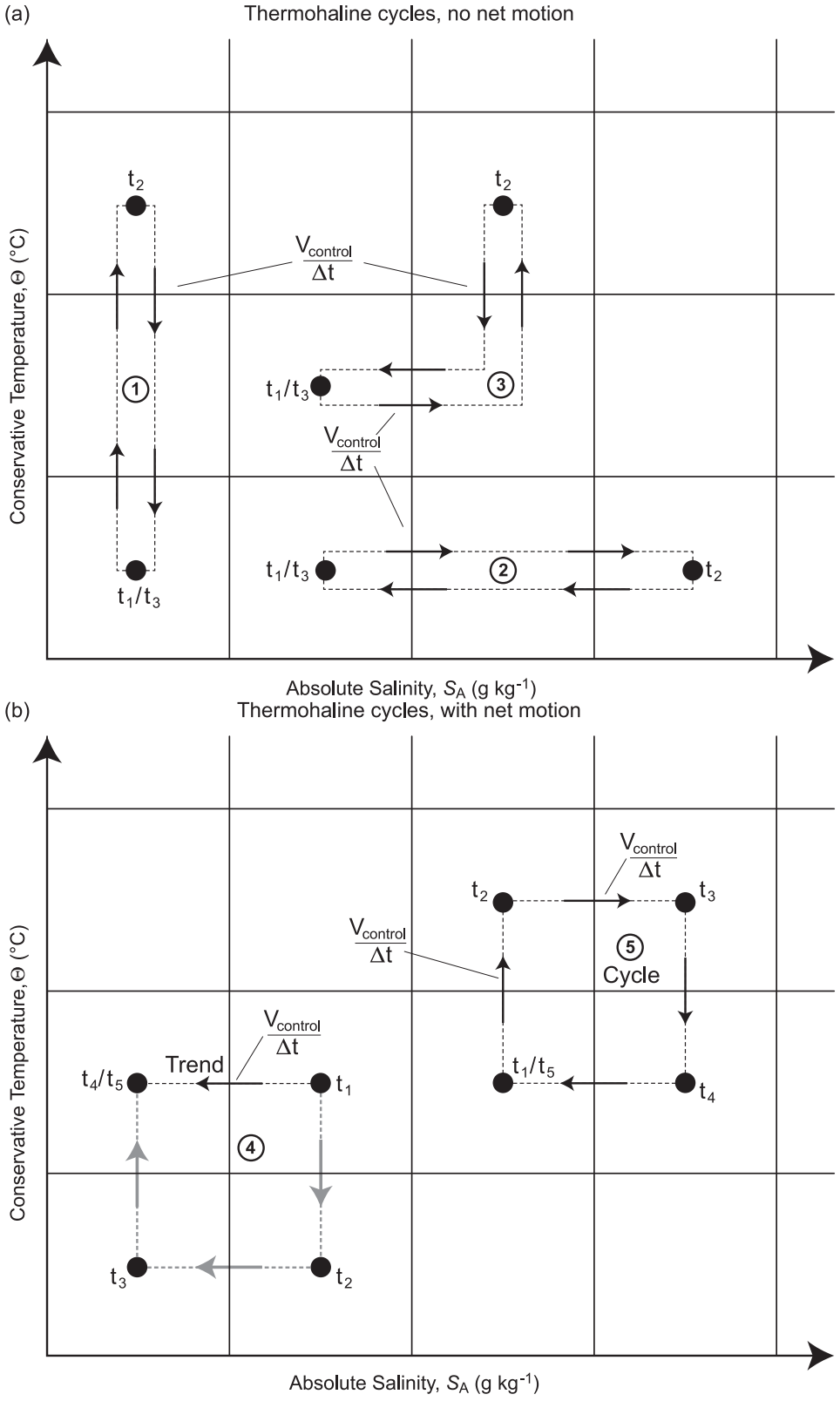

FIGURE 3.4: Circulation in (S_A, Θ) coordinates due to a shift of the ocean's volume distribution in (S_A, Θ) coordinates, with no net transport (left) or a net transport (right). Arrows indicate through which isotherms (between a certain S_A-interval) and isohalines (between a certain Θ-interval) the volume transport is assigned. Two arrows in opposite direction cancel out. Cycle 1 shows heating ($t_1 \to t_2$) and cooling ($t_2 \to t_3$), Cycle 2 shows salinification ($t_1 \to t_2$) and freshening ($t_2 \to t_3$). Cycle 3 shows heating and salinification ($t_1 \to t_2$) and cooling and freshening ($t_2 \to t_3$). Cycle 4 and 5 show net transport due to a diathermohaline trend and or cyclic motion respectively. Grey arrows of Cycle 4, show an incomplete cycle causing the diathermohaline trend, which will be closed when subtracting a trend, to define the cyclic component.

of V_{control} to cross isohalines, resulting in a similar volume transport in the positive S_{A}-direction (Fig. 3.4a, cycle 2). Although the fluid in the control volume has not moved in geographical space, its (S_{A}, Θ) values have changed, resulting in motion in (S_{A}, Θ) coordinates. The resulting volume transport can be calculated by analysing the total changes of the (S_{A}, Θ) values of the fluid, rather then analysing the displacements of the isohalines and isotherms (Appendix B).

A net displacement of fluid in (S_{A}, Θ) coordinates can be understood as a diathermohaline trend (Fig. 3.4b, cycle 4). However, if this displacement is continued over multiple time-steps, we can obtain both a diathermohaline trend *and* and a time-averaged steady-state and non-divergent component, which we will refer to as the diathermohaline cycle.

3.4.2 The diathermohaline cycle

The diathermohaline cycle in (S_{A}, Θ) coordinates, takes place when changes of (S_{A}, Θ) values in the control volume returns to their initial (S_{A}, Θ) values over time, but the heating and cooling (freshening and salinification) takes place at a different S_{A} (Θ), such that the net transports through isohalines for a certain Θ-range and isotherms for a certain S_{A}-range do not exactly cancel out (Fig. 3.4b, cycle 5). This cycle results in a net volume transport of $V_{\text{control}}/\Delta t$, across isohalines, for different Θ-ranges, and net volume transports across isotherms, for different S_{A}-ranges. Note that any cycle in which there are (simultaneous) changes of (S_{A}, Θ) values of the fluid in the control volume over time, which causes a transport across exactly the same isohalines and isotherms when moving away from and returning back to its initial state, results in no net transport over time (Fig. 3.4a, cycles 1,2 and 3 from t_1 to t_3).

For example, consider a volume in a motionless ocean, enclosed by a pair of isotherms and a pair of isohalines which change position with time (Fig. 3.5). For illustrative purposes we consider only the dynamics of three volumes that are within our grid indicated with $a-d$, 1) the volume V_Θ, of which Θ changes, 2) the volume $V_{S_{\text{A}}}$, of which S_{A} changes, and 3) the volume $V_{S_{\text{A}}\Theta}$, of which both S_{A} and Θ changes. We have the following sequence of events: i) the $(\Theta + d\Theta)$-isotherm changes position, warming the fluid in both V_Θ and $V_{S_{\text{A}}\Theta}$, ii) the $(S_{\text{A}} + dS_{\text{A}})$-isohaline changes position, salinifiing the fluid in both $V_{S_{\text{A}}}$ and $V_{S_{\text{A}}\Theta}$, iii) the $(\Theta + d\Theta)$-isotherm returns to its initial position, cooling the fluid in V_Θ and $V_{S_{\text{A}}\Theta}$ back to their original temperatures and finally, iv) the $(S_{\text{A}} + dS_{\text{A}})$-isohaline returns to its initial position, freshening the fluid in $V_{S_{\text{A}}}$ and $V_{S_{\text{A}}\Theta}$ to their initial states. Averaging over time we find that the diathermohaline volume transport through the isotherm (isohaline) due to the transport of the fluid in V_Θ ($V_{S_{\text{A}}}$) in (S_{A}, Θ) coordinates cancels (Fig. 3.4a, cycle 1 (2)). However, $V_{S_{\text{A}}\Theta}$ has undergone cyclic motion in (S_{A}, Θ)

coordinates that does not cancel out over time, thus leaving a net diathermohaline volume transports through isohalines and isotherms (Fig. 3.4b, cycle 5). Note that, for this particular example, the circulation in (S_A, Θ) coordinates is established without contributing to the geographical ocean circulation, only to the circulation in (S_A, Θ) coordinates.

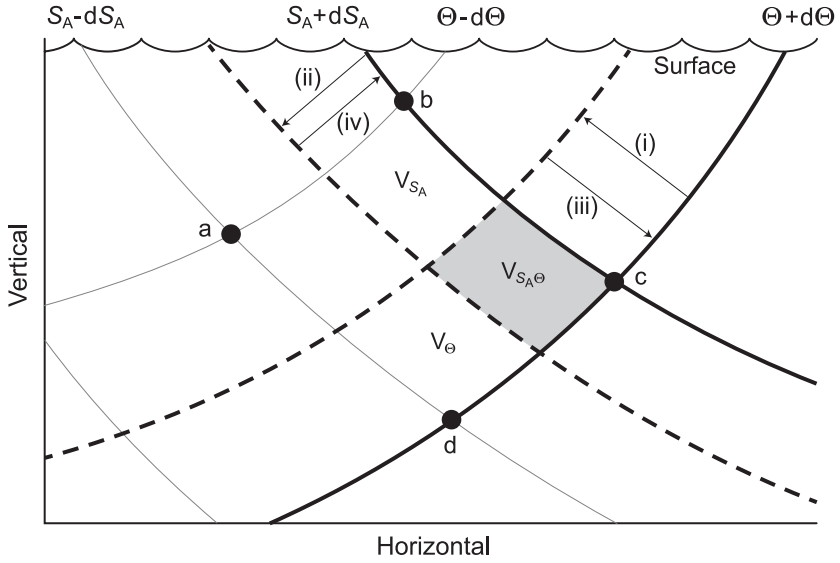

FIGURE 3.5: Schematic of movement of isohalines and isotherms that change the ocean's volume distribution in (S_A, Θ) coordinates. Events i, ii, iii and iv indicate displacement of the isotherms or isohalines due to heating, salinification, cooling and freshening respectively. The motion of V_Θ, V_{S_A} and the grey shaded volume $V_{S_\mathrm{A}\Theta}$ in (S_A, Θ) coordinates is described by cycle 1,2 and 5, respectively (Fig 3.4). Only $V_{S_\mathrm{A}\Theta}$ contributes to a net circulation in (S_A, Θ) coordinates.

3.4.3 The local thermohaline streamfunction

We have argued that diathermohaline volume transports can be decomposed into a diathermohaline cycle and trend. The diathermohaline trend represents net changes in the ocean's volume distribution in (S_A, Θ) coordinates. A trend can be the result of 1) the net change of the geographical position of the bounding isohalines and isotherms induced by a net change in local (S_A, Θ) values, and 2) a non-zero integral of $\mathbf{u}$ in the direction normal to the bounding isohalines and isotherms, over the surface area enclosing a volume.

The latter is only of interest for the construction of the advective thermohaline streamfunction, but is not an issue for an instantaneous velocity field in a Boussinesq ocean. Hence we focus on removing a potential trend in $\mathbf{u}^{\mathrm{iso}}_{S_\mathrm{A}\Theta}$, which does not allow us to represent $\mathbf{u}^{\mathrm{iso}}_{S_\mathrm{A}\Theta}$ with a streamfunction. The trend in $\mathbf{u}^{\mathrm{iso}}_{S_\mathrm{A}\Theta}$ is due to a time-averaged trend

in local changes of (S_A, Θ)

$$\begin{aligned} u^{\mathrm{tr}}_{S_\mathrm{A}} &= \frac{1}{|\nabla S_\mathrm{A}|}\frac{1}{\Delta t}\int_t^{t+\Delta t}\frac{\partial S_\mathrm{A}}{\partial t}dt \\ u^{\mathrm{tr}}_{\Theta} &= \frac{1}{|\nabla \Theta|}\frac{1}{\Delta t}\int_t^{t+\Delta t}\frac{\partial \Theta}{\partial t}dt. \end{aligned} \tag{3.8}$$

Note that, although the integral results in a constant, $|\nabla S_\mathrm{A}|$ and $|\nabla\Theta|$ may change in time and space. This results in $\mathbf{u}^{\mathrm{tr}}_{S_\mathrm{A}\Theta} = \left(u^{\mathrm{tr}}_{S_\mathrm{A}}, u^{\mathrm{tr}}_{\Theta}\right)$. Here $u^{\mathrm{tr}}_{S_\mathrm{A}}$ is the net velocity of the movement of isohalines in geographical space, in the direction normal to themselves, due to a local trend of S_A over time period Δt and u^{tr}_{Θ} is the net velocity of isotherms in geographical space, in the direction normal to themselves, due to a local trend of Θ. We can now use Eq. (3.8) to obtain the non-divergent component of the diathermohaline velocity, which can be represented by the local thermohaline streamfunction $(\Psi^{\mathrm{loc}}_{S_\mathrm{A}\Theta})$,

$$\begin{aligned} \Psi^{\mathrm{loc}}_{S_\mathrm{A}\Theta}(S_\mathrm{A},\Theta) &= \frac{1}{\Delta t}\int_t^{t+\Delta t}\int_{\Theta'\le\Theta|_{S_\mathrm{A}}} -u^{\mathrm{iso}}_{S_\mathrm{A}} - u^{\mathrm{tr}}_{S_\mathrm{A}} dA dt \\ &= -\frac{1}{\Delta t}\int_t^{t+\Delta t}\int_{S'_\mathrm{A}\le S_\mathrm{A}|_\Theta} -u^{\mathrm{iso}}_{\Theta} - u^{\mathrm{tr}}_{\Theta} dA dt. \end{aligned} \tag{3.9}$$

Here $\Psi^{\mathrm{loc}}_{S_\mathrm{A}\Theta}$ represents the thermohaline volume transport due to cyclic movement of isohalines and isotherms due to local changes in S_A and Θ. Cyclic refers to isohalines and isotherms (or S_A and Θ) moving away from their initial state and then subsequently returning back to it, within a given period of time Δt (e.g, Fig. 3.4b, cycle 5 and Fig. 3.5). To calculate $\Psi^{\mathrm{loc}}_{S_\mathrm{A}\Theta}$, we use a de-trended ocean hydrography (from either a model or observations). The local changes in (S_A, Θ) values need not to be periodic. Depending on the period Δt, they are expected to be dominated by different physical processes as for example, diurnal cycles, seasonal cycles or climate modes such as the El Niño-Southern Oscillation (ENSO) cycles.

3.5 The diathermohaline streamfunction

In the preceding sections we have shown that the diathermohaline velocity consists of two components, one related to geographical advection of fluid parcels and one due to local changes of both S_A and Θ. Following ZD12, we have expressed the advective component as an advective thermohaline streamfunction $(\Psi^{\mathrm{adv}}_{S_\mathrm{A}\Theta})$. In addition, we have expressed the component due to local changes in S_A and Θ, as the local thermohaline streamfunction $(\Psi^{\mathrm{loc}}_{S_\mathrm{A}\Theta})$. The sum of both thermohaline streamfunctions allows us to construct the diathermohaline streamfunction $(\Psi^{\mathrm{dia}}_{S_\mathrm{A}\Theta})$. This can be shown using only the component of the diathermohaline velocity that is cyclic in (S_A, Θ) coordinates, i.e.,

de-trended diathermohaline velocity $\mathbf{u}^{\rm dia}_{S_{\rm A}\Theta} - \mathbf{u}^{\rm tr}_{S_{\rm A}\Theta}$. Making use of (3.4) and (3.5) we obtain,

$$\begin{aligned}
\Psi^{\rm dia}_{S_{\rm A}\Theta} &= \frac{1}{\Delta t}\int_t^{t+\Delta t}\int_{\Theta'\le\Theta|_{S_{\rm A}}} u^{\rm adv}_{S_{\rm A}} - u^{\rm iso}_{S_{\rm A}} - u^{\rm tr}_{S_{\rm A}} dA dt \qquad (3.10)\\
&= -\frac{1}{\Delta t}\int_t^{t+\Delta t}\int_{S'_{\rm A}\le S_{\rm A}|_\Theta} u^{\rm adv}_{\Theta} - u^{\rm iso}_{\Theta} - u^{\rm tr}_{\Theta} dA dt\\
&= \Psi^{\rm adv}_{S_{\rm A}\Theta} + \Psi^{\rm loc}_{S_{\rm A}\Theta}.
\end{aligned}$$

Here $\Psi^{\rm dia}_{S_{\rm A}\Theta}$ represents the cyclic or non-divergent component of the steady-state geographical ocean circulation in $(S_{\rm A}, \Theta)$ coordinates. Note that $\Psi^{\rm dia}_{S_{\rm A}\Theta}$ is a 'dia'-transport and requires water-mass transformation to occur. Therefore $\Psi^{\rm dia}_{S_{\rm A}\Theta}$ is solely forced by, and can be directly related to, the thermohaline forcing. If there is no thermohaline forcing, we obtain $\Psi^{\rm dia}_{S_{\rm A}\Theta} = \Psi^{\rm adv}_{S_{\rm A}\Theta} + \Psi^{\rm loc}_{S_{\rm A}\Theta} = 0$. However, as $\Psi^{\rm adv}_{S_{\rm A}\Theta}$ and $\Psi^{\rm loc}_{S_{\rm A}\Theta}$ are not 'dia'-transports, geographical advection of water parcels may lead to cycles and an opposing advective cycle that does not require water-mass transformation (and therefore no thermohaline forcing), allowing for $\Psi^{\rm adv}_{S_{\rm A}\Theta} = -\Psi^{\rm loc}_{S_{\rm A}\Theta} \neq 0$. Therefore, circulations shown by $\Psi^{\rm adv}_{S_{\rm A}\Theta}$ and $\Psi^{\rm loc}_{S_{\rm A}\Theta}$, may also contain a signal driven by geographical advection which is not quantified. This limitation illustrates that one should be careful when interpreting the circulations shown by $\Psi^{\rm adv}_{S_{\rm A}\Theta}$ and $\Psi^{\rm loc}_{S_{\rm A}\Theta}$ as being caused by thermohaline forcing only. Note that the diathermohaline volume transport due to $\mathbf{u}^{\rm tr}_{S_{\rm A}\Theta}$ also requires a part of the available thermohaline forcing. This needs to be taken into account when providing an interpretation of $\Psi^{\rm dia}_{S_{\rm A}\Theta}$.

3.6 Application to model and observationally based hydrography

In the following we calculate $\Psi^{\rm dia}_{S_{\rm A}\Theta}$, $\Psi^{\rm adv}_{S_{\rm A}\Theta}$ and $\Psi^{\rm loc}_{S_{\rm A}\Theta}$ using output from a climate model and also calculate $\Psi^{\rm loc}_{S_{\rm A}\Theta}$ from an observational-based climatology.

3.6.1 Description of used model and observations

We use the final 10 years of a 3000 years spin up simulation of the University of Victoria Climate Model (UVIC). This model is an intermediate complexity climate model with horizontal resolution of 1.8^o latitude by 3.6^o longitude, 19 vertical levels and a 2D energy balance atmosphere (Sijp et al. (2006), specifically their case referred to as 'GM'). The ocean model is the Geophysical Fluid Dynamics Laboratory Modular Ocean Model version 2.2 (MOM2) with Boussinesq and rigid-lid approximations applied (Pacanowski,

1995). We use the monthly averaged potential temperature (θ, ^{o}C) and Practical Salinity (S_P).

The observation-based climatology we use is CARS 2009 (CARS). This is a global, except for the boundary at 75^{o}S, high-resolution (0.5^o x 0.5^o grid spacing, 79 vertical levels) seasonal atlas of $in-situ$ temperature (T), Practical Salinity (S_P), and several other properties (Ridgway et al., 2002, Ridgway and Dunn, 2003). At higher latitudes observations are limited and biased to the summer state. In summary CARS provides a gridded, time-continuous standard year value of S_P and T on each grid-point. To be able to compare the results with UVIC, we use monthly averaged values.

We have used the TEOS-10 software (IOC et al., 2010, McDougall and Barker, 2011) to convert both the UVIC model output and the CARS data to S_A and Θ. The practical details of the calculations of the different variables from both model and observations are provided in Appendix B.

3.6.2 The thermohaline volume transports and diathermohaline trend

The diathermohaline volume transport in (S_A, Θ) coordinates, for volumes with a certain S_A and Θ grid size can be calculated and compared for the advective and local thermohaline streamfunction and the diathermohaline trend (Fig. 3.6). The diathermohaline trend shows maximum values of the order of 1 Sv (1 Sv =10^6 m^3 s^{-1}), which is small compared to those of the advective and local streamfunctions, as expected from an equilibrated climate model. Note that, using the t-test, we found that none of these trends are significant to within the 95%. Hence, for UVIC $\Psi^{\mathrm{dia}}_{S_\mathrm{A}\Theta}$ represent UVIC's diathermohaline circulation and can be directly related to UVIC's thermohaline forcing. As CARS is constructed as a standard year, no diathermohaline trend can be calculated.

Climate trends (e.g., long-term warming of the ocean) lead to a permanent change in positions of isohalines and isotherms, thereby shifting the ocean's volume towards a different state. Diathermohaline trend terms that do not stem from a climate change, complicate the interpretation of the diathermohaline trend. For example the time period over which we average to analyse the diathermohaline trend is chosen to include an integer amount of closed cycles of the dominant cyclic motions in (S_A, Θ) coordinates. Climate variability modes that do not fit in the selected time period, will cause a net shift of the ocean's volume in (S_A, Θ) coordinates. Rounding errors due to time and spatial averaging of model or observational data, numerical diffusion and other possible sources of error, also lead to a diathermohaline trend in (S_A, Θ) coordinates.

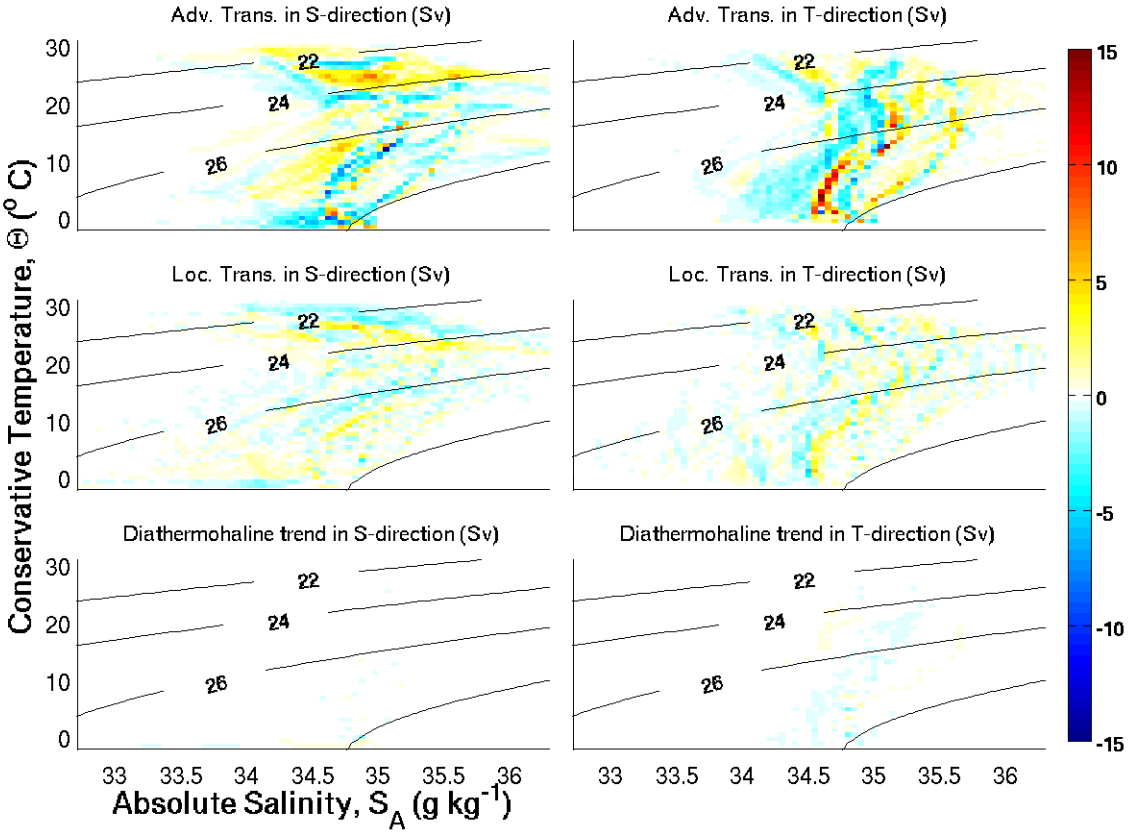

FIGURE 3.6: The diahaline (left) and diathermal (right) volume transports (in Sv) of the UVIC model for (upper) $\Delta\Psi^{\mathrm{adv}}_{S_\mathrm{A}\Theta}$, (middle) $\Delta\Psi^{\mathrm{loc}}_{S_\mathrm{A}\Theta}$ and the (lower) diathermohaline trend (for details about their calculation, see Appendix B). The intervals used to calculate a streamfunction difference are $d\Theta = 0.75$ °C and $dS_\mathrm{A} = 0.05$ g kg^{-1}. The black lines indicate the contours for potential density (σ_0).

3.6.3 The advective thermohaline streamfunction

$\Psi^{\mathrm{adv}}_{S_\mathrm{A}\Theta}$ is only calculated for UVIC as CARS does not provide $\mathbf{u}$. As we calculate $\Psi^{\mathrm{adv}}_{S_\mathrm{A}\Theta}$ using the same model output as Zika et al. (2012), we only provide a short summary of our results as they are similar to ZD12.

The three dominant circulation cells shown by $\Psi^{\mathrm{adv}}_{S_\mathrm{A}\Theta}$ (Fig. 3.7) can, in conjunction with knowledge of ocean basin's (S_A, Θ) properties, be related to a geographical location and associated thermohaline processes. We distinguish, i) a high latitude cell, related to processes in the Arctic region and the Southern Ocean such as Antarctic Bottom Water formation, ii) a tropical cell related to the equatorial shallow wind-driven circulation and surface freshwater and heat-fluxes and, iii) the global cell that spans a large range in (S_A, Θ) coordinates, that can be interpret as a globally interconnected ocean circulation.

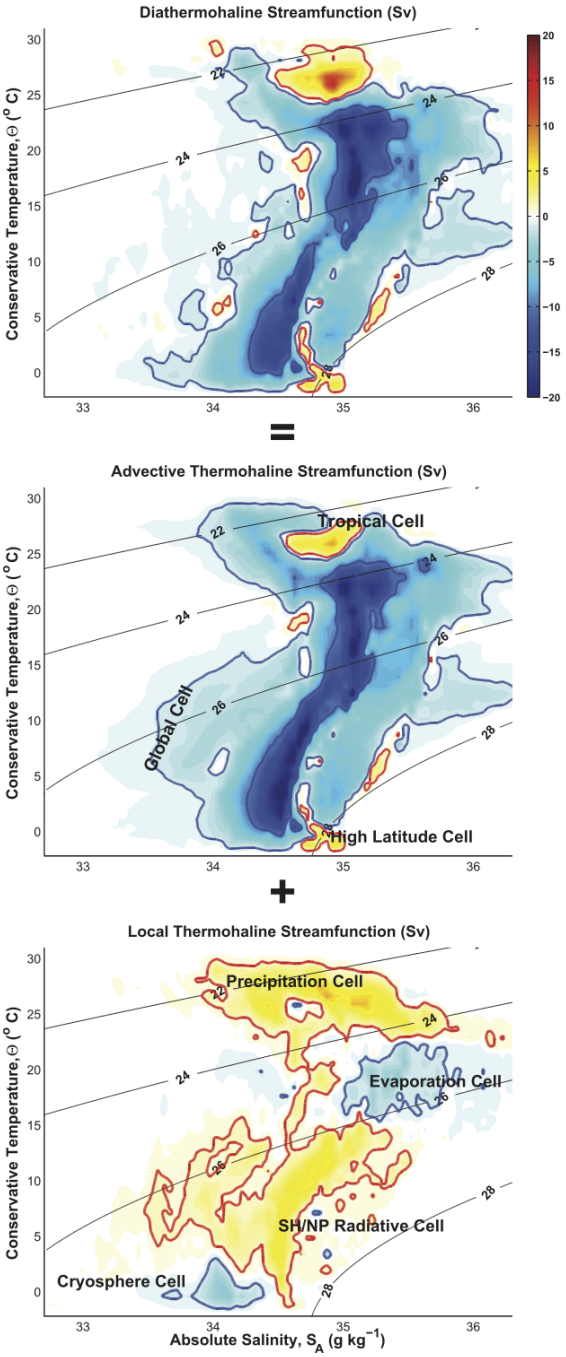

FIGURE 3.7: The UVIC model's $\Psi^{\mathrm{dia}}_{S_A\Theta}$ (top), $\Psi^{\mathrm{adv}}_{S_A\Theta}$ (middle) and $\Psi^{\mathrm{loc}}_{S_A\Theta}$ (bottom) circulations (Sv). The color scale applies to all panels. Blue (yellow) cells rotate clockwise (anti-clockwise). The blue lines show the [-15,-10, -1] Sv-contours, the red lines the 1Sv contour and the black lines the contours for potential density (σ_0).

3.6.4 The local thermohaline streamfunction

We have calculated $\Psi^{\rm loc}_{S_{\rm A}\Theta}$ for the UVIC model (Fig. 3.7) and CARS (Fig. 3.8). The majority of the circulation of $\Psi^{\rm loc}_{S_{\rm A}\Theta}$ is explained by near-surface dynamics, as the ocean abyss is not expected to have significant cyclic changes in $(S_{\rm A}, \Theta)$ values on sub-decadal time scales. For an interpretation of $\Psi^{\rm loc}_{S_{\rm A}\Theta}$, we will use the ocean's surface $(S_{\rm A}, \Theta)$ values to relate the circulation cells of $\Psi^{\rm loc}_{S_{\rm A}\Theta}$ shown in $(S_{\rm A}, \Theta)$ coordinates with geographical locations (Fig. 3.9).

An anti-clockwise rotating cell is found in an area in $(S_{\rm A}, \Theta)$ coordinates associated with equatorial surface waters (Fig. 3.9). It shows strong freshening due to precipitation, associated with the seasonal variability of the surface freshwater and heat fluxes related to the position and strength of the Inter-Tropical Convergence Zone (ITCZ) and is named precipitation cell.

A clockwise rotating cell is mainly related to evaporation over high $S_{\rm A}$-valued water masses (Fig. 3.9), which are most likely the formation regions of South Pacific and Indian Ocean subtropical mode water (Hanawa and Talley, 2001) and high salinity evaporation areas such as the Mediterranean, Persian Gulf, Red Sea and tropical Atlantic, and is named evaporation cell.

There is a clear separation in $(S_{\rm A}, \Theta)$ coordinates between the evaporation and precipitation cells and the southern hemisphere (SH) and North Pacific (NP) radiative cells, which are dominated by radiative heating and cooling (Fig. 3.9). The anticlockwise rotating SH radiative cell stretches over a wide temperature range in $(S_{\rm A}, \Theta)$ coordinates. This is due to summer radiative heating and winter radiative cooling in the Southern Ocean and adjacent ocean basins at subtropical latitudes (Fig. 3.9). The curved shape of the SH radiative cell can be explained by a change in the E-P fluxes from being dominated by freshening (precipitation dominating evaporation and possible cryospheric processes) at cold temperatures, to being dominated by salinification (evaporation dominating precipitation) at slightly warmer temperatures. As a result the streamfunction changes direction on the $S_{\rm A}$-axis, leading to the observed shape. The latter also explains the anticlockwise rotating NP radiative cell, due to a combination of the cryospheric processes and seasonal radiative heat fluxes. The NP radiative cell is separated from the SH radiative cell by the fresh North Pacific surface waters.

The clockwise rotating cryosphere cell represents a circulation at high latitudes. We remind the reader that CARS is based on limited high latitude observations, biased towards summer and extending only to 75^{o}S. This might reduce the magnitude and spread of the cryosphere cell in $S_{\rm A}\Theta$-coordinates and complicates the interpretation. However, we suggest the cryosphere cell represents cryospheric processes as we find that

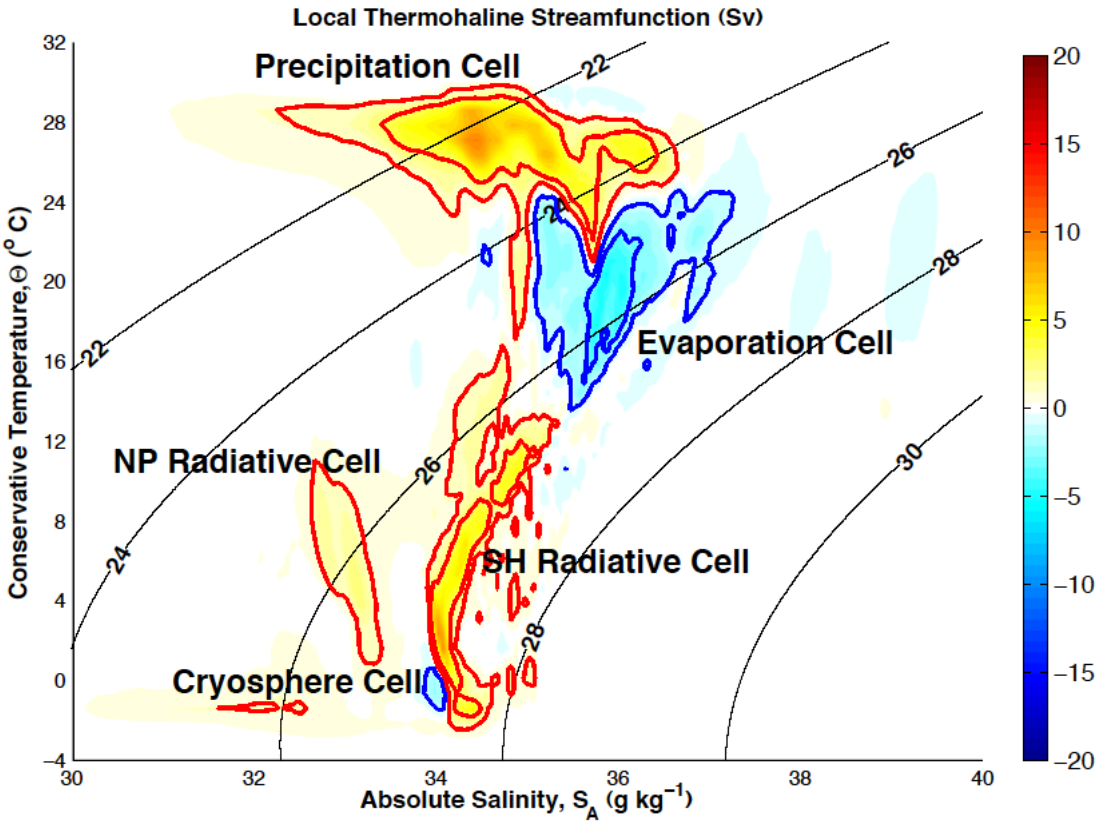

FIGURE 3.8: The $\Psi^{\mathrm{loc}}_{S_{\mathrm{A}}\Theta}$ circulation for CARS. Blue (yellow) cells rotate clockwise (anti-clockwise). Blue (red) contours show the -3Sv (3Sv) and -1Sv (1Sv) intervals. The black lines indicate the contours for potential density (σ_0).

warming (cooling) is associated with freshening (salinification), with minimum influence of seasonal radiative heat fluxes (Fig. 3.9).

Comparing $\Psi^{\mathrm{loc}}_{S_{\mathrm{A}}\Theta}$ from CARS (Fig. 3.8) with that from the UVIC model (Fig. 3.7) shows that the model has a reduced spread in (S_{A}, Θ)
coordinates. An incorrect model representation of the extremes in the thermohaline coordinates may be caused by, 1) excessive near-surface mixing (too much damping), 2) underestimation of the surface freshwater and heat fluxes (not enough forcing), 3) heating and cooling (freshening and salinification) takes place at the same salinity (temperature) because of incorrect modelling of the salt (heat) fluxes resulting in cancelation (Fig. 3.4a, processes 1,2 and 3), and 4) an incorrect representation of advection in the model, influencing the unquantified, advective driven component of $\Psi^{\mathrm{loc}}_{S_{\mathrm{A}}\Theta}$.

The reduced spread of the UVIC model precipitation cell, suggests an incorrect simulation of the ITCZ freshwater and heat fluxes. The evaporation cell also shows a reduced magnitude and spread at higher salinities suggesting a problem with the formation and properties of the South Pacific and Indian Ocean subtropical mode water and the tropical Atlantic surface waters.

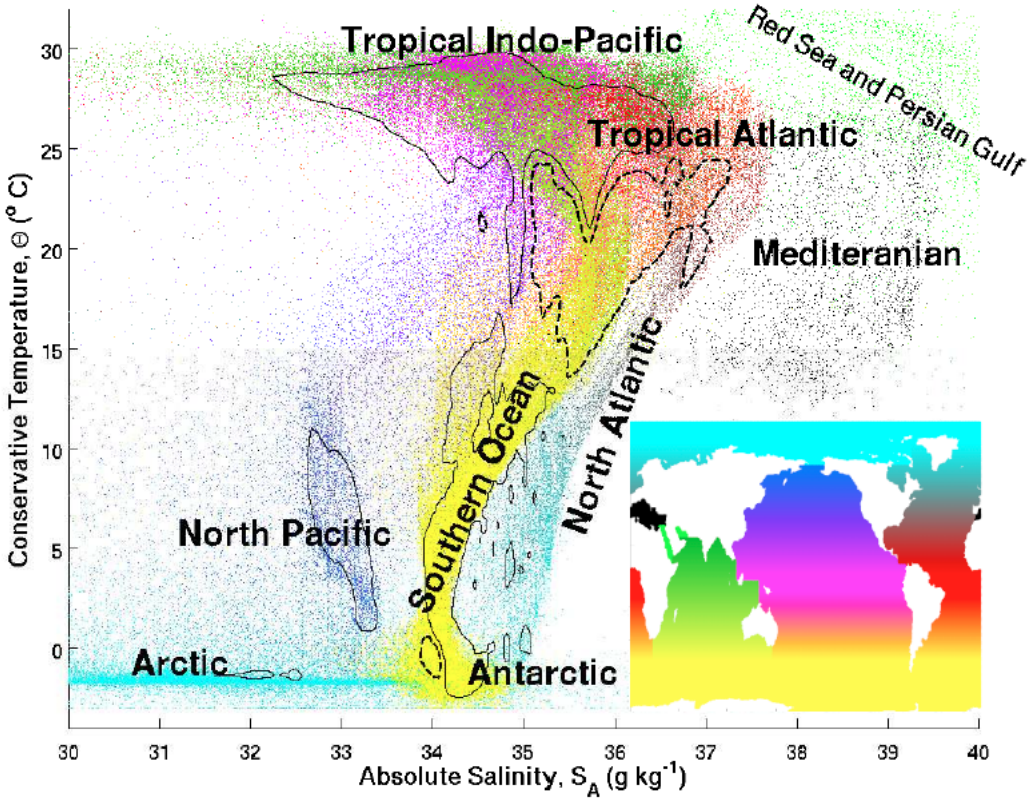

FIGURE 3.9: The ocean's surface (S_A, Θ) values from a full year of CARS, distributed in (S_A, Θ) coordinates. Colour indicates geographical location as shown by the inset. The 1Sv contours of $\Psi^{\mathrm{loc}}_{S_\mathrm{A}\Theta}$ for CARS (Fig. 3.8) are included. Dashed (Solid) black contours rotate clockwise (anti-clockwise).

Areas covered by the evaporation and precipitation cells in (S_A, Θ) coordinates are expected to diverge in time on the S_A-axis, if relatively salty water increases its salinity and relatively fresh water reduces its salinity (Durack et al., 2012). Such dynamics can be analysed from climatological trends and are related to changes in the surface freshwater and heat fluxes of these particular areas.

In the UVIC model, both SH and NP radiative cells have merged in (S_A, Θ) coordinates, suggesting that the surface freshwater pool in the North Pacific is not correctly modelled and coincides with the SH salinities. Differences in the SH surface freshwater fluxes between CARS and the UVIC model, suggest that the transition between the evaporation to precipitation dominated regime for decreasing temperatures for the SH radiative cell is not captured by the model. Finally the UVIC model cryosphere cell has an increased spread and magnitude compared to CARS, which has a bias towards the summer and lacks Arctic data.

3.7 Discussion

We have presented the derivation of the diathermohaline streamfunction ($\Psi^{\rm dia}_{S_{\rm A}\Theta}$), which is composed of an advective thermohaline streamfunction ($\Psi^{\rm adv}_{S_{\rm A}\Theta}$) and a local thermohaline streamfunction ($\Psi^{\rm loc}_{S_{\rm A}\Theta}$). The latter is calculated from both a model and observations. The circulation shown by $\Psi^{\rm dia}_{S_{\rm A}\Theta}$ (Fig. 3.7), enables physically unconnected volumes in the geographical ocean (e.g., in different ocean basins) bounded by similar isohalines and isotherms, to be represented by one single grid in $(S_{\rm A}, \Theta)$ coordinates, reducing the 3-dimensional spatial and temporal ocean circulation to a 2-dimensional time-averaged circulation in $(S_{\rm A}, \Theta)$ coordinates, that is driven by thermohaline forcing. The framework presented here could in principle be applied to any two coordinates defined by two conservative tracers.

To drive the observed circulation of $\Psi^{\rm loc}_{S_{\rm A}\Theta}$ freshwater and heat fluxes are required. Consequently, part of the available freshwater and heat fluxes will not be available to drive the circulation observed in the $\Psi^{\rm adv}_{S_{\rm A}\Theta}$. A quantitive insight in the relative importance of $\Psi^{\rm adv}_{S_{\rm A}\Theta}$ and $\Psi^{\rm loc}_{S_{\rm A}\Theta}$ is obtained by calculating the diapycnal salt ($F_{\rm Salt}(\rho_{\rm r})$) and heat ($F_{\rm Heat}(\rho_{\rm r})$) transports for reference potential density $\rho_{\rm r}$. Following Zika et al. (2012), this is given by

$$F_{\rm Heat}(\rho_{\rm r}) = \int_{\rho_{\rm r}} \rho c_p^0 \Theta d\Psi^{\rm dia}_{S_{\rm A}\Theta}, \quad F_{\rm Salt}(\rho_{\rm r}) = \int_{\rho_{\rm r}} S_{\rm A} d\Psi^{\rm dia}_{S_{\rm A}\Theta}, \tag{3.11}$$

where we have applied an integration along lines of constant reference potential density $\rho_{\rm r}$. The salt flux can be recalculated to an equivalent freshwater flux ($F_{\rm FW}(\rho_{\rm r}) = F_{\rm Salt}(\rho_{\rm r})/S_{\rm ref}$), when dividing it by a reference salinity ($S_{\rm ref} = 35$). The resulting diapycnal freshwater and heat transports for both $\Psi^{\rm adv}_{S_{\rm A}\Theta}$ and $\Psi^{\rm loc}_{S_{\rm A}\Theta}$, emphasise that $\Psi^{\rm loc}_{S_{\rm A}\Theta}$ requires a significant amount of the total available freshwater and heat fluxes and cannot be ignored when analysing the ocean's diathermohaline circulation (Fig. 3.10). Hence, only the combination of both $\Psi^{\rm adv}_{S_{\rm A}\Theta}$ and $\Psi^{\rm loc}_{S_{\rm A}\Theta}$ provide a diagnostic for modellers to analyse and understand the magnitude, structures and types of diathermohaline circulation in their models. Finally, in contrast to most other streamfunctions, $\Psi^{\rm loc}_{S_{\rm A}\Theta}$ can also be calculated from observational based products.

We have used surface $(S_{\rm A}, \Theta)$ properties to provide understanding of the observed circulation of $\Psi^{\rm loc}_{S_{\rm A}\Theta}$. Hieronymus et al. (2014) represented the different components of thermohaline forcing (boundary salt and heat fluxes and the epineutral and dianeutral salt and heat diffusion components) as water-mass transformation vectors in $(S_{\rm A}, \Theta)$ coordinates. Their study provides a tool to understand in more detail, how the diathermohaline circulation provided by $\Psi^{\rm dia}_{S_{\rm A}\Theta}$, is related with the different components of the thermohaline forcing.

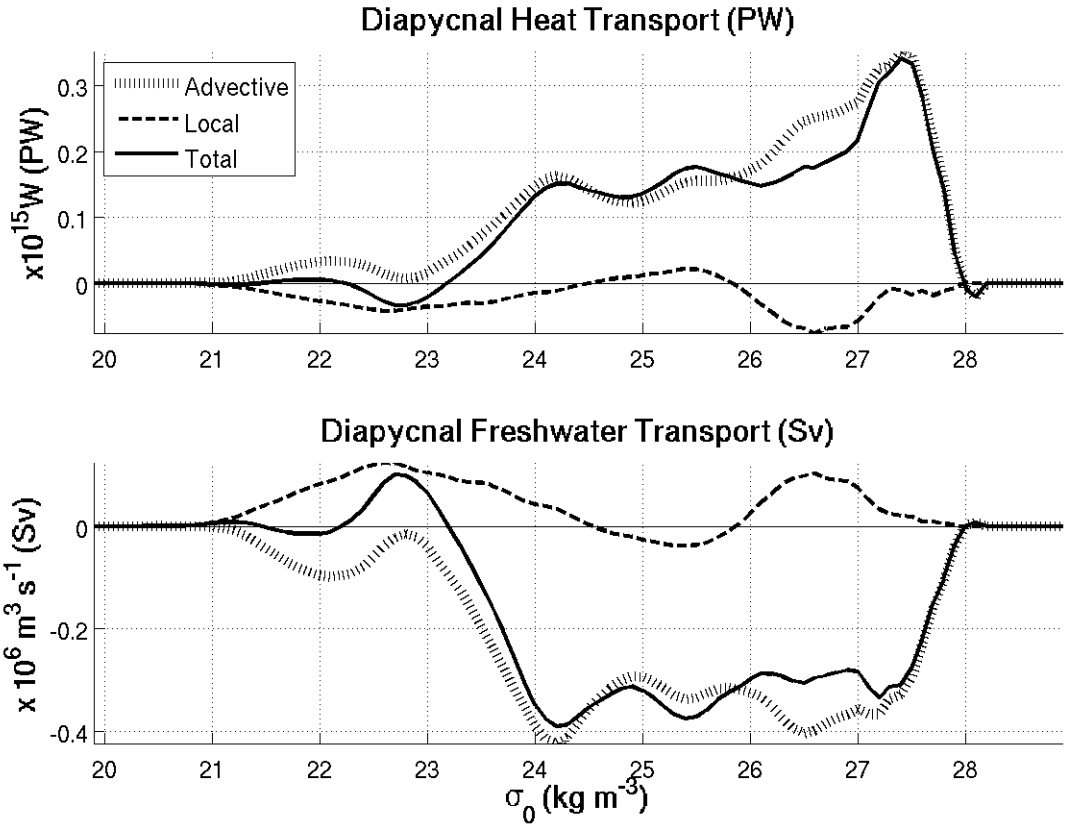

FIGURE 3.10: Diapycnal transport of heat in 10^{15}W (top) and freshwater in Sv (bottom) through potential density surfaces (σ_0) for the UVIC model for $\Psi^{\text{dia}}_{S_\text{A}\Theta}$ (solid), $\Psi^{\text{adv}}_{S_\text{A}\Theta}$ (dotted) and $\Psi^{\text{loc}}_{S_\text{A}\Theta}$ (dashed).

Ballarotta et al. (2013) showed that temporal and spatial averaging applied to construct the overturning streamfunction, significantly influences the observed circulation and requiring care with the interpretation. Zika et al. (2012) showed that the parameterised eddies have a significant influences on $\Psi^{\text{adv}}_{S_\text{A}\Theta}$. The study of the sensitivity of $\Psi^{\text{dia}}_{S_\text{A}\Theta}$, $\Psi^{\text{adv}}_{S_\text{A}\Theta}$ and $\Psi^{\text{loc}}_{S_\text{A}\Theta}$ to spatial and temporal averaging of the model's S_A, Θ and $\mathbf{u}$ output, is beyond the scope of this research. Hence one can only interpret our results to be valid on seasonal to decadal time-scales.

3.8 Conclusions

We have introduced the diathermohaline circulation, driven by boundary freshwater and heat fluxes and mixing processes (thermohaline forcing). The time-averaged non-divergent component of the diathermohaline circulation in (S_A, Θ) coordinates, is quantified by the diathermohaline streamfunction $\Psi^{\text{dia}}_{S_\text{A}\Theta}$. Here $\Psi^{\text{dia}}_{S_\text{A}\Theta}$ is composed of an advective and local component. The advective component is related to the geographical ocean circulation normal to isohaline and isothermal surfaces, as recently introduced in

the literature (ZD12), and here quantified by the advective thermohaline streamfunction, $\Psi^{\mathrm{adv}}_{S_\mathrm{A}\Theta}$. The local component is quantified by the local thermohaline streamfunction $\Psi^{\mathrm{loc}}_{S_\mathrm{A}\Theta}$. Here $\Psi^{\mathrm{loc}}_{S_\mathrm{A}\Theta}$ represents geographical displacements of isohalines and isotherms, that over time, return to their initial position, as a result of de-trended local changes in (S_A, Θ) values. $\Psi^{\mathrm{dia}}_{S_\mathrm{A}\Theta}$ is expressed as the sum of $\Psi^{\mathrm{adv}}_{S_\mathrm{A}\Theta}$ and $\Psi^{\mathrm{loc}}_{S_\mathrm{A}\Theta}$ and provides a model diagnostic which is related directly to thermohaline forcing. The time-averaged unsteady component of the diathermohaline circulation is referred to as the diathermohaline trend and represents permanent, time averaged water mass changes, related to thermohaline forcing.

Currently $\Psi^{\mathrm{dia}}_{S_\mathrm{A}\Theta}$ can only be calculated using models as it requires global knowledge of the 3-dimensional velocity field ($\mathbf{u}$). As presented $\Psi^{\mathrm{loc}}_{S_\mathrm{A}\Theta}$ can be calculated using model output and an ocean hydrography, allowing for a comparison between model and observed $\Psi^{\mathrm{loc}}_{S_\mathrm{A}\Theta}$. In future work we will present a technique using an inverse method that allows us to calculate $\Psi^{\mathrm{dia}}_{S_\mathrm{A}\Theta}$ from observational air-sea freshwater and heat fluxes and an ocean's hydrography, in combination with a representation of ocean mixing processes (Chapter 4 based on Groeskamp et al. (2014b)).

Chapter 4

A Thermohaline Inverse Method For Estimating Diathermohaline Circulation and Mixing

4.1 Introduction

Mixing in the ocean influences the earth's climate through its ability to alter the ocean's circulation and uptake and distribution of tracers such as heat, oxygen and carbon. An increased understanding of ocean mixing, both observationally and its representation in models, is necessary to better understand and model the ocean's influence on the climate system.

Currently ocean climate models parameterise interior ocean mixing as down-gradient epineutral diffusion (along isopycnal diffusion), with diffusion coefficient K, and dianeutral down-gradient turbulent diffusion due to small scale mixing with diffusion coefficient D (Redi, 1982, Griffies, 2004). The spatial and temporal varying magnitude of K and D are not easily obtained from theory. Therefore we require empirical (observationally) based estimates to improve our understanding of K and D.

Munk (1966) provided such an estimate using an approximate balance between (vertical) ocean advection and mixing along with tracer observations, to obtain a steady state estimate of D. Munk's study demonstrated that observed estimates of tracers can be used to obtain estimates of ocean circulation and mixing.

To obtain estimates of the structure and magnitude of the ocean circulation from observations, Stommel and Schott (1977) and Wunsch (1978) introduced inverse methods

into the field of oceanography. Ever since, many inverse studies have provided observationally based estimates of circulation (Schott and Stommel, 1978, Killworth, 1986, Cunningham, 2000, Sloyan and Rintoul, 2000, 2001) of which some used the diapycnal fluxes to provide estimates for D (Ganachaud and Wunsch, 2000, Lumpkin and Speer, 2007). Zhang and Hogg (1992) and Zika et al. (2010a), developed an inverse method that, simultaneously, solves for the circulation and both K and D.

Ocean circulation is often represented by a volumetric streamfunction, simplifying the 3-dimensional time varying (global) ocean circulation into a 2-dimensional time-averaged circulation. The streamfunction has been defined using different combinations of coordinates, both geographic and thermodynamic (Bryan et al., 1985, Döös and Webb, 1994, Hirst et al., 1996, Hirst and McDougall, 1998, Nycander et al., 2007). Based on an averaging technique developed by Nurser and Lee (2004), Ferrari and Ferreira (2011) have defined an advective meridional streamfunction, $\Psi_{C_1 y}$, for an instantaneous velocity field v and arbitrary tracer C_1. Zika et al. (2012) generalised this technique to compute a mean advective streamfunction, $\Psi_{C_1 C_2}$, of any two tracers, C_1 and C_2, for an instantaneous velocity field, $\mathbf{u} = (u, v, w)$. Here $\Psi_{C_1 C_2}$ represents the advective transport of fluid parcels in (C_1, C_2) coordinates. Zika et al. (2012) applied this to salinity S and temperature T coordinates to obtain the advective thermohaline streamfunction Ψ^{adv}_{ST}. In independent work Döös et al. (2012) also developed Ψ^{adv}_{ST}.

In Chapter 3 (based on, and hereafter referred to as, Groeskamp et al. (2014a)) we showed how the total circulation in (S, T) coordinates is driven by thermohaline forcing, i.e surface freshwater and heat fluxes and salt and heat fluxes by diffusive mixing. They showed that the total circulation in (S, T) coordinates is in fact a summation of the advective thermohaline streamfunction Ψ^{adv}_{ST} (as calculated in recent literature), the local thermohaline streamfunction Ψ^{loc}_{ST} and the thermohaline trend. The sum of Ψ^{adv}_{ST} and Ψ^{loc}_{ST} represents the total non-divergent diathermohaline ocean circulation in (S, T) coordinates, and is quantified by the diathermohaline streamfunction Ψ^{dia}_{ST}. Only $\Psi^{\text{dia}}_{ST} = \Psi^{\text{adv}}_{ST} + \Psi^{\text{loc}}_{ST}$ can be directly related to thermohaline forcing. Zika et al. (2012), Döös et al. (2012) and Groeskamp et al. (2014a) showed Ψ^{dia}_{ST}, Ψ^{adv}_{ST} and Ψ^{loc}_{ST} are all useful model diagnostics to understand the relation between thermohaline forcing and ocean circulation.

Calculation of Ψ^{dia}_{ST}, as in Groeskamp et al. (2014a), requires accurate 3-dimensional velocity data and an ocean hydrography. To avoid the use of velocity data to calculate a diathermal advection, Walin (1982) showed that the area-integrated surface heat flux between two outcropping isotherms, combined with a diffusive heat flux across the bounding isotherms can be used to calculate the diathermal advection in a steady state ocean (in which the volume enclosed between two isotherms remains constant). He thus

framed the relation between surface and interior heat fluxes and the cross isothermal ocean circulation.

To obtain the diathermohaline streamfunction as defined by Groeskamp et al. (2014a), we require both diathermal and diahaline transport. To obtain both transports we will, like Speer and Tziperman (1992) and Hieronymus et al. (2014), use salt and heat fluxes in combination with Walin's framework to estimate water-mass transformation rates, in (S,T) coordinates. Here a water-mass transformation is a change of the S and T properties of a water-mass, which can result in along- and cross-isopycnal transport (Speer, 1993, IOC et al., 2010). Speer (1993) suggested that in a steady state ocean the net divergence of the water-mass transformation due to surface heat and freshwater fluxes, projected in (S,T) coordinates, should be balanced by mixing, thus providing constraints on mixing estimates.

In the present chapter we will merge both the Munk (1966) and Walin (1982) frameworks in (S,T) coordinates, obtaining a balance between surface forcing, mixing and circulation. This is obtained using a 2-dimensional extension into (S,T) coordinates by applying Walin's framework to a volume bounded by a pair of isotherms *and* a pair of isohalines (Fig. 4.1). We can then provide an estimate of the diathermohaline circulation using boundary salt and heat fluxes and diffusive mixing. Representing the diathermohaline circulation by a diathermohaline streamfunction we develop the Thermohaline Inverse Method (THIM), that can be applied to observationally based ocean hydrography and surface heat and freshwater fluxes to simultaneously obtain estimates of both Ψ^{dia}_{ST} and the tracer diffusion coefficients K and D. We test the THIM by calculating Ψ^{dia}_{ST} directly using a model's hydrographic and velocity output as described by Groeskamp et al. (2014a) and compare this with an inverse estimate of Ψ^{dia}_{ST} based on the model's boundary fluxes of salt and heat in combination with its hydrography.

4.2 Diathermohaline streamfunction

This section is a summary of a derivation by Groeskamp et al. (2014a) leading to an expression for the diathermohaline streamfunction, $\Psi^{\mathrm{dia}}_{S_{\mathrm{A}}\Theta}$, which represent ocean circulation in Absolute Salinity S_{A} and Conservative Temperature Θ coordinates. Here Conservative Temperature is proportional to potential enthalpy (by the constant heat capacity factor c^0_p), which represents the 'heat content' per unit mass of seawater (McDougall, 2003, Graham and McDougall, 2013). Absolute Salinity is measured on the Reference Composition Salinity Scale (Millero et al., 2008) and represents the mass fraction of dissolved material in seawater (in g kg^{-1}), (IOC et al., 2010, McDougall et al., 2012).

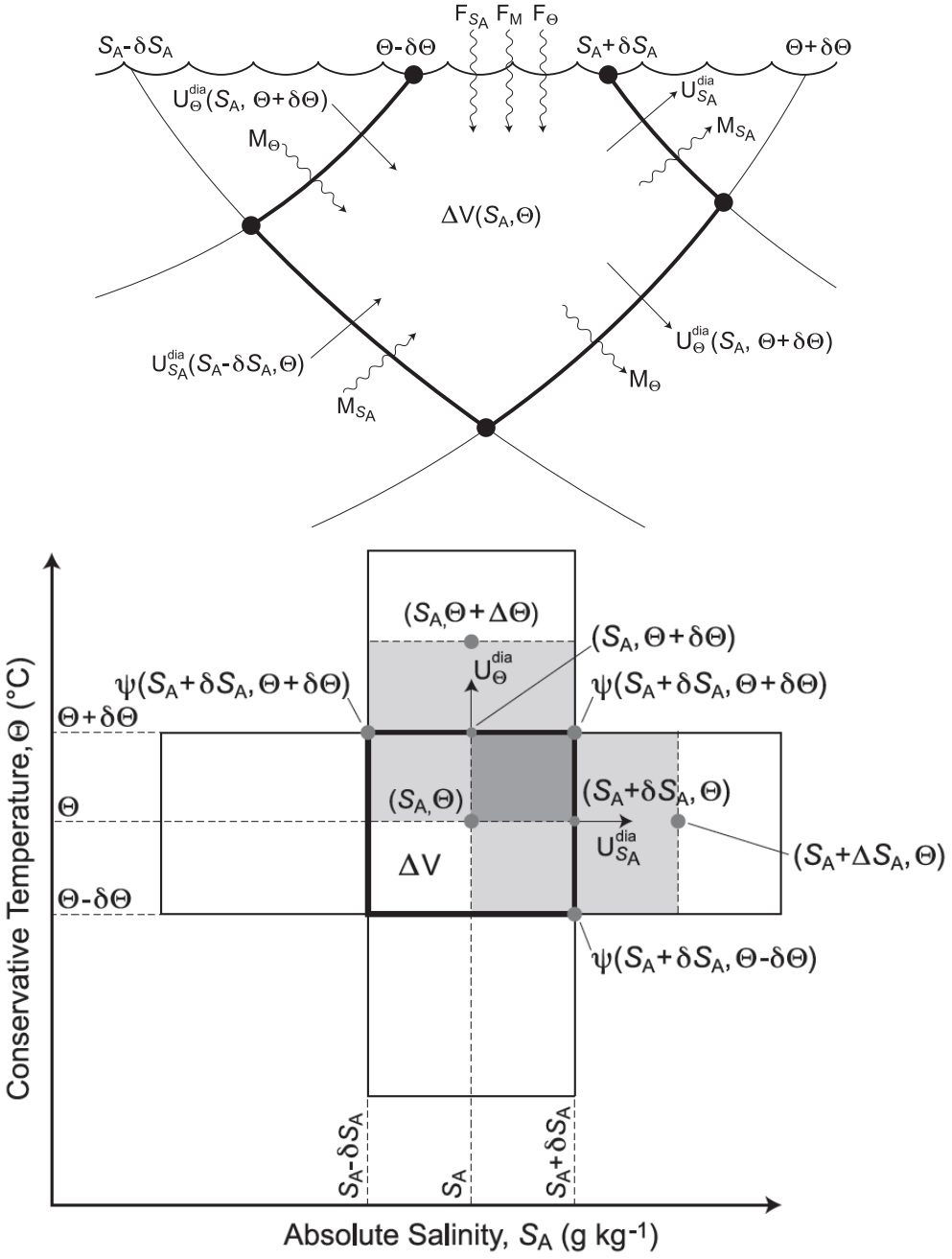

FIGURE 4.1: The left shows the 2-dimensional (S_A, Θ) (Thermohaline) version of the Walin (1982) framework in Cartesian-coordinates. Advection through the pair of isotherms and isohalines enclosing ΔV (bold black lines), requires a change in the S_A and Θ values of a part of ΔV. For such a change, the divergence of salt or heat fluxes is required. These are provided by the thermohaline forcing terms, which are the diffusion of salt and heat through the isotherms and isohalines (M_{S_A} and M_Θ, respectively) and the surface fluxes of mass, salt and heat ($F_{S_\mathrm{A}}, F_\Theta$ and F_m, respectively). The right shows the same ΔV represented in (S_A, Θ) coordinates (bold black lines). In these coordinates we have also defined the streamfunction, such that the diathermohaline streamfunction difference is equal to the net flux through the isotherm or isohaline, which itself is provided by salt and heat fluxes gridded in the grid spanning $(S_\mathrm{A} \pm \delta S_\mathrm{A}, \Theta \pm \delta\Theta)$, where (S_A, Θ) is the location at which $\mathbf{U}^{\mathrm{dia}}_{S_\mathrm{A}\Theta}$ is evaluated.

The superscript or prefix 'dia' indicates a transport through a surface. Hence we define $u_C^{\mathrm{dia}}(\mathbf{x},t)$ as the velocity of a fluid parcel through a surface of constant conserved tracer $C = C(\mathbf{x},t)$, where $\mathbf{x} = (x,y,z)$. Hence $u_C^{\mathrm{dia}}(\mathbf{x},t)$ can be obtained from the material derivative of C (Griffies, 2004, Groeskamp et al., 2014a),

$$\begin{aligned} u_C^{\mathrm{dia}} &= \frac{1}{|\nabla C|}\frac{DC}{Dt} \\ &= \frac{1}{|\nabla C|}\frac{\partial C}{\partial t} + \mathbf{u}\cdot\frac{\nabla C}{|\nabla C|} \\ &= \frac{1}{|\nabla C|}\left(f_C + m_C\right). \end{aligned} \tag{4.1}$$

Here $\mathbf{u} = \mathbf{u}(\mathbf{x},t) = (u(\mathbf{x},t), v(\mathbf{x},t), w(\mathbf{x},t))$ and the forcing terms $f_C = f_C(\mathbf{x},t)$ and $m_C = m_C(\mathbf{x},t)$ (both in C s^{-1}) are flux divergences of C due to boundary fluxes and diffusive mixing processes, respectively. Eq. (4.1) shows that $u_C^{\mathrm{dia}} = u_C^{\mathrm{dia}}(\mathbf{x},t)$ is the difference between the velocity of the fluid parcel in the direction normal to the surface of constant C $[\mathbf{u}\cdot(\nabla C/|\nabla C|)]$ and the movement of the surface itself $[(1/|\nabla C|)\,/\,(\partial C/\partial t)]$.

A trend in C over time period Δt, leads to a net shift of the geographical position of the surface of constant C. This shift can be expressed as a net velocity of the surface of constant C over Δt, given by,

$$u_C^{\mathrm{tr}} = \frac{1}{|\nabla C|}\frac{1}{\Delta t}\int_t^{t+\Delta t}\frac{\partial C}{\partial t}dt. \tag{4.2}$$

Here $\frac{1}{\Delta t}\int_t^{t+\Delta t}(...)dt = \overline{(...)}$, is a time averaged (later denoted by an overbar) and $u_C^{\mathrm{tr}} = u_C^{\mathrm{tr}}(\mathbf{x},t)$.

Inserting $C = S_{\mathrm{A}}(\mathbf{x},t)$ and $C = \Theta(\mathbf{x},t)$ in Eq. (4.1), we can define the diathermohaline velocity vector, $\mathbf{u}_{S_{\mathrm{A}}\Theta}^{\mathrm{dia}} = (u_{S_{\mathrm{A}}}^{\mathrm{dia}}, u_{\Theta}^{\mathrm{dia}})$ as the velocity with which the fluid parcel crosses isohalines and isotherms. Inserting $C = S_{\mathrm{A}}(\mathbf{x},t)$ and $C = \Theta(\mathbf{x},t)$ in Eq. (4.2), we can define the diathermohaline trend, $\mathbf{u}_{S_{\mathrm{A}}\Theta}^{\mathrm{tr}} = (u_{S_{\mathrm{A}}}^{\mathrm{tr}}, u_{\Theta}^{\mathrm{tr}})$ as the net velocity of a shift of the geographical position of the isohalines and isotherms, due to a trend in time in the local changes of S_{A} and Θ. Following Groeskamp et al. (2014a), for a Boussinesq ocean in which $\nabla\cdot\mathbf{u} = 0$, the diathermohaline streamfunction $\Psi_{S_{\mathrm{A}}\Theta}^{\mathrm{dia}}$ is then given by,

$$\begin{aligned} \Psi_{S_{\mathrm{A}}\Theta}^{\mathrm{dia}}(S_{\mathrm{A}},\Theta) &= \int_t^{t+\Delta t}\int_{\Theta'\le\Theta|_{S_{\mathrm{A}}}} u_{S_{\mathrm{A}}}^{\mathrm{dia}} - u_{S_{\mathrm{A}}}^{\mathrm{tr}}\,dA\,dt \\ &= -\int_t^{t+\Delta t}\int_{S'_{\mathrm{A}}\le S_{\mathrm{A}}|_{\Theta}} u_{\Theta}^{\mathrm{dia}} - u_{\Theta}^{\mathrm{tr}}\,dA\,dt. \end{aligned} \tag{4.3}$$

Here, $\int_{\Theta'\le\Theta|_{S_{\mathrm{A}}}} dA$ is the area integral over all Θ', smaller than or equal to Θ on a surface of constant S_{A} and $\int_{S'_{\mathrm{A}}\le S_{\mathrm{A}}|_{\Theta}} dA$ is the area integral over all S'_{A}, smaller than or equal to

S_A on a surface of constant Θ. For a statistically steady ocean, $\mathbf{u}^{tr}_{S_A\Theta} = 0$. Hence, $\Psi^{dia}_{S_A\Theta}$ represents the non-divergent component of the ocean circulation in (S_A, Θ) coordinates, while the diathermohaline trend represents the divergent component of this circulation.

From Eqs. (4.1) and (4.3) it is clear that $\Psi^{dia}_{S_A\Theta}$ can only be calculated if $\mathbf{u}(\mathbf{x}, t)$ is known. An expression that provides $\Psi^{dia}_{S_A\Theta}$ from commonly observed variables (ocean hydrography and boundary salt and heat fluxes) is obtained when inserting the last line of Eq. (4.1) into Eq. (4.3) thereby directly relating $\Psi^{dia}_{S_A\Theta}$ to thermohaline forcing,

$$\begin{aligned}\Psi^{dia}_{S_A\Theta}(S_A, \Theta) &= \int_t^{t+\Delta t} \int_{\Theta' \le \Theta|_{S_A}} \frac{f_{S_A} + m_{S_A}}{|\nabla S_A|} - u^{tr}_{S_A} dA dt \\ &= -\int_t^{t+\Delta t} \int_{S'_A \le S_A|_\Theta} \frac{f_\Theta + m_\Theta}{|\nabla \Theta|} - u^{tr}_\Theta dA dt. \end{aligned} \tag{4.4}$$

However, this expression requires knowledge of the the ocean's diffusive salt and heat fluxes everywhere. Unfortunately the ocean's spatial and temporal varying diffusive salt and heat fluxes are not well known, requiring us to develop a different method to derive $\Psi^{dia}_{S_A\Theta}$ from observations, which is what we do in this chapter.

4.3 The Diathermohaline Volume Transport

The diathermohaline velocity $\mathbf{u}^{dia}_{S_A\Theta}$ integrated over an area, results in a diathermohaline volume transport. In this section we will use the conservation of volume, salt and heat, to derive an expression for the diathermohaline volume transport as a function of thermohaline forcing. In Section 4.4, we relate the diathermohaline volume transport with $\Psi^{dia}_{S_A\Theta}$, to obtain an expression for $\Psi^{dia}_{S_A\Theta}$ as a function of the thermohaline forcing. This expression allows us to construct an inverse method that will provide an estimate for both the ocean's tracer diffusion coefficients and the diathermohaline streamfunction.

To express the conservation equations we consider a volume ΔV, bounded by a pair of isotherms that are separated by $\Delta\Theta$ $(= 2\delta\Theta)$ and a pair of isohalines which are separated by ΔS_A $(= 2\delta S_A)$. The volume's Θ ranges between $\Theta \pm \delta\Theta$ and S_A ranges between $S_A \pm \delta S_A$. As a result $\Delta V = \Delta V(S_A \pm \delta S_A, \Theta \pm \delta\Theta, t)$ may have any shape in (x, y, z)-coordinates (Fig. 4.1a), but it covers a square grid in (S_A, Θ) coordinates (Fig. 4.1b).

At the centre of ΔV, at coordinates (S_A,Θ), we define a diathermohaline volume transport vector. The diahaline volume transport, in the positive S_A-direction through the

area of the surface of constant S_A, for the Θ-range of $\Theta \pm \delta\Theta$ is given by,

$$U^{\mathrm{dia}}_{|S_\mathrm{A}}\left(S_\mathrm{A}, \Theta \pm \delta\Theta, t\right) = \int_{\Theta\pm\delta\Theta|_{S_\mathrm{A}}} u^{\mathrm{dia}}_{S_\mathrm{A}} dA. \tag{4.5}$$

The diathermal volume transport, in the positive Θ-direction through the area of the surface of constant Θ, for the S_A-range of $S_\mathrm{A} \pm \delta S_\mathrm{A}$, is given by,

$$U^{\mathrm{dia}}_{|\Theta}\left(S_\mathrm{A} \pm \delta S_\mathrm{A}, \Theta, t\right) = \int_{S_\mathrm{A}\pm\delta S_\mathrm{A}|_\Theta} u^{\mathrm{dia}}_{\Theta} dA. \tag{4.6}$$

This derivation results in the diathermohaline volume transport vector $\mathbf{U}^{\mathrm{dia}}_{S_\mathrm{A}\Theta} = \left(U^{\mathrm{dia}}_{|S_\mathrm{A}}, U^{\mathrm{dia}}_{|\Theta}\right)$.

Using $\mathbf{U}^{\mathrm{dia}}_{S_\mathrm{A}\Theta}$, we can construct the conservation equations for volume, salt and heat for ΔV. It would be more accurate to use conservation of mass in a non-Boussinesq ocean, but we leave this for future work. As $\Delta V = \Delta V(S_\mathrm{A} \pm \delta S_\mathrm{A}, \Theta \pm \delta\Theta, t)$, this results in $S_\mathrm{A} = S_\mathrm{A}(t)$ and $\Theta = \Theta(t)$, where S_A and Θ can only vary in time within the range $S_\mathrm{A} \pm \delta S_\mathrm{A}$ and $\Theta \pm \delta\Theta$, respectively. Using this and applying the Boussinesq approximation, the conservation of volume, salt and heat for ΔV is given by,

$$\frac{\partial \Delta V}{\partial t} + \nabla_{S_\mathrm{A}\Theta} \cdot \mathbf{U}^{\mathrm{dia}}_{S_\mathrm{A}\Theta} = \frac{1}{\rho_0} F_\mathrm{m} \tag{4.7}$$

$$\frac{\partial \Delta V S_\mathrm{A}}{\partial t} + \nabla_{S_\mathrm{A}\Theta} \cdot \left(S_\mathrm{A}\mathbf{U}^{\mathrm{dia}}_{S_\mathrm{A}\Theta}\right) = \frac{1}{\rho_0} M_{S_\mathrm{A}} \tag{4.8}$$

$$\frac{\partial \Delta V \Theta}{\partial t} + \nabla_{S_\mathrm{A}\Theta} \cdot \left(\Theta\mathbf{U}^{\mathrm{dia}}_{S_\mathrm{A}\Theta}\right) = \frac{1}{\rho_0 c_p^0}\left[F_\Theta + M_\Theta\right]. \tag{4.9}$$

Here we have used that the derivative of $U^{\mathrm{dia}}_{|S_\mathrm{A}}$ ($U^{\mathrm{dia}}_{|\Theta}$), with respect to S_A (Θ), is constant over the interval $S_\mathrm{A} \pm \delta S_\mathrm{A}$ ($\Theta \pm \delta\Theta$), such that we can define the thermohaline divergence operator,

$$\nabla_{S_\mathrm{A}\Theta} = \left(\Delta S_\mathrm{A}\frac{\partial}{\partial S_\mathrm{A}}, \Delta\Theta\frac{\partial}{\partial\Theta}\right). \tag{4.10}$$

The thermohaline divergence operator (Eq. 4.10), is a short hand notation for taking the difference of the outflow and inflow of volume and accompanied tracers, through the pair of isohalines that enclose ΔV that are separated exactly by ΔS_A, and isotherms separated exactly by $\Delta\Theta$.

In Eq. (4.7) F_m is the boundary mass flux into ΔV due to evaporation (E), precipitation (P), ice melt and formation and river runoff (R). We assumed that the boundary salt flux is zero, i.e. neglecting the formation of sea spray, interchange of salt with sea ice and salt entering from the ocean boundaries. Although the total amount of salt in the ocean remains constant, the ocean's salinity is modified by F_m (Huang, 1993, Griffies, 2004). F_Θ is the net convergence of heat into ΔV due to boundary fluxes. F_m and F_Θ can be obtained from surface freshwater and heat flux products. M_{S_A} and M_Θ are the

net convergence of salt and heat into ΔV due to *all* interior diffusive processes, and can be obtained from an ocean hydrography in combination with a mixing parameterisation.

After expanding the l.h.s. of Eqs. (4.8) and (4.9), we insert Eq. (4.7) into Eqs. (4.8) and (4.9) and we use that by definition in these coordinates $\partial S_\mathrm{A}/\partial\Theta = \partial\Theta/\partial S_\mathrm{A} = 0$. Taking the time average, this results in the following expression for $\overline{\mathbf{U}}^{\mathrm{dia}}_{S_\mathrm{A}\Theta} = \left(\overline{U}^{\mathrm{dia}}_{|S_\mathrm{A}}, \overline{U}^{\mathrm{dia}}_{|\Theta}\right)$,

$$\overline{U}^{\mathrm{dia}}_{|S_\mathrm{A}}\left(S_\mathrm{A}, \Theta \pm \delta\Theta\right) = \frac{1}{\rho_0 \Delta S_\mathrm{A}}\left(\overline{M_{S_\mathrm{A}}} - \overline{S_\mathrm{A} F_\mathrm{m}} - \rho_0 \overline{\Delta V \frac{\partial S_\mathrm{A}}{\partial t}}\right), \tag{4.11}$$

$$\overline{U}^{\mathrm{dia}}_{|\Theta}\left(S_\mathrm{A} \pm \delta S_\mathrm{A}, \Theta\right) = \frac{1}{\rho_0 c_p^0 \Delta\Theta}\left(\overline{F_\Theta} + \overline{M_\Theta} - \overline{\Theta F_\mathrm{m}} - \rho_0 c_p^0 \overline{\Delta V \frac{\partial \Theta}{\partial t}}\right). \tag{4.12}$$

Here we have obtained an expression for the diathermohaline volume transport out of ΔV, due to water-mass transformation as a result of a convergence of salt or heat into ΔV. This is equivalent to an extension of Walin (1982)'s framework in (S_A, Θ) coordinates. The vector $\overline{\mathbf{U}}^{\mathrm{dia}}_{S_\mathrm{A}\Theta} = \left(\overline{U}^{\mathrm{dia}}_{|S_\mathrm{A}}, \overline{U}^{\mathrm{dia}}_{|\Theta}\right)$ is equivalent to the $\mathbf{J}$ vector as defined by Hieronymus et al. (2014), except for the last terms on the r.h.s. of Eqs. (5.1) and (5.2).

We will now calculate the terms on the right hand side of the Eqs. (5.1) and (5.2) in detail. In Section 4.4 we relate $\overline{\mathbf{U}}^{\mathrm{dia}}_{S_\mathrm{A}\Theta}$ with $\Psi^{\mathrm{dia}}_{S_\mathrm{A}\Theta}$ such that we can estimate $\Psi^{\mathrm{dia}}_{S_\mathrm{A}\Theta}$, from observational based products, using the Thermohaline Inverse Method.

4.3.1 Boundary salt and heat fluxes.

The boundary mass flux into the ocean $\overline{F}_\mathrm{m}$ (kg s^{-1}) is given by the integral of $E-P-R$ over area A_b, bounded by a pair of isohalines and isotherms,

$$\overline{F}_\mathrm{m} = -\frac{1}{\Delta t}\int_t^{t+\Delta t}\int_{A_\mathrm{b}} \left[E - P - R\right] dA dt. \tag{4.13}$$

Modification of the ocean's salinity through $\overline{F}_\mathrm{m}$ can be calculated as,

$$\begin{aligned}\overline{S_\mathrm{A} F_\mathrm{m}} &= -\frac{1}{\Delta t}\int_t^{t+\Delta t} S_\mathrm{A}\int_{A_\mathrm{b}} \left[E - P - R\right] dA dt \\ &= -\overline{S}_\mathrm{A}\overline{F}_\mathrm{m} - \overline{S'_\mathrm{A} F'_\mathrm{m}}.\end{aligned} \tag{4.14}$$

Here we have applied Reynolds decomposition and averaging. Note that S'_A may only change within $S_\mathrm{A} \pm \delta S_\mathrm{A}$, hence S'_A approaches 0 whenδS_A approaches 0. A simple scale analyses shows that the heat flux equivalent $\overline{\Theta F_\mathrm{m}}$ in the heat-conservation Eq. (4.6) is negligible compared to the other terms.

The boundary heat flux into the ocean F_Θ (J s^{-1}) is the integral of the surface heat flux $f_h(x, y)$ due to long and shortwave radiation, and the latent and sensible heat flux and, geothermal heating over area A_b,

$$\overline{F}_\Theta = \frac{1}{\Delta t}\int_t^{t+\Delta t}\int_{A_\mathrm{b}} f_h dA dt. \tag{4.15}$$

Note that, if required, one can include effects of solar penetration below the surface (Iudicone et al., 2008).

4.3.2 Diffusive salt and heat Fluxes

Generally, tracer diffusion is parameterised according to two different physical processes, 1) epineutral down-gradient tracer diffusion due to mesoscale eddies by means of an eddy diffusion coefficient K and, 2) small-scale isotropic down-gradient turbulent diffusion by means of a turbulent diffusion coefficient D. The isotropic nature of D is discussed in Chapter 2 (based on McDougall et al. (2014)), but has previously been regarded to be diapycnal (Redi (1982), Griffies (2004), or vertical in the small slope approximation). To represent epineutral diffusion in Cartesian-coordinates, one makes use of a rotated tensor. The component of the diffusive tracer flux (in C m^3 s^{-1}), through a general surface of constant φ, with surface area A_φ, due to both eddy and turbulent diffusion, projected into Cartesian-coordinates is given by,

$$m_C^\varphi = -\int_{A_\varphi} \mathbf{K}\nabla C \cdot \frac{\nabla\varphi}{|\nabla\varphi|} dA. \tag{4.16}$$

This represents diffusion of any conserved tracer C through any surface φ. Here $\mathbf{K}$ is,

$$\mathbf{K} = \frac{K}{1+s^2}\begin{pmatrix} 1+\epsilon+s_y^2 & -s_x s_y & s_x \\ -s_x s_y & 1+\epsilon+s_x^2 & s_y \\ s_x & s_y & \epsilon+s^2 \end{pmatrix}, \tag{4.17}$$

where $\epsilon = D\left(1+s^2\right)/K$, and

$$\mathbf{s} = (s_x, s_y) = -\left(\frac{\frac{\partial\gamma^n}{\partial x}}{\frac{\partial\gamma^n}{\partial z}}, \frac{\frac{\partial\gamma^n}{\partial y}}{\frac{\partial\gamma^n}{\partial z}}\right). \tag{4.18}$$

Using Neutral Density, γ^n (McDougall, 1987a, Jackett and McDougall, 1997), $\mathbf{s}$ provides the neutral direction and $s^2 = s_x^2 + s_y^2$.

Diffusive Heat Flux

The down-gradient diathermal transport of heat (m_Θ^Θ), through a surface of constant Θ, between the S_A-range of $[S_\mathrm{A} \pm \delta S_\mathrm{A}]$, can be expressed as,

$$m_\Theta^\Theta = -\rho_0 c_p^0 \int_{S_\mathrm{A} \pm \delta S_\mathrm{A} | \Theta} \mathbf{K} \nabla \Theta \cdot \frac{\nabla \Theta}{|\nabla \Theta|} dA. \tag{4.19}$$

As isotherms and isohalines are not necessarily orthogonal in Cartesian-coordinates, there will also be a down-gradient diahaline diffusive transport of heat ($m_\Theta^{S_\mathrm{A}}$), through a surface of constant S_A, between the Θ-range of $[\Theta \pm \delta\Theta]$, given by:

$$m_\Theta^{S_\mathrm{A}} = -\rho_0 c_p^0 \int_{\Theta \pm \delta\Theta | S_\mathrm{A}} \mathbf{K} \nabla \Theta \cdot \frac{\nabla S_\mathrm{A}}{|\nabla S_\mathrm{A}|} dA \tag{4.20}$$

Using Eq. (4.19) and (4.20) we construct $\mathbf{m_\Theta} = (m_\Theta^{S_\mathrm{A}}, m_\Theta^\Theta)$ and use this to calculate the net convergence of heat into ΔV given by,

$$\overline{M}_\Theta = \frac{1}{\Delta t} \int_t^{t+\Delta t} \left(\nabla_{S_\mathrm{A}\Theta} \cdot \mathbf{m_\Theta} \right) dt. \tag{4.21}$$

Diffusive Salt Flux

The convergence of salt into ΔV is given by,

$$\overline{M}_{S_\mathrm{A}} = \frac{1}{\Delta t} \int_t^{t+\Delta t} \left(\nabla_{S_\mathrm{A}\Theta} \cdot \mathbf{m_{S_\mathrm{A}}} \right) dt. \tag{4.22}$$

Where $\mathbf{m_{S_\mathrm{A}}} = (m_{S_\mathrm{A}}^{S_\mathrm{A}}, m_{S_\mathrm{A}}^\Theta)$, and $m_{S_\mathrm{A}}^{S_\mathrm{A}}$ is the down-gradient diahaline diffusive transport of salt, through a surface of constant S_A, between the Θ-range of $[\Theta \pm \delta\Theta]$, given by,

$$m_{S_\mathrm{A}}^{S_\mathrm{A}} = -\rho_0 \int_{\Theta \pm \delta\Theta | S_\mathrm{A}} \mathbf{K} \nabla S_\mathrm{A} \cdot \frac{\nabla S_\mathrm{A}}{|\nabla S_\mathrm{A}|} dA, \tag{4.23}$$

and $m_{S_\mathrm{A}}^\Theta$ is the down-gradient diathermal diffusive transport of salt, through a surface of constant Θ, between the S_A-range of $[S_\mathrm{A} \pm \delta S_\mathrm{A}]$, given by,

$$m_{S_\mathrm{A}}^\Theta = -\rho_0 \int_{S_\mathrm{A} \pm \delta S_\mathrm{A} | \Theta} \mathbf{K} \nabla S_\mathrm{A} \cdot \frac{\nabla \Theta}{|\nabla \Theta|} dA. \tag{4.24}$$

4.3.3 Local Response

The local response is the last term on the r.h.s. of Eqs. (5.1) and (5.2), given by $\overline{L}_{S_\mathrm{A}} = \rho_0 \overline{\Delta V \frac{\partial S_\mathrm{A}}{\partial t}}$ for salt and $\overline{L}_\Theta = \rho_0 c_p^0 \overline{\Delta V \frac{\partial \Theta}{\partial t}}$ for heat. $\overline{L}_{S_\mathrm{A}}$ and $\overline{L}_\Theta$ are the amount of salt and heat per unit time, needed to change the S_A and Θ properties of ΔV by an

amount remaining within the defined (S_A, Θ) grid. As a result the observed changes in salt and heat do not lead to a diathermohaline transport, but nonetheless reduces the amount of salt and heat available for water-mass transformation. Applying Reynolds decomposition and averaging we obtain,

$$\overline{L}_{S_\mathrm{A}} = \rho_0 \overline{\Delta V' \frac{\partial S'_\mathrm{A}}{\partial t}}, \tag{4.25}$$

$$\overline{L}_{\Theta} = \rho_0 c_p^0 \overline{\Delta V' \frac{\partial \Theta'}{\partial t}}. \tag{4.26}$$

Note that both S'_A and Θ' deviate from (S_A, Θ) only within the range defined by $S_\mathrm{A} \pm \delta S_\mathrm{A}$ and $\Theta \pm \delta\Theta$, respectively. Hence S'_A and Θ' approach 0 when δS_A and $\delta\Theta$ approach 0.

4.4 The Thermohaline Inverse Model (THIM)

As we do not know the exact spatial and temporal distribution of K and D embedded in M_{S_A} and M_Θ in Eqs. (5.1) and (5.2), we formulate the Thermohaline Inverse Method (THIM), which uses an inverse technique that enables us to simultaneously estimate K, D and $\Psi_{S_\mathrm{A}\Theta}$.

We express the non-divergent component of $\overline{\mathbf{U}}^{\mathrm{dia}}_{S_\mathrm{A}\Theta}$ as a diathermohaline streamfunction difference in the S_A-direction,

$$\begin{aligned}
\Psi^{\mathrm{dia}}_{S_\mathrm{A}\Theta}(S_\mathrm{A}, \Theta + \delta\Theta) - \Psi^{\mathrm{dia}}_{S_\mathrm{A}\Theta}(S_\mathrm{A}, \Theta - \delta\Theta) &= \int_t^{t+\Delta t} \int_{\Theta \pm \delta\Theta|_{S_\mathrm{A}}} u^{\mathrm{dia}}_{S_\mathrm{A}} - u^{\mathrm{tr}}_{S_\mathrm{A}} \, dA dt \qquad (4.27)\\
&= \overline{U}^{\mathrm{dia}}_{|_{S_\mathrm{A}}}(S_\mathrm{A}, \Theta \pm \delta\Theta) - \overline{U}^{\mathrm{tr}}_{|_{S_\mathrm{A}}}(S_\mathrm{A}, \Theta \pm \delta\Theta)\\
&= \frac{1}{\rho_0 \Delta S_\mathrm{A}} \left[\overline{M_{S_\mathrm{A}}} - \overline{L}_{S_\mathrm{A}} - \overline{S_\mathrm{A} F_\mathrm{m}}\right] - \overline{U}^{\mathrm{tr}}_{|_{S_\mathrm{A}}}(S_\mathrm{A}, \Theta \pm \delta\Theta),
\end{aligned}$$

and in the Θ-direction,

$$\begin{aligned}
-\left[\Psi^{\mathrm{dia}}_{S_\mathrm{A}\Theta}(S_\mathrm{A} + \delta S_\mathrm{A}, \Theta) - \Psi^{\mathrm{dia}}_{S_\mathrm{A}\Theta}(S_\mathrm{A} - \delta S_\mathrm{A}, \Theta)\right] &= \int_t^{t+\Delta t} \int_{S_\mathrm{A} \pm \delta S_\mathrm{A}|_\Theta} u^{\mathrm{dia}}_{\Theta} - u^{\mathrm{tr}}_{\Theta} \, dA dt \qquad (4.28)\\
&= \overline{U}^{\mathrm{dia}}_{|_\Theta}(S_\mathrm{A} \pm \delta S_\mathrm{A}, \Theta) - \overline{U}^{\mathrm{tr}}_{|_\Theta}(S_\mathrm{A} \pm \delta S_\mathrm{A}, \Theta)\\
&= \frac{1}{\rho_0 c_p^0 \Delta\Theta} \left[\overline{F_\Theta} + \overline{M_\Theta} - \overline{L}_\Theta\right] - \overline{U}^{\mathrm{tr}}_{|_\Theta}(S_\mathrm{A} \pm \delta S_\mathrm{A}, \Theta).
\end{aligned}$$

Here we used Eqs. (5.1) and (5.2) to obtain the second line of Eqs. (4.27) and (4.28), and

$$\overline{U}^{\mathrm{tr}}_{|_{S_\mathrm{A}}}(S_\mathrm{A}, \Theta \pm \delta\Theta) = \int_t^{t+\Delta t} \int_{\Theta \pm \delta\Theta|_{S_\mathrm{A}}} u^{\mathrm{tr}}_{S_\mathrm{A}} \, dA dt \tag{4.29}$$

is the diahaline volume transport due to a trend in $S_\mathrm{A}(x, y, z, t)$, and

$$\overline{U}^{\mathrm{tr}}_{|\Theta}\left(S_\mathrm{A} \pm \delta S_\mathrm{A}, \Theta\right) = \int_t^{t+\Delta t} \int_{S_\mathrm{A} \pm \delta S_\mathrm{A}|\Theta} u^{\mathrm{tr}}_{\Theta} dA dt \tag{4.30}$$

is the diathermal volume transport due to a trend in $\Theta(x, y, z, t)$. Groeskamp et al. (2014a) showed that $\overline{U}^{\mathrm{tr}}_{|S_\mathrm{A}}$ and $\overline{U}^{\mathrm{tr}}_{|\Theta}$ can be obtained from an ocean hydrography only.

For each ΔV, two unique equations can be constructed and combined in the form $\mathbf{Ax} = \mathbf{b}$. Here $\mathbf{x}$ is a $1 \times M$ vector of unknown $\Psi_{S_\mathrm{A}\Theta}$-values and K and D coefficients, such that $M = (N_{S_\mathrm{A}} + 1)(N_\Theta + 1) + N_K + N_D$. Here N_K and N_D are the number of unknown coefficients used to represent spatial and temporal variation of epineutral and turbulent diffusion and N_{S_A} and N_Θ are the number of ΔV in the S_A and Θ direction, respectively. $\mathbf{A}$ is a $N \times M$ matrix of their coefficients, with $N = 2N_{S_\mathrm{A}} N_\Theta$, and $\mathbf{b}$ is a $1 \times N$ vector of the known forcing terms.

Both $\mathbf{A}$ and $\mathbf{b}$ are based on data that includes error, leading to unknown equation error. Hence we have N unknown equation errors and M unknown variables, leading to $N + M$ unknowns and N equations. Linear dependencies may reduce the effective number of equations N, always resulting in an underdetermined set of equations with an infinite number of solutions. An estimate for $\mathbf{x}$ can be obtained using an inverse technique that minimises χ^2, which is the sum of both the solution error and the equation error (Menke, 1984, Wunsch, 1996, McIntosh and Rintoul, 1997),

$$\chi^2 = \left(\mathbf{x} - \mathbf{x_0}\right)^{\mathbf{T}} \mathbf{W_c}^{-2} \left(\mathbf{x} - \mathbf{x_0}\right) + \mathbf{e^T W_r}^2 \mathbf{e}. \tag{4.31}$$

Rewriting the error as $\mathbf{e} = \mathbf{Ax} - \mathbf{b}$ and setting $\partial\chi^2/\partial\mathbf{x} = 0$, the solution can be written as:

$$\mathbf{x} = \mathbf{x_0} + \mathbf{W_c}^2 \mathbf{A^T} \left[\mathbf{A W_c}^2 \mathbf{A^T} + \mathbf{W_r}^{-2}\right]^{-1} \left(\mathbf{b} - \mathbf{A x_0}\right), \tag{4.32}$$

Here $\mathbf{x_0}$ is a prior estimate of $\mathbf{x}$ and $\mathbf{W_r}$ is the row (equation) weighting matrix and $\mathbf{W_c}$ is the column (variable) weighting matrix. If $\mathbf{x}$ and $\mathbf{e}$ are jointly normally distributed, the minimisation of χ^2 is equivalent to finding the most probable solution of $\mathbf{x}$, with a standard deviation given by the square root of the diagonal of the posterior covariance matrix given by (Menke, 1984),

$$\mathbf{C_p} = \mathbf{W_c}^2 - \mathbf{W_c}^2 \mathbf{A^T} \left[\mathbf{A W_c}^2 \mathbf{A^T} + \mathbf{W_r}^{-2}\right]^{-1} \mathbf{A W_c}^2, \tag{4.33}$$

Although this solution may have a correct statistical interpretation and can guide the choices of the weights, it may not always be physically realistic, particularly if a good estimate of the covariance structure is not available. Therefore we adopt a minimisation

process, based on Eq. (5.16) that provides a solution with a physically realistic interpretation rather than a statistical interpretation. Let $\mathbf{W_r}$ and $\mathbf{W_c}$ be diagonal with elements $1/\sigma_\mathbf{e}$ and $\sigma_\mathbf{x}$, respectively, such that we can rewrite Eqs. (5.16) as,

$$\begin{aligned} \chi^2 &= \chi_x^2 + \chi_e^2. \\ &= \sum_{m=1}^{M} \frac{(x_m - x_{0,m})^2}{\sigma_{x_m}^2} + \sum_{n=1}^{N} \frac{e_n^2}{\sigma_{e_n}^2}. \end{aligned} \tag{4.34}$$

To allow for a similar influence of each variable and equation on the solution, we require all elements of χ^2 and therefore χ_x^2 and χ_e^2, to have a similar non-dimensionalised order of magnitude. Hence, let $\mathbf{x_0}$ be our best estimate of $\mathbf{x}$ and let $\sigma_\mathbf{x}$ be our best estimate of the error between $\mathbf{x_0}$ and $\mathbf{x}$, such that $(x_m - x_{0,m})^2 / \sigma_{x_m}^2$ become order one values and $\chi_x^2 \approx M$. Equivalently, let $\sigma_\mathbf{e}$ be our best estimate of the equation error $\mathbf{e}$, such that $e_n^2/\sigma_{e_n}^2$ become order one values and $\chi_e^2 \approx N$.

To illustrate why we want $\chi_e^2 \approx N$ and $\chi_x^2 \approx M$, imagine using large values of $\sigma_\mathbf{e}$ compared to $\mathbf{e}$, such that $\chi_e^2 << N$. The solution then tends to $\mathbf{x} = \mathbf{x_0}$, by effectively minimising χ_x^2 meaning that the equations have no information content. In contrast, when $\sigma_\mathbf{x}$ is large compared to $\mathbf{x} - \mathbf{x_0}$, then $\chi_x^2 << M$ and the solution is obtained by minimising χ_e^2. The solution then tends to satisfy $\mathbf{Ax} = \mathbf{b}$ as accurately as possible, regardless of how far $\mathbf{x}$ is from $\mathbf{x_0}$. To avoid fitting $\mathbf{x}$ towards either the equations or $\mathbf{x_0}$, we suggest that one should find a physically realistic solution from a range of combinations for $\mathbf{x_0}$, $\sigma_\mathbf{x}$ and $\sigma_\mathbf{e}$ for which,

$$\frac{N}{10} \leq \chi_e^2 \leq 10N \text{and} \frac{M}{10} \leq \chi_x^2 \leq 10M. \tag{4.35}$$

Note that, if prior statistics are not well known, the sensitivity of the solution to the choice of $\mathbf{x_0}$, $\sigma_\mathbf{x}$ and $\sigma_\mathbf{e}$ may be larger than the standard deviation for a particular solution obtained from $\mathbf{C_p}$. We refer to the combination of (4.27) and (4.28) and the described inverse technique, as the Thermohaline Inverse Method (THIM).

4.5 The THIM applied to a numerical climate model

In this section we apply the THIM, to the hydrography and surface fluxes of an intermediate complexity numerical climate model's output, where the model's $\Psi^{\text{dia}}_{S_\text{A}\Theta}$, K and D are known.

4.5.1 The University of Victoria Climate Model

We use the final 10-years of a 3000-year spin up simulation of the University of Victoria Climate Model (UVIC). This model is an intermediate complexity climate model with horizontal resolution of 1.8^o latitude by 3.6^o longitude grid spacing, 19 vertical levels and a 2D energy balance atmosphere (Sijp et al. (2006), the case referred to as 'GM'). The ocean model is the Geophysical Fluid Dynamics Laboratory Modular Ocean Model version 2.2 (MOM2) using the Boussinesq approximation ($\rho \approx \rho_0 = 1035$ kg m^{-3}), a constant heat capacity ($c_p = 4000$ J K^{-1} kg^{-1}) with the rigid-lid approximations applied, and the surface freshwater fluxes are modelled by way of an equivalent salt flux (in kg m^{-2} s^{-1}) (Pacanowski, 1995). The model conserves heat and salt by conserving potential temperature θ (^{o}C) and Practical Salinity S_{P}. We use monthly averaged S_{P} and θ.

The vertical mixing coefficient increases with depth with a shape described by,

$$D_{\mathrm{uvic}} = 10^{-4}\left[0.8 + \frac{1.05}{\pi}\arctan\left(4.5\times10^{-3}\,(z-2500)\right)\right], \tag{4.36}$$

taking a value of 0.3×10^{-4} m^2 s^{-1} at the surface and increasing to 1.3×10^{-4} m^2 s^{-1} at the bottom. The model employs the eddy-induced advection parameterisation of Gent et al. (1995) with a constant diffusion coefficient of 1000 m^2 s^{-1}. Tracers are diffused in the isopycnal direction with a constant coefficient of K_{uvic}=1200 m^2 s^{-1}. The model adopts epineutral diffusion everywhere and uses a slope maximum of S_{max}=1/100, any slopes exceeding this limit are set to S_{max}.

4.5.2 Formulating the THIM for UVIC

At each (x, y, z)-coordinate tracer-location of UVIC, S_{P} and θ values are given and one can define six interfaces that encloses a volume. To calculate diffusion each interface is assumed to be a surface of constant S_{P} and θ. Adopting constant diffusion through a surface reduces the integral over the surface in Eq. (4.16), into a multiplication with the surface. Since the unit-normal of the surfaces are exactly in the x, y and z direction, we find the associated interfaces to be $A_{yz} = dydz$, $A_{xz} = dxdz$ and $A_{xy} = dxdy$. In the UVIC model the small slope approximation has been applied, such that the convergence of salt and heat due to the sum of both epineutral and vertical turbulent down-gradient

diffusion is given by,

$$M_{S_\mathrm{P}} = \nabla_{S_\mathrm{P}\theta} \cdot \left(\mathbf{K}_\mathrm{small} \nabla S_\mathrm{P} \mathbf{\Omega} + D \frac{\partial S_\mathrm{P}}{\partial z} A_{xy} \right), \tag{4.37}$$

$$M_\theta = \nabla_{S_\mathrm{P}\theta} \cdot \left(\mathbf{K}_\mathrm{small} \nabla \theta \mathbf{\Omega} + D \frac{\partial \theta}{\partial z} A_{xy} \right). \tag{4.38}$$

Here $\nabla_{S_\mathrm{P}\theta}$ is as Eq. (4.10) but for (S_P, θ) coordinates. We used the fact that $D/K << 1$, and $\mathbf{\Omega}$ is:

$$\mathbf{\Omega} = \begin{pmatrix} A_{yz} & 0 & 0 \\ 0 & A_{xz} & 0 \\ 0 & 0 & A_{xy} \end{pmatrix}, \tag{4.39}$$

and $\mathbf{K}_\mathrm{small}$ is,

$$\mathbf{K}_\mathrm{small} = K_\mathrm{uvic} \begin{pmatrix} 1 & 0 & s_x \\ 0 & 1 & s_y \\ s_x & s_y & s^2 \end{pmatrix}. \tag{4.40}$$

For the inverse model we use one unknown for both K and D. To take into account the vertical structure of D, we multiply $(\partial S_\mathrm{P}/\partial z A_{xy})|_z$ and $(\partial \theta/\partial z A_{xy})|_z$ by the vertical structure of D, given by $D_\mathrm{uvic}(z) \times 10^4$. This reduces the variables for small-scale turbulent diffusion to a single parameter (D = 1x10^{-4} m^2 s^{-1}) and yet retains the vertical structure as given by Eq. (4.36). The isopycnal gradients are obtained by using the locally referenced potential density values (σ_n) to calculate density gradients. The gradients at $z = z_k$ are obtained by finding $\sigma_n = \rho(S_\mathrm{P}, \theta, p_k)$ for the whole ocean according to McDougall et al. (2003), applied for all depth levels ranging from $k = 1 : N$, where N is the total number of vertical layers.

To obtain the time-averaged net convergence of salt and heat in (S_P, θ) coordinates we, i) sum M_{S_P} and M_θ, for each volume enclosed by the 6 interfaces, in (S_P, θ) coordinates according to their tracer value on the (x, y, z)-coordinate and then ii) take the time average (Figs. 4.2 and 4.3). We have chosen grid-sizes in (S_P, θ) coordinates ($\Delta\theta = 0.75$ and $\Delta S_\mathrm{P} = 0.1$) that distinguish the different water masses in the ocean's interior and provide approximately equal number of equations in both S_P and θ directions.

The surface freshwater flux is provided as an equivalent salt flux i.e. $F_{S_\mathrm{P}} = \overline{S_\mathrm{P} F_\mathrm{m}}$ as in Eq. (4.14), where we have neglected the prime-prime term. F_θ is calculated according to Eq. (4.15). The surface fluxes are gridded according to the surface grid S_P and θ values (Figs. 4.2 and 4.3). $\mathbf{L}_{S_\mathrm{P}\theta}$ is calculated according to Eq. (4.25) and the time derivative is calculated using the values of two subsequent months and gridded according to S_P and θ of the first month (Figs. 4.2 and 4.3). Using the above, Eqs. (4.27) and (4.28)

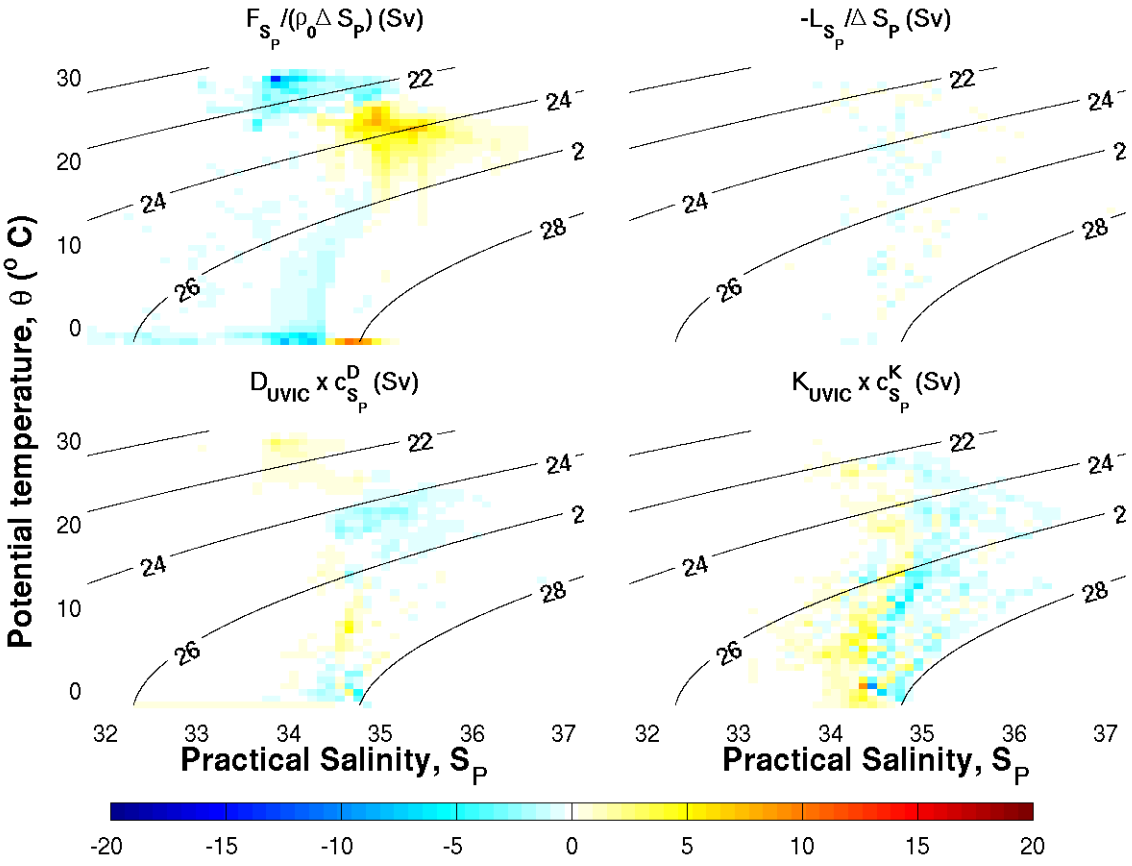

FIGURE 4.2: The 10-year averaged salt-flux-induced diahaline volume flux terms (in Sv, where 1Sv=10^6 m^3 s^{-1}) caused by a) the (equivalent) surface salt flux $F_{S_\mathrm{P}}/(\rho_0 \Delta S_\mathrm{P})$, b) the local response term $-L_{S_\mathrm{P}}/(\rho_0 \Delta S_\mathrm{P})$, c) the turbulent diffusion term $D_{\mathrm{uvic}} c^D_{S_\mathrm{P}}$ and d) isopycnal diffusion term $K_{\mathrm{uvic}} c^K_{S_\mathrm{P}}$. The grid sizes are $\Delta S_\mathrm{P} = 0.1$ and $\Delta\theta = 0.75$. Black lines are contours of potential density (σ_0).

applied to UVIC are,

$$\Psi_{S_\mathrm{P}\theta}(S_\mathrm{P}, \theta + \delta\theta) - \Psi_{S_\mathrm{P}\theta}(S_\mathrm{P}, \theta - \delta\theta) - K c^K_{S_\mathrm{P}} - D c^D_{S_\mathrm{P}} = b_{S_\mathrm{P}}, \tag{4.41}$$

and,

$$-\left[\Psi_{S_\mathrm{P}\theta}(S_\mathrm{P} + \delta S_\mathrm{P}, \theta) - \Psi_{S_\mathrm{P}\theta}(S_\mathrm{P} - \delta S_\mathrm{P}, \theta)\right] - K c^K_\theta - D c^D_\theta = b_\theta. \tag{4.42}$$

Here $c^K_C = \overline{(K_{\mathrm{uvic}}\Delta C)^{-1}\nabla_{S_\mathrm{P}\theta} \cdot (\mathbf{K}_{\mathrm{small}} \nabla C \mathbf{S})}$ and $c^D_C = \overline{(\Delta C)^{-1}\nabla_{S_\mathrm{P}\theta} \cdot ([C_z A_{xy}]_z D_{\mathrm{uvic}}(z) \times 10^4)}$ contain the tracer-gradient divergence, with which the diffusion coefficients are multiplied, after replacing C with S_P and θ. Then $b_{S_\mathrm{P}} = \left[\overline{F}_{S_\mathrm{P}} - \rho_0 \overline{L}_{S_\mathrm{P}}\right]/(\rho_0 \Delta S_\mathrm{P}) - \overline{U}^{\mathrm{tr}}_{S_\mathrm{P}}$ and $b_\theta = \left[\overline{F}_\theta - \rho_0 c^0_p \overline{L}_\theta\right]/(\rho_0 c^0_p \Delta\theta) - \overline{U}^{\mathrm{tr}}_\theta$.

Writing Eqs. (4.41) and (4.42) for each grid leads to a set of equations which can be written in the form $\mathbf{Ax} = \mathbf{b}$. Here $\mathbf{x} = (\Psi_{S_\mathrm{P}\theta}, K, D)$ and the coefficients with which

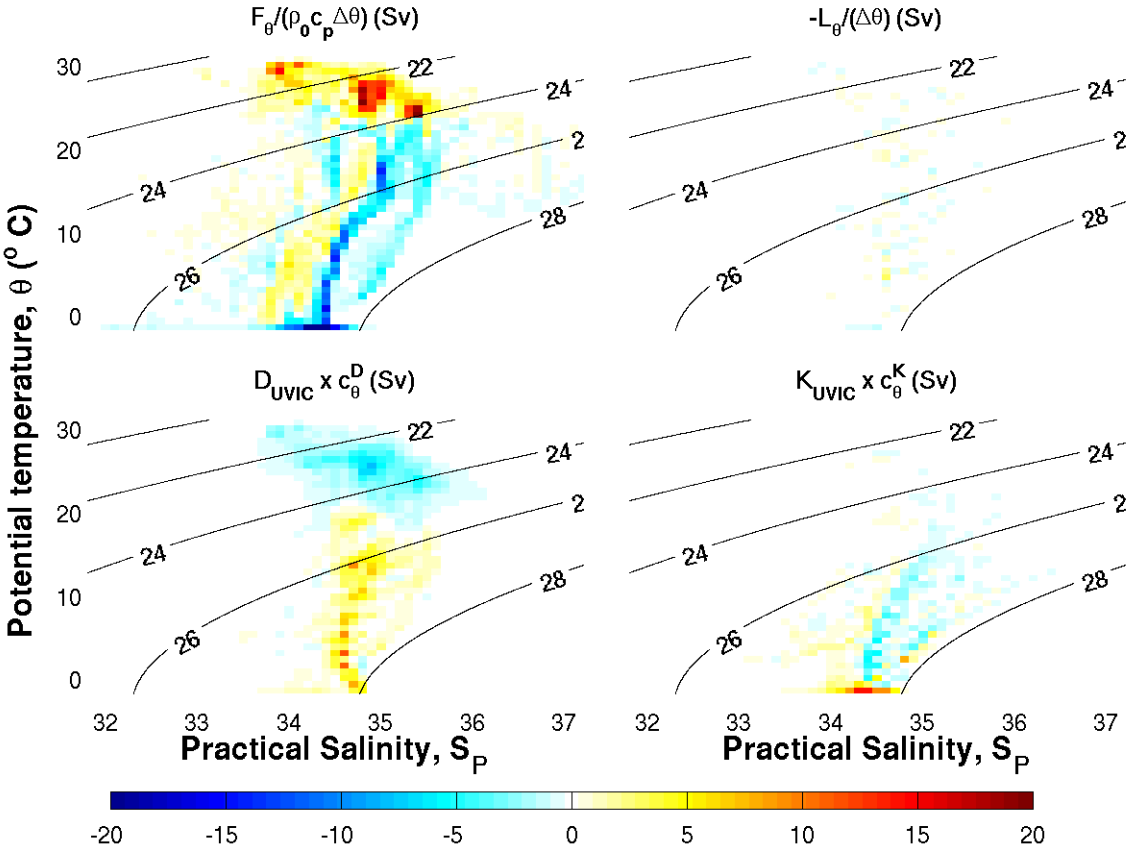

FIGURE 4.3: As Fig. 4.2 but then for the 10-year averaged heat-flux-induced diathermal volume flux terms (Sv).

we multiply $\mathbf{x}$ in $\mathbf{A}$ are 1 or -1 for $\Psi_{S_\mathrm{P}\theta}$, $c^K_{S_\mathrm{P}}$ and c^K_θ for K and $c^D_{S_\mathrm{P}}$ and c^D_θ for D and $\mathbf{b} = (b_{S_\mathrm{P}}, b_\theta)$.

4.5.3 The a-priori constraints

To provide a physically realistic estimate of $\mathbf{x}$ using the THIM, we need to include boundary conditions and specify $\mathbf{x_0}$, $\sigma_\mathbf{x}$ and $\sigma_\mathbf{e}$. We have omitted equations for which both $|K_\mathrm{uvic}c^K_{S_\mathrm{P}} - D_\mathrm{uvic}c^D_{S_\mathrm{P}}|$ and $|b_{S_\mathrm{P}}|$ are smaller than 0.1 Sv (1 Sv= 10^6 m^3 s^{-1}), as these equations do not have a signal to noise ratio that adds information to the solution. We have also applied this to the heat equations. We have also imposed that transport into a ΔV that does not exist in the ocean, is zero. That is, we have set $\Psi^\mathrm{dia}_{S_\mathrm{P}\theta} = 0$ if two or more neighbouring ΔV's do not exist in the ocean. The a-priori expected magnitude for K and D are $x^K_0 = K_\mathrm{uvic} = 1200$ m^2 s^{-1} and $x^D_0 = D_\mathrm{uvic} = 1 \times 10^{-4}$ m^2 s^{-1}. The a-priori expected magnitudes for $\Psi_{S_\mathrm{P}\theta}$ are unknown and therefore chosen to be $\mathbf{x}^\mathbf{\Psi}_\mathbf{0} = 0$. We obtain $N = 2709$ and $M = 1603$.

Row Weighting

Each equation represents a diathermohaline volume transport of a certain magnitude. An a-priori estimate of the magnitude of the error for each equation is given by,

$$\mathbf{e_0} = |\mathbf{A}\mathbf{x_0} - \mathbf{b}|. \tag{4.43}$$

Given that $\mathbf{x_0^\Psi} = 0$, this is equivalent to inserting $K = K_{\text{uvic}}$ and $D = D_{\text{uvic}}$ into the l.h.s. of Eqs. (4.41) and (4.42) and taking the absolute value of the difference between both sides of the equations. Assuming that 1) the errors in the equations are proportional to, but not necessarily equal to the size of the transports given by $\mathbf{e_0}$, and 2) that the salt and heat equations involve different physical processes and may therefore have a different proportionality to $\mathbf{e_0}$, the expected errors of the diahaline and diathermal volume transport ($\sigma_{\mathbf{e}}^{\mathbf{S}_\text{P}}$ and $\sigma_{\mathbf{e}}^{\theta}$, respectively) are then given by,

$$\begin{aligned} \sigma_{\mathbf{e}}^{\mathbf{S}_\text{P}} &= \sigma_e^{\min} + f_{S_\text{P}} \mathbf{e_0^{S_\text{P}}}, \\ \sigma_{\mathbf{e}}^{\theta} &= \sigma_e^{\min} + f_\theta \mathbf{e_0^\theta}. \end{aligned} \tag{4.44}$$

Here $\mathbf{e_0^{S_\text{P}}}$ and $\mathbf{e_0^\theta}$ are the upper bounds of a-priori estimates of error of the diahaline and diathermal volume transport, respectively (similar to Eq. (4.43)). We have included a minimum value of $\sigma_e^{\min} = 0.1$ Sv to avoid terms becoming too small. We allow the proportionality factor for the salt and heat equations, f_{S_P} and f_θ respectively, to vary between 0.01 and 1. This allows us to study the sensitivity of the solution to our choice of the equation error.

Column weighting

We will allow for a standard error of 25% of the expected values for K and D. This leads to $\sigma_x^K = 300$ m^2 s^{-1} and $\sigma_x^D = 2.5 \times 10^{-5}$ m^2 s^{-1}. The lack of information for $\mathbf{x_0^\Psi}$ can be compensated by a physically appropriate choice of $\sigma_{\mathbf{x}}^{\mathbf{\Psi}}$. Assuming that $\mathbf{x} \approx \Psi_{S_\text{P}\theta}^{\text{dia}}$, $\sigma_{\mathbf{x}}^{\mathbf{\Psi}}$ should reflect $2|\Psi_{S_\text{P}\theta}^{\text{dia}}|$ as this this takes into account the structure of $|\Psi_{S_\text{P}\theta}^{\text{dia}}|$, while the factor 2 allows for an easy fit of $\Psi_{S_\text{P}\theta}^{\text{dia}}$, within the range allowed by $\sigma_{\mathbf{x}}^{\mathbf{\Psi}}$.

To obtain an approximation of the structure of $|\Psi_{S_\text{P}\theta}^{\text{dia}}|$ without using prior knowledge of $\Psi_{S_\text{P}\theta}^{\text{dia}}$, we will assume that the size of $|\Psi_{S_\text{P}\theta}^{\text{dia}}|$ is proportional but not equal to, the average of the magnitude of all diathermohaline volume transports (as given by Eq. (4.43)), in which a particular $|\Psi_{S_\text{P}\theta}^{\text{dia}}|$ is involved (maximal 4). This structure is then normalised with a maximum of 40Sv, to obtain $\sigma_{\mathbf{x}}^{\mathbf{\Psi}} \approx 2|\Psi_{S_\text{P}\theta}^{\text{dia}}|$.

4.5.4 The solution

From the resulting range of solutions, we must choose the most physically realistic solution. We have chosen our solution to be the combination of $\sigma_{\mathbf{e}}^{\mathbf{S_P}}$ and $\sigma_{\mathbf{e}}^{\theta}$ at the ϵ_{rms} minimum within the range defined by Eq. (4.35). Here ϵ_{rms} is given by,

$$\epsilon_{rms} = \frac{\sqrt{\frac{1}{J}\sum_{j=1}^{J}\left(\Psi^{\text{dia}}_{S_\text{P}\theta,j} - \Psi^{\text{dia,inv}}_{S_\text{P}\theta,j}\right)^2}}{\frac{1}{J}\sum_{j=1}^{J}|\Psi^{\text{dia}}_{S_\text{P}\theta,j}|}. \tag{4.45}$$

J is the number of unknown streamfunction variables and ϵ_{rms} represents a weighted root-mean-square value of the difference between the diathermohaline streamfunction determined by the inverse method $\Psi^{\text{dia,inv}}_{S_\text{P}\theta}$ and the diathermohaline streamfunction calculated according to Groeskamp et al. (2014a). Hence, if $\epsilon_{\text{rms}} \geq 1$, our solution is no better than the solution given by our prior estimate $\Psi^{\text{dia,inv}}_{S_\text{P}\theta} = \mathbf{x_0^{\Psi}}$. If $\epsilon_{\text{rms}} < 1$, the solution is more accurate than our prior estimate, with a perfect solution, (i.e. $\Psi^{\text{dia,inv}}_{S_\text{P}\theta} = \Psi^{\text{dia}}_{S_\text{P}\theta}$), if $\epsilon_{\text{rms}} = 0$. The results of this solution are discussed in the next section.

4.6 Results and Discussion

In this section we discuss the skill of the THIM by comparing the UVIC-model's variables with the inverse estimates. For a detailed physical interpretation of the circulation cells of $\Psi^{\text{dia}}_{S_\text{P}\theta}$, we refer to Zika et al. (2012), Döös et al. (2012) and Groeskamp et al. (2014a).

4.6.1 The forcing terms

The surface salt flux binned in (S_P, θ) coordinates shows a diahaline transport in the direction of higher salinity values for salty water and in the direction of lower salinity values for fresh water (Fig. 4.2). A similar feature is observed for the surface heat flux binned in (S_P, θ) coordinates, which shows diathermal transport in the direction of higher temperatures for fluid parcels with high temperatures and in the direction of lower temperatures for fluid parcels with low temperatures (Fig. 4.3). Hence both the surface salt and heat fluxes lead to divergence of volume in (S_P, θ) coordinates. The surface divergence is balanced by convergence of volume in (S_P, θ) coordinates due to both the eddy and turbulent diffusive transport terms for salt and heat (Figs. 4.2 and 4.3). Note that the local term is very small compared to the surface and diffusive terms and the trend term is statistically insignificant for this particular model within the 95% confidence level of the student t-test (Groeskamp et al., 2014a). Hence, the

inverse method balances surface fluxes, mixing (of which the diffusion coefficients are estimated) and advection (represented by a the diathermohaline streamfunction).

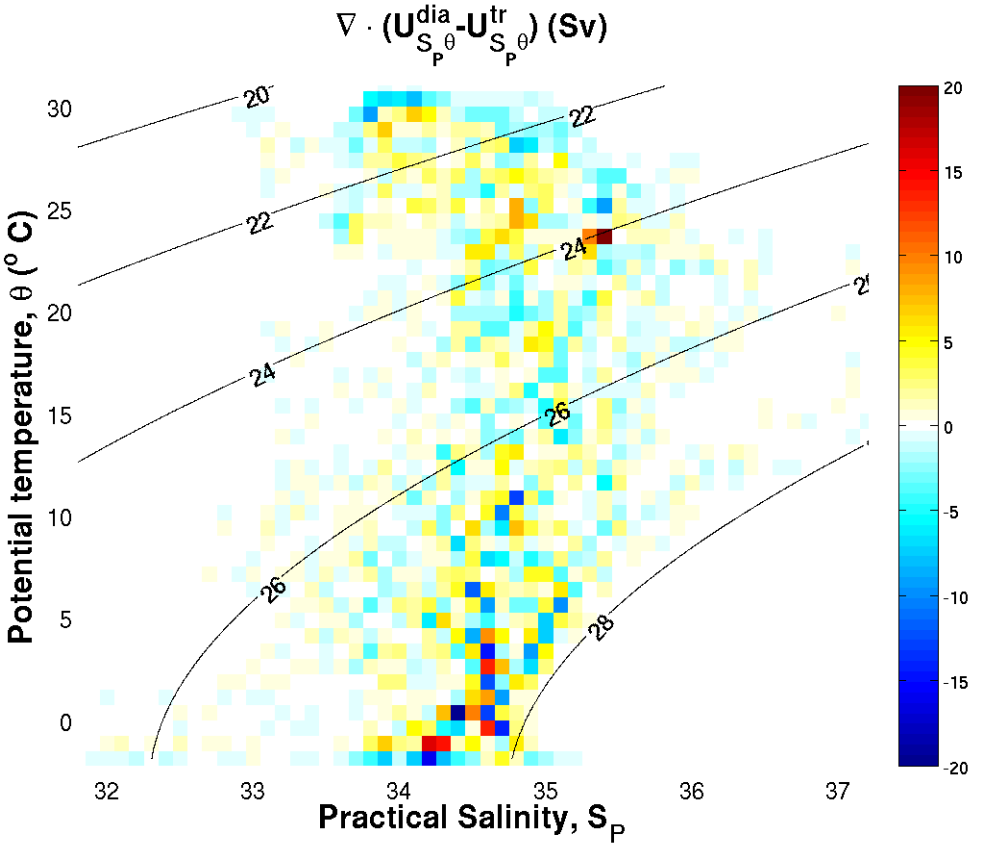

FIGURE 4.4: Shows that $\nabla_{S_P\theta} \cdot \left(\overline{\mathbf{U}}^{\text{dia}}_{S_P\theta} - \overline{\mathbf{U}}^{\text{tr}}_{S_P\theta}\right) \neq 0$. Here $\overline{\mathbf{U}}^{\text{dia}}_{S_P\theta}$ is calculated using $K = K_{\text{uvic}}$ and $D = D_{\text{uvic}}$. The black lines are the contours for potential density (σ_0).

Sources of errors or variations in the inverse estimates, apart from weighting coefficients, are numerical diffusion and limits on the temporal and spatial resolution. The latter leads to averaging and rounding errors of the ocean's hydrography and surface fluxes and results in unresolved fluxes at the sea surface and unresolved flux divergence in the ocean interior. For example, unresolved fluxes with periods less than a month may occur because we have used monthly-averaged values. Such fluxes are expected to have the largest influence on circulations that occur near the surface, as heat and salt fluxes are expected to vary at the surface on time scales shorter than a month. The numerical diffusion and unresolved fluxes lead to $\nabla_{S_P\theta} \cdot \left(\overline{\mathbf{U}}^{\text{dia}}_{S_P\theta} - \overline{\mathbf{U}}^{\text{tr}}_{S_P\theta}\right) \neq 0$ (Fig. 4.4), i.e. an imbalance between the diathermohaline circulation and fluxes of salt and heat. The larger this imbalance, the less accurate our inverse solution will be. Another result of this imbalance is that, even when we know the exact spatial and temporal structure of the diffusion coefficients (K and D), the numerical noise will not allow us to calculate a streamfunction directly from Eq. (4.4). Hence to obtain $\Psi_{S_P\theta}$ from salt and heat fluxes, will always require an (inverse) estimate.

4.6.2 The solution range

We first discuss the range of solutions and then discuss the results for the optimal solution, indicated by a black dot (Fig. 4.5). When f_{S_P} and f_θ (and therefore $\sigma_{\mathbf{e}}^{\mathbf{S_P}}$ and $\sigma_{\mathbf{e}}^{\theta}$, respectively) increase, χ_e^2/N decreases as expected (Fig. 4.5c). Simultaneously the solution is pushed more towards $\mathbf{x} = \mathbf{x_0}$, and because $\mathbf{x_0^\Psi} = 0$, this leads to a decrease in χ_x^2/M (Fig. 4.5c). For the optimal solution we find that $\chi_x^2/M = 0.69$ and $\chi_e^2/N = 9.94$, hence the solution is obtained mainly satisfying the equations, by using a relative small values for $\sigma_{\mathbf{e}}^{\mathbf{S_P}}$ and $\sigma_{\mathbf{e}}^{\theta}$ compared to $\mathbf{e}$. This is expected because we have limited knowledge of $\mathbf{x_0^\Psi}$.

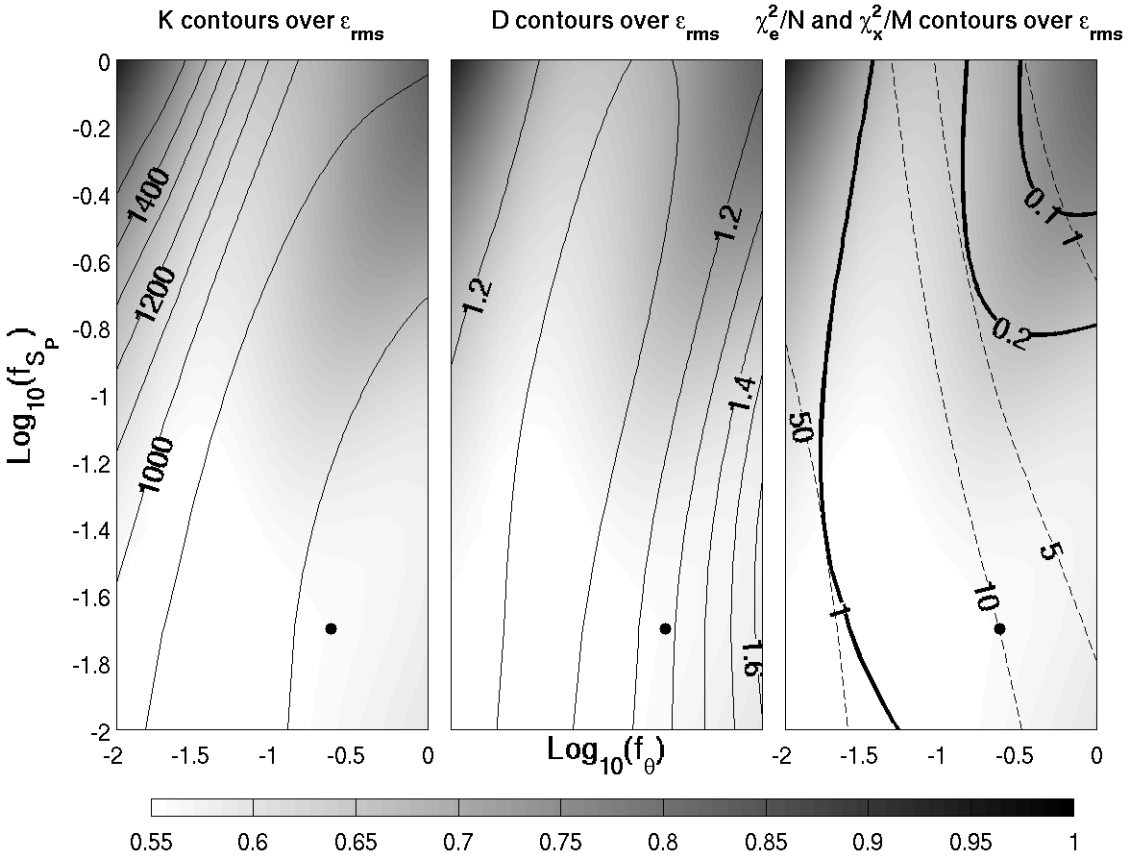

FIGURE 4.5: Contours of the inverse estimates of K (left) and D (middle) and the χ_e^2/N (dashed) and χ_x^2/M (solid) values (right), plotted on top of the associated ϵ_{rms} values (background color), for a range of the $\log_{10}$ of the row weighting values. With the variation of the weighting factor operating on the conservation of heat, given by f_θ, on the x-axis and the variation of the weighting factor operating on the conservation of salt, given by f_{S_P}, on the y-axis. Both f_θ and f_{S_P} range from 0.01 to 1. The lower the value of ϵ_{rms} (whiter) the closer the estimate of $\Psi_{S_P\theta}^{\text{dia,inv}}$ resembles $\Psi_{S_P\theta}^{\text{dia}}$. The black dot indicates the optimal solution defined by the minimum ϵ_{rms} value within the range given by Eq. (4.35).

As $\mathbf{x_0^\Psi}$ is not known and the forcing terms are not in perfect balance in this model when using $K = K_{\text{uvic}}$ and $D = D_{\text{uvic}}$ (Figs. 4.2 and 4.3), one will never obtain

$\Psi^{\text{dia,inv}}_{S_\text{P}\theta} = \Psi^{\text{dia}}_{S_\text{P}\theta}$ and simultaneously obtain $K = K_{\text{uvic}}$ and $D = D_{\text{uvic}}$. As a result, an improved estimate of $\Psi^{\text{dia,inv}}_{S_\text{P}\theta}$ can only be obtained by satisfying the equations, with less emphasise on fitting to $\mathbf{x} = \mathbf{x_0}$, and thus moving away from $K = K_{\text{uvic}}$ and $D = D_{\text{uvic}}$, but towards $\Psi^{\text{dia,inv}}_{S_\text{P}\theta} = \Psi^{\text{dia}}_{S_\text{P}\theta}$. This is particularity the case for K. This is not due to an incorrect formulation of the inverse method, it is a problem embedded in the model monthly means. The inverse solution behaves as expected, and for the whole range of solutions, both K and D are very reasonable approximations of K_{uvic} and D_{uvic} (Fig. 4.5c). This shows that the THIM is skilled in providing estimates of $\Psi^{\text{dia}}_{S_\text{P}\theta}$, K and D.

The optimal solution selected according to Section 4.5 gives $f_{S_\text{P}} = 0.02$ and $f_\theta = 0.24$, i.e. errors with a magnitude of 2% and 24%, for the conservation of salt and heat, respectively. This suggest that most of the error in the equations is created by the models heat flux terms.

4.6.3 The inverse estimate

For the optimal solution, $\Psi^{\text{dia,inv}}_{S_\text{P}\theta}$ and $\Psi^{\text{dia}}_{S_\text{P}\theta}$ are very similar (Fig. 4.6), with $\epsilon_{\text{rms}} = 0.56$. The standard deviation of $\Psi^{\text{dia,inv}}_{S_\text{P}\theta}$ obtained from $\mathbf{C_p}$ does not exceed 0.5Sv (and is generally much smaller) and is very small compared to $|\Psi^{\text{dia,inv}}_{S_\text{P}\theta}|$ (not shown).

The difference $\Psi^{\text{dia}}_{S_\text{P}\theta} - \Psi^{\text{dia,inv}}_{S_\text{P}\theta}$ is generally about 1 Sv, with the exception of some areas in (S_P, θ) coordinates (Fig. 4.7). To explain the differences, we use that the dynamics of the area in (S_P, θ) for which $\theta > 20^o$C are dominated by processes that occur near the surface, while the area for $\theta < 10^o$ and $S_\text{P} = 35 \pm 0.5$ g kg^{-1} are also strongly influenced by processes that occur in the ocean interior (Zika et al., 2012, Döös et al., 2012, Groeskamp et al., 2014a, Hieronymus et al., 2014). The magnitudes of the turbulent diffusion terms, which can be scaled by changing D, are large throughout the whole S_P and θ domain (D-terms in Figs. 4.2 and 4.3). The magnitude of the epineutral eddy diffusion terms, which can be scaled by changing K, are large only in the ocean interior (K-terms in Figs. 4.2 and 4.3). As a result, the large surface fluxes of salt and especially heat of the area in (S_P, θ) for which $\theta > 20^o$, can only be balanced by increasing the turbulent diffusion, increasing D. This will also result in an increased effect of turbulent diffusion in the oceans interior. The only way to compensate for this, is by reducing the magnitude of the epineutral eddy diffusion, reducing K. This idea is supported by the estimates of the diffusion coefficients. The estimate of K for the optimal solution is $K = 929 \pm 7$ m^2 s^{-1}, which is close to $K_{\text{uvic}} = 1200$ m^2 s^{-1}, but an underestimation. The estimate of D is $D = 1.27 \pm 0.01 \times 10^{-4}$ m^2 s^{-1}, which is close to $D_{\text{uvic}} = 1 \times 10^{-4}$ m^2 s^{-1}, but an overestimation. We note that numerical diffusion may also increase the total diffusion in the model, possibly contributing to the fact that $D > D_{\text{uvic}}$. As a result of

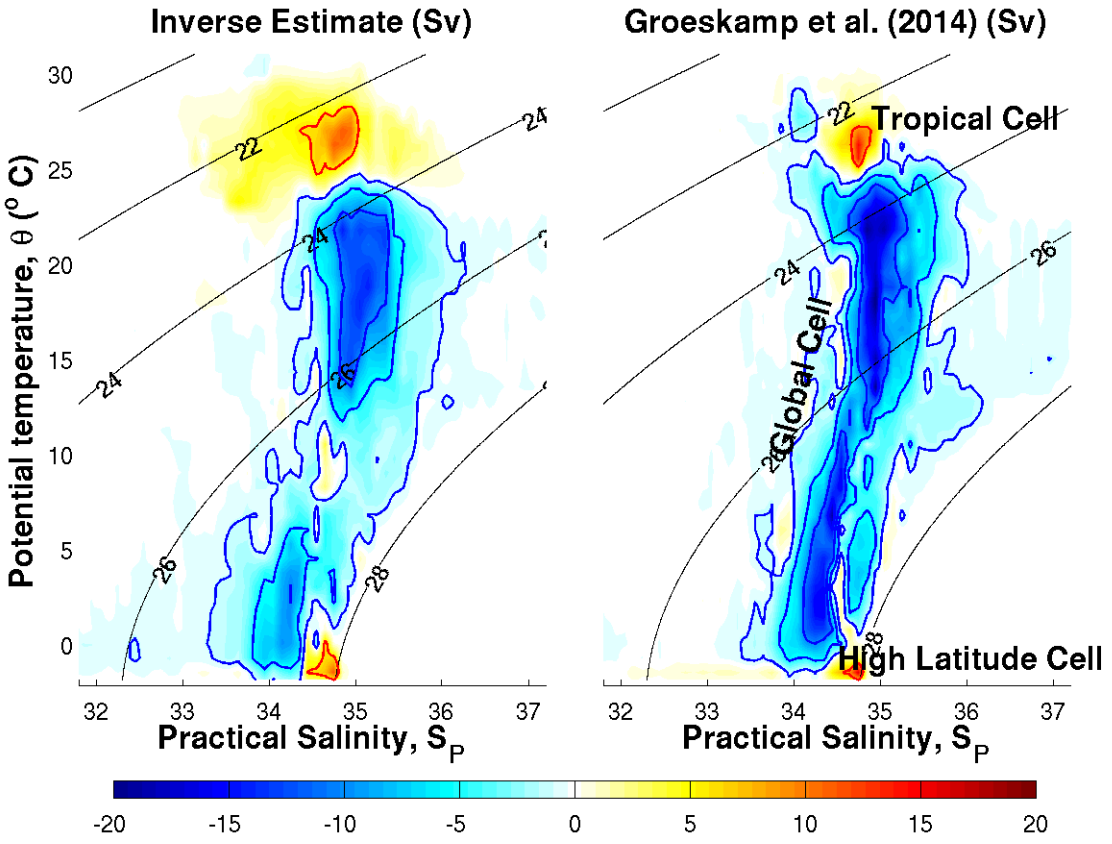

FIGURE 4.6: The inverse estimate $\Psi^{\mathrm{dia,inv}}_{S_\mathrm{P}\theta}$ (left) for the optimal solution, corresponding to the column weights given by the black dot in Fig. 4.5, and $\Psi^{\mathrm{dia}}_{S_\mathrm{P}\theta}$ calculated using the Groeskamp et al. (2014a) method (right). The blue lines show the [-15,-10, -1] Sv-contours, the red lines the 1Sv contour and the black lines the contours for potential density (σ_0). The cell names are adopted from Groeskamp et al. (2014a).

an increased D and reduced K we than find general differences given by $\Psi^{\mathrm{dia}}_{S_\mathrm{P}\theta} - \Psi^{\mathrm{dia,inv}}_{S_\mathrm{P}\theta}$ (Fig. 4.7).

The fact that the standard deviation for $\mathbf{x}$ obtained from $\mathbf{C_p}$ is much smaller than the variation of the solution as a result of changing $\sigma^{\mathbf{S_P}}_{\mathbf{e}}$ and $\sigma^{\theta}_{\mathbf{e}}$ (Fig. 4.5), indicates that the accuracy of the solution is limited by our prior knowledge of the formal statistical structure of the equation and solution errors, rather then the information content of the equations. This justifies our decision to choose the weights based on physical principles.

The similarity between $\Psi^{\mathrm{dia}}_{S_\mathrm{P}\theta}$ and $\Psi^{\mathrm{dia,inv}}_{S_\mathrm{P}\theta}$ is also evident when considering the diapycnal salt ($F_{\mathrm{Salt}}(\rho_\mathrm{r})$) and heat ($F_{\mathrm{Heat}}(\rho_\mathrm{r})$) transports for reference potential density ρ_r. Following (Zika et al., 2012) this is given by,

$$F_{\mathrm{Heat}}(\rho_\mathrm{r}) = \int_{\rho_\mathrm{r}} \rho c_p^0 \theta d\Psi^{\mathrm{dia}}_{S_\mathrm{P}\theta}, \tag{4.46}$$

$$F_{\mathrm{salt}}(\rho_\mathrm{r}) = \int_{\rho_\mathrm{r}} S_\mathrm{P} d\Psi^{\mathrm{dia}}_{S_\mathrm{P}\theta}.$$

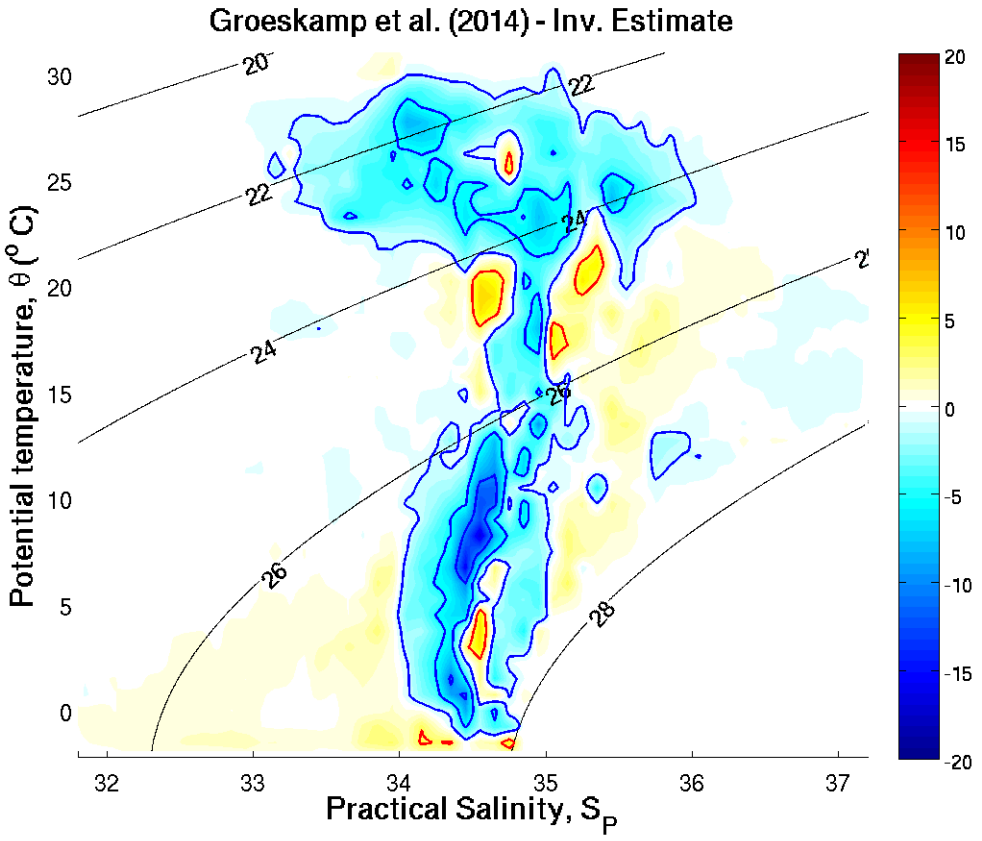

FIGURE 4.7: The difference $\Psi^{\text{dia}}_{S_{\text{P}}\theta} - \Psi^{\text{dia,inv}}_{S_{\text{P}}\theta}$. Contours are as in Fig. (4.6).

We have applied an integration along lines of constant reference potential density ρ_{r}. The salt flux can be expressed as an equivalent freshwater flux, by dividing it by a reference salinity ($F_{\text{FW}}(\rho_{\text{r}}) = F_{\text{Salt}}(\rho_{\text{r}})/S_{\text{ref}}, S_{\text{ref}} = 35$). At densities that cross the tropical cell 21 kg m^{-3} $< \sigma_0 <$24 kg m^{-3}, we have an overestimation of both the diapycnal freshwater and heat transport due to an increased magnitude of the tropical cell of $\Psi^{\text{dia,inv}}_{S_{\text{P}}\theta}$ compared to $\Psi^{\text{dia}}_{S_{\text{P}}\theta}$ (Fig. 4.8). Due to an underestimation of the global cell of $\Psi^{\text{dia,inv}}_{S_{\text{P}}\theta}$ compared to $\Psi^{\text{dia}}_{S_{\text{P}}\theta}$, we have a general underestimation of the magnitude of the diapycnal salt and heat transport for 24 kg m^{-3} $< \sigma_0 <$27 kg m^{-3} (Fig. 4.8). However, the similarity of the shapes of the diapycnal transports show the THIM is skilled in capturing $\Psi^{\text{dia,inv}}_{S_{\text{P}}\theta}$, regardless of the errors discussed previously.

4.6.4 Putting the THIM in perspective

Most inverse (box) models are designed with a focus on estimating the absolute velocity vector only. Currently inverse methods are one of few methods by which one is able to provide an estimate of mixing from observations. Inverse box methods that also estimate D often contain unknowns at the boundaries that require both dynamical constrains and conservation statements, increasing the complexity of the system and sensitivity to

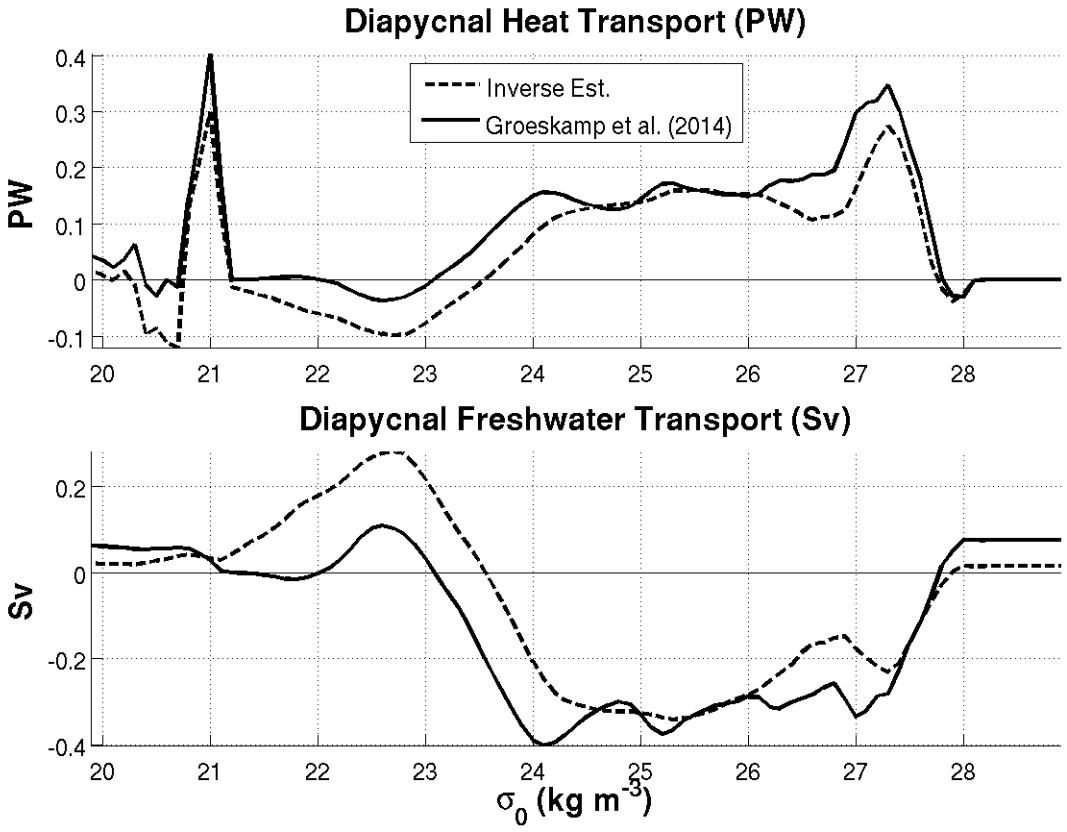

FIGURE 4.8: Diapycnal transport of heat (1PW = 10^{15}W, top) and freshwater (Sv, bottom) through potential density surfaces (σ_0) for $\Psi^{\mathrm{dia}}_{S_\mathrm{P}\theta}$ (solid) and $\Psi^{\mathrm{dia,inv}}_{S_\mathrm{P}\theta}$ (dashed).

prior estimates (Sloyan and Rintoul (2000, 2001) amongst many others). The THIM uses boxes bounded using 2 pair of tracer surfaces, analysed in tracer coordinates, rather than Cartesian coordinates. This reduces the complexity of the system to a set of simple tracer conservation equations. The global application of the THIM leads to strong constrains on the solution, as confirmed by the small error calculated using $\mathbf{C_P}$ and small variation of the solution for a wide range of choices of the row weighting. There are inverse models that provide global estimates of D (Ganachaud and Wunsch, 2000) or local estimates of both K and D (Zika et al., 2010b). However, to our knowledge the THIM is the only inverse estimates that can provide globally constrained estimates of both K and D, from observations.

Groeskamp et al. (2014a) showed that $\Psi^{\mathrm{dia}}_{S_\mathrm{A}\Theta} = \Psi^{\mathrm{adv}}_{S_\mathrm{A}\Theta} + \Psi^{\mathrm{loc}}_{S_\mathrm{A}\Theta}$. Here the local thermohaline streamfunction $\Psi^{\mathrm{loc}}_{S_\mathrm{A}\Theta}$ represents the circulation in (S_A, Θ) coordinates due to cyclic changes of the ocean's volume distribution in (S_A, Θ) coordinates, without motion in geographical space and can be calculated from an ocean hydrography. The advective thermohaline streamfunction, $\Psi^{\mathrm{adv}}_{S_\mathrm{A}\Theta}$ represents the non-divergent component of the geographical ocean circulation, in the direction normal to the isohalines and isotherms, in (S_A, Θ) coordinates, and require global observations of $\mathbf{u}$. However, using the THIM

and the calculation of $\Psi^{\mathrm{loc}}_{S_\mathrm{A}\Theta}$, as presented by Groeskamp et al. (2014a), we can calculate $\Psi^{\mathrm{adv}}_{S_\mathrm{A}\Theta} = \Psi^{\mathrm{dia}}_{S_\mathrm{A}\Theta} - \Psi^{\mathrm{loc}}_{S_\mathrm{A}\Theta}$, from the more readily observed salinity and temperature.

This study has shown that premultiplying the turbulent diffusive terms with a structure function is an appropriate method to reduce the number of unknown diffusion coefficients, while allowing for its spatial variation. When applying the THIM to observations, such structure functions can be applied to reduce the number of unknowns required to capture the spatial and temporal variation of K and D. When the THIM is applied to observation, choosing S_A and Θ as tracer coordinates utilises the extensive observational coverage of these tracers, reducing uncertainties in the solution. We therefore believe that the THIM has the potential to obtain well constraint global estimates of spatial and temporal varying values of K and D.

4.7 Conclusions

We have presented the Thermohaline Inverse Method (THIM), which estimates the diathermohaline streamfunction ($\Psi^{\mathrm{dia}}_{S_\mathrm{A}\Theta}$), epineutral eddy ($K$) and isotropic turbulent (D) diffusion coefficients. The THIM uses a balance between advection and water-mass transformation due to thermohaline forcing, in (S_A, Θ) coordinates. The thermohaline forcing, that is the surface freshwater and heat fluxes and diffusive salt and heat fluxes, can be obtained from ocean hydrography and surface flux products.

We have tested the THIM using a model's hydrography and surface fluxes and compared the inverse estimate of K, D and $\Psi^{\mathrm{dia}}_{S_\mathrm{A}\Theta}$ to the model's embedded diffusion coefficients and diathermohaline streamfunction. The latter was calculated independently as described in Groeskamp et al. (2014a), using the model's velocity output and hydrography. The results showed that the THIM is skilled in estimating K, D and $\Psi^{\mathrm{dia}}_{S_\mathrm{A}\Theta}$ and that the differences between the inverse estimate and the model are explained by an imbalance of the model's boundary fluxes and diffusive fluxes of both salt and heat and not due to an incorrect formulation of the inverse method. There is a large information content in the system and the resulting solution shows only little sensitivity to a wide range of row weighting coefficients. From this we conclude that the THIM can be applied to observationally-based products to produce well constrained observational based estimates of the ocean's diathermohaline circulation and mixing (Chapter 5).

Chapter 5

Diathermohaline Circulation and Mixing; An Inverse Estimate From Observations

5.1 Introduction

A key role of the ocean in the climate system is to store and redistribute tracers such as heat, fresh water and carbon dioxide. The ocean's ability to do this dependents on the strength of mixing processes. Although ocean models are sensitive to the strength and the spatial distribution of the parameterised mixing, our knowledge and understanding of mixing processes from observations is quite limited.

Mixing in ocean models is generally parameterised as, 1) epineutral down-gradient tracer diffusion due to mesoscale eddies through an eddy diffusion coefficient K (Redi, 1982) and, 2) small-scale isotropic down-gradient turbulent diffusion through a turbulent diffusion coefficient D. The isotropic nature of D is discussed in McDougall et al. (2014), but has previously been regarded to be diapycnal (Redi, 1982, Griffies, 2004), or vertical in the small slope approximation. Note that, as K represents mesoscale eddies, the magnitude of K depends on the resolution of models. The ratio of the diffusivities in these different directions are of order $K/D = 10^7$ for models with a resolution of about 3^o x 3^o, meaning that mixing processes in the epineutral direction are quite efficient compared to small-scale isotropic turbulent mixing (hereafter referred to as small-scale mixing).

Despite the relative smallness of small-scale mixing processes, they are critical in model simulations of the present day ocean and climate. Transports associated with mixing are significant and a key element in closing the ocean's global overturning circulation, in particular for the deepest half of the ocean (Munk, 1966, Munk and Wunsch, 1998, Ganachaud and Wunsch, 2000, Sloyan and Rintoul, 2001, Wunsch and Ferrari, 2004, Nikurashin and Ferrari, 2013). Sources of small-scale mixing are wind generated mixing by breaking of near-inertial waves near the surface and in the ocean interior (D'Asaro, 1985, Alford, 2001, Alford et al., 2011), dissipation of the internal tides (Nycander, 2005) and generation and dissipation of lee waves (Nikurashin and Ferrari, 2011). Observations have shown these effects partly organise themselves as increased small-scale mixing processes toward the ocean floor, concentrated in regions with both rough topography and relatively high bottom boundary currents (Polzin et al., 1997, Garabato et al., 2004, Ledwell et al., 2010, St. Laurent et al., 2012). Using satellite observations, Klocker and Abernathey (2013) obtained spatially varying magnitudes of eddy diffusivity K at the ocean's surface. Hence observations of both small-scale and eddy mixing show the need for parameterisations that take into account spatial and temporal variability of eddy mixing.

Different parameterisations have been developed to represent the small-scale interior ocean mixing in models, for example representing the general tendency of increased mixing near topography (Bryan and Lewis, 1979, St. Laurent et al., 2002) or small-scale mixing by dissipation of the internal tide (Nycander, 2005, Polzin, 2009, Melet et al., 2012). Despite our theoretical and observational understanding of small-scale mixing processes, models are still sensitive to subtle details in the parameterisations used(Melet et al., 2012).

Allowing for spatial variation of eddies in climate models can reduce systematic drift (Ferreira et al., 2005, Danabasoglu and Marshall, 2007). Pradal and Gnanadesikan (2014) found that changing the magnitude of the Redi diffusivity from 400 $m^2\ s^{-1}$ - 2400 $m^2\ s^{-1}$ induces tracer transports that lead to a difference in global warming of 1^oC over the course of about a century. Sijp et al. (2006) demonstrated that the thermohaline circulation is influenced by the choice of a model epineutral tracer diffusion scheme through its influences on the stability of North Atlantic Deep Water formation. A correct parameterisation of the spatial and temporal varying effect of eddies in coarse-resolution climate models is therefore essential.

The lack of knowledge of the spatial and temporal distribution of the magnitude of diffusion coefficients that represent ocean mixing processes in the ocean limits our ability to improve ocean models. Providing further constraints on this distribution is thus essential

for improving our ability to model the ocean. Here we attempt to provide such constraints using the Thermohaline Inverse Method (THIM, Chapter 4, hereafter referred to as Groeskamp et al. (2014b)), a method that balances water-mass transformation rates and advection in (S,T) coordinates, to obtain estimates of the diathermohaline streamfunction Ψ^{dia}_{ST} and the diffusion coefficients K and D. Here Ψ^{dia}_{ST} represents the total non-divergent diathermohaline ocean circulation in (S,T) coordinates (Chapter 3, hereafter referred to as Groeskamp et al. (2014a)). The strength of the THIM is that it separates the spatial and temporal changes in the ocean's hydrography due to water-mass transformation from that by advection. This results in a balance between water-mass transformation rates and salt and heat fluxes due to boundary forcing and mixing, which we use to constrain our mixing estimates (Speer, 1993, Hieronymus et al., 2014).

5.2 The Thermohaline Inverse Method

This section provides a short summary of the derivation by Groeskamp et al. (2014a,b) of the Thermohaline Inverse Method (THIM) that estimates diffusion coefficients and the diathermohaline streamfunction $\Psi^{\text{dia}}_{S_\text{A}\Theta}$. The latter represent the non-divergent component of the ocean circulation in Absolute Salinity S_A and Conservative Temperature Θ coordinates. Here Conservative Temperature is proportional to potential enthalpy (by the constant heat capacity factor c^0_p), representing the 'heat content' per unit mass of seawater (McDougall, 2003, Graham and McDougall, 2013). Absolute Salinity is measured on the Reference Composition Salinity Scale (Millero et al., 2008) and is an approximation to the mass fraction of dissolved material in seawater (in g kg^{-1}) (McDougall et al., 2012), and is the salinity variable of the IOC et al. (2010) thermodynamic description of seawater.

5.2.1 The Diathermohaline Streamfunction

Groeskamp et al. (2014a) showed that the non-divergent diathermohaline volume transport represented by $\Psi^{\text{dia}}_{S_\text{A}\Theta}$ is the sum of the local thermohaline streamfunction $\Psi^{\text{loc}}_{S_\text{A}\Theta}$ and the advective thermohaline streamfunction $\Psi^{\text{adv}}_{S_\text{A}\Theta}$. Here $\Psi^{\text{loc}}_{S_\text{A}\Theta}$ represents the circulation in (S_A,Θ) coordinates due to cyclic changes of the ocean's volume distribution in (S_A,Θ) coordinates, without motion in geographical space. $\Psi^{\text{loc}}_{S_\text{A}\Theta}$ can be directly calculated from an ocean hydrography. $\Psi^{\text{adv}}_{S_\text{A}\Theta}$, represents the non-divergent component of the geographical ocean circulation, in the direction normal to the isohalines and isotherms, in (S_A,Θ) coordinates. $\Psi^{\text{adv}}_{S_\text{A}\Theta}$ has hitherto been calculated directly from global calculations of $\mathbf{u}$ from ocean models (Zika et al., 2012, Döös et al., 2012). Using a model,

Hieronymus et al. (2014) provided a thorough analyses of the circulation cells of $\Psi^{\mathrm{dia}}_{S_\mathrm{A}\Theta}$. A similar decomposition into a local and an advective streamfunction was obtained for the atmospheric circulation represented by the hydrothermal streamfunction in dry static energy and latent heat coordinates (Kjellsson et al., 2013, Kjellsson, 2014). However, here the local component was shown to be small compared to the advective component.

Groeskamp et al. (2014b) developed the THIM, to allow for an observational based estimate of diffusion coefficients and $\Psi^{\mathrm{dia}}_{S_\mathrm{A}\Theta}$. Using this observational based estimate of $\Psi^{\mathrm{dia}}_{S_\mathrm{A}\Theta}$ and the prior evaluation of $\Psi^{\mathrm{loc}}_{S_\mathrm{A}\Theta}$ (Groeskamp et al., 2014a), we can calculate $\Psi^{\mathrm{adv}}_{S_\mathrm{A}\Theta} = \Psi^{\mathrm{dia}}_{S_\mathrm{A}\Theta} - \Psi^{\mathrm{loc}}_{S_\mathrm{A}\Theta}$, without the need for measurements of $\mathbf{u}$.

5.2.2 The Thermohaline Inverse method

Consider a volume ΔV, bounded by a pair of isotherms that are separated by $\Delta\Theta$ $(= 2\delta\Theta)$ and a pair of isohalines which are separated by ΔS_A $(= 2\delta S_\mathrm{A})$. The volume's Θ ranges between $\Theta \pm \delta\Theta$ and S_A ranges between $S_\mathrm{A} \pm \delta S_\mathrm{A}$ (See Fig. 3.2 and 4.1 for a sketch of this volume element ΔV). Following Groeskamp et al. (2014b) we define the diahaline volume transport $\overline{U}^{\mathrm{dia}}_{|_{S_\mathrm{A}}}(S_\mathrm{A}, \Theta \pm \delta\Theta)$, to be the volume transport in the positive S_A-direction through the area of the surface of constant S_A, for the Θ-range of $\Theta \pm \delta\Theta$. The diathermal volume transport $\overline{U}^{\mathrm{dia}}_{|_\Theta}(S_\mathrm{A} \pm \delta S_\mathrm{A}, \Theta)$ is defined as the volume transport in the positive Θ-direction through the area of the surface of constant Θ, for the S_A-range of $S_\mathrm{A} \pm \delta S_\mathrm{A}$. These areas are a global collection of all such areas in Cartesian coordinates. The superscript or prefix 'dia' indicates a transport through a surface, which is the difference between the velocity of a fluid parcel in the direction normal to a surface and the movement of the surface itself in this direction (Griffies, 2004, Groeskamp et al., 2014a).

Using the conservation equations for volume, salt and heat for ΔV for a Boussinesq ocean, the diahaline and diathermal volume transports (the combination of them is referred to as diathermohaline volume transport) are expressed as a function of water-mass transformation due to thermohaline forcing. The non-divergent component of the diathermohaline volume transport can be represented by the diathermohaline streamfunction, so that we obtain the following expression that relates the diathermohaline streamfunction, with the diathermohaline volume transport and thermohaline forcing in the S_A direction (see Eqs. 4.27 and 4.28),

$$\begin{aligned}\Psi^{\mathrm{dia}}_{S_\mathrm{A}\Theta}(S_\mathrm{A}, \Theta + \delta\Theta) - \Psi^{\mathrm{dia}}_{S_\mathrm{A}\Theta}(S_\mathrm{A}, \Theta - \delta\Theta) &= \overline{U}^{\mathrm{dia}}_{|_{S_\mathrm{A}}}(S_\mathrm{A}, \Theta \pm \delta\Theta) - \overline{U}^{\mathrm{tr}}_{|_{S_\mathrm{A}}}(S_\mathrm{A}, \Theta \pm \delta\Theta) \\ &= \frac{1}{\rho_0 \Delta S_\mathrm{A}}\left[\overline{M_{S_\mathrm{A}}} - \overline{L}_{S_\mathrm{A}} - \overline{S_\mathrm{A} F_\mathrm{m}}\right] - \overline{U}^{\mathrm{tr}}_{|_{S_\mathrm{A}}}(S_\mathrm{A}, \Theta \pm \delta\Theta),\end{aligned} \tag{5.1}$$

and in the Θ-direction,

$$
\begin{aligned}
-\left[\Psi^{\mathrm{dia}}_{S_\mathrm{A}\Theta}\left(S_\mathrm{A}+\delta S_\mathrm{A},\Theta\right)-\Psi^{\mathrm{dia}}_{S_\mathrm{A}\Theta}\left(S_\mathrm{A}-\delta S_\mathrm{A},\Theta\right)\right] &= \overline{U}^{\mathrm{dia}}_{|_\Theta}\left(S_\mathrm{A}\pm\delta S_\mathrm{A},\Theta\right)-\overline{U}^{\mathrm{tr}}_{|_\Theta}\left(S_\mathrm{A}\pm\delta S_\mathrm{A},\Theta\right) \qquad (5.2)\\
&= \frac{1}{\rho_0 c_p^0 \Delta\Theta}\left[\overline{F_\Theta}+\overline{M_\Theta}-\overline{L}_\Theta\right]-\overline{U}^{\mathrm{tr}}_{|_\Theta}\left(S_\mathrm{A}\pm\delta S_\mathrm{A},\Theta\right).
\end{aligned}
$$

Here $\overline{U}^{\mathrm{tr}}_{|_{S_\mathrm{A}}}$ and $\overline{U}^{\mathrm{tr}}_{|_\Theta}$ are the divergent diahaline and diathermal volume transports due to a temporal trend in $S_\mathrm{A}(x,y,z,t)$, and $\Theta(x,y,z,t)$, respectively. The trend terms $\overline{U}^{\mathrm{tr}}_{|_{S_\mathrm{A}}}$ and $\overline{U}^{\mathrm{tr}}_{|_\Theta}$ are required to obtain the non-divergent component of $\overline{U}^{\mathrm{dia}}_{|_{S_\mathrm{A}}}$ and $\overline{U}^{\mathrm{dia}}_{|_\Theta}$, as only that component can be expressed by a streamfunction. Groeskamp et al. (2014a) showed that $\overline{U}^{\mathrm{tr}}_{|_{S_\mathrm{A}}}$ and $\overline{U}^{\mathrm{tr}}_{|_\Theta}$ can be obtained using from the trend in an ocean hydrography.

In the second line of Eqs. (5.1) and (5.2) we have expressed $\overline{U}^{\mathrm{dia}}_{|_{S_\mathrm{A}}}$ and $\overline{U}^{\mathrm{dia}}_{|_\Theta}$ as a function of thermohaline forcing, where F_m is the boundary mass flux into ΔV due to evaporation, precipitation, ice melt and formation and river runoff. We assume that the boundary salt flux is zero, i.e. neglecting the formation of sea spray, interchange of salt with sea ice and salt entering from the ocean boundaries. Although the total amount of salt in the ocean remains constant, the ocean's salinity is modified by F_m (Huang, 1993, Griffies, 2004). F_Θ is the net convergence of heat into ΔV due to boundary fluxes. The correlation term between Θ and F_m, $\overline{\Theta F_\mathrm{m}}/\left(\rho_0 c_p^0 \Delta\Theta\right)$, over the volume ΔV is negligible compared to the other terms in Eq. (5.2). M_{S_A} and M_Θ are the net convergence of salt and heat into ΔV due to *all* interior diffusive processes and include the unknown spatial and temporal distribution of the diffusion coefficients K and D. The gradients on which K and D operate can be obtained from an ocean hydrography in combination with a mixing parameterisation, and will be discussed in detail in Section 5.4.

$\overline{L}_{S_\mathrm{A}} = \rho_0\overline{\Delta V'\partial S'_\mathrm{A}/\partial t}$ and $\overline{L}_\Theta = \rho_0 c_p^0\overline{\Delta V'\partial\Theta'/\partial t}$ are the local response terms. They represent the amount of salt and heat per unit time, needed to change the S_A and Θ properties of ΔV by an amount sufficiently small to remain within the defined (S_A,Θ) grid. $\overline{L}_{S_\mathrm{A}}$ and $\overline{L}_\Theta$ are merely a consequence of the discretisation into (S_A,Θ) classes and approach 0 when δS_A and $\delta\Theta$ approach 0 (Groeskamp et al., 2014b).

5.3 The Data

The observation-based climatology we use is CARS 2009 (CARS). This is a global climatology, except for the boundary at 75^{o}S. It has a high-resolution (0.5^o x 0.5^o grid spacing, 79 vertical levels) and provides seasonal *in-situ* temperature (T), Practical Salinity (S_P), and several other properties (Ridgway et al., 2002, Ridgway and Dunn, 2003). At higher latitudes observations are limited and biased to the summer state. CARS provides a

gridded, time-continuous standard year value of S_{P} and T. Here we use monthly averaged values and apply the TEOS-10 software (IOC et al., 2010, McDougall and Barker, 2011) to convert the CARS data to S_{A} and Θ. The resulting data is stabilised ($N^2 > 0$ everywhere) using a minimal adjustment of Absolute Salinity, within the measurement error (Jackett and McDougall, 1995, Barker and McDougall, 2015).

The magnitude of the eddy diffusion coefficient required to parameterise mesoscale eddies in a model, depends on the resolution of the model. The higher the resolution, the smaller the required eddy diffusion coefficient as the eddy fluxes are explicitly resolved. To be able to compare our results with coarse resolution climate models, we have also produced a low resolution version of CARS (hereafter referred to as LR-CARS), in which the tracer at each location is the average of the surrounding tracer values of the CARS atlas dataset in a 3^o x 3^o grid-box.

For the air-sea salt and heat fluxes we use the global air-sea heat and water flux components computed from version 2 of CORE (Common Ocean Reference Experiment) atmospheric state fields starting from 1949 until 2006, at monthly mean resolution (Yeager and Large, 2008, Dataset). It is provided at a resolution of 1^o x 1^o grid spacing (360 $\times$ 180 longitude $\times$ latitude). We have produced a "standard year" by averaging surface fluxes for each calendar month, and interpolated onto the CARS grid.

5.4 Water-mass transformation terms from observations

In this section we will calculate the forcing and mixing terms in Eqs. (5.1) and (5.2). The water-mass transformation due to the local response terms $\overline{L}_{S_{\mathrm{A}}}/(\rho_0 \Delta S_{\mathrm{A}})$ and $\overline{L}_{\Theta}/(\rho_0 c_p^0 \Delta\Theta)$ are not shown as they are very small and do not influence the inverse estimate. As CARS represents a 'standard year', there is no trend term.

5.4.1 Boundary forcing

Following the technique described by Groeskamp et al. (2014b), the surface salt and heat fluxes ($\overline{S_{\mathrm{A}} F_{\mathrm{m}}}/(\rho_0 \Delta S_{\mathrm{A}})$ and $\overline{F_{\Theta}}/(\rho_0 c_p^0 \Delta\Theta)$, respectively), are calculated using the CORE data. They are binned and averaged into (S_{A}, Θ) coordinates according to the (S_{A}, Θ) values obtained from CARS at the surface of the ocean.

5.4.2 Mixing

Water-mass transformation due to diffusion of salt and heat is given by $\overline{M_{S_\mathrm{A}}}/(\rho_0 \Delta S_\mathrm{A})$ and $\overline{M_\Theta}/(\rho_0 c_p^0 \Delta\Theta)$, respectively (Eqs. 5.1 and 5.2). Although the diffusion coefficients are unknown, using the CARS climatology the gradients on which they operate and the area through which they diffuse, can be calculated, multiplied and binned into (S_A, Θ) coordinates. In CARS S_A and Θ are given on each (x, y, z)-coordinate around which six interfaces are defined to enclose a volume. To calculate the diffusive flux, each interface is assumed to be a surface of constant S_A and Θ with a constant diffusion coefficient for that surface. Hence water-mass transformation rates due to diffusion are given by the tracer gradient across that particular surface, multiplied by the area and a constant diffusion coefficient for that surface. Since the unit-normal of the surfaces are exactly in the x, y and z-direction, we find the associated interfaces to be $A_{yz} = dydz$, $A_{xz} = dxdz$ and $A_{xy} = dxdy$. We then take the convergence of the resulting transport, in (S_A, Θ) coordinates.

We include the variation in mixing strength using structure functions that premultiply the tracer gradients upon which the diffusion coefficients operate. The structure functions are based on prior knowledge of the physics of mixing and reduce the number of unknown diffusion coefficients that need to be solved for. The remainder of this section provides details of the structure functions and associated scaling and calculation of the tracer gradients.

Small-scale diffusion

Small-scale diffusion is parameterised by multiplying the small-scale diffusion coefficient D with isotropic tracer gradients. To include the effect of increased small-scale mixing near topography we will use a structure function based on Bryan and Lewis (1979) (leaving more complex parameterisations as future work),

$$f_D(z) = 0.80 + \frac{1.05}{\pi} \arctan\left(4.5 \times 10^{-3}\,[z - 2500]\right). \tag{5.3}$$

Here $f_D(0) = 0.3$ (at the surface), increasing to 1.3 for depths greater than 2000 m, mimicking the effect of increased small-scale mixing near the bottom (Fig. 5.1b). Note that the original structure by Bryan and Lewis (1979) is given by $D_\mathrm{BL} = 10^{-4} f_D(z)$. The terms that multiply D are given by,

$$A^D_{S_\mathrm{A}} = \frac{1}{\rho_0 \Delta S_\mathrm{A}} \nabla_{S_\mathrm{A}\Theta} \cdot f_D(z) \nabla S_\mathrm{A} \mathbf{R}, \tag{5.4}$$

$$A^D_{\Theta} = \frac{1}{\rho_0 c_p^0 \Delta\Theta} \nabla_{S_\mathrm{A}\Theta} \cdot f_D(z) \nabla\Theta \mathbf{R}. \tag{5.5}$$

Here the Cartesian coordinate divergence operator is given by $\nabla = (\partial/\partial x, \partial/\partial y, \partial/\partial z)$, the thermohaline divergence operator $\nabla_{S_\mathrm{A}\Theta} = (\Delta S_\mathrm{A}\partial/\partial S_\mathrm{A}, \Delta\Theta\partial/\partial\Theta)$ calculates the divergence in (S_A, Θ) coordinates (Groeskamp et al., 2014b), and

$$\mathbf{R} = \begin{pmatrix} A_{yz} & A_{yz} \\ A_{xz} & A_{zz} \\ A_{xy} & A_{xy} \end{pmatrix}. \tag{5.6}$$

The result is a structure in (S_A, Θ) coordinates that, when multiplied by D, is equal to the water-mass transformation rates due to small-scale mixing processes in the world ocean.

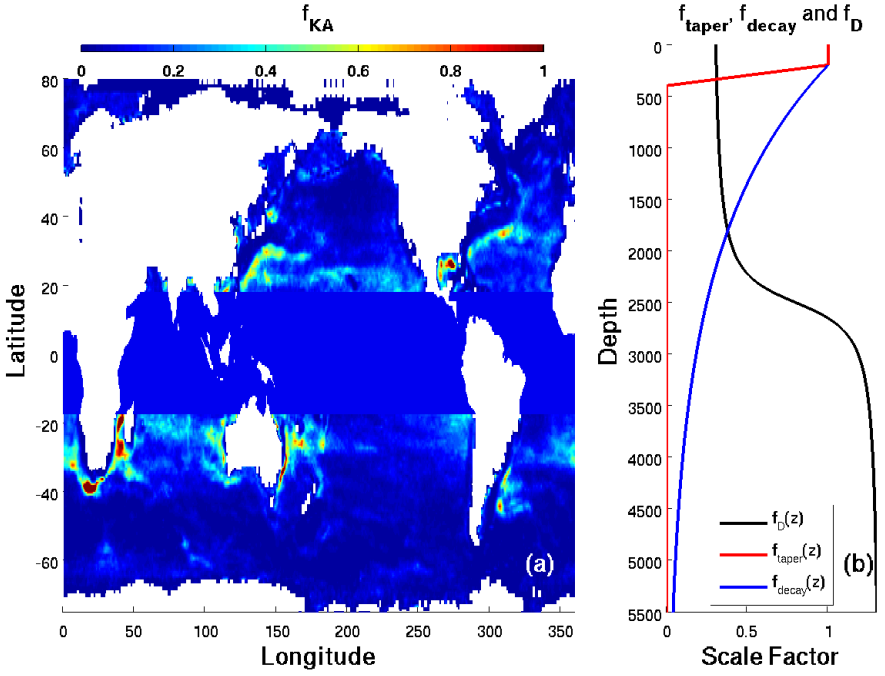

FIGURE 5.1: Mixing structure functions. The left panel (a) shows the structure of $f_\mathrm{KA}(x, y)$, the right panel (b) shows $f_\mathrm{taper}(z)$, $f_\mathrm{decay}(z)$ and $f_D(z)$

Eddy diffusion

Tracer transport by eddies in ocean models is achieved by either advection through the quasi-Stokes streamfunction parameterisation (Gent and McWilliams, 1990, Gent et al., 1995, McDougall and McIntosh, 2001), and by diffusion through the Redi parameterisation (Redi, 1982). In this chapter we deal with tracer diffusion by eddies through the Redi parameterisation. In the ocean's mixed layer there is horizontal diffusion of tracers due to mesoscale eddies, while in the ocean interior there is isopycnal diffusion of tracers. Hence we separate the diffusion into an eddy diffusion coefficient that operates on horizontal gradients K_H and one based on isopycnal gradients K_I.

Horizontal tracer gradients are given by ($\nabla_{\mathrm{H}} C = (\partial C/\partial x, \partial C/\partial y, 0)$). Isopycnal gradients ($\nabla_{\mathrm{N}} C$) require a rotation tensor (Redi, 1982), and we invoke the small slope approximation (Gent and McWilliams, 1990), as provided by Eq. 2.13,

$$\nabla_{\mathrm{N}} C = \begin{pmatrix} 1 & 0 & s_x \\ 0 & 1 & s_y \\ s_x & s_y & s^2 \end{pmatrix} \begin{pmatrix} \frac{\partial C}{\partial x} \\ \frac{\partial C}{\partial y} \\ \frac{\partial C}{\partial z} \end{pmatrix}. \tag{5.7}$$

Here $(s_x, s_y) = -(\gamma_x^n, \gamma_y^n)/\gamma_z^n$ providing the neutral direction and $s^2 = s_x^2 + s_y^2$. The neutral directions are obtained using the locally referenced potential density values (σ_k) to calculate density gradients. The gradients at $z = z_k$ are obtained by finding potential density referenced to p_k, $\sigma_k = \rho(S_{\mathrm{A}}, \Theta, p_k)$ for the whole ocean according to IOC et al. (2010), applied to all depth levels ranging from $k = 1 : N$, where N is the total number of vertical layers.

The transition between diffusion coefficients operating on horizontal gradients in the mixed layer to isopycnal gradients in the interior is captured by a linear tapering from horizontal mixing to isopycnal mixing between $z_{\mathrm{bsml}} = 200\mathrm{m}$ and $z_{\mathrm{bwml}} = 400\mathrm{m}$. Here z_{bsml} and z_{bwml} are estimates of the depths of the bottom of the summer and winter mixed layer, respectively. The taper function (Fig. 5.1b) is given by ,

$$f_{\mathrm{taper}}(z) = \begin{cases} 1 & z < z_{\mathrm{bsml}} \\ \frac{z_{\mathrm{bwml}} - z}{z_{\mathrm{bwml}} - z_{\mathrm{bsml}}} & z_{\mathrm{bsml}} \leqslant z \leqslant z_{\mathrm{bwml}} \\ 0 & z_{\mathrm{bwml}} < z \end{cases}. \tag{5.8}$$

As ocean eddies in the interior are thought to be less energetic than near the surface, there is thought to be less eddy diffusion in the ocean interior. To capture this effect we scale the gradients by a vertical decay profile given by,

$$f_{\mathrm{decay}}(z) = \begin{cases} 1 & z < z_{\mathrm{bsml}} \\ e^{-\frac{z - z_{\mathrm{bsml}}}{h(x,y) - z_{\mathrm{bsml}}} \ln(\eta)} & z_{\mathrm{bsml}} \leqslant z \end{cases}. \tag{5.9}$$

Here $f_{\mathrm{decay}}(z_{\mathrm{bsml}}) = 1$ and $f_{\mathrm{decay}}(h) = \eta$ and we have used that $h(x, y) = h = 4000\mathrm{m}$ and $\eta = 0.1$ (Fig. 5.1b).

The horizontal variation in the magnitude of horizontal eddy diffusion is based on observations by Klocker and Abernathey (2013). They used eddy mixing length theory in combination with satellite observations to obtain estimates of the magnitude of eddy diffusion at the surface of the ocean. Their magnitudes are applicable for models that do not resolve the largest eddies used for their estimates. However, the spatially varying structure remains an indication of where there is enhanced or reduced eddy mixing. We

will only use their structure rather than their absolute values, because, 1) the resolution of CARS is high enough to resolve some eddies used for the estimate by Klocker and Abernathey (2013), 2) their estimate is invalid for $\pm 18^o$ latitude and 3) their estimate allows certain freedom for fitting the magnitude through the use of a constant mixing efficiency. We have adopted a constant diffusion coefficients of 1000 m^2 s^{-1} for 0 ± 18^o latitude, representative of the global average of their results. We have limited the lowest values of their structure to 250 m^2 s^{-1} and the highest values to 10000 m^2 s^{-1} and nondimensionalised it by dividing through its maximum (thus 10000 m^2 s^{-1}), resulting in $f_{\mathrm{KA}}(x,y)$ which has values between 0 and 1 and a detailed spatial variation of the effects of eddy mixing (Fig. 5.1a).

Using the structure functions, the terms that operate on the horizontal eddy diffusion coefficient K_{H} are given by,

$$A^{K_{\mathrm{H}}}_{S_{\mathrm{A}}} = \frac{1}{\rho_0 \Delta S_{\mathrm{A}}} \nabla_{S_{\mathrm{A}}\Theta} \cdot f_{\mathrm{taper}} f_{\mathrm{KA}} \nabla_{\mathrm{H}} S_{\mathrm{A}} \mathbf{R}, \tag{5.10}$$

$$A^{K_{\mathrm{H}}}_{\Theta} = \frac{1}{\rho_0 c^0_p \Delta \Theta} \nabla_{S_{\mathrm{A}}\Theta} \cdot f_{\mathrm{taper}} f_{\mathrm{KA}} \nabla_{\mathrm{H}} \Theta \mathbf{R}. \tag{5.11}$$

The terms that operate on the isopycnal diffusion coefficient K_{I} are given by,

$$A^{K_{\mathrm{I}}}_{S_{\mathrm{A}}} = \frac{1}{\rho_0 \Delta S_{\mathrm{A}}} \nabla_{S_{\mathrm{A}}\Theta} \cdot f_{\mathrm{decay}} \left(1 - f_{\mathrm{taper}}\right) f_{\mathrm{KA}} \nabla_{\mathrm{N}} S_{\mathrm{A}} \mathbf{R}, \tag{5.12}$$

$$A^{K_{\mathrm{I}}}_{\Theta} = \frac{1}{\rho_0 c^0_p \Delta \Theta} \nabla_{S_{\mathrm{A}}\Theta} \cdot f_{\mathrm{decay}} \left(1 - f_{\mathrm{taper}}\right) f_{\mathrm{KA}} \nabla_{\mathrm{N}} \Theta \mathbf{R}. \tag{5.13}$$

The water-mass transformation rates due to horizontal and isopycnal eddy diffusion are obtained by multiplying these structures with the horizontal and isopycnal eddy diffusion coefficient respectively. These constant values arise as part of the inverse solution.

5.5 The inverse technique

In Eqs. (5.1) and (5.2) we have obtained an expression for the diathermohaline volume transport out of ΔV, due to water-mass transformation as a result of a convergence of salt or heat into ΔV. For each ΔV, two unique equations can be constructed,

$$\Psi^{\mathrm{dia}}_{S_{\mathrm{A}}\Theta}\left(S_{\mathrm{A}}, \Theta + \delta\Theta\right) - \Psi^{\mathrm{dia}}_{S_{\mathrm{A}}\Theta}\left(S_{\mathrm{A}}, \Theta - \delta\Theta\right) - DA^{D}_{S_{\mathrm{A}}} - K_{\mathrm{H}} A^{K_{\mathrm{H}}}_{S_{\mathrm{A}}} - K_{\mathrm{I}} A^{K_{\mathrm{I}}}_{S_{\mathrm{A}}} = b_{S_{\mathrm{A}}} \tag{5.14}$$

$$-\left[\Psi^{\mathrm{dia}}_{S_{\mathrm{A}}\Theta}\left(S_{\mathrm{A}} + \delta S_{\mathrm{A}}, \Theta\right) - \Psi^{\mathrm{dia}}_{S_{\mathrm{A}}\Theta}\left(S_{\mathrm{A}} - \delta S_{\mathrm{A}}, \Theta\right)\right] - DA^{D}_{\Theta} - K_{\mathrm{H}} A^{K_{\mathrm{H}}}_{\Theta} - K_{\mathrm{I}} A^{K_{\mathrm{I}}}_{\Theta} = b_{\Theta} \tag{5.15}$$

These equations can be combined in the form $\mathbf{Ax} = \mathbf{b}$. Here $\mathbf{x}$ is a $1 \times M$ vector of unknown $\Psi_{S_A\Theta}$-values and the unknown diffusion coefficients K_H, K_I and D. These unknown diffusion coefficients are the constants that multiply their respective structure functions described in Section 5.6. $\mathbf{b}$ is a $1 \times N$ vector of the known forcing terms and $\mathbf{A}$ is a $N \times M$ matrix of the coefficients that multiply $\mathbf{x}$.

An estimate for $\mathbf{x}$ can be obtained using an inverse technique that minimises χ^2, which is the sum of both the solution error and the equation error (Menke, 1984, Wunsch, 1996, McIntosh and Rintoul, 1997),

$$\chi^2 = (\mathbf{x} - \mathbf{x_0})^T \mathbf{W_c}^{-2} (\mathbf{x} - \mathbf{x_0}) + \mathbf{e}^T \mathbf{W_r}^2 \mathbf{e}. \tag{5.16}$$

Here $\mathbf{e} = \mathbf{Ax} - \mathbf{b}$ is the equation error, $\mathbf{x_0}$ is a prior estimate of $\mathbf{x}$. Here $\mathbf{W_r}$ is the row (equation) weighting matrix and $\mathbf{W_c}$ is the column (variable) weighting matrix and are both diagonal with elements $1/\sigma_\mathbf{e}$ and $\sigma_\mathbf{x}$, respectively. The elements are chosen to obtain an approximate equal influence of each variable and equation on the solution, as discussed in more detail in the remainder of this section. An estimate of the random error on the inverse estimate is given by the square root of the diagonal of the posterior covariance matrix,

$$\mathbf{C_p} = \mathbf{W_c}^2 - \mathbf{W_c}^2 \mathbf{A^T} \left[\mathbf{A} \mathbf{W_c}^2 \mathbf{A}^T + \mathbf{W_r}^{-2} \right]^{-1} \mathbf{A} \mathbf{W_c}^2, \tag{5.17}$$

However, the variations in the solution due to the prior choice of the weighting coefficients may be larger than the estimate of the random error associated with that particular choice.

For the analyses we have chosen grid-sizes in (S_A, Θ) coordinates to be $\Delta\Theta = 0.2$ ^{o}C and $\Delta S_A = 0.035$ g kg^{-3}, having a resolution high enough to distinguish different water masses in the ocean's interior and provide approximately equal number of equations in both S_A and Θ directions, such that both have an equal influence on the solution.

5.5.1 The a-priori estimates and constraints

The a-priori expected magnitudes for $\Psi_{S_A\Theta}$ are unknown, such that $\mathbf{x_0^\Psi} = 0$. We can however, provide accurate a-priori estimates of the diffusion coefficients. As the divergence by surface forcing is balanced by the convergence due to mixing, their maximum transformation rates should be very similar. This allows us to scale the structures provided by A_C^D, $A_C^{K_H}$ and $A_C^{K_I}$ (Eqs. (5.14) and (5.15)) with a diffusion coefficient that does not exceed the maximum water-mass transformation given by the boundary forcing. For

the small-scale diffusion coefficient its prior estimate x_0^D is given by,

$$x_0^D = \frac{\max|\left(F_{S_\mathrm{A}}, F_\Theta\right)|}{\max|\left(A^\mathrm{D}_{S_\mathrm{A}}, A^\mathrm{D}_\Theta\right)|} \tag{5.18}$$

We have repeated this for the a-priori estimate of the horizontal and isopycnal eddy diffusion coefficients $x_0^{K_\mathrm{H}}$ and $x_0^{K_\mathrm{I}}$, respectively. For the LR-CARS, the gradients upon which the eddy diffusion coefficients operate will be less than those of the CARS dataset, such that Eq. (5.18) allows for a larger prior estimate of the eddy diffusion coefficients. From CARS to LR-CARS there is an increase of a factor 2 and 6 for $x_0^{K_\mathrm{H}}$ and $x_0^{K_\mathrm{I}}$, respectively (Table 5.1). As expected there is hardly any change in x_0^D.

Using the prior estimates of the diffusion coefficients, we have omitted equations that are associated with transports less then 1% of the maximum transport as these equations do not have a signal to noise ratio that adds information to the solution. We have also omitted equations that are isolated in (S_A, Θ) coordinates, as they may potentially become free variables, reducing the constraints on the solution.

Coefficient	CARS	LR-CARS
x_0^D	8.1 x 10^{-5} m^2 s^{-1}	9.4 x 10^{-5} m^2 s^{-1}
$x_0^{K_\mathrm{H}}$	11906 m^2 s^{-1}	23286 m^2 s^{-1}
$x_0^{K_\mathrm{I}}$	616 m^2 s^{-1}	3708 m^2 s^{-1}

TABLE 5.1: Prior estimate of the diffusion coefficients calculated using the scaling argument given by Eq. (5.18).

Row Weighting

Using $x_0^{K_\mathrm{H}}$, $x_0^{K_\mathrm{I}}$ and x_0^D we can calculate an a-priori estimate of the diahaline volume transport $\overline{U}^{\mathrm{dia},0}_{|_{S_\mathrm{A}}}$ and diathermal volume transport $\overline{U}^{\mathrm{dia},0}_{|_\Theta}$. As $\overline{U}^{\mathrm{tr}}_{|_{S_\mathrm{A}}}$ and $\overline{U}^{\mathrm{tr}}_{|_\Theta}$ are negligible for CARS, the volume divergence in (S_A, Θ) coordinates as a result of our a-priori estimate of the diffusion coefficients is given by,

$$E^0 = \nabla_{S_\mathrm{A}\Theta} \cdot \left(\overline{U}^{\mathrm{dia},0}_{|_{S_\mathrm{A}}}, \overline{U}^{\mathrm{dia},0}_{|_\Theta}\right). \tag{5.19}$$

Here E^0 shows which grids in (S_A, Θ) coordinates and associated equations, are most imbalanced (Fig. 5.2a). The larger this imbalance is, the larger the uncertainty in the associated transport equations will be. As each equation is related with two grids, we have chosen $\sigma^{\mathbf{\Psi}}_{\mathbf{x}}$ to be proportional to 1/4 (it is spread over 4 sides) of the maximum divergence of the two grids a particular equation is associated with. This reduces its influence on the solution with increased volume divergence.

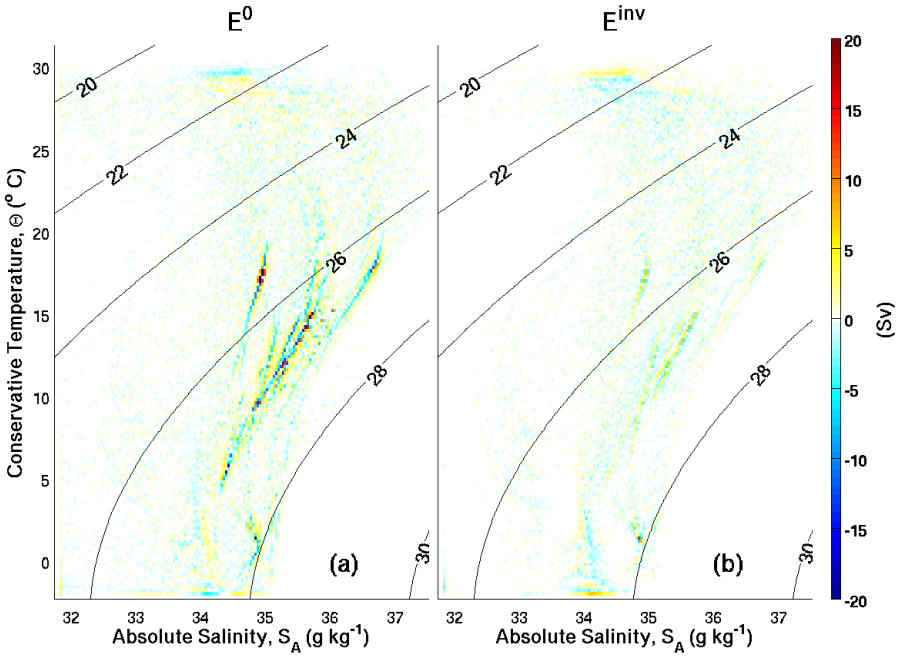

FIGURE 5.2: Volume divergence rates (Sv) in (S_A, Θ) coordinates. Panel (a) shows E^0, the volume divergence as a result of evaluating Eq. (5.19) using the prior estimates of the diffusion coefficients ($x_0^{K_H}$, $x_0^{K_I}$ and x_0^D). Panel (b) shows E^{inv}, the volume divergence as a result of evaluating Eq. (5.19) using the inverse estimates of the diffusion coefficients (K_H, K_I and D). Positive (negative) values indicate convergence (divergence). Black contours represent the surface referenced potential density anomaly values.

Column weighting

We will allow for a standard error of 50% of the prior estimate of the diffusion coefficients, leading to $\sigma_x^{K_H} = 0.5x_0^{K_H}$, $\sigma_x^{K_I} = 0.5x_0^{K_I}$ and $\sigma_x^D = 0.5x_0^D$. The lack of information for $\mathbf{x_0^\Psi}$ can be compensated by a physically appropriate choice of $\sigma_\mathbf{x}^\mathbf{\Psi}$. Assuming that $\mathbf{x} \approx \Psi^{dia}_{S_A\Theta}$, $\sigma_\mathbf{x}^\mathbf{\Psi}$ should reflect $2|\Psi_{S_A\Theta}|$ as this takes into account the structure of $|\Psi^{dia}_{S_A\Theta}|$, while the factor 2 allows for an easy fit of $\Psi^{dia}_{S_A\Theta}$, within the range allowed by $\sigma_\mathbf{x}^\mathbf{\Psi}$.

To obtain an approximation of the structure of $|\Psi^{dia}_{S_A\Theta}|$ without using prior knowledge of $\Psi^{dia}_{S_A\Theta}$, we will assume that the size of $|\Psi^{dia}_{S_A\Theta}|$ is proportional but not equal to, the average of the magnitude of the prior estimate of the diathermohaline volume transports $\left(\overline{U}^{dia,0}_{|_{S_A}}, \overline{U}^{dia,0}_{|_\Theta}\right)$, a particular $|\Psi^{dia}_{S_A\Theta}|$ is involved in (maximal 4, i.e. one through each side). This structure is then normalised with a maximum of 30 Sv, to obtain $\sigma_\mathbf{x}^\mathbf{\Psi} \approx 2|\Psi^{dia}_{S_A\Theta}|$ (Fig. 5.3).

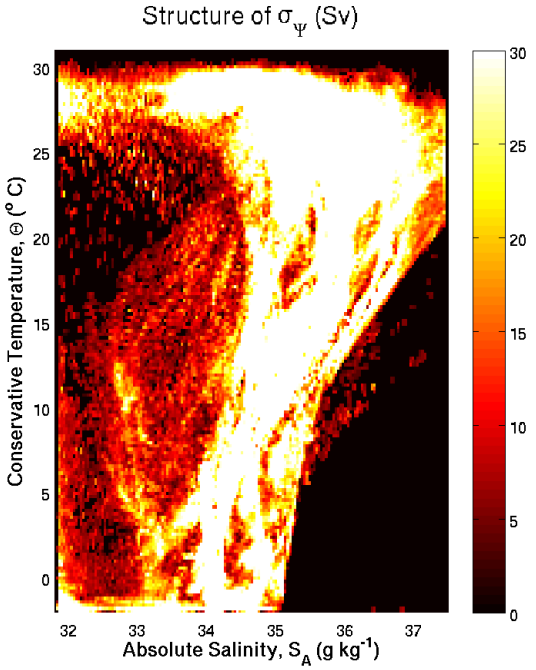

FIGURE 5.3: The column weighting for $\Psi^{\text{dia}}_{S_\text{A}\Theta}$ given by σ_Ψ.

5.6 Results

In this section we discuss the results obtained from the inverse estimate, based on an inversion with one particular choice of weighting parameters as described in the previous section, for CARS and for LR-CARS. The standard deviation associated with the results is calculated using $\mathbf{C_p}$ (Eq. 5.17). The sensitivity and variation of the solution to variation of weighting is discussed in Appendix C. For the solution discussed we have obtained $\chi^2_e = 3.76$ and $\chi^2_x = 0.14$, both within the range $0.1 \leq \left(\chi^2_x, \chi^2_e\right) \leq 10$ as suggested in Groeskamp et al. (2014b). As $\chi^2_e > \chi^2_x$, the solution is obtained with more emphasise on minimising equation error than minimising $\mathbf{x} - \mathbf{x_0}$.

5.6.1 The water-mass transformations

The surface freshwater and heat fluxes lead to water-mass transformation rates in Sverdrups ($1\text{Sv} = 10^6\ \text{m}^3\ \text{s}^{-1}$). Multiplying $A^D_{S_\text{A}}$ by the inverse solution of D results in water-mass transformation due to salt diffusion by small-scale mixing processes in (S_A, Θ) coordinates. A similar calculation can be done for the horizontal and isopycnal eddy diffusion and for the heat terms. The resulting water-mass transformation for surface and diffusive fluxes show blue colours when volume transports are directed towards lower salinities or temperatures (freshening and cooling) and red colours when directed towards higher salinities or temperatures (salinification or warming) (Fig. 5.4).

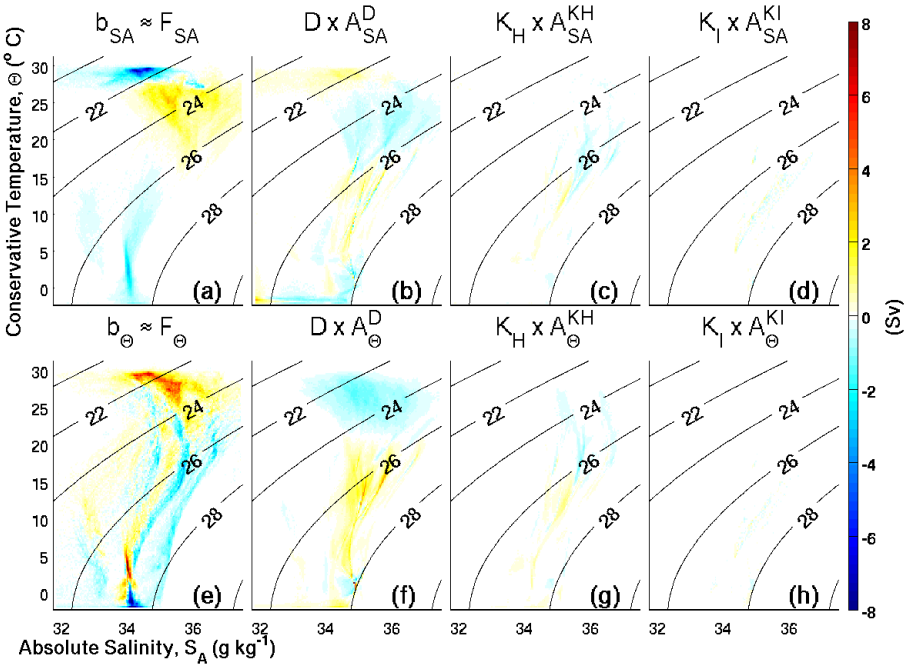

FIGURE 5.4: The water-mass transformation rates (Sv) in (S_A, Θ) coordinates due to salt fluxes (upper panels a-d) and heat fluxes (lower panels (e-h). Separated into surface forcing (a,e), small-scale diffusion (b,f), horizontal eddy diffusion (c,g) and isopycnal eddy diffusion (d,h). Positive (negative) values indicate a volume transport directed towards higher (lower) S_A and Θ values. Black contours represent the surface referenced potential density anomaly values.

Surface Forcing

The distribution of the surface salt fluxes show three areas of freshening and one area of salinification (Fig. 5.4a). For $\Theta > 20^o$C, an area which we relate with the (sub) tropical mixed layer, already fresh water is freshened even more and already salty water is salinified even more. The freshening at lower temperatures ($\Theta < 15^o$C) is also acting upon already relative fresh water, associated with higher latitudes in the Southern Hemisphere ($S_A \approx 34$ g kg^{-1}) and in the North Pacific ($S_A \approx 32.7$ g kg^{-1}) (Fig. 5.4a). The water-mass transformation due to surface freshwater fluxes acts to increase salinity gradients. Note the lack of freshwater fluxes for the $\sigma_0 = 27 - 28$ kg m^{-3}, which may be because for example Brine rejection is not included in these fluxes.

The distribution of the surface heat flux shows a general tendency for warming of already warm waters ($\Theta > 20^o$C, (Fig. 5.4a)). Then there is a sloping band of heating and cooling aligned next to each other for $S_A = [34 - 36]$ g kg^{-1} and $\Theta = [5 - 25]$ ^{o}C. This band is a result of seasonal cycles at mid latitudes. When considering a constant S_A, the heating is at a higher temperature than the cooling. This water-mass transformation due to surface heat fluxes acts to increase temperature gradients. This is also valid for

the strong warming/cooling dipole at $\Theta = [-2 - 5]$ and $S_{\mathrm{A}} \approx 34.1$ g kg^{-1}, related to heat fluxes at high latitudes.

Small-scale diffusion

Water-mass transformation due to small scale mixing processes is larger than that due to eddy mixing processes and is abundant in (S_{A}, Θ) coordinates (Fig. 5.4b and 5.4f). As mixing acts to destroy tracer gradients, the small-scale mixing results in an opposite structure to that of surface forcing (Fig. 5.4a and 5.4e), especially for $\Theta > 20^o$C. This places strong constraints on the inverse estimate of $D = 6.52 \pm 0.04$ x 10^{-5} m^2 s^{-1} for CARS (Table (5.2), slightly lower than the original value of $D_{BL} = 1$ x 10^{-4} m^2 s^{-1}, used by Bryan and Lewis (1979)). Recall that this value of $D = 6.52 \pm 0.04$ x 10^{-5} m^2 s^{-1} multiplies the shape function $f_D(z)$ (Eq. 5.3).

By multiplying D with the average of $f_{BL}(z)$ over a particular depth, we obtain (global) averages for D. We obtain $D_{\mathrm{z}>-2000\mathrm{m}} = 2.2$ x 10^{-5} m^2 s^{-1} for the upper 2000m and $D_{\mathrm{z}\leq-2000\mathrm{m}} = 7.5$ x 10^{-5} m^2 s^{-1} for depths greater than 2000m. We used 2000m to separate interior from upper ocean, as this is the depth to which small-scale mixing is required to bring up bottom waters, before isopycnal upwelling becomes relevant, reducing the required mixing to close the circulation (Toggweiler and Samuels, 1998, Sloyan and Rintoul, 2001). The upper ocean estimate corresponds very well with the observed values by Waterhouse et al. (2014) and the inverse estimates of Lumpkin and Speer (2007) and Zika et al. (2010b), even though the latter was a local estimate. The deep value corresponds to that of Lumpkin and Speer (2007), but is an order of magnitude lower than that of Waterhouse et al. (2014). Our global average (i.e full depth structure average) gives $D_{\mathrm{global}} = 5.54$ x 10^{-5} m^2 s^{-1}, lower than $D_{\mathrm{Munk}} = 1.3$ x 10^{-4} (Munk, 1966), and an order of magnitude lower than Ganachaud and Wunsch (2000) and Waterhouse et al. (2014). The small-scale mixing results for LR-CARS can be found in Table 5.2 and are not discussed as they are similar to that of CARS.

Horizontal eddy diffusion

Although confined to a smaller area in (S_{A}, Θ) coordinates, the water-mass transformation rates due to horizontal eddy diffusion in the upper 400m of the ocean, have significant magnitudes and are abundant (Fig. 5.4c and 5.4g). We obtain $K_{\mathrm{H}} = 1634 \pm 50$ m^2 s^{-1}. This value is a maximum value that multiplies the structure function and corresponds to a resolution of 0.5^ox0.5^o (CARS). The global average value of K_{H}, $K_{\mathrm{H,global}} = 123 \pm 4$ m^2 s^{-1}. For LR-CARS K_{H} is about 1.5 times larger. Climate models often take their (horizontal) eddy diffusion coefficients to be similar to that of

Estimate	CARS	LR-CARS
D	6.52 ± 0.04 x 10^{-5} m^2 s^{-1}	6.81 ± 0.04 x 10^{-5} m^2 s^{-1}
D_{global}	5.54 ± 0.03 x 10^{-5} m^2 s^{-1}	5.79 ± 0.03 x 10^{-5} m^2 s^{-1}
$D_{z>-2000m}$	2.2 x 10^{-5} m^2 s^{-1}	2.3 x 10^{-5} m^2 s^{-1}
$D_{z\leq-2000m}$	7.5 x 10^{-5} m^2 s^{-1}	7.8 x 10^{-5} m^2 s^{-1}
K_{H}	1634 ± 50 m^2 s^{-1}	2461 ± 118 m^2 s^{-1}
$K_{\text{H,global}}$	123 ± 4 m^2 s^{-1}	185 m^2 s^{-1}
K_{I}	80 ± 8 m^2 s^{-1}	667 ± 56 m^2 s^{-1}
$K_{\text{I,global}}$	2.4 ± 0.2 m^2 s^{-1}	20 ± 2 m^2 s^{-1}
$\frac{K_{\text{H,global}}}{D_{\text{global}}}$	2.2 x 10^6	3.2 x 10^6
$\frac{K_{\text{H,global}}}{K_{\text{I,global}}}$	50	9.25

TABLE 5.2: The inverse estimate of the diffusion coefficients and their global or depth averaged equivalents.

the quasi-Stokes (GM) coefficient, being of the order of 1000 m^2 s^{-1}, much larger than our estimate.

Isopycnal eddy diffusion

By definition the isopycnal eddy diffusion only effects the interior circulation of the ocean, reducing its spread in (S_{A}, Θ) coordinates (Fig. 5.4d and 5.4h). We obtain a maximum of $K_{\text{I}} = 80 \pm 8$ m^2 s^{-1} that multiplies the structure function and $K_{\text{I,global}} = 2.4 \pm 0.2$ m^2 s^{-1}. For LR-CARS we find that $K_{\text{I}} = 667 \pm 56$ m^2 s^{-1}, is a factor 8 larger than CARS K_{I} and compares well with the values obtained by Zika et al. (2010b). Do note that $K_{\text{I,global}} = 20 \pm 2$ m^2 s^{-1} for LR-CARS, which is about a factor 50 smaller than that typically used in models.

As a result of the strong constraints on D and K_{H}, the uncertainty embedded in the inverse estimate may reduce the constraints on K_{I}, increasing the uncertainty on the estimate of K_{I}. In Appendix C it is shown that changing prior estimates and column weighting mainly impacts K_{I} and to a lesser extend K_{H} or D. However, it turns out that the solution obtained from the sensitivity test is similar to what we present here, but with a slightly larger standard deviation (Table C.1).

Combining the water-mass transformation rates

Clearly the global sum of the water-mass transformation rates due to horizontal and isopycnal eddy diffusion is smaller than that due to small-scale mixing processes and surface forcing, especially for higher temperatures related to near-surface dynamics. Hieronymus et al. (2014) obtained a similar result from a model (their Fig. 6), in

agreement with Bates et al. (2014) who showed eddy diffusivities are suppressed near the equator. Note however, that the smallness of the globally averaged contribution of eddy diffusion to water-mass transformations still allows their contribution to be significant locally, both in Cartesian and (S_A, Θ) coordinates (Fig. 5.4c,d,g and 5.4h).

For $\Theta > 25^o$C, small-scale mixing is the only compensation to the surface fluxes, clearly illustrating that the water-mass transformations due to salt fluxes (A-D) and heat fluxes (E-H) do not add up to zero. The residual creates a net water-mass transformation that is expressed as a diathermohaline streamfunction difference, used to estimate $\Psi^{\rm dia}_{S_A\Theta}$.

5.6.2 The Streamfunctions

$\Psi^{\rm dia}_{S_A\Theta}$ (Fig. 5.5a), shows the non-divergent circulation based on the net water-mass transformations rates (Fig. 5.4) estimated simultaneously with the diffusion coefficients. $\Psi^{\rm dia}_{S_A\Theta}$ is the sum of the processes that drive the circulations in $\Psi^{\rm adv}_{S_A\Theta}$ (Fig. 5.5b) and $\Psi^{\rm loc}_{S_A\Theta}$ (Fig. 5.5c), where $\Psi^{\rm adv}_{S_A\Theta} = \Psi^{\rm dia}_{S_A\Theta} - \Psi^{\rm loc}_{S_A\Theta}$. The interpretation of $\Psi^{\rm loc}_{S_A\Theta}$ is unchanged from that thoroughly explained in Groeskamp et al. (2014a), hence we focus on $\Psi^{\rm dia}_{S_A\Theta}$ and $\Psi^{\rm adv}_{S_A\Theta}$. Red cells rotate anti-clockwise and blue cells rotate clockwise.

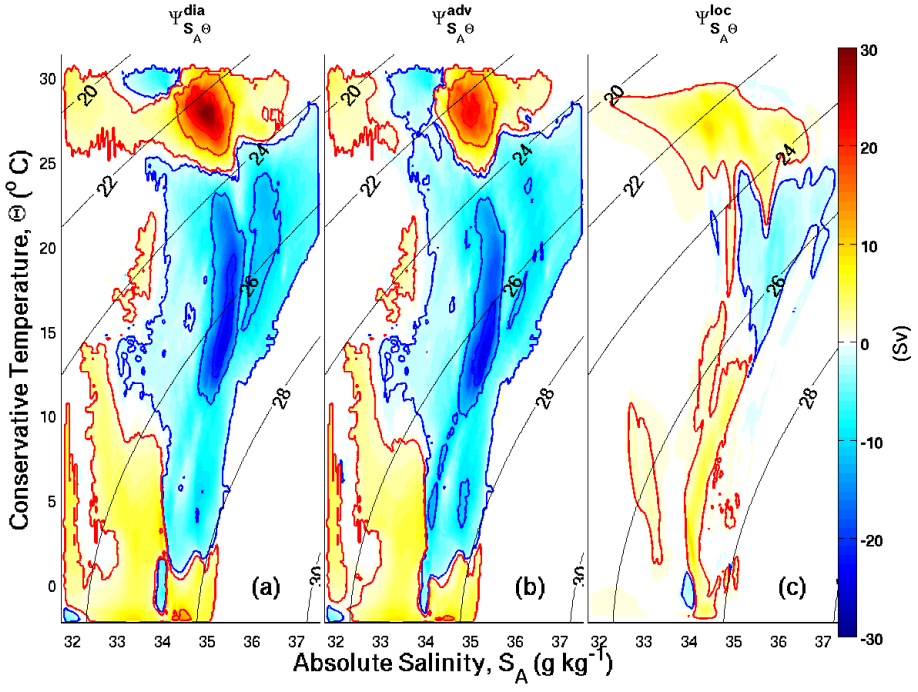

FIGURE 5.5: Panel (a) shows the Inverse estimate of the diathermohaline streamfunction $\Psi^{\rm dia}_{S_A\Theta}$, panel (b) shows the advective thermohaline streamfunction $\Psi^{\rm adv}_{S_A\Theta}$ calculated as the difference between $\Psi^{\rm dia}_{S_A\Theta}$ and the local thermohaline streamfunction $\Psi^{\rm loc}_{S_A\Theta}$, as shown in panel (c). Blue (red/yellow) cells rotate clockwise (counterclockwise). The blue lines show the contours of -1, -10 and -20 Sv; the red lines show the 1, 10, 20 Sv contours. Black contours represent the surface referenced potential density anomaly values.

Tropical cells

For $\Theta > 25^o$C, an area in (S_A, Θ) coordinates related to the upper 200 m of the ocean (Fig. 5.7) in the (sub) tropics, a large proportion of the surface salt and heat fluxes is balanced by (small-scale) mixing processes. There is no influence of eddy diffusion in the upper 200 m (Fig. 5.4c,g and 5.7), which is in agreement with the findings by Ferrari and Ferreira (2011) and Hieronymus et al. (2014), for ocean models. The residual water-mass transformation results in a strong residual anti-clockwise circulation (Fig. 5.5b), which may be considered the observational based equivalent of the Tropical cell, identified as a shallow wind-driven (near) equatorial cell (Döös et al., 2012).

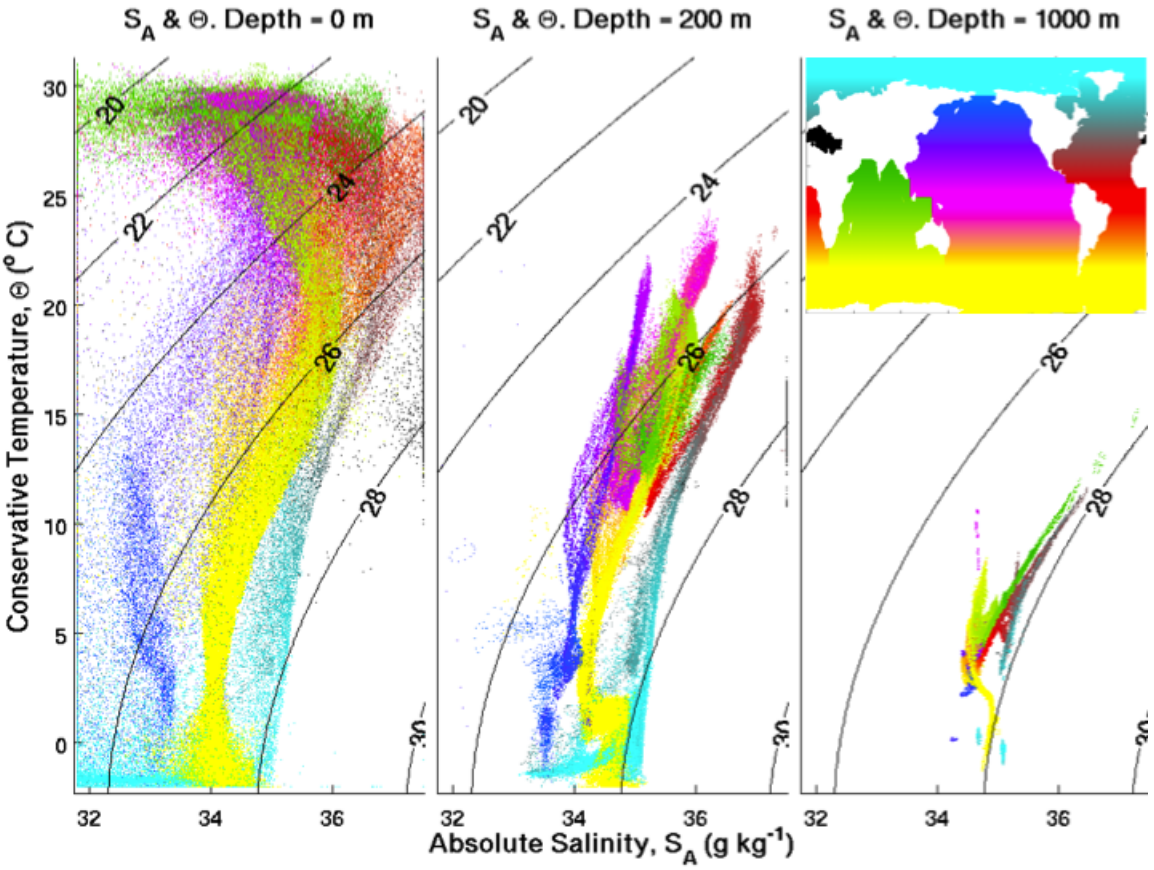

FIGURE 5.6: The ocean's S_A and Θ distribution in (S_A, Θ) coordinates for (a) the surface, (b) 200 m depth and (c) 1000 m depth, using a full year of CARS. Colour indicates geographical location as shown by the inset in panel (c). Black contours represent the surface referenced potential density anomaly values.

Hieronymus et al. (2014) found that the tropical cell (calculated from an ocean model), is composed of an Atlantic and an Indo-Pacific circulation. We also find a slight extension into the Atlantic, however the main difference is the extension of this cell in $\Psi^{\mathrm{dia}}_{S_\mathrm{A}\Theta}$, at similar temperatures, but centred at $S_\mathrm{A} \approx 32$ g kg^{-1}. This cell exists only in the upper 100m of the freshest area in the Indian Ocean (Figs. 5.7 and 5.6) and is most likely related to the circulation in the Bay of Bengal, where freshwater discharge due to the

summer monsoon lead to the observed low salinities (Schott and McCreary Jr., 2001, Schott et al., 2002). For $\Psi^{\text{adv}}_{S_\text{A}\Theta}$, this cell is separated from the tropical cell.

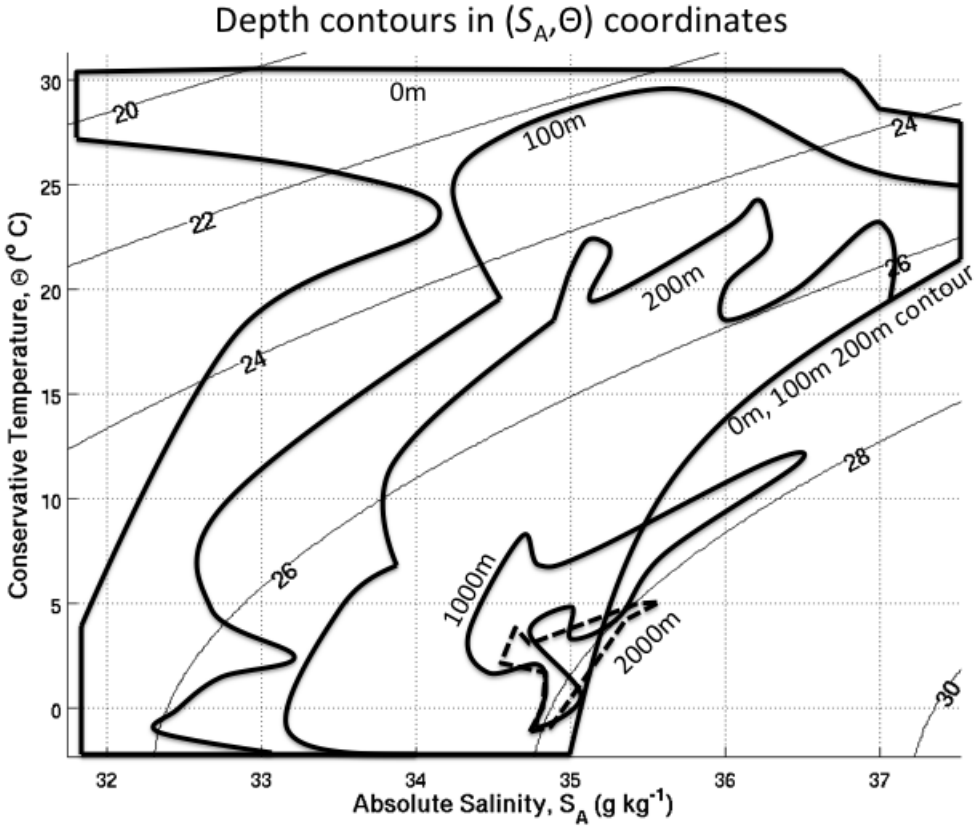

FIGURE 5.7: The thick black lines show the contours of the most extreme S_A and Θ water masses found in (S_A, Θ) coordinates for all the ocean volume at a particular depths. The thin black contours represent the surface referenced potential density anomaly values.

Global cell

The large clockwise rotating (blue) circulation cell in $\Psi^{\text{dia}}_{S_\text{A}\Theta}$ (Fig. 5.5b), is a result of a balance between surface forcing, small-scale diffusion and both horizontal and isopycnal eddy diffusion (Fig. 5.4). This cell is very similar in both $\Psi^{\text{dia}}_{S_\text{A}\Theta}$ and $\Psi^{\text{adv}}_{S_\text{A}\Theta}$ and can be considered to be mainly related to advection. This cell is called the global cell as it includes global diffusion as a mechanism to close the circulation (Munk, 1966, Gordon, 1986, Broecker, 1991) and isopycnal upwelling (Toggweiler and Samuels, 1998, Sloyan and Rintoul, 2001). The global integrated sum of the isopycnal eddy diffusion is only significant compared to the other terms, in an area in (S_A, Θ) coordinates related to depths greater than 1000 m (Figs. 5.7 and 5.4). The outskirts of this cell (the 1 Sv contour) show a globally interconnected ocean circulation, mainly for depths shallower than 200 m. However the increased magnitude for $S_\text{A} \approx 35$ g kg^{-1} and $\Theta \approx [10 - 25]^o$C,

is a circulation able to connect the surface with the interior, just like those for $S_A \approx 35$ g kg^{-1} and $\Theta \approx 5^o$C (Fig. 5.5). In general the global cell tends to connect the different ocean basins with the Southern Ocean at different depths, making it the observational based equivalent of the global Cell found by Zika et al. (2012), Döös et al. (2012) and Hieronymus et al. (2014) for an ocean model (Figs. 5.5b and 5.6).

Cold cells

Both $\Psi^{adv}_{S_A\Theta}$ and $\Psi^{dia}_{S_A\Theta}$ shows two anti-clockwise rotating cells at low temperatures (Fig. 5.5) for $S_A = [34-35]$ g kg^{-1} and $\Theta = [-2-2]$ ^{o}C related to circulations in the Antarctic, and for which $S_A = [32.5-34]$ g kg^{-1} and $\Theta = [-2-8]$ ^{o}C, related to circulation in the Arctic and North Pacific (Fig. 5.6).

The Antarctic cell is related with strong surface cooling, but small surface freshwater fluxes. However, it covers an area in (S_A, Θ) coordinates that connects surface dynamics with the interior. All three mixing processes are at play, with a dominant role for small-scale mixing processes. A peak in the heat flux due to small scale mixing-processes is observed on the $\sigma_0 = 28$ kg m^{-3} contour at $S_A = 35$ g kg^{-1} (Fig. 5.4f). This is the ocean interior heat transport due to small-scale mixing. Hence, this circulation cell represents the Antarctic Bottom Water (AABW) and Lower Circumpolar Deep Water (LCDW) circulation and can be identified as the observational based equivalent of the AABW cell as observed by Zika et al. (2012) and Döös et al. (2012) for an ocean model. However, the AABW we observe occupies a wider S_A and Θ range than the models used by Zika et al. (2012) and Döös et al. (2012).

The Arctic cell occupies a region covered by a combination of the Arctic and the North Pacific at depths shallower than 200m (Figs. 5.5b, 5.6 and 5.7), mainly induced by surface freshwater and heat forcing (Fig. 5.4). It reflects the North Pacific (sub-polar) Gyre with effect of the Bering straight outflow. This is a clockwise circulating gyre that transports cold and fresh water equatorwards on the eastern side of the basin, leading to warming and evaporation (salinification) by surface heat fluxes on its circulation pathway to the western side of the basin. There the Kuroshio current transports it northward, leading to cooling and freshening by net freshwater flux from precipitation and discharge from Bering Strait. As a result of the strong freshening there is no deep-water formation as for example in the North Atlantic. This North Pacific gyre cell (NPG) has not been identified in any of the model-based versions of $\Psi^{adv}_{S_A\Theta}$ (Zika et al., 2012, Döös et al., 2012) or $\Psi^{dia}_{S_A\Theta}$ (Groeskamp et al., 2014a, Hieronymus et al., 2014). This is likely a result of models not having the appropriate combination of freshwater fluxes from Bering Straight discharge and precipitation in the North Pacific, such that

the North Pacific and the related circulation is not distinguished from the other basins in (S_A, Θ) coordinates.

The cell observed at $S_A \approx 32$ g kg^{-1} and $\Theta = [0 - 10]^o$ C is a manifestation in the Arctic that may be related to ice dynamics in combination with strong seasonal warming and cooling leading to a very shallow buoyancy driven circulation. However, due to sparseness of data in these regions this remains speculative.

5.7 Discussion

In this section we use the inverse estimate of $\Psi^{\text{dia}}_{S_A\Theta}$ and the diffusion coefficients, to calculate diapycnal freshwater and heat transport and redistribution and energy consumption by small-scale mixing processes. We will then discuss the accuracy of the inverse estimate and the implications of the results.

5.7.1 Diapycnal salt and heat transport

The circulation cells of the streamfunctions lead to diapycnal transports of freshwater and heat. By calculating this transport and relating it to the physical mechanism driving the particular circulation cell, we can quantify the relative contribution of different physical mechanisms that lead to diapycnal freshwater and heat transports. Using Eq. (4.47) (based on Zika et al. (2012)) we calculate the diapycnal transport of freshwater (F_{FW}) and heat (F_{Heat}) for the different circulation cells (Fig. 5.8). Positive values indicate a transport towards higher densities, while negative indicate a transport to lower densities. The related divergence of F_{FW} and F_{Heat}, can be integrated to calculate the accumulation of freshwater ($F^{\text{accum}}_{\text{FW}}$) and heat ($F^{\text{accum}}_{\text{Heat}}$) into density ranges as a result of this redistribution, given by

$$F^{\text{accum}}_{\text{FW}} = -\Delta\sigma_0 \int_{\sigma_0}^{\sigma_0+\Delta\sigma_0} \frac{\partial F_{\text{FW}}}{\partial \sigma_0} d\sigma_0, \tag{5.20}$$

$$F^{\text{accum}}_{\text{Heat}} = -\Delta\sigma_0 \int_{\sigma_0}^{\sigma_0+\Delta\sigma_0} \frac{\partial F_{\text{Heat}}}{\partial \sigma_0} d\sigma_0. \tag{5.21}$$

If the integration of Eqs. (5.20) and (5.21) are performed over the whole σ_0-domain, the sum will be zero as the streamfunctions only lead to a redistribution of heat and freshwater. However, this redistribution leads to a depletion and accumulation over particular density ranges. We have integrated over these density ranges to quantify the redistribution of freshwater and heat into different density classes by the different circulation cells (Table. 5.3). Clockwise cells (blue) transport heat (freshwater) towards

higher (lower) densities while anti-clockwise cells (red) transport heat (freshwater) towards lower (higher) densities.

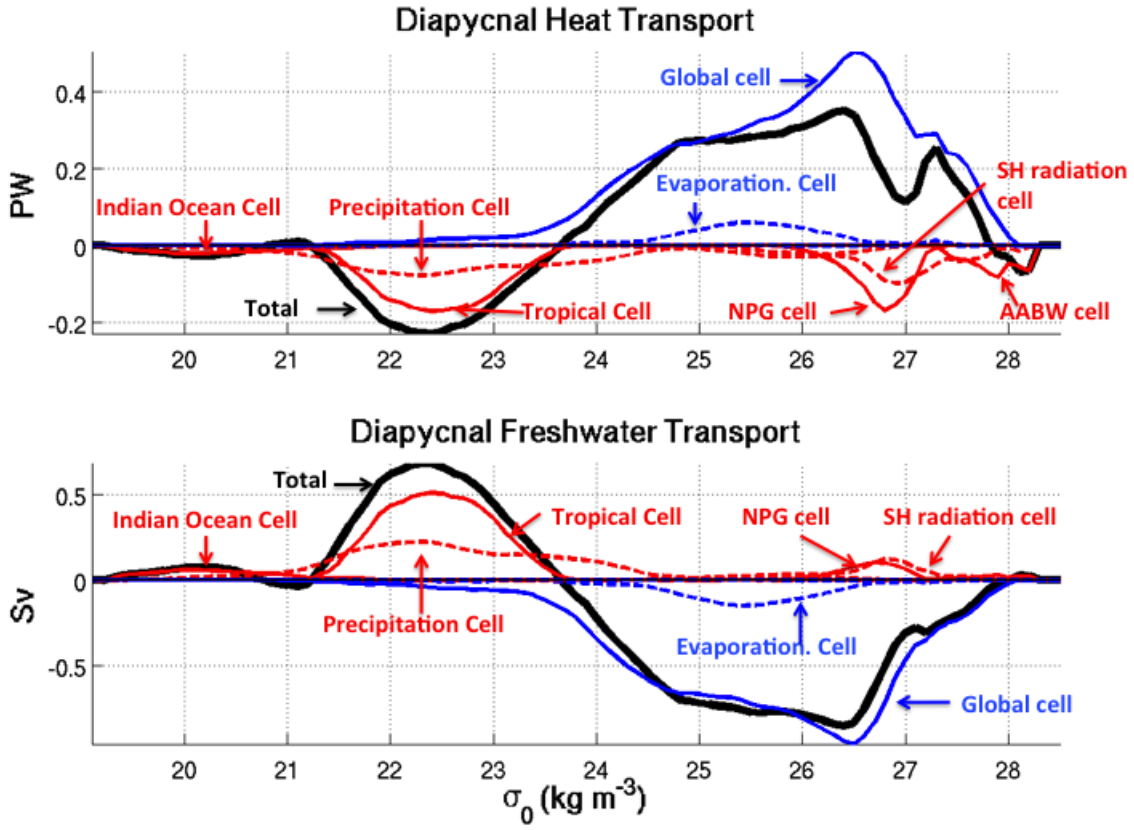

FIGURE 5.8: The diapycnal transport of heat (top, 1 PW = 10^{15} W) and freshwater (bottom, in Sv) through surface referenced potential density surfaces. Blue lines indicate transports by blue (clockwise rotating) cells and red lines indicate transport by yellow (counterclockwise) rotating cells. Dashed (solid) lines indicate transports due to cells of the local (advective) thermohaline streamfunction. The black line is the total transport. The text indicates the particular cells the transports are related to.

Only the global cell and the AABW cell are related to dynamics that allow for a direct freshwater and heat transport between the surface and the interior, other cells are related to dynamics that are more shallow (Zika et al., 2012, Döös et al., 2012, Groeskamp et al., 2014a). The global cell leads to the largest freshwater and heat transports (Table. 5.3 and Fig. 5.8). The cell redistributes 0.51 PW, taken from density classes associated with the upper 200 m (σ_0 = 22.0 - 26.5 kg m^{-3}, Fig. 5.7) to density classes associated with both surface and interior (σ_0 = 26.5 - 28.1 kg m^{-3}, Fig. 5.7). The global redistributes 0.97 Sv of freshwater in the opposite direction, leading to a net warming and salinification of the ocean interior. The AABW cell has a small freshwater transport signal, but transports 0.11 PW towards lighter densities, between density classes that can be related to both the surface and the interior (Table. 5.3, all between σ_0 = 27.4 - 28.2 kg m^{-3}, Fig. 5.7).

The tropical cell is the largest of the shallow cells and transports about 0.17 PW of heat over density classes related to the mixed layer (Table. 5.3, all between σ_0 = 21.0 - 23.8 kg m^{-3}, Fig. 5.7), hence it is a redistribution horizontally and within the upper 200 m of the ocean. The related freshwater transport of 0.5 Sv is in the opposite direction. The North Pacific gyre cell has a heat transport of 0.17 PW, but much smaller freshwater transport of 0.11 Sv. This cell redistributes the heat from density classes related to the northern branch of the circulation over those related to the southern branch of the circulation (Table. 5.3 and Fig. 5.6a). Hence, a southward heat transport and a northward freshwater transport is observed.

The Southern Hemisphere Radiative cell is a surface based cell leading to a net heat transport of 0.11 PW from the bottom of the mixed layer to the surface and a freshwater transport of 0.13 Sv in opposite direction. While the Precipitation and Evaporation cells have only small heat transports, they have a large freshwater transports of 0.23 Sv and 0.16 Sv, respectively. The precipitation cell transports freshwater from density classes most likely at the surface towards density classes most likely near the bottom of the mixed layer, while the Evaporation cells has the opposite effect. The NP Radiative cell and the Bay of Bengal cell have very small transports associated with their circulations.

Circulation Cell	**Heat** (PW)	**Freshwater** (Sv)	**Lowest σ_0-** range (kg m^{-3})	**Highest σ_0-** range (kg m^{-3})
Global Cell	0.51	0.97	22.0 - 26.5	26.5 - 28.1
Tropical Cell	0.17	0.51	21.0 - 22.4	22.4 - 23.8
NPG Cell	0.17	0.11	25.7 - 26.8	26.8 - 27.4
S. H. Radiative Cell	0.11	0.13	26.0 - 27.0	27.0 - 27.8
AABW Cell	0.10	0.04	27.4 - 27.8	27.8 - 28.2
Precipitation Cell	0.08	0.23	20.0 - 22.4	22.4 - 24.5
Evaporation Cell	0.07	0.16	24.0 - 25.5	25.5 - 26.8
N. P. Radiative Cell	0.03	0.03	σ_0 <26	26> σ_0
Bay of Bengal Cell	0.02	0.06	σ_0 <20	20> σ_0

TABLE 5.3: Freshwater and heat transport from one density class to another by the different circulation cells of the advective and local thermohaline streamfunction. Blue (red) cells transport heat from low (high) density to high (low) density. Blue (red) cells transport freshwater from high (low) density to low (high) density.

5.7.2 Dissipation of Turbulent Kinetic Energy

The THIM provides estimates of D that allow us to quantify the kinetic energy required for the observed small-scale mixing and may provide new insights on the pathways of energy in the ocean. Using the Osborn (1980) relationship between the isotropic diffusion of small-scale mixing processes and energy dissipation in combination with our inverse

estimate of D, we calculate the power used for small-scale mixing:

$$P(x, y, z, t) = \rho V \Gamma^{-1} N^2 D f_D(z), \tag{5.22}$$

where $\Gamma = 0.2$ is the mixing efficiency, N^2 is the Buoyancy frequency, ρ is *in-situ* density (calculated using IOC et al. (2010) software) and V is the volume. The global depth integrated distribution of P is dominated by the high values of N^2 near the surface, resulting in maximum dissipation near coasts and high dissipation at low latitudes (Fig. 5.9a). The total globally integrated energy used by small-scale mixing is 2.85 TW, of which only 0.36 TW (13%), 0.65 TW (23%) and 1.4 TW (49%) is dissipated via small-scale mixing processes below 2000 m, 1000 m and 500 m respectively (Fig. 5.9b). Hence 1.45 TW (51%) is dissipated in the upper 500 m only, which is consistent with the the idea that most of the mixing occurs near the surface (Wunsch and Ferrari, 2004). This result will be sensitive to our parameterisation used for small-scale mixing given by $Df_D(z)$ (Fig. 5.1b). The parameterisation used does not allow for separation of the different processes that lead to the small-scale mixing observed. However, the total 2.85 TW is comparable to the 3.5 TW of energy available from tides (Munk and Wunsch, 1998). The total energy conversion of 1.4 TW for depths greater than 500 m is in the same order as the available energy for mixing through the sum of the conversion of energy from the barotropic tide to internal tide ($O(1)$ TW Nycander (2005)) and that from the geostrophic flow into lee waves ($O(0.2)$ TW Nikurashin and Ferrari (2011)).

Using only surface freshwater and heat fluxes, we find that the mixing required to maintain the observed S_A and Θ distribution of the ocean, is of the same order as obtained through other methods. Separating the parameterisation used for small-scale mixing into different physical mechanism rather then the single vertical profile as used in this study (Fig. 5.1b), could lead to more insightful estimates of the required energy for the different small-scale mixing processes.

5.7.3 Uncertainty and improvements to the solution

Using the inverse solution we can calculate the divergence of volume for each grid in (S_A, Θ) coordinates, given by E^inv (Fig. 5.2b), similar to E^0 in Eq. (5.19) (Fig. 5.2a), but using the inverse estimate of the diffusion coefficients rather than the prior estimates. For a perfect solution volume is exactly conserved in each grid and $E^\mathrm{inv} = 0$. Note that the integral of E^inv over the whole domain is zero, as there is no net gain of volume, only a redistribution.

This imbalance quantified by $E^\mathrm{inv} \neq 0$ is most likely a result of limited spatial and temporal variability of the mixing parameterisations, imperfect representation of the

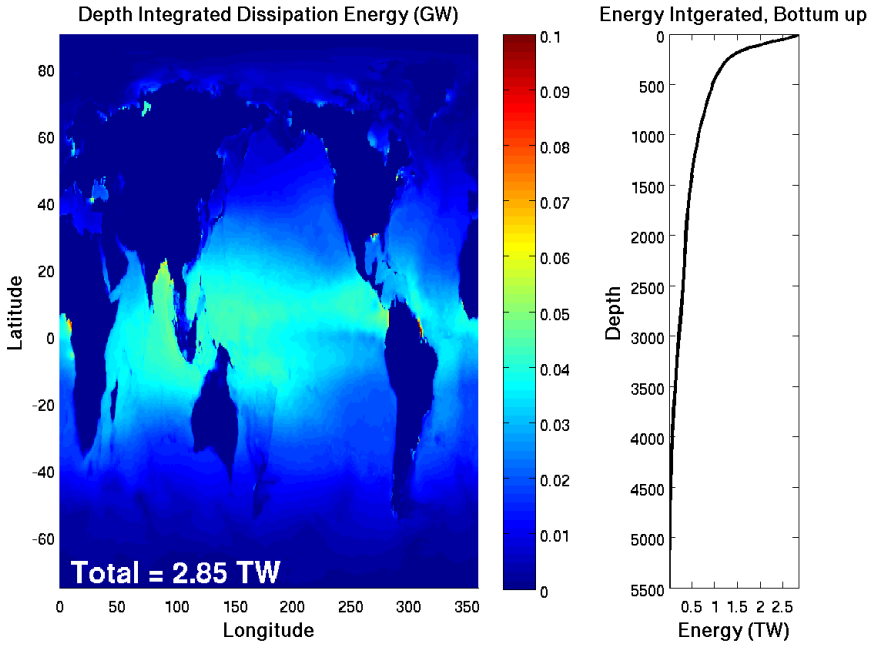

FIGURE 5.9: Panel (a) shows the depth integrated spatial distribution of required energy (1 GW = 10^9W) to sustain small-scale mixing. Panel (b) shows the bottom up, global integration of energy (1 TW = 10^{12}W) used by small-scale mixing processes.

surface fluxes (CORE2, especially large uncertainties associated with their values at high latitudes). Equivalently an imperfect representation of the ocean's hydrography (CARS) due to averaging processes, irregular spatial and temporal resolution of data and ignoring the unknown trend, will also result in errors on our estimate.

Improvements can be made by including solar penetration depth, which was pointed out by Iudicone et al. (2008) to be significant for the near-surface water-mass transformation rates, or by using geothermal heating which can locally be of importance for water-mass transformation rates. Also the lack of Brine rejection terms in the surface freshwater fluxes will reduce the accuracy of the solution, because their inclusion would influence water-mass transformation for dense water. Different prior choices of weighting also influences the solution.

The fact that E^{inv} is not random, reflects inaccuracies in the representation of physics in the model rather than random noise in the data. The missing physics is most likely due to our choice of the mixing parameterisation. The globally uniform vertical decay of the epineutral eddy diffusion is a simplification of the actual vertical decay structure of the epineutral diffusion, and we could have used a mixed layer depth parameterisation rather than a taper zone to completely separate horizontal from epineutral eddy diffusion. Also, the use of the Bryan and Lewis (1979) profile may lead to increased constraints on D through D being the only compensation of the surface fluxes near the surface (Fig. 5.4).

These constraints have an effect on the interior estimate of D, through the predetermined vertical shape of D and perhaps make D sensitive to the choice of the combination between the surface flux product and the climatology used. This could be one reason why our interior estimate of D is lower than that by Waterhouse et al. (2014), however their estimates may be biased toward a greater magnitude as most measurements in the deep ocean are obtained in areas with enhanced small-scale mixing. We anticipate that the constraints on the interior estimate of D can be improved using more complex parameterisation that can separate surface mixing from that by internal wave breaking in the deep ocean (Melet et al., 2012, Nikurashin and Ferrari, 2013). Including separation between the small-scale mixing above and below 2000 m depth may shed light on how small scale-mixing influences the global overturning circulation by transporting bottom water to the level where isopycnal upwelling plays a significant role (Toggweiler and Samuels, 1998, Sloyan and Rintoul, 2001, Talley, 2013, Ferrari, 2014).

5.7.4 Implications of the results

Models often use the same diffusion coefficient for the eddy induced quasi-Stokes advection (Gent and McWilliams, 1990, Gent et al., 1995, McDougall and McIntosh, 2001) and the Redi parameter for tracer diffusion (Redi, 1982). The Redi parameter for models generally varies by about a factor 5, between 400 $m^2\ s^{-1}$ and 2000 $m^2\ s^{-1}$ and can lead to a different prediction of the global temperature of 1^oC for climate simulation runs (Pradal and Gnanadesikan, 2014) or influence the stability of the overturning circulation (Sijp et al., 2006). The results presented here show a global Redi diffusivity that is about 50 times smaller than that typically used in numerical ocean models. This suggest that surface freshwater and heat fluxes under-estimate the production of isopycnal anomalies and/or that models should separate the quasi-Stokes parameterisation from the Redi parametrisation as the Redi diffusivity for passive tracers is overestimated and should be much smaller than the quasi-Stokes diffusivity. The THIM can be used to obtain constraints on the size of the eddy diffusion coefficients associate with a particular resolution of a model.

We find that K_H/K_I is larger for CARS than for LR-CARS (Table (5.2)), suggesting that more isopycnal eddies are resolved, rather than horizontal eddies, with increasing resolution. Perhaps suggesting that the isopycnal eddies are smaller. Previous inverse estimates by Zika et al. (2009) for the Southern Ocean have obtained a ratio K_H/D very similar to that of ours.

Most of the surface fluxes are balanced by small-scale mixing near the surface. Hence, the magnitude of small-scale mixing is of importance to determine the residual water-mass transformations that lead to $\Psi^{\mathrm{dia}}_{S_{\mathrm{A}}\Theta}$. This is especially the case for the water-mass transformation in the upper 200 m, where the globally integrated eddy diffusion is not significant. For other depths the horizontal and isopycnal eddy diffusion does lead to significant water-mass transformation rates, influencing the resulting cells of $\Psi^{\mathrm{dia}}_{S_{\mathrm{A}}\Theta}$. As small-scale mixing influences the transports represented by $\Psi^{\mathrm{dia}}_{S_{\mathrm{A}}\Theta}$, small-scale mixing must also influence the related diapycnal freshwater and heat transports. Hence the THIM may also be a useful tool to diagnose and compare the impact of different mixing parameterisations on global heat budgets.

Regardless of the uncertainties discussed above and the fact that we have not included any prior knowledge of the streamfunction structure (we remind the reader that $\mathbf{x}^{\mathbf{\Psi}}_{\mathbf{0}} = 0$) the THIM provides a robust estimate of $\Psi^{\mathrm{dia}}_{S_{\mathrm{A}}\Theta}$ that includes the existence of the Global, Tropical and AABW cell, that have also been observed in ocean models Zika et al. (2012), Döös et al. (2012), Hieronymus et al. (2014). The Global cell represents an observationally based quantification of the component of the globally interconnected ocean circulation induced by water-mass transformation, in one coordinate system. Historically this quantification was obtained combining knowledge of the volume transport of each water-mass derived from independent measurements and estimates of the ocean's tracer distribution and circulation (Stommel, 1958, Stommel and Arons, 1959, Gordon, 1986, Broecker, 1991, Schmitz, 1995, Ganachaud and Wunsch, 2000, Talley, 2013). Here it is obtained from measurements of air-sea fluxes and the ocean hydrography only, without the use of prior knowledge of inter-basin transports and connections.

$\Psi^{\mathrm{dia}}_{S_{\mathrm{A}}\Theta}$ has potentially revealed two new circulation cells, one related to the surface circulation in the bay of Bengal and one is related to the North Pacific (sub polar) gyre and the Bering Straight outflow. The AABW cell shows a larger spread in (S_{A}, Θ) coordinates than previously observed in models, which is not surprising as most models have trouble accurately representing AABW formation.

5.8 Conclusions

We have applied the THIM to an observational-based climatology in combination with surface flux products, resulting in observationally based estimates of horizontal and epineutral eddy diffusion coefficients K_{H} and K_{I}, respectively, the small-scale mixing coefficient D and the diathermohaline streamfunction $\Psi^{\mathrm{dia}}_{S_{\mathrm{A}}\Theta}$.

We used the estimate of $\Psi^{\mathrm{dia}}_{S_{\mathrm{A}}\Theta}$ to calculate $\Psi^{\mathrm{adv}}_{S_{\mathrm{A}}\Theta}$, which could previously only be calculated from numerical models as it required global, high resolution and full depth knowledge of the velocity field. $\Psi^{\mathrm{adv}}_{S_{\mathrm{A}}\Theta}$, 1) shows a robust tropical cell, 2) suggests the existence of two new cells related to a circulation in the Bay of Bengal and the North Pacific (sub-tropical) gyre, not previously identified by model-based calculations of $\Psi^{\mathrm{adv}}_{S_{\mathrm{A}}\Theta}$, 3) shows a wider spread of the AABW cell compared to model based versions and 4) reveals a globally interconnected ocean circulation.

Most of the water-mass transformation occurs at the surface of the ocean and is balanced by small-scale mixing. This suggest that changes in the small-scale mixing parameterisations applied in ocean models will influence the solution of $\Psi^{\mathrm{dia}}_{S_{\mathrm{A}}\Theta}$ and the associated diapycnal freshwater and heat transports between different density classes. The particular set-up of the THIM results in very strong constraints on D, enabling the method to estimate very small values of $D = 6.52 \pm 0.04$ x 10^{-5} m^2 s^{-1}, which previous inverse solution (box-inverse models) could not reliably estimate (Zika et al., 2010a). The obtained results for D are in line with other observations, especially for the upper 1000 m. Standard relationships between D, the stratification and energy dissipation show that 2.85 TW of energy is used for small-scale mixing, of which 1.4 TW is used in the upper 500 m of the ocean and 0.36 TW is used below 2000 m. Hence most mixing occurs near the surface, but small-scale mixing is important below 2000 m depth, to close the global ocean circulation. When applying different parameterisations for the vertical structures of D, one can attempt a separation of the energy by internal wave or background mixing.

The horizontal and isopycnal eddy diffusion coefficients are both strongly constrained. The isopycnal diffusion coefficient is about a factor 50 lower than those generally used in models, suggesting that the surface fluxes do not accurately represent epineutral anomalies of S_{A} and Θ and/or that models should separate the advective tracer transports through the quasi-Stokes (GM) parameterisation, from the diffusive tracer transport through the Redi parameterisation and that the latter should be much smaller than the quasi-Stokes parameterisation. Globally, the water-mass transformation due to lateral eddy diffusion is small compared to that by small-scale diffusion, however they can locally be very important.

Chapter 6

Conclusions

The work presented in this thesis provides a better understanding of the relationship between freshwater and heat fluxes due to surface fluxes and mixing, and the resulting changes in the ocean circulation and distribution of water-masses. To achieve this we first provided an improved understanding of the geometry of interior ocean mixing (Chapter 2) and used this in the development of a new diagnostic that defined circulation in tracer-tracer coordinates (Chapter 3). This diagnostic is then applied to Absolute Salinity (S_A) and Conservative Temperature (Θ) coordinates to study the relation between salt and heat fluxes that lead to water-mass transformation, and circulation in (S_A, Θ) coordinates expressed as the diathermohaline streamfunction $\Psi^{\mathrm{dia}}_{S_\mathrm{A}\Theta}$. The resulting formalism is then further developed into an inverse method that estimates diffusion coefficients and $\Psi^{\mathrm{dia}}_{S_\mathrm{A}\Theta}$, using only an ocean hydrography and surface freshwater and heat fluxes (Chapter 4). This method is tested against a model and proves to be skilful in providing well constrained estimates of the unknown diffusion coefficients and $\Psi^{\mathrm{dia}}_{S_\mathrm{A}\Theta}$. As a result the method is applied to an observational-based gridded hydrography and surface fluxes to obtain well constrained estimates of diffusion coefficient and $\Psi^{\mathrm{dia}}_{S_\mathrm{A}\Theta}$ from observations (Chapter 5). The results provide an improved understanding of the water-mass transformation component of the global ocean circulation and the spatial and temporal varying magnitude of mixing parameterised through diffusion coefficients. This application of the THIM to a model and an observational-based climatology provides a diagnostic to compare the circulation and mixing in models with that obtained from observations. The methods developed in this thesis are only the beginning and have a lot of potential for further development that allows for better understanding and estimates of both diffusion coefficients and $\Psi^{\mathrm{dia}}_{S_\mathrm{A}\Theta}$. In the remainder of this section we will discuss some of the insights obtained from this thesis and potential for future work.

6.1 Interior ocean mixing

The method developed to analyse circulation in tracer-tracer coordinates is applied in (S_A, Θ) coordinates, because these are the ideal coordinates to analyse water-mass transformation and mixing, which are key components of the ocean circulation. To implement mixing in this formalism a careful re-evaluation of the parameterisation and geometry of interior ocean mixing was performed and lead to the understanding described in Chapter 2. It was found that under the small-slope approximation there is a small gradient of tracer in a direction in which there is no actual epineutral gradient of tracer. The difference between the correct epineutral tracer gradient and the small-slope approximation to it, is explained geometrically and points in the direction of the thermal wind. The fraction of the epineutral flux in this direction is very small and is negligible for all foreseeable applications. As the small-slope approximation to the epineutral diffusion tensor Redi (1982), Gent and McWilliams (1990) is used in many ocean models, this requires rectification. Also a clarification was added that explains that small-scale mixing processes act to diffuse tracers isotropically (i.e. directionally uniformly in space), hence not dianeutral or vertical as often used in ocean models. Both realisations affect the diffusion tensor that is used in ocean models and in the study presented in this thesis.

6.2 Circulation in tracer-tracer coordinates

The formalism developed in Chapter 3 allows the analyses of the non-divergent component of ocean circulation in tracer-tracer coordinates, by calculating transport through surfaces of constant tracers. The transport is calculated taking into account, 1) the advective component related to geographical displacements in the direction normal to tracer iso-surfaces, quantified by an advective streamfunction, and 2) a local component, related to local changes in tracer-values, without a geographical displacement, quantified by a local (temporal) streamfunction. The sum of both provides the transport through tracer surfaces and is quantified by the dia-streamfunction. Note that, the local streamfunction only exists when both coordinates are not constant in space and time.

The application of the formalism to (S_A, Θ) coordinates resulted in the diathermohaline streamfunction $\Psi^{dia}_{S_A\Theta}$, being the sum of the advective thermohaline streamfunction $\Psi^{adv}_{S_A\Theta}$ (as previously defined by Zika et al. (2012) and Döös et al. (2012)) and the local thermohaline streamfunction $\Psi^{loc}_{S_A\Theta}$. The $\Psi^{loc}_{S_A\Theta}$ is calculated using only an ocean hydrography and allows for direct comparison between models and observations. We have related the circulations shown in the local streamfunction to the dynamics of the seasonal cycles of freshwater and heat fluxes such as summer/winter warming/cooling, the Inter-Tropical

Convergence Zone (ITCZ) and cryosphere processes. We show that only $\Psi^{\rm dia}_{S_{\rm A}\Theta}$ can be directly related to freshwater and heat fluxes and that its decomposition into the advective and local component provides an understanding of the observed circulation cells. The formalism developed in Chapter 3 provides a powerful tool to analyse the impact of the different mixing parameterisations and surface fluxes products used in numerical models and on the ocean circulation and the climate. This allows for comparison amongst numerical ocean models and observational-based gridded climatologies.

6.3 Water-mass transformations from observations

Although $\Psi^{\rm loc}_{S_{\rm A}\Theta}$ can be calculated using model output and an ocean hydrography, $\Psi^{\rm adv}_{S_{\rm A}\Theta}$ can only be calculated using models as it requires global knowledge of the 3-dimensional velocity field ($\mathbf{u}$). Hence the formalism developed in Chapter 3 requires a model to calculate $\Psi^{\rm dia}_{S_{\rm A}\Theta}$.

In Chapter 4 we developed an inverse method that allows us to estimate $\Psi^{\rm dia}_{S_{\rm A}\Theta}$ from observations and obtains well constrained estimates of the diffusion coefficients. These estimates are obtained by exploiting the balance between diathermohaline circulation and water-mass transformation. The latter is caused by surface freshwater and heat fluxes and mixing parameterised as diffusion coefficients operating on tracer gradients. The spatial and temporal variability of diffusion is represented by structure functions that premultiply tracer gradients with a factor that corresponds to the relative role of mixing for that particular time and space. This reduces the number of unknown diffusion coefficients that need to be estimated, while maintaining the freedom to estimate the spatial and temporal variability of the magnitude of mixing in the ocean. As the tracer gradients and the surface fluxes can be obtained from a hydrography and surface flux products, respectively, we obtain a balance between observational based values and the unknown diffusion coefficients and circulation in $(S_{\rm A}, \Theta)$ coordinates (represented by $\Psi^{\rm dia}_{S_{\rm A}\Theta}$). The resulting system of equations is solved using an inverse technique and tested against a numerical model. This showed that the THIM provides accurate estimates of the unknowns ($\Psi^{\rm dia}_{S_{\rm A}\Theta}$, and the epineutral and small-scale diffusion coefficients).

Encouraged by the results of Chapter 4, in Chapter 5 we apply the THIM to observations and obtain well constrained estimates of the epineutral and small-scale diffusion coefficients and $\Psi^{\rm dia}_{S_{\rm A}\Theta}$. Note that $\Psi^{\rm adv}_{S_{\rm A}\Theta}$ can now be calculated as the difference between $\Psi^{\rm dia}_{S_{\rm A}\Theta}$ and $\Psi^{\rm loc}_{S_{\rm A}\Theta}$. This provided the first observational based streamfunctions in $S_{\rm A}, \Theta)$ coordinates that can be used for comparison with numerical ocean model based streamfunctions. Through the decomposition into the advective and local thermohaline streamfunction and the driving water-mass transformation rates due to either surface

or diffusive fluxes, the observed circulation cells in $\Psi^{\text{dia}}_{S_\text{A}\Theta}$ can be explained. We now list some key points from the application of the THIM to observations.

- Most of the water-mass transformation occurs at the surface of the ocean and is balanced by small-scale mixing. This suggests that changes in the small-scale mixing parameterisations will influence the solution of $\Psi^{\text{dia}}_{S_\text{A}\Theta}$ and the associated volume transport and diapycnal freshwater and heat transports.

- The resulting $\Psi^{\text{dia}}_{S_\text{A}\Theta}$ shows both previously identified and unidentified circulations. Two new cells are found and are most likely related to a circulation in the Bay of Bengal and the North Pacific (sub-tropical) gyre.

- Previously identified cells that are also found are the Tropical cell, Global cell and Antarctic Bottom Water Cell. The AABW cell shows a wider spread compared to model based versions, which can most likely be explained by a combination of incorrect parameterisation of AABW formation in models and high uncertainties in the used measurements at high latitudes. The Global cell shows a globally interconnected ocean circulation, which is a quantification of the water-mass transformation based component of the global conveyor belt.

- The THIM is able to obtain well constrained estimates of small-scale diffusion coefficient $D = 6.52 \pm 0.04$ x 10^{-5} m^2 s^{-1}. This has been proven difficult in previous inverse studies. Our global estimate of D is lower than most studies, mainly because our estimate of D for depths greater than 1000 m is lower than observational based estimates of Waterhouse et al. (2014), while very similar for the upper 1000m. This may be due to 1) most observation of D in the interior are in areas of enhanced mixing, perhaps biasing the estimate of Waterhouse et al. (2014), and 2) our estimate of D may be too constrained in the interior through the use of a structure function, or 3) the dense water formation is too weakly represented by the surface fluxes due to for example the lack of brine rejection.

- A total of 2.85 TW of energy is used for small-scale mixing, of which 1.4 TW is used in the upper 500 m and 0.36 TW is used below 2000 m. Hence, most mixing occurs near the surface, but a significant proportion of small-scale mixing is used below 2000 m depth, closing the global ocean circulation.

- The isopycnal diffusion coefficient is about a factor 50 lower than those typically used in models, suggesting that the surface fluxes used do not accurately represent epineutral anomalies of S_A and Θ and/or that models should separate the advective tracer transports through the quasi-Stokes parameterisation from the diffusive tracer transport through the Redi parameterisation, and that the latter

should be much smaller than the quasi-Stokes parameterisation. Globally, the water-mass transformation due to lateral eddy diffusion is small compared to that by small-scale diffusion, however they can locally be very important.

- Estimates of diapycnal freshwater and heat transports of the different circulation cells are provided. For example the global cell is the largest transporter of both freshwater (about 1 Sv) and heat (about 0.5 PW) from depths shallower than about 300 m, to depths potentially greater than 2000 m. In future work such analyses may provide a more detailed analyses of the freshwater and heat transport pathways and storage in the ocean.

6.4 Implications and future work

The results obtained so far shed light on the spatial and temporal variability of water-mass transformation and its influence on the ocean circulation. In future work the sensitivity of the results to the choice of column and row weighting, the mixing structures functions used and the surface flux products and climatologies need to be better understood. The estimates can also be improved by including solar penetration depth (Iudicone et al., 2008), geothermal heating and cryosphere processes such as ice melt and brine rejection as these are all expected to be significant and provide further constraints on the solution.

The use of different structure functions and the magnitudes of the related diffusion coefficients is important to enable improvement to mixing parameterisations in numerical ocean models. For example, if the smallness of the epineutral diffusion coefficient as found in Chapter 5 holds, this should be implemented in numerical ocean models. The THIM is a tool that can provide observational based constraints on magnitudes of diffusion coefficients used to multiply different structure functions for models with different resolutions.

In future work, the THIM can be combined with other existing inverse models, especially with the Tracer-Contour Inverse Method (TCIM, Zika et al. (2010a). The TCIM includes the useful aspects of the box-inverse model (Wunsch, 1978), beta-spiral model (Stommel and Schott, 1977) and the Bernoulli inverse method (Killworth, 1986) and allows estimates of both circulation in geographical space and diffusion coefficients. The combination of the THIM and TCIM may provide further constraints on the diffusion coefficients, especially for the ocean interior, and improved estimates of both the geographical circulation and diathermohaline circulation.

An important future application of the tools developed in this thesis is to generalise the tracer-tracer circulation and inverse techniques to tracers other than temperature and salinity. Groeskamp et al. (2015) has provided the first such steps for oceanography by applying the formalism to anthropogenic carbon (C_{A}) and potential density anomaly (σ_0) coordinates. The resulting dia-, advective- and local carbon-density streamfunction shows a circulation that leads to both subduction and re-ventilation of anthropogenic carbon and provides insight in the related mechanism leading to the role of the ocean in the global carbon budget. In the future an inverse application may provide insights to what extent these processes occur in the real ocean.

The method developed in Chapter 3 has also been applied to the atmosphere to obtain the hydrothermal streamfunction in dry static energy and latent heat coordinates (Kjellsson et al., 2013). As latent heat in the atmosphere can be related to salinity in the ocean through evaporation, future work should include the exploration of a coupling between the hydrothermal streamfunction and the diathermohaline streamfunction, to obtain a global 'climate' streamfunction that allows a thermodynamic analyses of both the ocean and atmosphere simultaneously (Kjellsson, 2014).

This thesis provides tools to improve our understanding of the component of the ocean circulation due to water-mass transformation, resulting from surface and diffusive fluxes of freshwater and heat. Water-mass transformations have a large impact on the climate by altering the ocean circulation and the related transport, redistribution and storage of tracers such as heat, freshwater and carbon. Hence, a better understanding of water-mass transformations and its effect on the climate, are essential for our ability to model future climates. The tools developed in this thesis isolate the effect of water-mass transformation on the ocean circulation and allow for a careful analyses of all contributing factors. Thus the techniques and applications developed in this thesis provide tools that are ideal to improve the understanding of the impact of water-mass transformation on ocean circulation and climate. Future work should aim to improve the tools and insights presented in this thesis and its application to ocean modelling, ideally resulting in a convergence between results obtained from observation-based and model calculation of the same variables, improving our ability to accurately model the climate.

Acknowledgements

The acknowledgements is most likely the most read part of any PhD thesis. I will exploit this to thank some people.

PhD research for me is a job that provides me with the opportunity to understand if I'm suited to be a scientist. It also allows me to build my basic scientific knowledge and how to implement this into the scientific community. How well this goes is to a certain extent a result of your supervision. The supervision I have experienced during this PhD thesis has been fantastic. I could not have imagined working with a better team.

First Young Trevor, science is not your work, science is your life and you seem to enjoy nothing more than doing science. This is a huge inspiration and has lead to a fantastic collaboration that includes unique moments in which we have been able to share the development of new ideas and new understanding of the world (often using the whiteboard in your office). Your always positive attitude and compliments have made me become a confident young scientist and will influence the rest of my life. Not to forget your relaxed attitude, introducing me to many fellow colleagues, and always quick responses. Trevor, thank you for guiding me in this Journey.

Bernadette, you provide solid ground. If I get lost in theory and mathematics, you are always able to bring me back to reality. This has been an incredibly valuable learning curve for me. Also your efficiency and approach to science will become part of how I will approach science in the future. Your personal and scientific guidance have been of great value, providing the perfect leverage for the guidance that Trevor provides. Also thank you for protecting me from many bureaucratic distractions. Bernadette, thank you for guiding me in this Journey.

If Trevor is now my academic father, and Bernadette is my academic mother, then Jan Zika is most definitely my (big) academic brother. Thank you for having shared with me many of your ideas that have formed the core of this PhD thesis. You are an example for young scientists and I value both our scientific and personal relationship that we have developed during the past 3.5 years. Jan, thank you for being my big brother.

I would also like to thank Nathan Bindoff for scientific discussion and for solving many practical bureaucratic problems that have made my life as a PhD student many times easier.

Simon Wotherspoon is an awesome QMS coordinator and has made my life and that of many other QMS students as easy as possible by sheltering us from as many bureaucratic distractions as possible.

I thank Leo Maas, even though you may not have been my supervisor during my PhD Thesis, but through my Master thesis you provided me with some basic capabilities which have had an enormous contribution to my life as a scientist. I'm also happy that you have always provided a place to work at the NIOZ institute during my visits to the Netherlands, where we have had animated discussion that have benefited the work presented in this thesis.

Of course I also thank my other co-authors Frédéric Laliberté, Peter McIntosh and Stephen Griffies for being a part of my thesis and for what I have learned from them. Also Andrew Lenton, Richard Matear and Clothilde Langlais for their collaboration on work that sprouted from this thesis.

Andrew Meijers is thanked for his help in the first half a year here in Tasmania, both a personal and scientific level. Including the introduction to Tricycle coffee, which I have kept drinking until the very end of my time in Tassie.

Martin Marzloff, thank you for the many runs that we shared that have made me so much more productive.

I thank Paul Barker and Ken Ridgeway for both scientific discussion and help as well as creating a fun work environment in the office.

Also I thank Willem Sijp for providing the UVIC model output and associated discussion. I thank Terry O'Kane for his computer power. I thank Kristoffer Doos, Jonas Nycander, Johan Nillson Daniele Iudicone, Gurvan Madec, Simon Josey, Angelique Melet, Max Nikurashin, Andreas Klocker for valuable discussions on this work. I would also like to thank Walter Munk, for the dinners and meetings that we have shared in Sydney and Hobart; these have been an amazing inspiration for a young scientist.

Doing PhD research effects me on a scientific and personal level. Hence there are people that are not in the scientific world that I would like to thank, because without them, this would have been impossible. I would like to thank my parents and Malou. Malou who is my perfect balance and is always there for me. Your faith in me and encouragements to do what I do, have been essential for this thesis. Thank you for sharing our lives and in the last 4 years, the great adventure in Tasmania. My parents, who might not have a clue what I'm doing (scientifically), they are always there for me, and believe in me no matter what.

Appendix A

The slope of the neutral tangent plane

Here we first prove that even though the two-dimensional gradients $-\mathbf{k} \times (\mathbf{k} \times \nabla_N C)$ and $\nabla_n C$ point in different directions, that the projected gradients of Absolute Salinity and Conservative Temperature, $\nabla_n S_\mathrm{A}$ and $\nabla_n \Theta$, are parallel and that the neutrality condition $\beta \nabla_n S_\mathrm{A} = \alpha \nabla_n \Theta$ applies to the projected gradients in the neutral tangent plane.

The neutral tangent plane, as discussed in sections 2.1 and 2.2, has the property that the gradients of Absolute Salinity and Conservative temperature in this plane cause equal and opposite contributions to the gradient of locally-referenced potential density, that is,

$$\alpha \nabla_N \Theta = \beta \nabla_N S_\mathrm{A} \tag{A.1}$$

This balancing of the gradients of S_A and Θ through β and α is called the 'neutrality condition' and Eq. (2.8) and Eq. (A.1) show that this neutrality condition applies to the three-dimensional gradients $\nabla_N S_\mathrm{A}$ and $\nabla_N \Theta$. Using Eqn. (2.15) we can express $\nabla_N S_\mathrm{A}$ and $\nabla_N \Theta$ in terms of the corresponding gradients $\nabla_n S_\mathrm{A}$ and $\nabla_n \Theta$ in the projected non-orthogonal coordinate system, and we form the linear combination $\alpha \nabla_N \Theta - \beta \nabla_N S_\mathrm{A}$, which we know to be zero

$$\alpha \nabla_N \Theta - \beta \nabla_N S_\mathrm{A} = \mathbf{e} + \frac{(\mathbf{e} \cdot \nabla_n z)}{(1 + S^2)} \mathbf{m} = 0, \tag{A.2}$$

where we have used the shorthand notation $\mathbf{e} = \alpha \nabla_n \Theta - \beta \nabla_n S_\mathrm{A}$. This vector Eq. (A.2) can only be satisfied if both $\mathbf{e} \cdot \nabla_n z = 0$ and $\mathbf{e} = 0$, which reduces to the requirement

that $\mathbf{e} = 0$. Hence, we have found that the neutrality condition Eq. (A.1) implies that

$$\alpha \nabla_n \Theta = \beta \nabla_n S_A \quad \text{and hence that} \quad \nabla_n \Theta \| \nabla_n S_A, \tag{A.3}$$

a result previously found by Griffies and Greatbatch (2012). That is, even though the two-dimensional gradients $\nabla_n \Theta$ and $-\mathbf{k} \times (\mathbf{k} \times \nabla_N \Theta)$ are neither equal nor parallel (and the same comment applies to the corresponding gradients of Absolute Salinity), the projected two-dimensional epineutral gradients $\nabla_n \Theta$ and $\nabla_n S_A$ are parallel and they obey the neutrality condition $\alpha \nabla_n \Theta = \beta \nabla_n S_A$, just as their three-dimensional cousins $\nabla_N \Theta$ and $\nabla_N S_A$ also obey the neutrality condition $\alpha \nabla_N \Theta = \beta \nabla_N S_A$.

Now we find the expression for the slope of the neutral tangent plane $\nabla_n z$, with our discussion complementing that found in Section 6.5 of Griffies (2004). The projected non-orthogonal gradient of a scalar C in a neutral tangent plane is related to that at constant height by Eq. (2.10), namely $\nabla_n C = \nabla_z C + C_z \nabla_n z$, where C_z is the exactly vertical gradient at constant longitude and latitude and all of $\nabla_n C$, $\nabla_z C$ and $\nabla_n z$ are exactly two-dimensional gradients. Applying this equation to Absolute Salinity and Conservative Temperature, and taking the linear combination with the thermal expansion coefficient and the saline contraction coefficient gives

$$\alpha \nabla_n \Theta - \beta \nabla_n S_A = \alpha \nabla_z \Theta - \beta \nabla_z S_A + \nabla_n z \, (\alpha \Theta_z - \beta S_{A_z}) \,, \tag{A.4}$$

and from Eq. (A.3) we know that the left-hand side of this equation is zero so the slope of the neutral tangent plane is (where N is the buoyancy frequency)

$$\nabla_n z = (s_x, s_y) = -\frac{(\alpha \nabla_z \Theta - \beta \nabla_z S_A)}{(\alpha \Theta_z - \beta S_{A_z})} = -\frac{g}{N^2} \, (\alpha \nabla_z \Theta - \beta \nabla_z S_A) \,. \tag{A.5}$$

This equation serves to define the x and y components s_x and s_y of the vector slope $\nabla_n z$. For later use we use the shorthand notation s^2 for the inner product $\nabla_n z \cdot \nabla_n z$.

It can also be shown that the two-dimensional projected gradient of pressure P in the neutral tangent plane can be expressed as

$$\nabla_n P = -\frac{(\alpha \nabla_P \Theta - \beta \nabla_P S_A)}{(\alpha \Theta_P - \beta S_{A_P})} \tag{A.6}$$

Appendix B

Calculating $\Psi^{\mathrm{dia}}_{S_\mathrm{A}\Theta}$ from models or observations

B.1 Calculating $\Psi^{\mathrm{dia}}_{S_\mathrm{A}\Theta}$ from models or observations

In this appendix we will explain the technical details how to calculate the thermohaline volume transports and related streamfunctions, using ocean hydrographic data of a model and observational-based product as described in Section 5.6.

B.1.1 Discretization Processes

We calculate $\Psi^{\mathrm{dia}}_{S_\mathrm{A}\Theta}$ as a sum of $\Psi^{\mathrm{adv}}_{S_\mathrm{A}\Theta}$ and $\Psi^{\mathrm{loc}}_{S_\mathrm{A}\Theta}$. The streamfunctions are defined on discrete (S_A, Θ) intervals. The (S_A, Θ) values at (x_i, y_j, z_k, t_n). Here we have $i = 1 - I$, $j = 1 - J$, $k = 1 - K$ and $n = 1 - N$, were I, J and K indicate the number of grid points in the east, north and downward direction, respectively, and N is the number of time steps. Around each (x_i, y_j, z_k, t_n) one can define 6 interfaces between adjacent tracer locations, which together, enclose a volume $\Delta V_{i,j,k}$. We omit the n-index as $\Delta V_{i,j,k}$ does not change in time, as the data is on a fixed geographical grid. At grid-point (x_i, y_j, z_k, t_n), we have a $S_\mathrm{A}^{i,j,k,n}$ and $\Theta_{i,j,k,n}$ value, located at the centre of $\Delta V_{i,j,k}$.

In addition to the geographical-discretization there is also a discretisation in (S_A, Θ) coordinates. Consider volume ΔV, bounded by a pair of isotherms that are separated by $2d\Theta$ and a pair of isohalines which are separated by $2dS_\mathrm{A}$. The volume's Θ ranges between $\Theta \pm d\Theta$ and S_A ranges between $S_\mathrm{A} \pm dS_\mathrm{A}$. While ΔV may have any shape in Cartesian-coordinates, it covers a square grid in (S_A, Θ) coordinates (Fig. 3.2).

A position in $(S_{\rm A}, \Theta)$ coordinates is given by $(S_{\rm A}^m, \Theta^p)$. Here $m = 1 - M$ and $p = 1 - P$ and M and P indicates the number of grid points in respectively the S_A and Θ-direction. We find the isotherms to be at $\Theta^p \pm d\Theta$ and the isohalines to be at $S_{\rm A}^m \pm dS_{\rm A}$. We argue that $d\Theta$ and $dS_{\rm A}$ must be small enough to distinguish between different water masses in the ocean's interior and large enough to contain a significant amount of the ocean volume in a grid. For the circulation to be described by an equal resolution in both $(S_{\rm A}, \Theta)$ coordinates directions, we adjust the ratio between $d\Theta$ and $dS_{\rm A}$ to be about $dS_{\rm A} = 0.05$ g kg^{-1} and $d\Theta = 0.75$ ^{o}C.

B.1.2 Calculating $\Delta\Psi^{\rm loc}_{S_{\rm A}\Theta}$ from ocean hydrography products.

Here we provide the practical method to calculate $\Delta\Psi^{\rm loc}_{S_{\rm A}\Theta}$, which is used to calculate $\Psi^{\rm loc}_{S_{\rm A}\Theta}$. Let us define $\overline{\mathbf{U}}^{\rm iso}_{S_{\rm A}\Theta} = \left(\overline{U}^{\rm iso}_{|_{S_{\rm A}}}, \overline{U}^{\rm iso}_{|_\Theta}\right)$ as the time-averaged (denoted by the overbar) thermohaline volume transport vector due to movement of isohalines and isotherms, where $\overline{U}^{\rm iso}_{|_{S_{\rm A}}}(S_{\rm A}, \Theta \pm d\Theta)$ is the time-averaged volume transport in the positive $S_{\rm A}$-direction through the area of the surface of constant $S_{\rm A}$, which has a Θ-range between $\Theta \pm d\Theta$, due to the movement of isohalines induced by local changes of $S_{\rm A}$ and Θ, and is given by,

$$\overline{U}^{\rm iso}_{|_{S_{\rm A}}}(S_{\rm A}, \Theta \pm d\Theta) = \frac{1}{\Delta t}\int_t^{t+\Delta t}\int_{\Theta\pm d\Theta|_{S_{\rm A}}} -u^{\rm iso}_{S_{\rm A}}\, dA dt. \tag{B.1}$$

Here $\int_{\Theta\pm d\Theta|_{S_{\rm A}}} dA$ integrates over the area that has a constant salinity of $S_{\rm A}$ and Θ range of $\Theta \pm d\Theta$. Equivalently, $\overline{U}^{\rm iso}_{|_\Theta}(S_{\rm A} \pm dS_{\rm A}, \Theta)$ is the time-averaged volume transport in the positive Θ-direction through the area of the surface of constant Θ, which has a $S_{\rm A}$-range between $S_{\rm A} \pm dS_{\rm A}$, due to the movement of isotherms, and is given by,

$$\overline{U}^{\rm iso}_{|_\Theta}(S_{\rm A} \pm dS_{\rm A}, \Theta) = -\frac{1}{\Delta t}\int_t^{t+\Delta t}\int_{S_{\rm A}\pm dS_{\rm A}|_\Theta} -u^{\rm iso}_{\Theta}\, dA dt. \tag{B.2}$$

Let it be clear that the size of $\overline{\mathbf{U}}^{\rm iso}_{S_{\rm A}\Theta}$ depends on the gridsizes $dS_{\rm A}$ and $d\Theta$ and is not a thermohaline streamfunction difference, because $\mathbf{u}^{\rm iso}_{S_{\rm A}\Theta}$ may include a trend. To calculate $\overline{\mathbf{U}}^{\rm iso}_{S_{\rm A}\Theta}$ from the hydrography, we use that, when isohalines and isotherms move in space and time, they change the distribution of the ocean's volume in $(S_{\rm A}, \Theta)$ coordinates. Therefore to calculate $\overline{\mathbf{U}}^{\rm iso}_{S_{\rm A}\Theta}$, we will address the change of the ocean's volume in $(S_{\rm A}, \Theta)$ coordinates in time.

In summary one tracks the path of $\Delta V_{i,j,k}$ in time, in $(S_{\rm A}, \Theta)$ coordinates and assigns the related volume transport to the crossed isotherms (isohalines) in-between the associated $S_{\rm A}$ (Θ) range. Repeating this for each time step, for all the defined volumes in the ocean and taking the time average of all contributions to obtain $\overline{\mathbf{U}}^{\rm iso}_{S_{\rm A}\Theta}$. One needs only the

time series of volumes $(S_{\rm A}, \Theta)$ values, such that an ocean hydrography is sufficient to calculate $\overline{\mathbf{U}}^{\rm iso}_{S_{\rm A}\Theta}$, applying the following steps:

1. Consider $\Delta V_{i,j,k}$ and the associated $S_{\rm A}^{i,j,k,n}$ and $\Theta_{i,j,k,n}$, at (x_i, y_j, z_k, t_n).

2. Then consider $\Delta V_{i,j,k}$ and the associated $S_{\rm A}^{i,j,k,n+1}$ and $\Theta_{i,j,k,n+1}$, at (x_i, y_j, z_k, t_{n+1}). Hence, it is the same volume at the same position, but analysing the tracer values at the next time step, i.e., $t = t_{n+1}$ rather then $t = t_n$.

3. If $S_{\rm A}^{i,j,k,n} \neq S_{\rm A}^{i,j,k,n+1}$ and/or $\Theta_{i,j,k,n} \neq \Theta_{i,j,k,n+1}$, *and* as a result of this change, $\Delta V_{i,j,k}$ has moved to a different $(S_{\rm A}, \Theta)$ grid, than there will be motion of $\Delta V_{i,j,k}$ in $(S_{\rm A}, \Theta)$ coordinates, in time. The associated volume transport can be calculated as: $U^{\rm iso}_{i,j,k,n} = \Delta V_{i,j,k}/\Delta t$ with $\Delta t = (t_{n+1} - t_n)$. If the change in $S_{\rm A}$ and/or Θ is not sufficiently large to move the $(S_{\rm A}, \Theta)$ value to the next grid, then this change does not contribute to the volume flux across isotherms or isohalines. With very small values for $dS_{\rm A}$ and $d\Theta$ (i.e., a high resolution), this becomes less important.

4. The volume transport $U^{\rm iso}_{i,j,k,n}$, associated with the displacement of $\Delta V_{i,j,k}$ in $(S_{\rm A}, \Theta)$ coordinates in time, has to be assigned to the correct $S_{\rm A}$-interval of the isotherms that $\Delta V_{i,j,k}$ has crossed and to the correct Θ-interval of the isohalines that $\Delta V_{i,j,k}$ has crossed. We find these intervals by applying the shortest-route method. This method uses a straight line in $(S_{\rm A}, \Theta)$ coordinates, between the grid that $\Delta V_{i,j,k}$ occupies at $t = t_n$, and the grid that $\Delta V_{i,j,k}$ occupies at $t = t_{n+1}$ (Fig. B.1). The volume transport $U^{\rm iso}_{i,j,k,n}$, is then assigned to the Θ-interval ($S_{\rm A}$-interval) on the isohalines (isotherms) that are crossed by this straight line, which is the shortest route in $(S_{\rm A}, \Theta)$ coordinates. In case of only warming this is a vertical line, crossing only isotherms. In case of salinification this is a horizontal line, crossing isohalines only. When there is a change in both $S_{\rm A}$ and Θ, there will be a volume transport across both isohalines and isotherms. It should be clear that the motion of one $\Delta V_{i,j,k}$ in $(S_{\rm A}, \Theta)$ coordinates at a succession of times, can cause a transport assigned to multiple intervals on isohalines and isotherms.

5. For volume $\Delta V_{i,j,k}$ we repeat this for $n = 1 : N$ time steps and we will then take the time average of all contributions. This will also be applied to all volumes in space, such that we obtain

$$\overline{\mathbf{U}}^{\rm iso}_{S_{\rm A}\Theta} = \frac{1}{N-1} \sum_{n=1}^{N} \sum_{i=1}^{I} \sum_{j=1}^{J} \sum_{k=1}^{K} U^{\rm iso}_{i,j,k,n}. \tag{B.3}$$

Note that the above has not removed the trend from $\overline{\mathbf{U}}^{\rm iso}_{S_{\rm A}\Theta}$. To calculate $\Psi^{\rm loc}_{S_{\rm A}\Theta}$ we require:

$$\Delta\Psi^{\rm loc}_{S_{\rm A}\Theta} = \overline{\mathbf{U}}^{\rm iso}_{S_{\rm A}\Theta} - \overline{\mathbf{U}}^{\rm tr}_{S_{\rm A}\Theta} \tag{B.4}$$

The calculation of $\overline{\mathbf{U}}^{\mathrm{tr}}_{S_\mathrm{A}\Theta}$ is basically similar to that of $\overline{\mathbf{U}}^{\mathrm{iso}}_{S_\mathrm{A}\Theta}$. By replacing $\mathbf{u}^{\mathrm{iso}}_{S_\mathrm{A}\Theta}$ with $\mathbf{u}^{\mathrm{tr}}_{S_\mathrm{A}\Theta}$ in (B.1) and (B.2) and than repeating steps 1-5 as for $\overline{\mathbf{U}}^{\mathrm{iso}}_{S_\mathrm{A}\Theta}$, while we consider only the motion of $\Delta V_{i,j,k}$ in (S_A, Θ) coordinates between the initial state at $t = t_1$ and the final state at $t = t_N$, as that is what provides the net transport over the considered time, i.e., the diathermohaline trend.

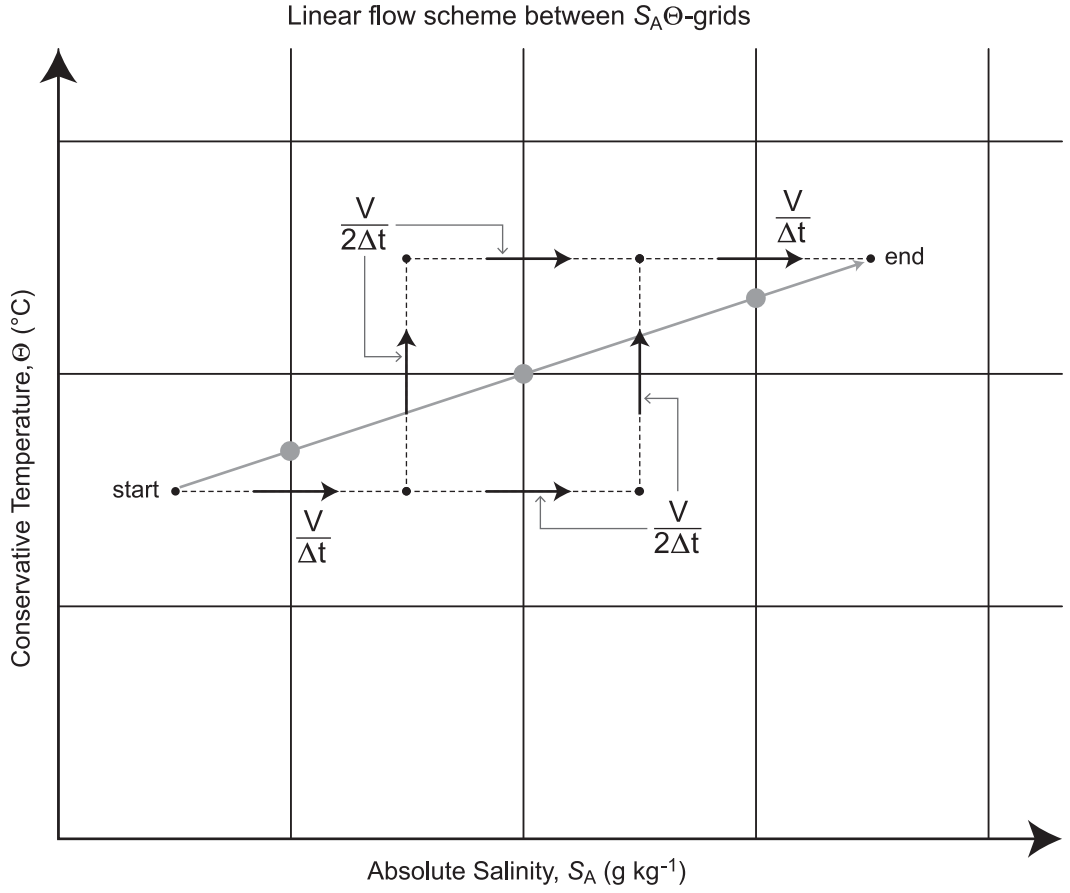

FIGURE B.1: The shortest route concept. The volume transport $V/\Delta t$, related to a displacement of a volume V in (S_A, Θ) coordinates in time, has to be assigned to the correct S_A-interval (Θ-interval) of the isotherms (isohaline) that V has crossed, as indicated by the grey dots. These intervals are obtained when drawing a straight line between the initial grid and the final grid that V occupies. When the line crosses a mid-point between isohalines and isotherms, half of the transport is assigned to both directions.

B.1.3 Calculating $\Delta\Psi^{\mathrm{adv}}_{S_\mathrm{A}\Theta}$ from an ocean model.

To calculate $\Delta\Psi^{\mathrm{adv}}_{S_\mathrm{A}\Theta}$ one requires the 3-dimensional velocity from a model. Following Zika et al. (2012) we recognise that tracers in the UVIC model are advected by the sum of an Eularian mean velocity ($\mathbf{u}^{\mathbf{EM}}$) and quasi-Stokes velocity ($\mathbf{u}^{\mathbf{GM}}$). Hence we use

$$\mathbf{u} = \mathbf{u}^{\mathbf{EM}} + \mathbf{u}^{\mathbf{GM}}. \tag{B.5}$$

We can use this to calculate $\Delta\Psi^{\mathrm{adv}}_{S_\mathrm{A}\Theta}$ as follows:

1. Consider $U^{\mathrm{adv}}_{i,n} = (\mathbf{u}_{i,n} \cdot \mathbf{e_1})A_i$ is the volume transport through a grid interface A_i, in the positive x-direction ($\mathbf{e_1} = (1, 0, 0)$) and the associated $S^{i,j,k,n}_\mathrm{A}$ and $\Theta_{i,j,k,n}$, at (x_i, y_j, z_k, t_n).

2. Consider $S^{i+1,j,k,n}_\mathrm{A}$ and $\Theta_{i+1,j,k,n}$, at (x_{i+1}, y_j, z_k, t_n).

3. If $S^{i,j,k,n}_\mathrm{A} \neq S^{i+1,j,k,n}_\mathrm{A}$ and/or $\Theta^{i,j,k,n} \neq \Theta_{i+1,j,k,n}$, *and* the resulting combination of (S_A, Θ) values occupies a different (S_A, Θ) grid, then the volume transported through A_i, i.e $U^{\mathrm{adv}}_{i,n}$, is normal to isotherms and/or isohalines. The volume transport $U^{\mathrm{adv}}_{i,n}$ will then be assigned to the correct S_A-interval of the crossed isotherms and to the correct Θ-interval of the crossed isohalines, using the shortest route method.

4. Repeat this for all (x_i, y_j, z_k, t_n)-locations and also for the y and z directions and take their sum. Then take the time average over all available time steps to obtain

$$\Delta\Psi^{\mathrm{adv}}_{S_\mathrm{A}\Theta} = \frac{1}{N}\sum_{n=1}^{N}\left[\sum_{i=1}^{I} U^{\mathrm{adv}}_{i,n} + \sum_{i=1}^{J} U^{\mathrm{adv}}_{j,n} + \sum_{i=1}^{K} U^{\mathrm{adv}}_{k,n}\right]. \tag{B.6}$$

B.1.4 Calculating $\Psi^{\mathrm{adv}}_{S_\mathrm{A}\Theta}$ and $\Psi^{\mathrm{loc}}_{S_\mathrm{A}\Theta}$.

As $\Delta\Psi^{\mathrm{adv}}_{S_\mathrm{A}\Theta}$ and $\Delta\Psi^{\mathrm{iso}}_{S_\mathrm{A}\Theta}$ are no longer continuous, neither will $\Psi^{\mathrm{adv}}_{S_\mathrm{A}\Theta}$ and $\Psi^{\mathrm{loc}}_{S_\mathrm{A}\Theta}$ be continuous. A volume transport is defined as the total transport through a Θ-range (S_A-range) on an isohaline (isotherm). This is exactly between the 'corners' of an (S_A, Θ) grid. The coordinates of the corners of the grid, with at the centre $(S^m_\mathrm{A}, \Theta^p)$, are given by $(S^m_\mathrm{A} + dS_\mathrm{A}, \Theta^p + d\Theta)$, for the top right corner, $(S^m_\mathrm{A} + dS_\mathrm{A}, \Theta^p - d\Theta)$ bottom right corner, $(S^m_\mathrm{A} - dS_\mathrm{A}, \Theta^p + d\Theta)$, top left corner and $(S^m_\mathrm{A} - dS_\mathrm{A}, \Theta^p - d\Theta)$ for the bottom left corner.

For a grid with $(S^m_\mathrm{A}, \Theta^p)$ at its centre, we define diahaline and diathermal transports in positive Θ and S_A-direction. Thus the diahaline transport takes place at $S^m_\mathrm{A} + dS_\mathrm{A}$ and in between $\Theta^p \pm d\Theta$. Thus the diahaline volume transport is given by $\Delta\Psi^{\mathrm{adv}}_{S_\mathrm{A}\Theta}(S^m_\mathrm{A} + dS_\mathrm{A}, \Theta^p \pm d\Theta)$. Equivalently the diathermal volume transport in the positive Θ-direction, for the grid with $(S^m_\mathrm{A}, \Theta^p)$ at its centre, at $\Theta^p + d\Theta$ in between salinity range $S^m_\mathrm{A} \pm dS_\mathrm{A}$, is given by $\Delta\Psi^{\mathrm{adv}}_{S_\mathrm{A}\Theta}(S^m_\mathrm{A} \pm S^m_\mathrm{A}, \Theta^p + d\Theta)$ (Fig. B.2).

As $\Psi^{\mathrm{adv}}_{S_\mathrm{A}\Theta}$ is calculated using a summation of $\Delta\Psi^{\mathrm{adv}}_{S_\mathrm{A}\Theta}$, that only adds up at discrete locations, which are defined to be exactly those corner points. Hence we can only

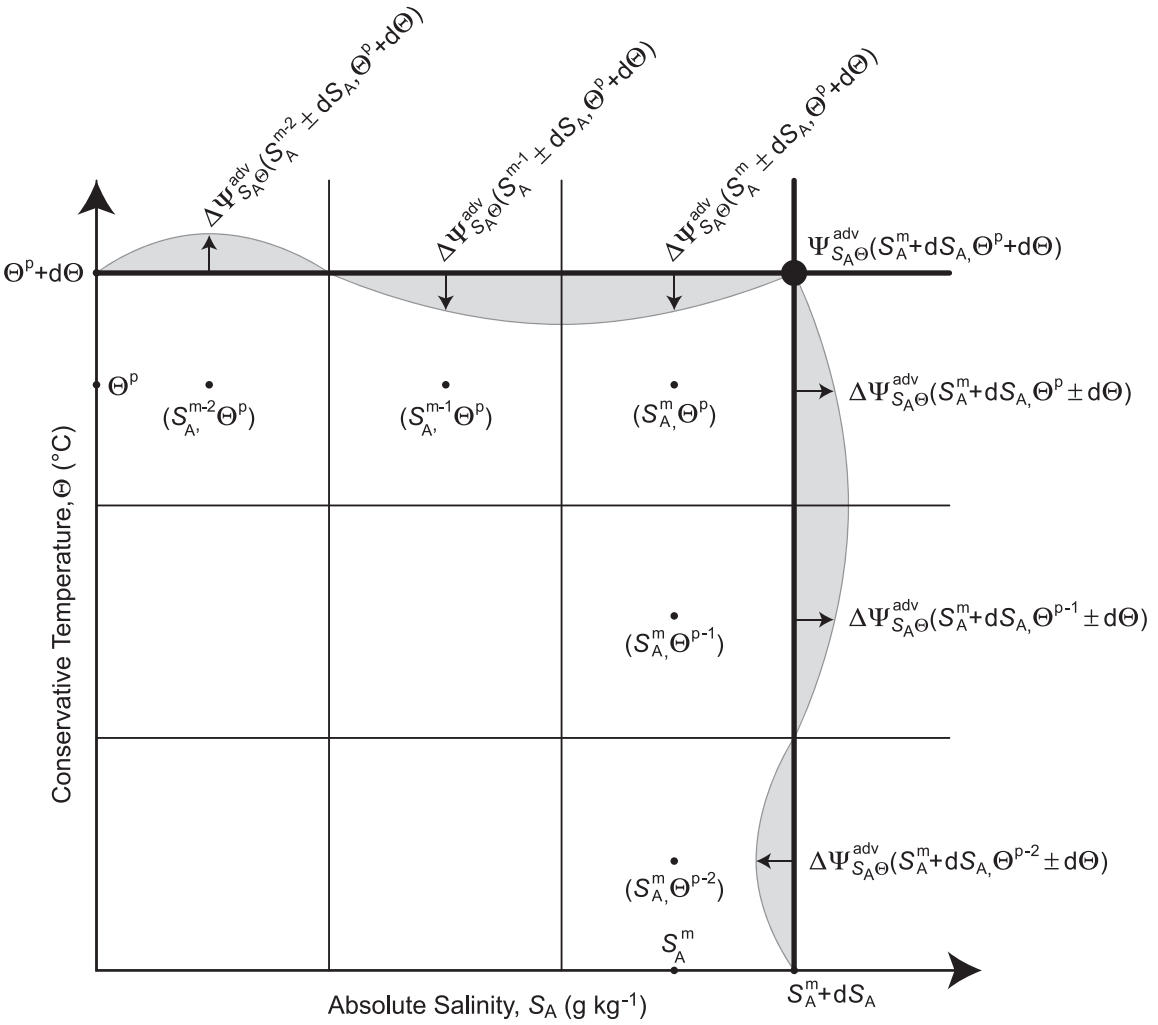

FIGURE B.2: The advective thermohaline streamfunction ($\Psi^{\rm adv}_{S_{\rm A}\Theta}$) is obtained from an integration over $\mathbf{u}^{\rm adv}_{S_{\rm A}\Theta}$ (illustrated by the dashed grey area and given by Eq. (3.7)) or a summation over volume transports expressed as a streamfunction difference for discrete intervals. The latter is given by Eq. (B.7) and illustrated by the black arrows.

define $\Psi^{\rm adv}_{S_{\rm A}\Theta}$, at the corner points. Calculating $\Psi^{\rm adv}_{S_{\rm A}\Theta}(S^m_{\rm A}+dS_{\rm A},\Theta^p+d\Theta)$ using our discretization, leads to

$$\begin{aligned}\Psi^{\rm adv}_{S_{\rm A}\Theta}(S^m_{\rm A}+dS_{\rm A},\Theta^p+d\Theta) &= \sum_{i=1}^{P}\Delta\Psi^{\rm adv}_{S_{\rm A}\Theta}(S^m_{\rm A}+dS_{\rm A},\Theta^p) \\ &= -\sum_{i=1}^{M}\Delta\Psi^{\rm adv}_{S_{\rm A}\Theta}(S^m_{\rm A},\Theta^p+d\Theta).\end{aligned} \tag{B.7}$$

This summation reduces to an integration again when ΔS_{A} and $\Delta\Theta$ are taken infinitesimal small. A similar exercise obtains $\Psi^{\mathrm{loc}}_{S_{\mathrm{A}}\Theta}$

$$\begin{aligned}\Psi^{\mathrm{loc}}_{S_{\mathrm{A}}\Theta}(S^m_{\mathrm{A}}+dS_{\mathrm{A}},\Theta^p+d\Theta) &= \sum_{i=1}^{P}\Delta\Psi^{\mathrm{loc}}_{S_{\mathrm{A}}\Theta}(S^m_{\mathrm{A}}+dS_{\mathrm{A}},\Theta^p\pm d\Theta^p) \\ &= -\sum_{i=1}^{M}\Delta\Psi^{\mathrm{loc}}_{S_{\mathrm{A}}\Theta}(S^m_{\mathrm{A}}\pm dS^m_{\mathrm{A}},\Theta^p+d\Theta).\end{aligned} \tag{B.8}$$

Appendix C

Sensitivity test

An estimate of the uncertainty in the inverse estimate as a result of a prior-estimate of the expected error in the data is provided by $\mathbf{C_p}$ of Eq. (5.17). However, this estimate does not reflect the sensitivity of variations in the choices of a-priori column and row weighting, and the a-prior estimate of the solution. In some cases, these choices allow for a wider range of results than suggested by the standard deviation obtained from $\mathbf{C_p}$.

We test only the sensitivity of the solution to prior estimates of which we are less confident. These are only $x_0^{K_\mathrm{H}}$, $x_0^{K_\mathrm{I}}$, x_0^D and $\sigma_x^{K_\mathrm{I}}$. Although we have strong confidence that the scaling argument of Eq. (5.18) provides a very well understood estimate of $x_0^{K_\mathrm{H}}$, $x_0^{K_\mathrm{I}}$, x_0^D, one could argue either that the maximum values do not have to be exactly equal, or that one would scale using for example the 5% highest values, rather than just the maximum. Either way, we do not expect $x_0^{K_\mathrm{H}}$, $x_0^{K_\mathrm{I}}$, x_0^D to vary within a factor 2 of their prior estimates as the resulting transports would become too large or very low.

The unknowns K_H and D are involved in many equations and are thereby constrained by a large information content, leading to strong constraints on their estimate. In that sense, K_I is less constrained. This could lead to the solution preferring a very small K_I. To test this, we will vary $\sigma_x^{K_\mathrm{I}}$ between 20% and 100 % of its prior estimate $x_0^{K_\mathrm{I}}$. In the latter case, the inverse estimate is likely to result in $K_\mathrm{I} = 0$ if the unknown was unconstrained by the equations.

We calculate the inverse estimate for $\sigma_x^{K_\mathrm{I}} = [0.2, 0.5, 1]$ x $x_0^{K_\mathrm{I}}$ and we vary $x_0^{K_\mathrm{H}}$, $x_0^{K_\mathrm{I}}$, x_0^D using [0.5,1,2] times the magnitude obtained from the scaling described in Eq. (5.18). This leads to $3^4 = 81$ inverse solutions of which the average value and the standard deviation are provided in (Table C.1) for both CARS and LR-CARS. The sensitivity test shows that the results presented in the text are practically similar to that obtained

from the sensitivity test, with the only difference that the magnitude of the standard deviation is slightly larger for the sensitivity test.

We find that the results for K_I vary between 40 m^2 s^{-1} and 140 m^2 s^{-1} over the whole domain, mainly due to the change in $x_0^{K_\mathrm{I}}$ (Fig. C.1). The second largest influence on the result is the increase in $x_0^{K_\mathrm{H}}$, leading to lower values of K_I. This indicates that some part of the water-mass transformations in (S_A, Θ) coordinates are counteracted by both K_H and K_I, such that if one is larger, the other is smaller. The effect of changing x_0^D and $\sigma_x^{K_\mathrm{I}}$ is negligible. The latter shows that K_I is well constrained.

The estimate of K_H varies between 1200 m^2 s^{-1} and 2600 m^2 s^{-1} and is mainly sensitive to the prior choice of $x_0^{K_\mathrm{H}}$ (not shown). Finally, the estimate of D varies between 6.1 x 10^{-5} m^2 s^{-1} and 6.9 x 10^{-5} m^2 s^{-1}, and is mainly due to a change in the prior choice of x_0^D (not shown). The sensitivity is practically similar for CARS and LR-CARS (not shown).

Sensitivity Estimate	CARS	LR-CARS
D	6.57 ± 0.25 x 10^{-5} m^2 s^{-1}	6.83 ± 0.26 x 10^{-5} m^2 s^{-1}
K_H	1748 ± 529 m^2 s^{-1}	2621 ± 774 m^2 s^{-1}
K_I	82 ± 30 m^2 s^{-1}	671 ± 251 m^2 s^{-1}

TABLE C.1: The average result of the inverse estimate of all tested combinations of different prior estimates of $x_0^{K_\mathrm{H}}$, $x_0^{K_\mathrm{I}}$ and x_0^D and σ_{K_I}. Compared to Table 5.2 the results are practically similar, except for an increased standard deviation

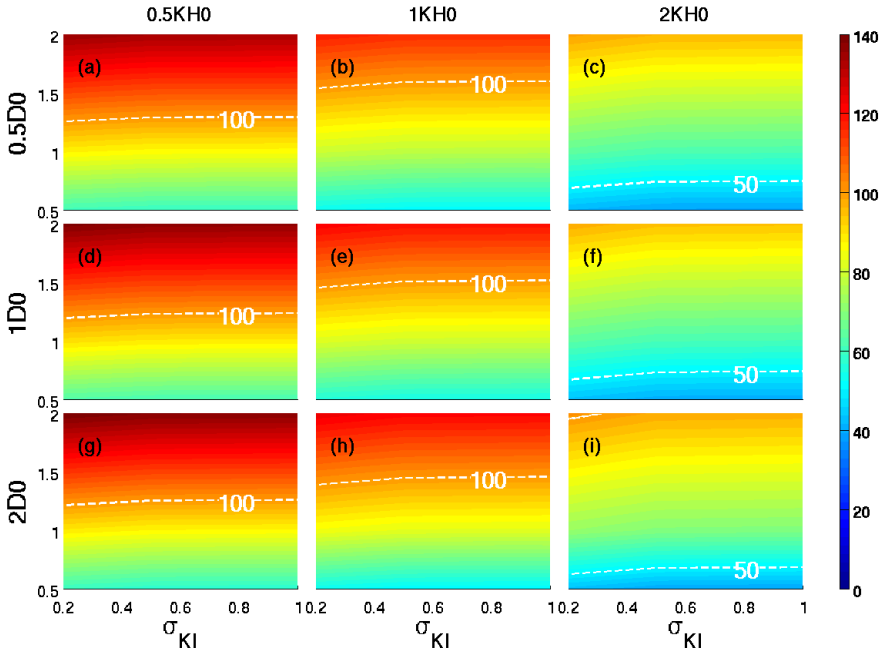

FIGURE C.1: The sensitivity of K_{I} to changes in $x_0^{K_{\mathrm{H}}}$, $x_0^{K_{\mathrm{I}}}$ and x_0^{D} and $\sigma_{K_{\mathrm{I}}}$. The x-axis shows the factor that multiplies $x_0^{K_{\mathrm{I}}}$ to obtain $\sigma_{K_{\mathrm{I}}}$. The y-axis shows the factor with which we multiplied $x_0^{K_{\mathrm{I}}}$. Panels in the x-direction are calculated using 0.5, 1 and 2 times $x_0^{K_{\mathrm{H}}}$, from left to right. Panels in the y-direction are calculated using 0.5, 1 and 2 times $x_0^{K_{\mathrm{H}}}$, from top to bottom. The color indicates the estimate of K_{I} in $\mathrm{m}^2\ \mathrm{s}^{-1}$.

Bibliography

Abernathey, R. P. and J. Marshall

2013. Global surface eddy diffusivities derived from satellite altimetry. *Journal of Geophysical Research: Oceans*, 118(2):901–916.

Alford, M. H.

2001. Internal Swell Generation: The Spatial Distribution of Energy Flux from the Wind to Mixed Layer Near-Inertial Motions. *Journal of Physical Oceanography*, 31(8):2359–2368.

Alford, M. H., M. F. Cronin, and J. M. Klymak

2011. Annual Cycle and Depth Penetration of Wind-Generated Near-Inertial Internal Waves at Ocean Station Papa in the Northeast Pacific. *Journal of Physical Oceanography*, 42(6):889–909.

Badin, G. and R. G. Williams

2010. On the Buoyancy Forcing and Residual Circulation in the Southern Ocean: The Feedback from Ekman and Eddy Transfer. *Journal of Physical Oceanography*, 40(2):295–310.

Ballarotta, M., S. Drijfhout, T. Kuhlbrodt, and K. Döös

2013. The residual circulation of the Southern Ocean: Which spatio-temporal scales are needed? *Ocean Modelling*, 64(0):46–55.

Barker, P. M. and T. McDougall

2015. Minimal adjustment of vertical salinity and temperature profiles to achieve specified static stability. *Unpublished Manuscript in Preparation.*

Bates, M., R. Tulloch, J. Marshall, and R. Ferrari

2014. Rationalizing the Spatial Distribution of Mesoscale Eddy Diffusivity in Terms of Mixing Length Theory. *Journal of Physical Oceanography*, 44(6):1523–1540.

Bleck, R.

1978a. Finite difference equations in generalized vertical coordinates, I, Total energy conservation. *Contrib. Atmos. Phys.*, 51:360–372.

Bleck, R.

1978b. Finite difference equations in generalized vertical coordinates, II, Potential vorticity conservations. *Contrib. Atmos. Phys.*, 52:95–105.

Boccaletti, G., R. Ferrari, A. Adcroft, D. Ferreira, and J. Marshall

2005. The vertical structure of ocean heat transport. *Geophys. Res. Lett.*, 32(10).

Brennecke, W.

1921. Die ozeanographischen Arbeiten der Deutschen Antarktischen Expedition 1911–1912. *Aus dem Archiv der Deutschen Seewarte*, 1(39):216.

Broecker, W. S.

1982. *Tracers in the Sea.* Eldigio Press, Palisades, New York, pp 690.

Broecker, W. S.

1987. The biggest chill. *Natural History Magazine.*

Broecker, W. S.

1991. The great ocean conveyor. *Oceanography*, 4(2).

Bryan, K. and L. J. Lewis

1979. A water mass model of the World Ocean. *Journal of Geophysical Research: Oceans*, 84(C5):2503–2517.

Bryan, K., J. L. Sarmiento, and B. Saltzman

1985. *Modeling Ocean Circulation*, volume Volume 28, Part A, Pp. 433–459. Elsevier.

Cunningham, S.

2000. Circulation and volume flux of the North Atlantic using synoptic hydrographic data in a Bernoulli inverse. *Journal of Marine Research*, 58(1):1–35.

Danabasoglu, G. and J. Marshall

2007. Effects of vertical variations of thickness diffusivity in an ocean general circulation model. *Ocean Modelling*, 18(2):122–141.

D'Asaro, E. A.

1985. The Energy Flux from the Wind to Near-Inertial Motions in the Surface Mixed Layer. *Journal of Physical Oceanography*, 15(8):1043–1059.

Dataset, C. G. A.-S. F.

. Core.2 global air-sea flux dataset ds260.2 published by the cisl data support section at the national center for atmospheric research, boulder, co. Accessed - 26 mar 2013, U.S. National Center for Atmospheric Research [Climate and Global Dynamics Division], U.S. Geophysical Fluid Dynamics Laboratory [NOMADS], U.K. Hadley Centre

for Climate Prediction and Research, and U.S. National Centers for Environmental Prediction,.

Defant, A.

1941. Schichtung und Zirkulation des Atlantischen Ozeans. Die Troposphare. *In: Wissenschaftliche Ergebnisse der Deutschen Atlantischen Expedition auf dem Forschungs- und Vermessungsschiff 'Meteor' 1925–1927,*, 6(first part, 3, Berlin, pp. 289–411 (The Troposphere: Scientific Results of the German Atlantic Expedition of the Research Vessel 'Meteor' 1925–1927, Emery, W.J. (Ed.), 1981 Amerind, New Delhi, 113 pp.).).

Döös, K., J. Nilsson, J. Nycander, L. Brodeau, and M. Ballarotta

2012. The World Ocean Thermohaline Circulation. *Journal of Physical Oceanography*, 42(9):1445–1460.

Döös, K. and D. J. Webb

1994. The Deacon Cell and the Other Meridional Cells of the Southern Ocean. *Journal of Physical Oceanography*, 24(2):429–442.

Durack, P. J., S. E. Wijffels, and R. J. Matear

2012. Ocean Salinities Reveal Strong Global Water Cycle Intensification During 1950 to 2000. *Science*, 336(6080):455–458.

Ellis, H.

1751. A letter to the Rev. Dr. Hales, F.R.S. from Captain Henry Ellis, F.R.S. *Philosophical Transactions of the Royal Society of London*, (47):211–214.

Ferrari, R.

2014. Oceanography: What goes down must come up. *Nature*, 513(7517):179–180.

Ferrari, R. and D. Ferreira

2011. What processes drive the ocean heat transport? *Ocean Modelling*, 38(3–4):171 – 186.

Ferreira, D., J. Marshall, and P. Heimbach

2005. Estimating Eddy Stresses by Fitting Dynamics to Observations Using a Residual-Mean Ocean Circulation Model and Its Adjoint. *Journal of Physical Oceanography*, 35(10):1891–1910.

Ganachaud, A. and C. Wunsch

2000. Improved estimates of global ocean circulation, heat transport and mixing from hydrographic data. *Nature*, 408(6811):453–457.

Garabato, A. C. N.

2012. A perspective on the future of physical oceanography. *Philosophical Transactions of the Royal Society A: Mathematical, Physical and Engineering Sciences*, 370(1980):5480–5511.

Garabato, A. C. N., K. L. Polzin, B. A. King, K. J. Heywood, and M. Visbeck

2004. Widespread Intense Turbulent Mixing in the Southern Ocean. *Science*, 303(5655):210–213.

Gargett, A. E., T. R. Osborn, and P. W. Nasmyth

1984. Local isotropy and the decay of turbulence in a stratified fluid. *Journal of Fluid Mechanics*, 144:231–280 M3 – 10.1017/S0022112084001592.

Gent, P. R. and J. C. McWilliams

1990. Isopycnal Mixing in Ocean Circulation Models. *Journal of Physical Oceanography*, 20(1):150–155.

Gent, P. R., J. Willebrand, T. J. McDougall, and J. C. McWilliams

1995. Parameterizing Eddy-Induced Tracer Transports in Ocean Circulation Models. *Journal of Physical Oceanography*, 25(4):463–474.

Gordon, A. L.

1986. Interocean exchange of thermocline water. *Journal of Geophysical Research: Oceans*, 91(C4):5037–5046.

Gordon, A. L.

1991. The role of thermohaline circulation in global climate change. *In: Lamont–Doherty Geological Observatory 1990 & 1991 Report, Lamont–Doherty Geological Observatory of Columbia University, Palisades, New York*, Pp. 44–51.

Graham, F. S. and T. J. McDougall

2013. Quantifying the Nonconservative Production of Conservative Temperature, Potential Temperature, and Entropy. *Journal of Physical Oceanography*, 43(5):838–862.

Griffies, S. M.

1998. The Gent–McWilliams Skew Flux. *Journal of Physical Oceanography*, 28(5):831–841.

Griffies, S. M.

2004. *Fundamentals of ocean climate models.* Princeton University Press.

Griffies, S. M. and R. J. Greatbatch

2012. Physical processes that impact the evolution of global mean sea level in ocean climate models. *Ocean Modelling*, 51(0):37–72.

Groeskamp, S., A. Lenton, R. J. Matear, B. M. Sloyan, and C. Langlais
2015. Redistribution and Accumulation of Anthropogenic CO2 in the ocean - a tracer-tracer coordinate analysis. *In Preparation for Global Biogeochemical Cycles.*

Groeskamp, S., J. D. Zika, T. J. McDougall, B. M. Sloyan, and F. Laliberté
2014a. The Representation of Ocean Circulation and Variability in Thermodynamic Coordinates. *Journal of Physical Oceanography.*

Groeskamp, S., J. D. Zika, B. M. Sloyan, T. J. McDougall, and P. C. McIntosh
2014b. A Thermohaline Inverse Method for Estimating Diathermohaline Circulation and Mixing. *Journal of Physical Oceanography*, 44(10):2681–2697.

Hanawa, K. and L. D. Talley
2001. *Ocean Circulation and Climate.*, chapter Mode Waters, Pp. 373–386. International Geophysics Series. Academic Press.

Hieronymus, M., J. Nilsson, and J. Nycander
2014. Water Mass Transformation in Salinity-Temperature Space. *Journal of Physical Oceanography.*

Hirst, A. C., D. R. Jackett, and T. J. McDougall
1996. The Meridional Overturning Cells of a World Ocean Model in Neutral Density Coordinates. *Journal of Physical Oceanography*, 26(5):775–791.

Hirst, A. C. and T. J. McDougall
1998. Meridional Overturning and Dianeutral Transport in a z-Coordinate Ocean Model Including Eddy-Induced Advection. *Journal of Physical Oceanography*, 28(6):1205–1223.

Hogg, N. G.
1987. A least-squares fit of the advective-diffusive equations to Levitus Atlas data. *Journal of Marine Research*, 45(2):347–375.

Holloway, G.
1986. Estimation of oceanic eddy transports from satellite altimetry. *Nature*, 323(6085):243–244.

Huang, R. X.
1993. Real Freshwater Flux as a Natural Boundary Condition for the Salinity Balance and Thermohaline Circulation Forced by Evaporation and Precipitation. *Journal of Physical Oceanography*, 23(11):2428–2446.

IOC, SCOR, and IAPSO
2010. *The international thermodynamic equation of seawater – 2010: Calculation*

and use of thermodynamic properties. Intergovernmental Oceanographic Commission, Manuals and Guides. UNESCO (English), [Available online at www.TEOS-10.org].

Iselin, C. O.

1939. The influence of vertical and lateral turbulence on the characteristics of the waters at mid-depths. *Eos, Transactions American Geophysical Union*, 20(3):414–417.

Iudicone, D., G. Madec, and T. J. McDougall

2008. Water-Mass Transformations in a Neutral Density Framework and the Key Role of Light Penetration. *Journal of Physical Oceanography*, 38(7):1357–1376.

Jackett, D. R. and T. J. McDougall

1995. Minimal Adjustment of Hydrographic Profiles to Achieve Static Stability. *Journal of Atmospheric and Oceanic Technology*, 12(2):381–389.

Jackett, D. R. and T. J. McDougall

1997. A Neutral Density Variable for the World's Oceans. *Journal of Physical Oceanography*, 27(2):237–263.

Killworth, P. D.

1986. A Bernoulli Inverse Method for Determining the Ocean Circulation. *Journal of Physical Oceanography*, 16(12):2031–2051.

Kjellsson, J.

2014. Weakening of the global atmospheric circulation with global warming. Pp. 1–14.

Kjellsson, J., K. Döös, F. B. Laliberté, and J. D. Zika

2013. The Atmospheric General Circulation in Thermodynamical Coordinates. *Journal of the Atmospheric Sciences*, 71(3):916–928.

Klocker, A. and R. Abernathey

2013. Global Patterns of Mesoscale Eddy Properties and Diffusivities. *Journal of Physical Oceanography*, 44(3):1030–1046.

Klocker, A. and T. J. McDougall

2010. Quantifying the Consequences of the Ill-Defined Nature of Neutral Surfaces. *Journal of Physical Oceanography*, 40(8):1866–1880.

Ledwell, J. R., L. C. St. Laurent, J. B. Girton, and J. M. Toole

2010. Diapycnal Mixing in the Antarctic Circumpolar Current. *Journal of Physical Oceanography*, 41(1):241–246.

Lenz, E.

1845. Bermerkungen uber die Temperatur des Weltmeeres in verschiedenen Tiefen. In *Bulletin de la Classe Physico-Mathematique de l'Academie Imperiale des Sciences de Saint-Petersbourg 5*, Pp. 67–74.

Lumpkin, R. and K. Speer

2007. Global Ocean Meridional Overturning. *Journal of Physical Oceanography*, 37(10):2550–2562.

Macdonald, A. M., S. Mecking, P. E. Robbins, J. M. Toole, G. C. Johnson, L. Talley, M. Cook, and S. E. Wijffels

2009. The WOCE-era 3-D Pacific Ocean circulation and heat budget. *Progress in Oceanography*, 82(4):281–325.

MacKinnon, J.

2013. Oceanography: Mountain waves in the deep ocean. *Nature*, 501(7467):321–322.

MacKinnon, J., L. S. Laurent, and A. N. Garabato

2013. Diapycnal mixing processes in the ocean interior. In *Ocean Circulation and Climate: A 21st Century Perspective. 2nd Ed*, G. Siedler, S. Griffies, J. Gould, and J. Church, eds., Pp. 159–184. Academic Press.

Marotzke, J., P. Welander, and J. Willebrand

1988. Instability and multiple steady states in a meridional-plane model of the thermohaline circulation. *Tellus A*, 40A(2):162–172.

Marsh, R.

2000. Recent Variability of the North Atlantic Thermohaline Circulation Inferred from Surface Heat and Freshwater Fluxes. *Journal of Climate*, 13(18):3239–3260.

Marshall, D.

1997. Subduction of water masses in an eddying ocean. *Journal of Marine Research*, 55(2):201–222.

Marshall, J., D. Jamous, and J. Nilsson

1999. Reconciling thermodynamic and dynamic methods of computation of water-mass transformation rates. *Deep Sea Research Part I: Oceanographic Research Papers*, 46(4):545 – 572.

McDougall, T. and P. M. Barker

2011. *Getting started with TEOS-10 and the Gibbs Seawater (GSW) Oceanographic Toolbox.* SCOR/IAPSO, WG127, ISBN 978-0-646-55621-5.

McDougall, T. J.

1984. The Relative Roles of Diapycnal and Isopycnal Mixing on Subsurface Water Mass Conversion. *Journal of Physical Oceanography*, 14(10):1577–1589.

McDougall, T. J.

1987a. Neutral Surfaces. *Journal of Physical Oceanography*, 17(11):1950–1964.

McDougall, T. J.

1987b. Thermobaricity, cabbeling, and water-mass conversion. *Journal of Geophysical Research: Oceans*, 92(C5):5448–5464.

McDougall, T. J.

1995. The Influence of Ocean Mixing on the Absolute Velocity Vector. *Journal of Physical Oceanography*, 25(5):705–725.

McDougall, T. J.

2003. Potential Enthalpy: A Conservative Oceanic Variable for Evaluating Heat Content and Heat Fluxes. *Journal of Physical Oceanography*, 33(5):945–963.

McDougall, T. J. and J. A. Church

1986. Pitfalls with the Numerical Representation of Isopycnal Diapycnal Mixing. *Journal of Physical Oceanography*, 16(1):196–199.

McDougall, T. J., S. Groeskamp, and S. M. Griffies

2014. On geometrical aspects of interior ocean mixing. *Journal of Physical Oceanography*, 44(8):2164–2175.

McDougall, T. J. and D. R. Jackett

1988. On the helical nature of neutral trajectories in the ocean. *Progress In Oceanography*, 20(3):153 – 183.

McDougall, T. J. and D. R. Jackett

2005. The material derivative of neutral density. *Journal of Marine Research*, 63(1):159–185.

McDougall, T. J. and D. R. Jackett

2007. The Thinness of the Ocean in S-Θ-p Space and the Implications for Mean Diapycnal Advection. *Journal of Physical Oceanography*, 37(6).

McDougall, T. J., D. R. Jackett, F. J. Millero, R. Pawlowicz, and P. M. Barker

2012. A global algorithm for estimating Absolute Salinity. *Ocean Science*, 8(6):1117–1128.

McDougall, T. J., D. R. Jackett, D. G. Wright, and R. Feistel

2003. Accurate and computationally efficient algorithms for potential temperature and density of seawater. *Journal of Atmospheric and Oceanic Technology*, 20(5):730–741.

McDougall, T. J. and P. C. McIntosh

2001. The Temporal-Residual-Mean Velocity. Part II: Isopycnal Interpretation and the Tracer and Momentum Equations. *Journal of Physical Oceanography*, 31(5):1222–1246.

McIntosh, P. C. and S. R. Rintoul

1997. Do Box Inverse Models Work? *Journal of Physical Oceanography*, 27(2):291–308.

Melet, A., R. Hallberg, S. Legg, and K. Polzin

2012. Sensitivity of the Ocean State to the Vertical Distribution of Internal-Tide-Driven Mixing. *Journal of Physical Oceanography*, 43(3):602–615.

Menke, W.

1984. *Geophysical Data Analysis: Discrete Inverse Theory.*, number 978-0-12-397160-9. Elsevier Inc.

Merz, A.

1925. Die Deutsche Atlantische Expedition auf dem Vermessungs- und Forschungsschiff 'Meteor'. 1. *Bericht. Sitzungsberichte der Preussischen Akademie der Wissenschaften, Physikalische–Mathematische Klasse,*, Pp. 562–588.

Millero, F. J., R. Feistel, D. G. Wright, and T. J. McDougall

2008. The composition of Standard Seawater and the definition of the Reference-Composition Salinity Scale. *Deep Sea Research Part I: Oceanographic Research Papers*, 55(1):50–72.

Munk, W. and C. Wunsch

1998. Abyssal recipes II: energetics of tidal and wind mixing. *Deep Sea Research Part I: Oceanographic Research Papers*, 45(12):1977–2010.

Munk, W. H.

1966. Abyssal recipes. *Deep Sea Research and Oceanographic Abstracts*, 13(4):707–730.

Nikurashin, M. and R. Ferrari

2011. Global energy conversion rate from geostrophic flows into internal lee waves in the deep ocean. *Geophysical Research Letters*, 38(8):L08610.

Nikurashin, M. and R. Ferrari

2013. Overturning circulation driven by breaking internal waves in the deep ocean. *Geophysical Research Letters*, 40(12):3133–3137.

Nurser, A. J. G. and M.-M. Lee

2004. Isopycnal Averaging at Constant Height. Part I: The Formulation and a Case Study. *Journal of Physical Oceanography*, 34(12):2721–2739.

Nurser, A. J. G. and R. Marsh

1998. Water mass transformation theory and the meridional overturning streamfunction. In *WOCE News letters*, volume 31, Pp. 36–39.

Nurser, A. J. G., R. Marsh, and R. G. Williams

1999. Diagnosing Water Mass Formation from Air–Sea Fluxes and Surface Mixing. *Journal of Physical Oceanography*, 29(7):1468–1487.

Nycander, J.

2005. Generation of internal waves in the deep ocean by tides. *Journal of Geophysical Research: Oceans*, 110(C10):C10028.

Nycander, J.

2010. Energy Conversion, Mixing Energy, and Neutral Surfaces with a Nonlinear Equation of State. *Journal of Physical Oceanography*, 41(1):28–41.

Nycander, J., J. Nilsson, K. Döös, and G. Broström

2007. Thermodynamic Analysis of Ocean Circulation. *Journal of Physical Oceanography*, 37(8):2038–2052.

Osborn, T. R.

1980. Estimates of the Local Rate of Vertical Diffusion from Dissipation Measurements. *Journal of Physical Oceanography*, 10(1):83–89.

Pacanowski, R.

1995. *MOM2 Documentation, User's Guide, and Reference Manual.* NOAA/Geophysical Fluid Dynamics Laboratory.

Polzin, K. L.

2009. An abyssal recipe. *Ocean Modelling*, 30(4):298–309.

Polzin, K. L., J. M. Toole, J. R. Ledwell, and R. W. Schmitt

1997. Spatial Variability of Turbulent Mixing in the Abyssal Ocean. *Science*, 276(5309):93–96.

Pradal, M.-A. and A. Gnanadesikan

2014. How does the Redi parameter for mesoscale mixing impact global climate in an Earth System Model? *Journal of Advances in Modeling Earth Systems*, Pp. n/a–n/a.

Rahmstorf, S.

2002. Ocean circulation and climate during the past 120,000 years. *Nature*, 419(6903):207–214.

Redi, M. H.

1982. Oceanic Isopycnal Mixing by Coordinate Rotation. *Journal of Physical Oceanography*, 12(10):1154–1158.

Rennel, J.

1832. *An Investigation of the Currents of the Atlantic Ocean, and of Those Which Prevail between the Indian Ocean and the Atlantic*. J.G. & F. Rivington, London.

Richardson, P. L.

2008. On the history of meridional overturning circulation schematic diagrams. *Progress In Oceanography*, 76(4):466 – 486.

Ridgway, K. and J. Dunn

2003. Mesoscale structure of the mean East Australian Current System and its relationship with topography. *Progress in Oceanography*, 56(2):189 – 222.

Ridgway, K. R., J. R. Dunn, and J. L. Wilkin

2002. Ocean Interpolation by Four-Dimensional Weighted Least Squares—Application to the Waters around Australasia. *Journal of Atmospheric and Oceanic Technology*, 19(9):1357–1375.

Rintoul, S. R. and C. Wunsch

1991. Mass, heat, oxygen and nutrient fluxes and budgets in the North Atlantic Ocean. *Deep Sea Research Part A. Oceanographic Research Papers*, 38, Supplement 1(0):S355–S377.

Rumford, B.

1798. Of the propagation of heat in fluids. In *Essays, Political, Economical and Philosophical*, D. W. Caldwell, T., ed., volume (Reprinted In: Brown, S.C. (Ed), Collected Works of Count Rumford, vol. 1. The Nature of Heat, Belknap Press of Harvard University Press, Cambridge MA, 1968, pp. 117–284, 507 pp.)., Pp. 199–313. London.

Schmitz, W. J.

1995. On the interbasin-scale thermohaline circulation. *Reviews of Geophysics*, 33(2):151–173.

Schott, F. and H. Stommel

1978. Beta spirals and absolute velocities in different oceans. *Deep Sea Research*, 25(11):961 – 1010.

Schott, F. A., M. Dengler, and R. Schoenefeldt

2002. The shallow overturning circulation of the Indian Ocean. *Progress in Oceanography*, 53(1):57–103.

Schott, F. A. and J. P. McCreary Jr.

2001. The monsoon circulation of the Indian Ocean. *Progress in Oceanography*, 51(1):1–123.

Schott, G.

1902. Oceanographie und maritime Meteorolgie. *In: Wissenschaftliche Ergebnisse der Deutschen Tiefsee-Expedition auf dem Dampfer 'Valdivia'*, 1:403.

Sijp, W. P., M. Bates, and M. H. England

2006. Can Isopycnal Mixing Control the Stability of the Thermohaline Circulation in Ocean Climate Models? *Journal of Climate*, 19(21):5637–5651.

Simmons, H.

2004. Tidally driven mixing in a numerical model of the ocean general circulation. *Ocean Modelling*, 6(3-4):245–263.

Sloyan, B. M. and S. R. Rintoul

2000. Estimates of Area-Averaged Diapycnal Fluxes from Basin-Scale Budgets. *Journal of Physical Oceanography*, 30(9):2320–2341.

Sloyan, B. M. and S. R. Rintoul

2001. The Southern Ocean Limb of the Global Deep Overturning Circulation. *Journal of Physical Oceanography*, 31(1):143–173.

Solomon, H.

1971. On the Representation of Isentropic Mixing in Ocean Circulation Models. *Journal of Physical Oceanography*, 1(3):233–234.

Speer, K.

1993. Conversion among North Atlantic surface water types. *Tellus Series A - Dynamic Meteorology and Oceanography*, 45A(1):72–79.

Speer, K. G. and E. Tziperman

1992. Rates of Water Mass Formation in the North Atlantic Ocean. *Journal of Physical Oceanography*, 22(1):93–104.

Spiess, F.

1928. Die Meteor-Fahrt. Forschungen und Ergebnisse der Deutschen Atlantischen Expedition. *1925–1927. Dietrich Reimer. Berlin, 375 pp. (The Meteor Expedition, Scientific Results of the German Atlantic Expedition, 1925–1927. Emery, W.J. (Ed), 1985. Amerind Publishing, New Delhi, 429 pp.).*

St. Laurent, L., A. C. Naveira Garabato, J. R. Ledwell, A. M. Thurnherr, J. M. Toole, and A. J. Watson

2012. Turbulence and Diapycnal Mixing in Drake Passage. *Journal of Physical Oceanography*, 42(12):2143–2152.

St. Laurent, L. C., H. L. Simmons, and S. R. Jayne

2002. Estimating tidally driven mixing in the deep ocean. *Geophysical Research Letters*, 29(23):2106.

Starr, V. P.

1945. A Quasi-Lagrangian System of Hydrodynamical Equations. *Journal of Meteorology*, 2(4):227–237.

Stommel, H.

1948. The westward intensification of wind-driven ocean currents. *Trans. Amer. Geophys. Union 29.2*, Pp. 202–206.

Stommel, H.

1957. A survey of ocean current theory. *Deep Sea Research (1953)*, 4(0):149–184.

Stommel, H.

1958. The abyssal circulation. *Deap-Sea Research*, 5:80–82.

Stommel, H. and A. B. Arons

1959. On the abyssal circulation of the world ocean —II. An idealized model of the circulation pattern and amplitude in oceanic basins. *Deep Sea Research (1953)*, 6(0):217–233.

Stommel, H. and F. Schott

1977. The beta spiral and the determination of the absolute velocity field from hydrographic station data. *Deep Sea Research*, 24(3):325 – 329.

Talley, L.

2013. Closure of the global overturning circulation through the Indian, Pacific, and Southern Oceans: Schematics and transports. *Oceanography*, 26(1):80–97.

Toggweiler, J. R. and B. Samuels

1998. On the Ocean's Large-Scale Circulation near the Limit of No Vertical Mixing. *Journal of Physical Oceanography*, 28(9):1832–1852.

Veronis, G.

1975. *Numerical Models of Ocean Circulation.*, chapter The role of models in tracer studies, Pp. 133–146. National Academy of Science.

Walin, G.

1982. On the relation between sea-surface heat flow and thermal circulation in the ocean. *Tellus*, 34(2):187–195.

Waterhouse, A. F., J. A. MacKinnon, J. D. Nash, M. H. Alford, E. Kunze, H. L. Simmons, K. L. Polzin, L. C. St. Laurent, O. M. Sun, R. Pinkel, L. D. Talley, C. B. Whalen, T. N. Huussen, G. S. Carter, I. Fer, S. Waterman, A. C. Naveira Garabato, T. B. Sanford, and C. M. Lee

2014. Global Patterns of Diapycnal Mixing from Measurements of the Turbulent Dissipation Rate. *Journal of Physical Oceanography*, 44(7):1854–1872.

Wunsch, C.

1977. Determining the General Circulation of the Oceans: A Preliminary Discussion. *Science*, 196(4292):871–875.

Wunsch, C.

1978. The North Atlantic general circulation west of 50 °W determined by inverse methods. *Rev. Geophys.*, 16 ,(4):583–620.

Wunsch, C.

1996. *The Ocean Circulation Inverse Problem*, number 9780521480901. Cambridge University Press.

Wunsch, C. and R. Ferrari

2004. Vertical mixing, energy, and the general circulation of the oceans. *Annual Review of Fluid Mechanics*, 36(1):281–314.

Wunsch, C., D. Hu, and B. Grant

1983. Mass, Heat, Salt and Nutrient Fluxes in the South Pacific Ocean. *Journal of Physical Oceanography*, 13(5):725–753.

Wust, G.

1935. Schichtung und Zirkulation des Atlantischen Ozeans. Die Stratophare. *In: Wissenschaftliche Ergebnisse der Deutschen Atlantischen Expedition auf dem Forschungs- und Vermessungsschiff 'Meteor' 1925–1927*, 6(first part, 2, Berlin 180 pp. (The Stratosphere of the Atlantic Ocean, Emery, W.J. (Ed), 1978 Amerind, New Delhi, 112 pp.).).

Yeager, S. G. and W. G. Large

2008. CORE.2 Global Air-Sea Flux Dataset.

Dataset. http://dx.doi.org/10.5065/D6WH2N0S. Dataset. http://dx.doi.org/10.5065/D6WH2N0S. Dataset. http://dx.doi.org/10.5065/D6WH2N0S. Accessed - 26 Mar 2013, Research Data Archive at the National Center for Atmospheric Research, Computational and Information Systems Laboratory.

Young, W. R.

2011. An Exact Thickness-Weighted Average Formulation of the Boussinesq Equations. *Journal of Physical Oceanography*, 42(5):692–707.

Zhang, H.-M. and N. G. Hogg

1992. Circulation and water mass balance in the Brazil Basin. *Journal of Marine Research*, 50(3):385–420.

Zhurbas, V. and I. S. Oh

2004. Drifter-derived maps of lateral diffusivity in the Pacific and Atlantic Oceans in relation to surface circulation patterns. *Journal of Geophysical Research: Oceans*, 109(C5):C05015.

Zika, J. D., M. H. England, and W. P. Sijp

2012. The Ocean Circulation in Thermohaline Coordinates. *Journal of Physical Oceanography*, 42(5):708–724.

Zika, J. D., T. J. McDougall, and B. M. Sloyan

2010a. A Tracer-Contour Inverse Method for Estimating Ocean Circulation and Mixing. *Journal of Physical Oceanography*, 40(1):26–47.

Zika, J. D., T. J. McDougall, and B. M. Sloyan

2010b. Weak Mixing in the Eastern North Atlantic: An Application of the Tracer-Contour Inverse Method. *Journal of Physical Oceanography*, 40(8):1881–1893.

Zika, J. D., W. P. Sijp, and M. H. England

2013. Vertical Heat Transport by the Ocean Circulation and the Role of Mechanical and Haline Forcing. *Journal of Physical Oceanography*, 43(10):2095–2112.

Zika, J. D., B. M. Sloyan, and T. J. McDougall

2009. Diagnosing the Southern Ocean Overturning from Tracer Fields. *Journal of Physical Oceanography*, 39(11):2926–2940.